Washington University in St. Louis
Washington University Open Scholarship

McKelvey School of Engineering Theses & Dissertations | McKelvey School of Engineering

Summer 8-15-2018

Brain-Computer Interfaces using Electrocorticography and Surface Stimulation

Jesse Wheeler
Washington University in St. Louis

Follow this and additional works at: https://openscholarship.wustl.edu/eng_etds

 Part of the Biomedical Engineering and Bioengineering Commons, and the Biophysics Commons

Recommended Citation

Wheeler, Jesse, "Brain-Computer Interfaces using Electrocorticography and Surface Stimulation" (2018). *McKelvey School of Engineering Theses & Dissertations*. 382.
https://openscholarship.wustl.edu/eng_etds/382

This Dissertation is brought to you for free and open access by the McKelvey School of Engineering at Washington University Open Scholarship. It has been accepted for inclusion in McKelvey School of Engineering Theses & Dissertations by an authorized administrator of Washington University Open Scholarship. For more information, please contact digital@wumail.wustl.edu.

WASHINGTON UNIVERSITY IN ST. LOUIS
School of Engineering and Applied Science
Department of Biomedical Engineering

Dissertation Examination Committee:
Daniel W. Moran, Chair
Dennis L. Barbour
Eric C. Leuthardt
Kevin J. Otto
Lawrence H. Snyder

Brain-Computer Interfaces using Electrocorticography and Surface Stimulation

by

Jesse J. Wheeler

A dissertation presented to
The Graduate School
of Washington University in
partial fulfillment of the
requirements for the degree
of Doctor of Philosophy

August 2018
St Louis, Missouri

© 2018, Jesse J. Wheeler

Table of Contents

List of Figures

List of Tables

Acknowledgements

First, I want to thank my family and friends for their consistent support (and prodding) that helped me to complete this work.

I'd like to thank Robert Dunbar who first recognized and encouraged my interest in neurotechnology, and Glen Reitz, who helped me get my start in research related to brain-computer interfaces as a young undergraduate student.

I am very thankful for Donna Reedy, Adam Rouse, Jordan Williams, Tom Pearce, Piyush Karande, Johnathan Landes, and all the other members of the Moran and Leuthardt Labs who provided countless thoughtful discussions and invaluable assistance throughout this body of work.

I'd also like to thank my colleagues at Draper Laboratory for their patience and support while I was writing this dissertation.

Thanks also to my thesis committee for their encouragement and guidance.

I'd like to acknowledge the Cognitive, Computational Systems Neuroscience training grant sponsored by the National Science Foundation that provided financial support for this work and facilitated multi-disciplinary studies with a diverse cohort of very talented researchers.

Last of all, a very special thank you to Dan Moran who mentored me through both my undergraduate studies and doctoral work. I'm forever grateful for your guidance and friendship.

Jesse J. Wheeler

Washington University in St. Louis
July 2018

Abstract

The brain connects to, modulates, and receives information from every organ in the body. As such, brain-computer interfaces (BCIs) have vast potential for diagnostics, medical therapies, and even augmentation or enhancement of normal functions. BCIs provide a means to explore the furthest corners of what it means to think, to feel, and to act—to experience the world and to be who you are. This work focuses on the development of a chronic bi-directional BCI for sensorimotor restoration through the use of separable frequency bands for recording motor intent and providing sensory feedback via electrocortical stimulation. Epidural cortical surface electrodes are used to both record electrocorticographic (ECoG) signals and provide stimulation without adverse effects associated with penetration through the protective dural barrier of brain. Chronic changes in electrode properties and signal characteristics are discussed, which inform optimal electrode designs and co-adaptive algorithms for decoding high-dimensional information. Additionally, a multi-layered approach to artifact suppression is presented, which includes a systems-level design of electronics, signal processing, and stimulus waveforms. The results of this work are relevant to a wider range of applications beyond ECoG and BCIs that involve closed-loop recording and stimulation throughout the body. By enabling simultaneous recording and stimulation through the techniques described here, responsive therapies can be developed that are tuned to individual patients and provide precision therapies at exactly the right place and time. This has the potential to improve targeted therapeutic outcomes while reducing undesirable side effects.

Chapter 1

Introduction

1.1 Brain-computer Interfaces (BCIs)

Over recent years, there has been a growing interest in BCIs for both medical and non-medical applications. The brain connects to, modulates, and receives information from every organ in the body. As such, connections to the brain provide vast potential for diagnostics, medical therapies, and even augmentation or enhancement of normal functions. Connections to the brain provide a means to explore the furthest corners of what it means to think, to feel, and to act—to experience the world and to be who you are.

Connections to the brain can take many forms and can be categorized in many ways. Brain interfaces can be described by the signal modality that they use, which includes electrical, magnetic, acoustic, chemical, optical, and more. Brain interfaces can also be described by one-way transmission of information to or from the brain, or bi-directional transmission. Brain interfaces can also be described by their location relative to the brain and surrounding tissue, which may be invasive (within the brain), minimally-invasive (near to the brain), or non-invasive (outside of the body). Finally, brain interfaces can be described by the application in which they are used, including motor, auditory, visual, memory, neuropsychiatric, and more.

In the past, the term brain-computer interface referred to the requisite percutaneous connection between the brain and an external computer to provide the intensive processing for

both read and write functionality. However, recent advances in micro-electronics, embedded processing, miniaturized hermetic packages, and telemetry have enabled next-generation implantable and wearable systems that no longer resemble the large external computer systems of the past. Accelerated advancements in neurotechnology will surely continue to re-define brain-computer interfaces and create new capabilities and applications beyond imagination. This body of work represents a step in that direction, with the aim to develop a minimally-invasive bi-directional BCI.

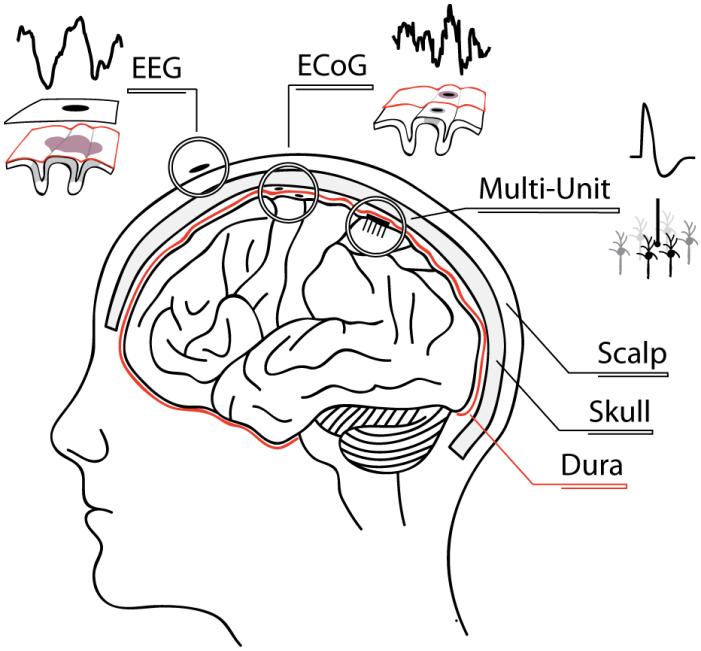

Figure 1.1: Common BCI Modalities

Illustration of three different BCI modalities that can be characterized as invasive (multi-unit microelectrodes), minimally-invasive (ECoG surface electrodes), and non-invasive (EEG scalp electrodes). Also illustrated are the types of signals and scale of spatial resolution associated with each modality.

This work focuses on the development of a bi-directional BCI based upon cortical surface electrodes with read capability to control movement in a virtual environment and write capability to deliver virtual sensory feedback via electrocortical stimulation. Cortical surface electrodes are used to record electrocorticographic (ECoG) signals without penetrating the brain, which is an attractive modality for a brain interface because 1) it is minimally-invasive—located outside of the brain, and 2) it has the potential for high spatiotemporal resolution due to its electrical modality and proximity to the brain beneath the skull. This is in contrast to other electrical modalities like

micro-electrodes, which are invasive and suffer chronic degradation due to foreign body responses, and electroencephalography (EEG), which is non-invasive and suffers from poor resolution.

While the focus of this work is on ECoG and electrocortical stimulation, the results are broadly applicable to other modalities and uses. For example, the ECoG electrode analyses presented can be applied to microelectrodes and electrodes designed for the peripheral nervous system. The signal analyses presented can be applied to EEG and local field potentials (LFPs). The co-adaptive algorithm presented in this thesis can be applied to other BCI modalities and any general framework in which humans and machines must interact and learn together. And finally, the approach to a bi-directional BCI can be used with other modalities in the central or peripheral nervous systems and can be applied to a broad spectrum of applications that involve closed-loop neuromodulation.

1.2 Specific Aims

Two specific aims were selected for examination in this dissertation. The first aim was focused on examining fundamental characteristics of electrodes and their effects on chronic recording and stimulation, which spanned finite-element modeling, materials analysis, electrochemistry, and electrophysiology. The second was focused on the development of a bi-directional BCI system, which spanned hardware design, signal processing, hyper-dimensional statistics, novel algorithm development, and behavioral task design.

Aim 1: Evaluate the effects of electrode contact size and material coating on the recording and stimulation capabilities of chronically implanted epidural arrays. Platinum electrodes of varying size (ranging from 300-1200 μm) will be coated with

electrodeposited films of iridium oxide (IROX) and poly-(ethylenedioxythiophene) (PEDOT) and implanted over macaque monkey sensorimotor cortex. A combination of electrophysiological and electrochemical analyses will be used to track and model changes in impedances at the electrode-tissue interface and evaluate the impact on recording and stimulation. Results will guide the design of optimal electrode arrays for chronic bi-directional BCIs.

Aim 2: Assess the feasibility of a bi-directional BCI system capable of decoding volitional control signals in the presence of stimulation through the use of separable recording and stimulation frequency bands. A multi-stage amplification system will be designed to remove high-frequency artifacts and used to record epidural ECoG signals in the presence of electrocortical stimulation. This hardware will consist of a low-noise high-rail pre-amplification headstage that will attenuate high frequency signals prior to amplification and digitization of desired low-frequency signals in a subsequent stage. Both performance of the hardware and the ability to accurately decode motor control signals in the presence of stimulation will be evaluated

1.3 Dissertation Organization

The experiments conducted in support of this dissertation were performed between 2008 and 2012 and focused on early non-human primate studies. Results from these studies were subsequently used to guide two translational human studies with paralyzed volunteers: first, for restoration of movement through the control of a neuroprosthetic device (Wang et al., 2013), and second for sensory restoration through direct cortical surface stimulation (Hiremath et al., 2017). Additionally, results from these studies have guided the development of several advanced closed-

loop neuromodulation systems at Draper Laboortory that will provide transformative capabilities beyond what I could have imagined when I began this work nearly a decade ago (Wheeler et al., 2015).

The following dissertation is organized such that each chapter builds upon the results of previous chapters. Chapter 2 begins with an in-depth study of the electrode-tissue interface and explores how electrode size and material affect stimulation and recording capabilities in chronic implants. Chapter 3 builds upon chronic impedance data and models and explores how electrode size and material affect ECoG signal quality over time. In addition, a series of analyses are performed to better characterize ECoG signals, specifically driving toward what is signal and what is noise. Chapter 4 builds upon these signal characteristics to develop a motor BCI capable of multi-dimensional control. A key innovation here is the development of a co-adaptive algorithm to accelerate learning and performance, which has broader impact in any application involving human-machine interactions. Finally, Chapter 5 builds upon results from the motor BCI to incorporate simultaneous stimulation toward a fully bi-directional BCI. Here, stimulation of sensory cortex is explored for producing virtual sensory percepts, and the design and performance of an artifact suppressing amplifier is described, which enables ECoG signals to be recorded during simultaneous stimulation. Results from Chapter 5 extend behond neuroprosthetics with applications in a number of next-generation closed-loop neuromodulation therapies.

Chapter Title	Aim 1	Aim 2
2 – Electrodes for Epidural ECoG Recording and Stimulation	X	
3 – Characteristics of Chronic ECoG Recordings	X	
4 – A Motor BCI: Multi-dimensional Control using a Coadaptive Decoder		X
5 – A Bi-directional BCI: Control with Sensory Feedback		X

Table 1.1: Organization of the Dissertation Regarding Aims

Chapter 2

Electrodes for Epidural ECoG Recording and Electrocortical Surface Stimulation

2.1 Introduction

2.1.1 An Overview of Epidural Electrodes

Electrocorticographic recordings (ECoG) and electrocortical stimulation through surface electrodes have become well-established in modern clinical and research applications. ECoG recordings and electrocortical stimulation were pioneered by Penfield in the 1930s to map cortex and identify epileptogenic foci in the treatment of epilepsy (Penfield, 1939) (Penfield & Boldrey, 1937). While the first documented use of ECoG recordings in a human patient utilized epidural electrodes, subdural electrodes have become the standard in modern intraoperative epileptic monitoring and mapping. However, in recent years, epidural electrocortical stimulation has been increasingly used in a number of clinical applications, such as the treatment of pain (Zaghi, Heine, & Fregni, 2010), depression (Kopell et al., 2011; Nahas et al., 2010), aphasia (Balossier, Etard, Descat, & Vivien D, 2012), stroke (Brown, Lutsep, Cramer, & Weinand, 2003; M. Huang et al., 2008; Levy et al., 2008; Yamamoto et al., 2011), and a variety of movement disorders (Katayama, Oshima, Fukaya, Kawamata, & Yamamaoto, 2002; Nguyen, Pollin, Fève, Geny, & Cesaro, 1998; Romito et al., 2007). Likewise, epidural ECoG has gained attention as a high-resolution alternative to invasive intracortical and subdural recordings for brain control of neuroprosthetic devices (Moran, 2010; A. G. Rouse, Williams, Wheeler, & Moran, 2013; Adam G Rouse & Moran, 2009;

J. J. Williams, Rouse, Thongpang, Williams, & Moran, 2013) and has been the focus of next-generation closed-loop devices capable of modulating therapies based upon real-time cortical recordings (A G Rouse et al., 2011; Stanslaski et al., 2012).

A notable advantage of epidural electrodes is that they avoid disruption of the dura that provides a protective barrier around the central nervous system. Penetration of the dura is associated with serious health risks including edema, infarction, hematomas, encephalitis, and infection, which may be exacerbated by cerebral spinal fluid (CSF) leakage (Fountas, 2011). Unlike penetrating microelectrodes that are capable of recording neural action potentials due to their small interfacial surface area and proximity to neural sources, larger-area epidural electrodes record field potentials resulting from integrated neural activity (Moran, 2010). Reactive tissue responses severely diminish the efficacy of indwelling microelectrodes for recording and stimulation by increasing electrode impedance, which consequently reduces the strength of neural signals, increases thermal and current noise, and requires larger voltages to drive electrical stimulation. While epidural electrodes avoid many of the risks associated with penetration of the dura, little is known about how epidural electrode function is affected by contact size and material as quantified by chronic *in vivo* changes in impedance.

Traditionally, surface electrodes have been constructed of platinum (Pt) metal disks ranging from 1 to 5 mm in diameter with interdisk spacings of 5-10 mm. Recent advances in fabrication techniques have enabled the development of high-density micro-scale electrode arrays that are printed onto thinner, more flexible substrates with the intent of providing higher resolution recording and stimulation capabilities (Kim, Wilson, Williams, Microfabrication, & Arrays, 2007; Molina-Luna et al., 2007; Rubehn, Bosman, Oostenveld, Fries, & Stieglitz, 2009). However, decreased electrode size comes at the cost of increased impedance, which adds noise to recordings

and decreases the range of current that can be safely applied during stimulation (Merrill, Bikson, & Jefferys, 2005; Shannon, 1992). The application of conductive coatings to microelectrodes has been shown to dramatically reduce impedances in vitro, and for short periods in vivo (Cogan & Model, 2006; Rylie a Green, Lovell, Wallace, & Poole-Warren, 2008; Lu et al., 2010; Ludwig et al., 2011; Luo, Weaver, Zhou, Greenberg, & Cui, 2011; Venkatraman et al., 2011; Wilks, Koivuniemi, Thongpang, Williams, & Otto, 2009; Wilks, Richardson-burns, Hendricks, Martin, & Otto, 2009). However, the long-term effectiveness and durability of coatings have not been assessed for larger micro- to milli-scale chronically implanted cortical surface electrodes. Therefore, this study aimed to quantify the effects of electrode size and material on the impedances of micro- to milli-scale electrodes and provide a detailed account of impedance changes associated with chronically implanted epidural electrode arrays.

2.1.2 Current Exchange Across the Electrode-Tissue Interface

At the electrode-tissue interface, the total current flow between the electrical device and surrounding tissue results from both faradaic (resistive) and non-faradaic (capacitive) processes. Faradaic currents involve the movement of electrons across the electrode-electrolyte interface due to electro-chemical redox reactions at the electrode surface. The impedance to faradaic current flow is dependent upon the availability of conduction electrons in the metal electrode, the associated redox reaction rates, and the mass transport of reactants and products to and from the interface. Non-faradaic currents result from charging and discharging the electrical "double-layer" formed by opposing charges on either side of the electrode-tissue interface, without the movement of charge across the electrode surface. The impedance to non-faradaic current flow is directly

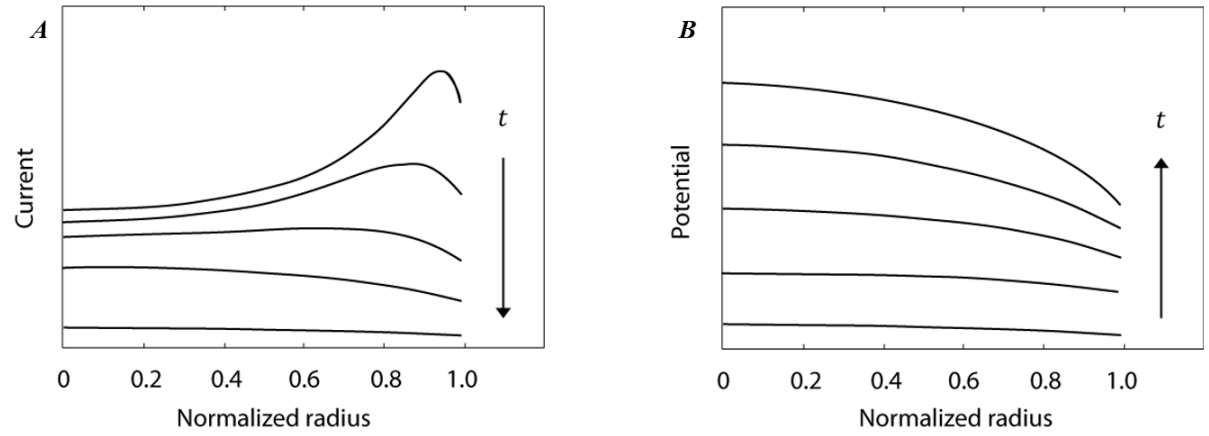

Figure 2.1: Current and Potential Distributions on the Surface of an Electrode

Illustrations of the evolution of the current density **(A)** and the potential distribution **(B)** across the surface of a disk electrode. At $\boldsymbol{t = 0}$, the current is highest at the edges while the potential is uniform across the electrode surface. With increasing time, the high-current edge effects diminish and the potential distribution at the center of the disk increases relative to the edges. As $\boldsymbol{t \to \infty}$, and reactants are depleted at the electrode surface, the current distribution will become flat, and the potential will be largest in the center. Illustrations are based upon (Newmann 1966) and (Behrend et al. 2008).

related to the effective capacitance of the electrode-tissue interface which can be influenced by surface adsorption or adhesion of atoms, ions, biomolecules, and gases. Both faradaic and non-faradaic impedances depend upon the electrode material, interactions with the surrounding media, and the electrochemical area available to participate in redox reactions and charge storage. (For a review of the electrode-tissue interface, see Cogan 2008; Brummer et al. 1983; Geddes & Roeder 2003).

When a step current is applied to an electrode, the current density is initially highest at the corners and edges of the electrode but shifts toward the center at a rate determined by locally-distributed time constants. These time constants (and the non-uniform distributions) are dynamic and depend upon the geometry and material of the electrode, the nature of reactions mediating charge transfer, and the concentration gradients of reactants in solution. Analytic equations for distributions associated with resistive planar disk electrodes were first derived by Newman-

(Newman, 1966a) and later by Rubinstein for recessed electrodes (Rubinstein, Spelman, Soma, & Suesserman, 1987). Under the assumptions of a uniform potential across the surface of the electrode and negligible effects of mass-transport and reaction kinetics (these are valid for high-frequency waveforms) the current density is described by the *primary distribution.* The primary distribution predicts that the current density at the center of a disk electrode will be approximately half of the average (or global) current density, and the density at edges will approach infinity (Newman, 1966b). From the primary distribution, Newman derived an asymptotic high-frequency solution resistance, $R_{sol} = 1/4\sigma r$, where σ reflects the conductivity of the surrounding media and r is the electrode radius.

When mass-transport and reaction kinetics cannot be ignored (i.e. for low-frequency waveforms) and reactants are depleted at the electrode surface, the steady-state current distribution will become uniform, and the potential distribution will become non-uniform. Newman also analytically derived this potential distribution, which is characterized by an arched profile where the potential is larger in the center of the disk than the edges (Newman, 1966b). Simulations of time-varying distributions associated with capacitive electrodes also show non-uniformities in response to voltage steps (Behrend, Ahuja, & Weiland, 2008; Myland & Oldham, 2005). In these simulations, initial current densities peak near the periphery, but subsequent tangential currents quickly redistribute the current density toward a more uniform distribution across the surface of the electrode. These results suggest that high frequency impedances should be a function of electrode circumference while low frequencies should be dependent upon the electrode area. While these predictions have been experimentally verified with bench top measurements in saline (Ahuja, Behrend, Whalen III, Humayun, & Weiland, 2008) it remains to be known how

impedances relate to electrode radius *in vivo*. Electrical conduction across the electrode-tissue interface is further detailed in the Appendix.

2.1.3 Characteristics of Electrode Materials and Conductive Coatings

Noble metals like platinum have provided suitable, reversible charge exchange for stimulation and low impedances for recording with large-area chronically implanted electrodes, but their utility for micro- and milli-scale electrodes has been limited. Highly conductive materials like metal oxides and intrinsically conductive polymers are promising alternatives to platinum for sub-millimeter diameter electrodes, but a long-term head-to-head evaluation in chronic implants is lacking. When comparing different electrode materials for chronic implants, the biocompatibility, toxicity, and stability must be considered in addition to metrics specific to the utility of the electrode for stimulation and recording applications. Electrical conduction of electrode materials is further detailed in the Appendix.

The utility of an electrode material for stimulation is often assessed by the cathodal charge storage capacity (CSC_c) determined from ramped cyclic voltammetry (CV). The CSC_c quantifies the amount of charge that can be delivered within the voltage limits of hydrolysis, or the "water window" (Cogan, 2008). The most suitable measure of an electrode's utility for recording is the electrical impedance determined from electrochemical impedance spectroscopy (EIS). Electrical impedances should be measured within a frequency range appropriate for the spectral content of the recorded signal. Impedance measures are generally not well-suited for inferences regarding stimulation since they are based upon an assumption of linearity about a fixed point (typically the open cell potential) according to the small signal approximation. During stimulation, voltage

excursions often extend well outside this linear range. It has become standard in the literature to report the 1 kHz impedance of electrodes, which coincides with the dominant spectral power of action potentials that have widths of about 1 ms. In far-field cortical recordings, like ECoG, signal power decreases at approximately 1/frequency such that the noise floor (which is determined by the electrodes and amplifier) prohibits signal resolution above several hundred hertz. The dominant frequencies of interest for ECoG include the beta-band (15 Hz – 30 Hz) and gamma-band (60 Hz – 120 Hz) (J. J. Williams et al., 2013). Therefore, it is proposed that the 100 Hz impedance should be reported when evaluating electrodes for ECoG.

Platinum metal is one of the most common and well-studied electrode materials and is standard in many implantable bioelectric interfaces (Brummer & Turner, 1975, 1977a, 1977b) . Platinum is a noble metal and has been shown to be non-toxic (Dymond, 1976) and non-reactive (Stensaas & Stensaas, 1978) in long-term implants. Charge exchange across the platinum electrode occurs via faradaic (hydrogen atom plating, Pt oxide formation and reduction) and non-faradaic (double-layer charging) processes (Cogan, 2008; Merrill et al., 2005). The faradaic reactions are considered pseudo-capacitive since they are confined to a surface monolayer and are easily reversed so products do not accumulate in surrounding tissues. Although platinum provides a very stable interface for recording and stimulation with large-area electrodes, as the electrode area decreases, alternative materials are necessary to maintain high charge injection capacities and low impedances.

Iridium oxide (IROX) has gained popularity as a superior electrode material due to its large electrochemical surface area and ability to quickly and reversibly inject charge. While traditionally formed by electrochemical activation of the surfaces of iridium electrodes (AIROF), iridium oxide films can also be applied to other metals by reactive sputtering in oxidizing plasma

(SIROF) or by electroplating from solution (EIROF). Charge exchange in iridium oxide is pseudo-capacitive and involves the transition between the Ir^{3+} and Ir^{4+} redox states within the oxide. IROX has been shown to be biocompatible (Agnew, Yuen, Mccreery, & Clayton, 1986; Göbbels et al., 2010) and offers a dramatically improved charge injection capacity and impedance characteristic compared to platinum (Cogan, 2008). However, the instability of IROX following sustained stimulation *in vitro* raises questions regarding its suitability for chronic implants where stability is imperative (Wilks, Richardson-burns, et al., 2009).

Poly (3,4-ethylenedioxythiophene) (PEDOT) is an intrinsically conductive polymer with a high electronic and ionic conductivity that can be polymerized with a wide variety of counter-ions and biomolecules to alter its morphology and biocompatibility. PEDOT is most commonly polymerized with either poly (styrene sulfonate) (PSS) or para (toluene sulfonate) (pTS) as a counter-ion to enhance conductivity, solubility, and stability. Arguments for PSS emphasize its larger size and molecular weight compared to pTS, which may help to physically trap the dopant within the polymer, and improve stability (Rozlosnik, 2009). Arguments for pTS emphasize its superior biocompatibility as determined by cytotoxicity studies (R. A. Green, Poole-warren, Lovell, & Member, 2007). PEDOT coatings on microelectrodes have out-performed IROX with respect to charge injection capacity and impedance. In addition, coatings show moderate stability following sustained stimulation in saline (Wilks, Richardson-burns, et al., 2009) and after 2 weeks post-implantation in rat cortex without repetitive stimulation (Venkatraman et al., 2011). Although PEDOT stands out as one of the most promising conductive coatings for implantable neural prostheses, its long-term performance in comparison to IROX and uncoated platinum remains unknown.

2.1.4 Wound-healing and the Foreign Body Response

The biotic response to an implant involves both wound healing and immunoreactive processes, which are commonly referred to as the 'foreign body response'. Wound healing is initiated by the process of implantation, whereas the foreign body response implicates the presence of an indwelling foreign material for an extended period. While a distinction between the cause and nature of these processes is apparent, they proceed simultaneously and are interactive, such that the severity of one may worsen the other. Implantation of epidural arrays involves the disturbance of the scalp, skull, and dura, but does not breach the dural lining, as illustrated in Figure 2.2. Wound healing and immunoreactive responses involving CNS-specific processes are expected to be minimal, if not absent from the overall biotic response. Detailed histological studies of the biotic response specific to epidural cortical implants are lacking, although general pathologies of wound healing and immunoreactive processes are well documented. Comprehensive reviews have been provided by Stroncek & Reichert 2008 and Anderson et al. 2009 and a summary as it pertains to epidural implants is provided here.

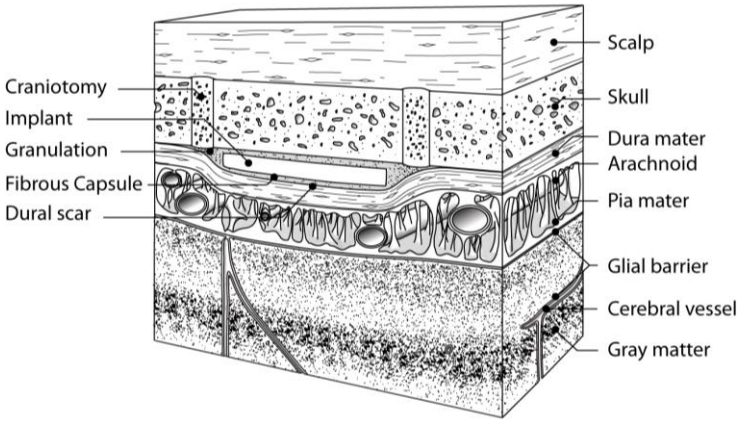

Figure 2.2: Implanted Electrode and Surrounding Tissue

Illustration of the placement of an implanted epidural electrode array in relation to the underlying meningeal layers, like the dura, and surrounding tissues. Expected tissue responses from wound healing and the foreign body response are indicated around the craniotomy and sub-cranial space, which include granulation, fibrosis, and dural scaring.

Hemostasis and inflammation occur immediately following implantation and may persist for as long as a week post-implantation. During hemostasis, disrupted blood vessels release peripheral blood

cells, plasma, proteins, and other molecules into the wound site created during implantation. An accumulation of fluid and necrotic tissue may cause edema and pressure surrounding the implant. Proteins, such as albumin, fibrinogen, and others will adsorb to the surface of the implant to form a matrix for subsequent macrophage activity. Macrophages that bind to the adherent protein layer on the implant surface often undergo cytoskeletal remodeling to form multinucleated foreign body giant cells (FBGC) that encapsulate the implant. The phenotypes of FBGCs depend upon surrounding environmental signals. For epidural cortical implants, FBGCs near overlying injured skull may express osteoclast markers, whereas FBGCs near underlying abraded dura may express fibroblast markers. Prolonged adhesion of macrophages and FBGCs to the implant's surface creates a harsh microenvironment between the implant and the encapsulating tissue that may lead to oxidation, pitting, cracking, and corrosion. (Stroncek & Reichert 2008; Anderson et al. 2009).

Primary tissue repair will commence within days to weeks, which includes increased cell proliferation, capillary budding, and the synthesis of extracellular matrix (ECM). The ECM provides scaffolding for granulation cells and fibroblasts to fill voids in the tissue surrounding the implant. Similarly, voids in bone will be filled with osteoblasts that secrete layers of collagen and bone matrix that will mineralize over subsequent weeks and form lamellar bone. Following primary tissue repair, remodeling and secondary tissue repair will occur, where fibrotic tissue will progressively align and condense to reduce the wound size, and eventually form a dense fibrous scar that may become tightly adhered to adjacent dura and skull. Likewise, bone will harden and regain its pre-injured strength. (Stroncek & Reichert 2008; Anderson et al. 2009).

2.1.5 Relationship Between Impedance and Tissue Response

The nature and severity of the biotic response may have drastic consequences on the function of an implanted bioelectric device partly due to changes in the electrical properties of the electrode and surrounding tissue. Changes in electrode impedance may be caused by etching due to the release of corrosive agents like free radicals, enzymes, and acids from macrophages and FBGCs via "frustrated phagocytosis" (Anderson et al., 2009), or by adsorption of ions, proteins, and gases to the electrode surface (Newbold et al., 2010). Impedance changes in surrounding tissue may be caused by edema, accumulation of ECM, and the formation of dense fibrotic encapsulation tissue (J. C. Williams, Hippensteel, Dilgen, Shain, & Kipke, 2007). The biotic processes which affect the impedances of electrodes and tissue will vary over the life of the implant, and consequently, so will the function of the implanted bioelectric device.

Histological analyses are the standard for assessing the biotic response around electrodes, but the necessary methods limit evaluations of time-varying responses in living animals. Impedance spectroscopy provides an alternative non-destructive measure of the biotic response through the use of equivalent circuit models for both electrodes and tissue. A variety of circuit models for each have been described and compared elsewhere (Franks, Schenker, Schmutz, & Hierlemann, 2005; Lempka et al., 2009; McConnell, Butera, & Bellamkonda, 2009; J. C. Williams et al., 2007) and generally consist of a combination of resistive and capacitive circuit elements to mimic the frequency-dependent (dispersive) changes in the dielectric properties of the electrode or biological material. These dispersions appear as semi-circular arcs when complex impedance data are plotted in the Nyquist plane (reactance vs resistance). The two dominant dispersions

observed in *in vivo* impedance spectra are the low-frequency α-dispersion, which is caused by counter-ion diffusion, and the high-frequency β-dispersion, which is caused by the charging of cellular membranes (Grimnes, Rikshospitalet, & Schwan, 2002). The evaluation of high-frequency β-dispersions in complex impedance data has been used to assess tissue accumulation around a variety of implanted electrodes (Lempka et al., 2009; McConnell et al., 2009; J. C. Williams et al., 2007). Furthermore, sufficiently large stimulation through electrodes has been shown to reduce the presence of β-dispersions, and presumably the extent of encapsulation tissue through "rejuvenation" (Johnson, Otto, & Kipke, 2005; Lempka et al., 2009; Otto, Johnson, & Kipke, 2006). Therefore, tracking the impedance spectra of implanted electrodes provides both a quantitative assessment of their bioelectric function and an indirect, non-destructive measure of the chronic biotic response.

2.2 Purpose of the Study

This study aims to provide a direct side-by-side comparison of the behavior and utility of electrodes of varying size and material for stimulation and recording, as determined by CSC_c and impedance, respectively. *In vitro* experiments in PBS were used to assess the effects of coating and size on charge exchange and impedance in the absence of the biotic response via CV and EIS measurements. *In vivo* experiments in chronically implanted animals were used to assess the long-term stability of coatings as well as the effects of contact size in the presence of reactive tissue responses via EIS. Stimulation and CV were excluded from *in vivo* experiments in order to minimize rejuvenation effects that might alter the natural biotic response. Collectively, these experiments are intended to provide a comprehensive understanding of electrode behavior with

respect to the conductive material, contact size, and tissue response in order to guide the development and use of chronically implanted bioelectric devices.

2.3 Methods

2.3.1 Electrode Array Design

The thin-film electrode arrays were constructed using MEMs fabrication techniques and consisted of three primary layers. The bottom and top insulation layers were constructed of 12 µm thick spin-coated polyimide (HD4110, HD Microsystems), and the middle layer of 50 µm wide interconnecting traces and electrode contacts was formed by photolithography and metal deposition of chromium (10 nm), gold (200 nm) and platinum (20 nm) for a total thickness of 230 nm. The flexible electrode arrays were based upon a folding design in which all electrode contacts faced downward *toward* the cortex and the references and ground faced upward *away* from the cortex (Figure 2.3). The purpose of the upward-facing references and ground was to create "quiet" electrical references for ECoG recording, where signals generated by cortex would be largely silenced compared to global common-mode noise. The downward-facing electrodes consisted of 32 disc-shaped contacts arranged in rows of four interleaved diameters (300 µm, 600 µm, 900 µm, and 1200 µm). The two designated references were also disc-shaped contacts of 300 µm and 1200 µm diameter. A large-area (36.8 mm^2) "H"-shaped pad was used to both shield the references and provide a stable low-impedance electrical ground. The polyimide substrate was also punctated by rows of 500 µm perforations to improve the "biological transparency" of the implant by facilitating transport and signaling through the device. Electrode contacts on two of the six implanted arrays were coated with activated iridium oxide, and another two arrays were coated with PEDOT:pTS.

Electrode contacts on the remaining two arrays, as well as the ground pads on all arrays, were left as uncoated platinum.

2.1.1 Electrochemical Methods

All electrochemical processes were conducted with an Autolab Potentiostat/Galvanostat PGSTAT12 (Eco Chemie, Utrecht, Netherlands) with a built-in frequency response analyzer (FRA2, Brinkmann Instruments, Westbury, NY). *In vitro* electrodeposition, CV, and EIS were performed within a Faraday cage and utilized a three-electrode configuration, where the electrode

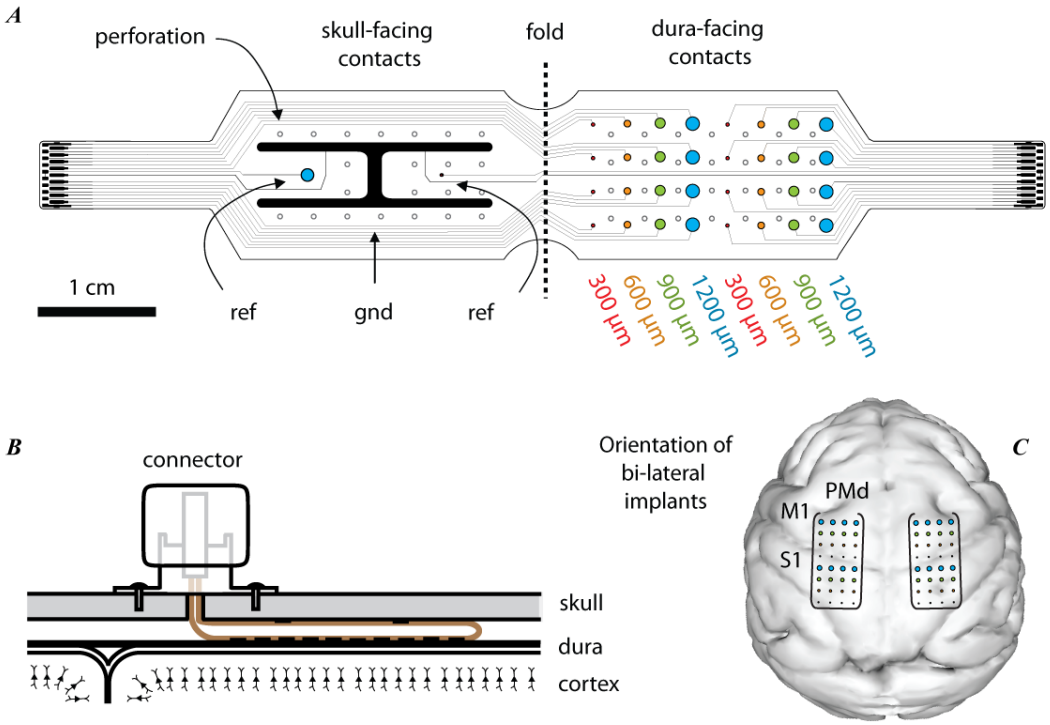

Figure 2.3: Thin-film Electrodes for Chronic Impedance Characterization

Thin-film polyimide arrays were constructed using MEMs fabrication processes and consisted of platinum disk electrode contacts printed onto a flexible polyimide substrate that was punctated by perforations for improved biological transparency **(A).** Arrays were based upon a folding design where 32 electrode contacts of four different sizes faced downward toward the cortical surface and two references and a large-area ground faced upward toward the overlying skull as shown in **(B)**. Six arrays were implanted bilaterally into the epidural spaces of three macaque monkeys, covering primary motor (M1) and primary somatosensory (S1) cortex **(C)**. Two of the implanted arrays consisted of uncoated platinum electrodes, two with electrodes coated with EIROF, and two with coatings of PEDOT.

contact served as the working electrode (WE), a large-area platinum wire served as the counter electrode (CE) and an Accumet, gel-filled, KCl saturated calomel electrode (SCE) served as the reference electrode (RE). *In vitro* CV and EIS were performed in 1X phosphate buffered saline (PBS). Because polyimide is known to absorb water, all arrays were soaked in PBS for at least 30 minutes prior to testing in order to achieve steady-state hydration. *In vivo* EIS utilized a two-electrode configuration where the electrode contact served as the working electrode (WE) and the large-area ground served as both the counter electrode (CE) and reference electrode (RE). CV data recorded for each electrode represented the mean of three cyclic voltage ramps between -0.6 V and 0.8 V at a rate of 1 V/s. EIS data were measured in response to voltage-controlled 25 mV (rms) sinusoids with logarithmically spaced frequencies spanning 3 Hz to 15 kHz. CV and EIS were performed on each array in PBS to assess the quality of coatings prior to implantation. Beginning the first day post-implantation, EIS measurements were recorded 2-3 times per week at regularly spaced intervals throughout the lifetime of each implant. (For a review of electrochemical methods, refer to Cogan 2008 or Bard & Faulkner 2001). The underlying theory of these electrochemical methods is further detailed in the Appendix.

Electrodeposited iridium oxide films (EIROF) were formed from an aqueous solution of 4 mM $IrCl_4$, 40 mM oxalic acid, and 340 mM K_2CO_3 brought to a pH of about 10.3 that had rested in darkness for 48 hours. The iridium oxide film was formed by applying 50 cyclic voltage ramps between 0 V and 0.55 V (vs Ag/AgCl) at 50 mV/s followed by 1600 1 Hz pulses between the same voltage limits. (Marzouk et al., 1998; Meyer, Cogan, Nguyen, & Rauh, 2001; Yamanaka, 1989). PEDOT was electrochemically deposited and polymerized from an aqueous monomer solution of 0.1 M ethylenedioxythiophene (EDOT) and 0.05 M paratoluene sulfonate (pTS) dissolved in 50% DI water and 50% acetonitrile. PEDOT:pTS coatings were formed by applying a galvanostatic

current of 2 mA/cm^2 for 7.5 min. (R a Green et al., 2013). All electrodes were rinsed in deionized water, stored dry in sealed plastic containers, and sterilized in an ethylene oxide gas chamber prior to implantation.

2.3.2 Epidural Implantation of Electrode Arrays

Six electrode arrays were surgically implanted bi-laterally into three male juvenile macaque monkeys under anesthetic conditions and using aseptic surgical techniques. With the animal's head fixed on a standard stereotaxic frame, two 22 mm craniotomies were performed over each hemisphere. Through each craniotomy, surrounding dura was carefully detached from the overlying skull to produce a subcranial pocket into which the arrays could be easily placed without damage to the applied conductive coatings or underlying cortex. Each array was positioned approximately parallel to the midline and spanned primary motor (M1) to primary sensory (S1) cortex. The arrays were pseudorandomly assigned to each monkey to ensure that each coating combination (Pt-EIROF, EIROF-PEDOT, and PEDOT-Pt) was represented within a monkey. Once the arrays were implanted and the craniotomies sealed, high-density zero insertion force (ZIF) connectors (Tucker Davis Technologies, Alachua, FL) were used to access each electrode channel for regular *in vivo* impedance measurements.

2.4 *In Vitro* Results

2.4.1 Randles Circuit Model for the Electrode-Tissue Interface

The *in vitro* data are well-described by the behavior of a simple Randles circuit model (Figure 2.5A). Although more complex models have been described elsewhere (Geddes, 1997),

the simplicity of the Randles circuit allows for direct and meaningful interpretations of data. In the model presented here, the series resistor, R_s, represents a spreading resistance that is equal to Newmann's radius-dependent solution resistance, R_{sol}. The parallel resistor, R_p, represents the impedance to faradaic current flow across the electrode interface. The parallel capacitor, C_p, represents the impedance to non-faradaic current flow due to double-layer charging and discharging.

Following the standard systems approach of transforming the time-varying representation of a system to a frequency-varying representation via the Laplace transformation, the normalized current expected from a voltage signal applied to the Randles circuit is given by:

$$\frac{I(s)}{A} = \frac{V(s)}{A\,Z(s)} = \frac{V(s)G(s)}{A} \tag{2.1}$$

$$\frac{G(s)}{A} = \frac{1 + sR_pC_p}{A\left[\left(R_s + R_p\right) + sR_sR_pC_p\right]} \tag{2.2}$$

where $G(s)$ is the non-normalized transfer function. In terms of the area-normalized specific resistance and capacitance:

$$R_p' = R_pA \text{ and } C_p' = C_p/A \tag{2.3}$$

$$\frac{G(s)}{A} = \frac{1 + sR_p'C_p'}{\left(AR_s + R_p'\right) + sAR_sR_p'C_p'} \tag{2.4}$$

Assuming the series resistance is equal to Newman's solution resistance, $R_s = R_{sol} = 1/4\sigma r$:

$$R_s' = R_s A = \pi r / 4\sigma \tag{2.5}$$

$$\frac{G(s)}{A} = \frac{1 + sR_p'C_p'}{\left(R_s' + R_p'\right) + sR_s'R_p'C_p'} \tag{2.6}$$

Therefore, I/A is fully described by normalized parameters (marked by $'$) where R_p' and C_p' are geometry-independent material properties and R_s' is proportional to the electrode radius.

The impedance of the of the Randles circuit is given by the reciprocal of $G(s)$:

$$\frac{V(s)}{I(s)} = Z(s) = \frac{1}{G(s)} = \frac{\left(R_s + R_p\right) + sR_sR_pC_p}{1 + sR_pC_p} \tag{2.7}$$

Using systems terminology, the transfer function for impedance is in the form of a first-order low-pass filter with a pole located at $-1/R_pC_p$ and a zero located at $-\left(R_s + R_p\right)/R_sR_pC_p$. The corresponding time constant for this system is $\tau = R_pC_p$.

Based upon these derivations, when modeling current densities, the Randles circuit is described by $R_s' = area \times R_{sol}$, $R_p' = area \times R_p$, and $C_p' = C_p/area$. For disk electrodes, $R_s' = \pi r/4\sigma$, which increases linearly with radius, while R_p' and C_p' are constants that represent the area-independent specific resistance and capacitance of the electrode material. Simulated effects on CV and EIS due to changes in the model's parameters are illustrated in Figure 2.5. These simulated effects are useful for both developing an intuition about the behavior of the electrode-electrolyte interface and interpreting the actual CV and EIS data.

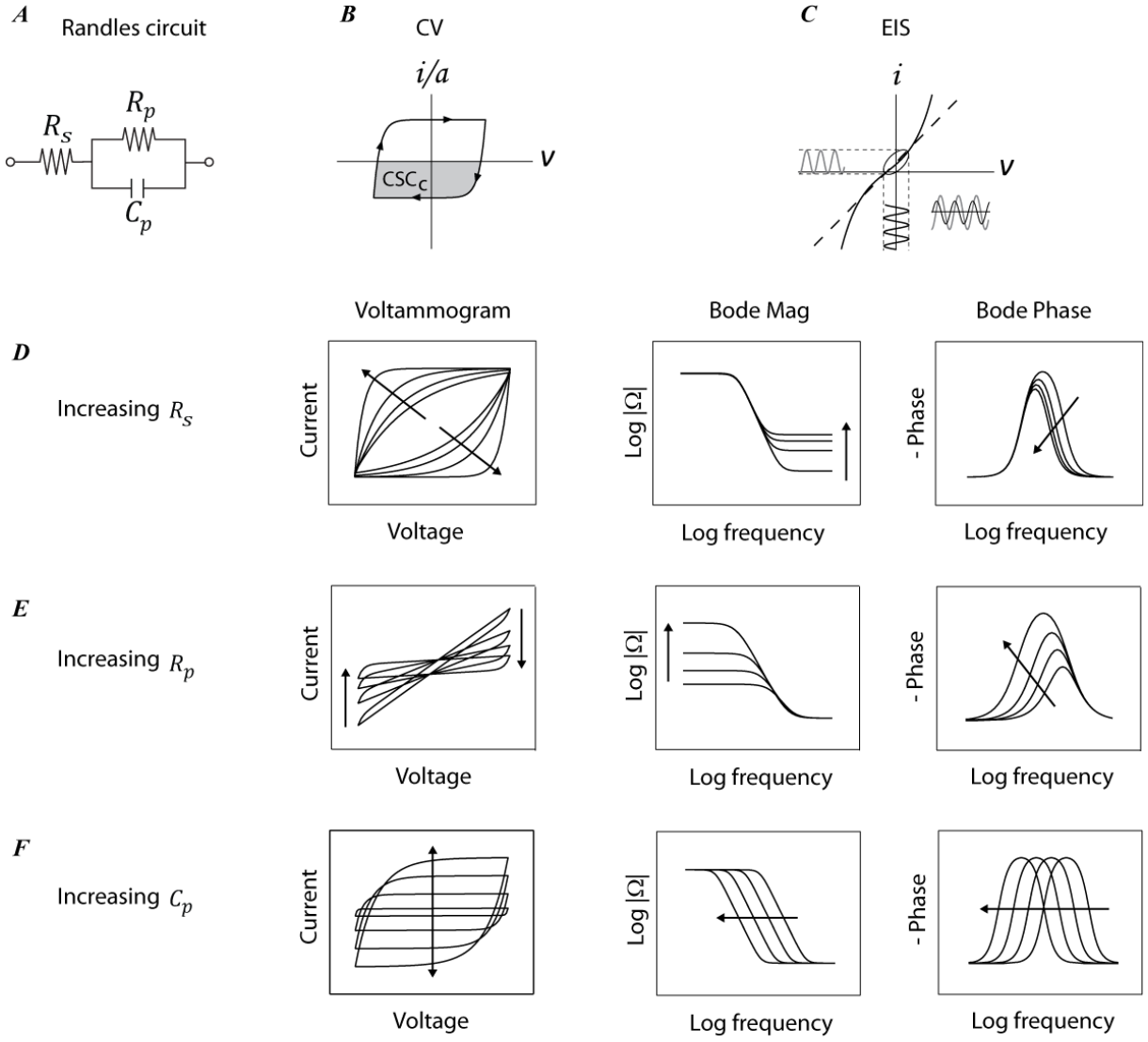

Figure 2.5: Effects of Randles Electrode Model Parameters on CV and EIS

Randles circuit model **(A)** with effects on CV **(B)** and EIS **(C)** data due to variations in the series resistance $\boldsymbol{R_s}$ **(row D)**, parallel resistance $\boldsymbol{R_p}$ **(row E)**, and parallel capacitance $\boldsymbol{C_p}$ **(row F)** with all other parameters held fixed.

2.4.2 Coatings Increase Charge Exchange for Stimulation Electrodes

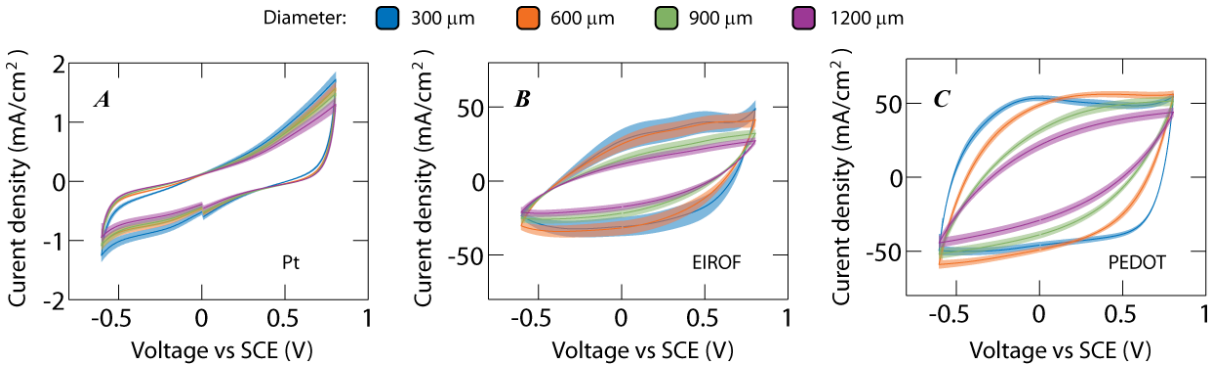

Figure 2.6: Effects of Coatings and Size on Cyclic Voltammograms

Plots show normalized CVs (1V/s) for each coating and electrode diameter. Differences in CV profiles between materials are dominated by the effect of increased interfacial capacitance in order from Pt **(A)** to EIROF **(B)** to PEDOT **(C).** Differences in CV profiles between electrode sizes are dominated by the effect of increased spreading resistance with decreased electrode diameter (as illustrated in Figure 2.5).

Results from *in vitro* CVs show that EIROF and PEDOT coatings dramatically improve charge exchange through increased interfacial capacitance and decreased interfacial resistance. Electrodes with smaller diameters were associated with higher normalized CSC_cs as shown in Figure 2.6. The normalized CSC_cs is the integral within the voltammograms in Figure 2.7, which are normalized by the geometric surface area of the electrode. It is important

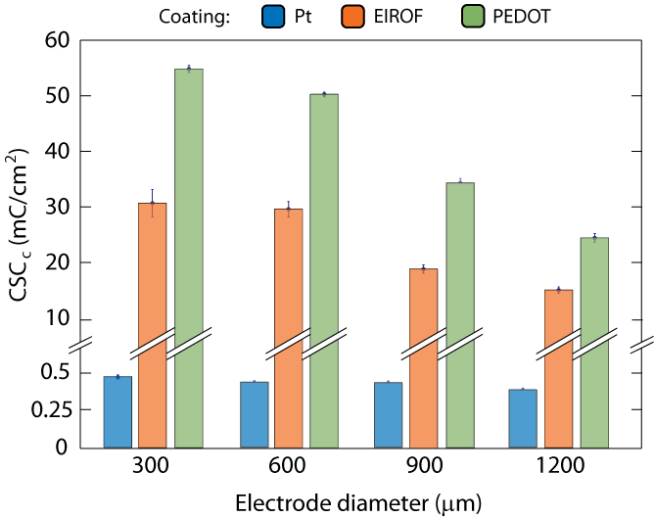

Figure 2.7: Effects Coatings and Size on CSC

Normalized CSC_c for each coating and electrode diameter show significant increases from Pt to EIROF to PEDOT for all electrode sizes. The increasingly "box-like" CV profiles of small-diameter electrodes resulted in larger normalized CSC_C for all coatings as a consequence of the lower normalized spreading resistance ($\boldsymbol{Rs' = \pi r/4\sigma}$).

to note that these results *do not* suggest that coatings were more effective on smaller diameter electrodes. Instead, the increasingly "box-like" CV profiles associated with smaller diameters are a result of decreased values of R_s' in the normalized Randles model, which correspond to increases in Newman's solution resistance (see simulated CV effects in Figure 2.5). Both EIROF and PEDOT coatings significantly increased the CSC_c of all electrode sizes, with PEDOT providing a nearly 2-fold increase over EIROF. For the smallest diameter electrodes (300 µm), CSC_c increased from 0.5 ± 0.2 mC/cm^2 with platinum to 30.9 ± 22.1 mC/cm^2 with EIROF and 55.1 ± 10.2 mC/cm^2 with PEDOT. For the largest diameter electrodes (1200 µm), CSC_c increased from 0.4± 0.1 mC/cm^2 with platinum to 15.3 ± 9.3 mC/cm^2 with EIROF and 24.7 ± 11.6 mC/cm^2 with PEDOT.

2.4.3 Coatings Decrease Impedance Magnitudes and Phase Lags for Recording Electrodes

The impedance magnitudes of coated electrodes (EIROF and PEDOT) were significantly lower than uncoated platinum electrodes (Figure 2.8A). Coatings reduced impedances magnitudes most dramatically at low frequencies compared to high frequencies (for 300 µm diameter contacts, magnitudes decreased by approximately two orders of magnitude at 100 Hz vs one order of magnitude at 1kHz). PEDOT impedance magnitudes were significantly lower than EIROF, but only by about half. Below 1kHz, the impedance magnitudes of uncoated platinum electrodes showed an approximate $1/f$ ($f^{-0.89}$) relationship to frequency. Near 10 kHz, impedance magnitudes of platinum flattened and approached asymptotic levels as predicted by Newman's equation for solution resistance (R_S). Impedance spectra of coated electrodes were approximately flat compared to platinum, which indicates a very low interfacial resistance. Interestingly,

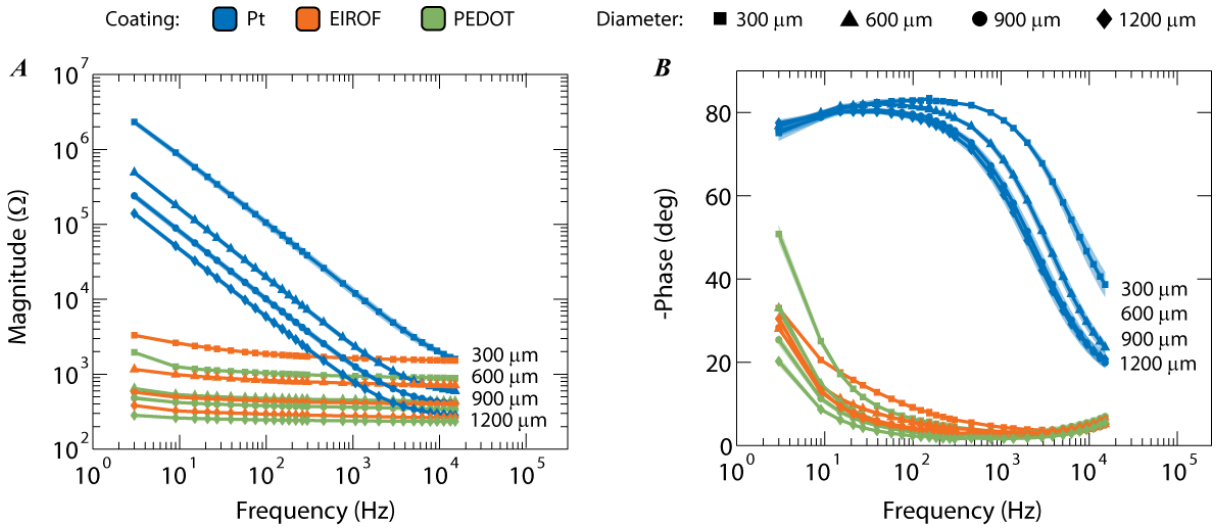

Figure 2.8: Effects of Coatings and Size on EIS

Plots show impedance magnitudes **(A)** and phase lags **(B)** combined across all electrodes by coating (color) and size (symbol). Coated electrodes had significantly lower impedances and phase lags than uncoated platinum electrodes across all contact sizes. The decrease in magnitude and leftward shift in phase lag between Pt and coated electrodes is characteristic of increased interfacial capacitance and lower interfacial resistance. The separation of magnitudes at high frequencies is an effect of increased spreading resistance with smaller electrodes.

asymptotic R_S levels for EIROF were approximately equal to or slightly higher than platinum at high frequencies.

The impedance phases of coated electrodes were significantly lower than uncoated platinum electrodes (Figure 2.8B). Like impedance magnitudes, the difference in phase shifts between coated and uncoated electrodes was largest between 10 Hz to 1 kHz (for 300 µm diameter contacts, the phases lags were reduced by approximately 80 degrees at 100 Hz). Generally, the differences in phase lags between PEDOT and EIROF were not large and not significantly different. The phase lags of uncoated platinum electrodes transitioned from approximately -90 degrees at the lowest frequencies toward 0 degrees at high frequencies near 10 kHz. The phase lags of coated electrodes were significantly lower than uncoated electrodes across all frequencies and appeared to transition toward -90 degrees at low frequencies below 10 Hz. The difference in phase spectra

between platinum and coated electrodes was consistent with a leftward shift toward lower frequencies associated with an increase in the interfacial capacitance of the coated electrodes.

2.4.4 Coatings Shift the Impedance-radius Relationship Toward Circumference Dependence

The relationship between impedance magnitude and contact radius was well-described by a power-law relationship $Z = 1/r^{\alpha}$. The value of the radius exponent was determined by linear regression of log-impedance onto log-diameter, where the slope of the line indicated the exponent of the power law for each material (Figure 2.9A). Exponents were frequency-dependent and ranged between -1 (a $1/r$ relationship, indicating a circumference-dependence) and -2 ($1/r^2$,

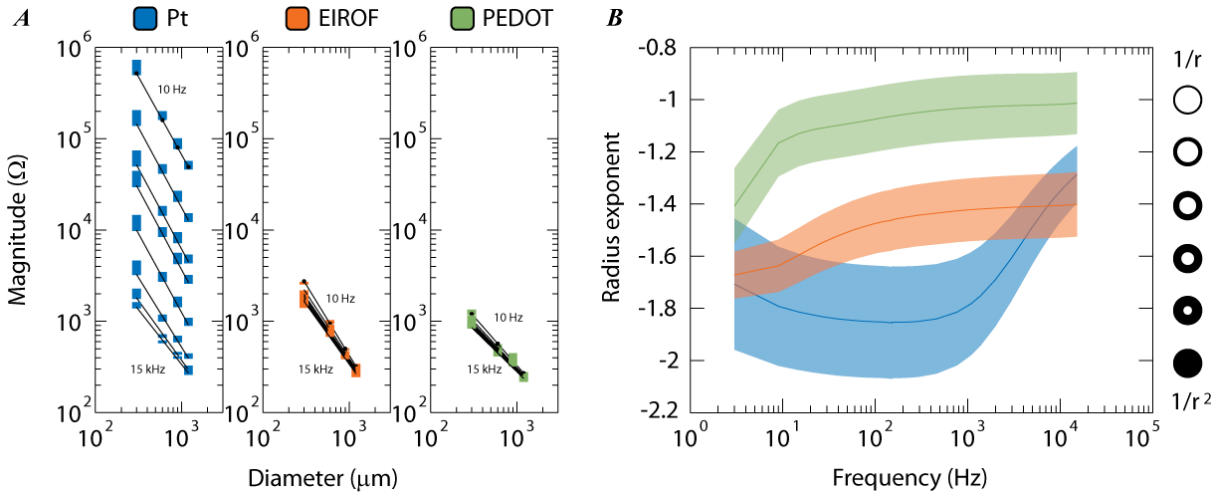

Figure 2.9: Relationship between Electrode Radius and Impedance

Linear regressions of log-diameter vs log-impedance **(A)** and frequency-dependence of regression slopes **(B)** for each material show how impedances are related to electrode diameters according to the power law: $Z=1/r^{\alpha}$. Shaded areas in **(A)** indicate 1 standard deviation around the mean impedance of each size group. Shaded areas in **(B)** indicate 95% confidence intervals of the regression slopes. The slopes of the regression lines in log-log space are equal to the exponent (α) of the power-law relationship between impedance magnitude and the electrode radius. Platinum electrodes showed an area-dependence at frequencies below 3 kHz (exponent = -1.5) and a circumference-dependence at frequencies above. The impedance magnitudes of PEDOT electrodes were approximately circumference dependent across all frequencies, while those of EIROF fell between platinum and PEDOT.

indicating an area-dependence) (Figure 2.9B). For platinum, the power-law exponent indicated a mid-way transition (α = -1.5) at 3 kHz between area-dependence at low frequencies and a circumference-dependence at high frequencies. PEDOT showed a circumference-dependence at all frequencies above 10 Hz. EIROF demonstrated behavior in between platinum and PEDOT. Results for platinum are consistent with those reported by Ahuja (Ahuja et al., 2008). At high frequencies the capacitance of electrodes allowed current to discharge across the edges of the electrode-tissue interface faster than charge could accumulate tangentially toward the center of the electrode. At low frequencies, current exchange across the interface was slower and allowed time for a more uniform current distribution to form across the electrode surface. For EIROF, and particularly, PEDOT electrodes, high interfacial capacitance and low interfacial resistance likely facilitated very rapid current flow through the edges of electrodes even at relatively low frequencies.

2.5 *In Vivo* Results

Following implantation of the arrays, impedances of all electrodes were measured every 2-3 days for the duration of the implant in order to track how impedances change during wound healing and in the presence of immunoreactive tissue responses. Prior to detailed analyses, a 3-way (size x coating x subject) ANOVA (MATLAB, *anovan*) was conducted to determine the significance and effect size of each factor. The results of the ANOVA indicated that both size and coating effects were large (>10% variance explained) and significant ($p < 0.01$) in the first week, but only size was large and significant beyond the third month. At all time points and frequencies, electrode size effects accounted for the largest percentage of variance. Subject effects were significant at various time points but were always very small (<3% variance explained). Therefore,

for detailed analyses of size and coating effects, data were grouped according to size and coating across subjects. To emphasize long-term trends in impedances over day-to-day variability, impedance time courses were smoothed with a 3-pt filter. All shaded regions indicate standard errors of the mean.

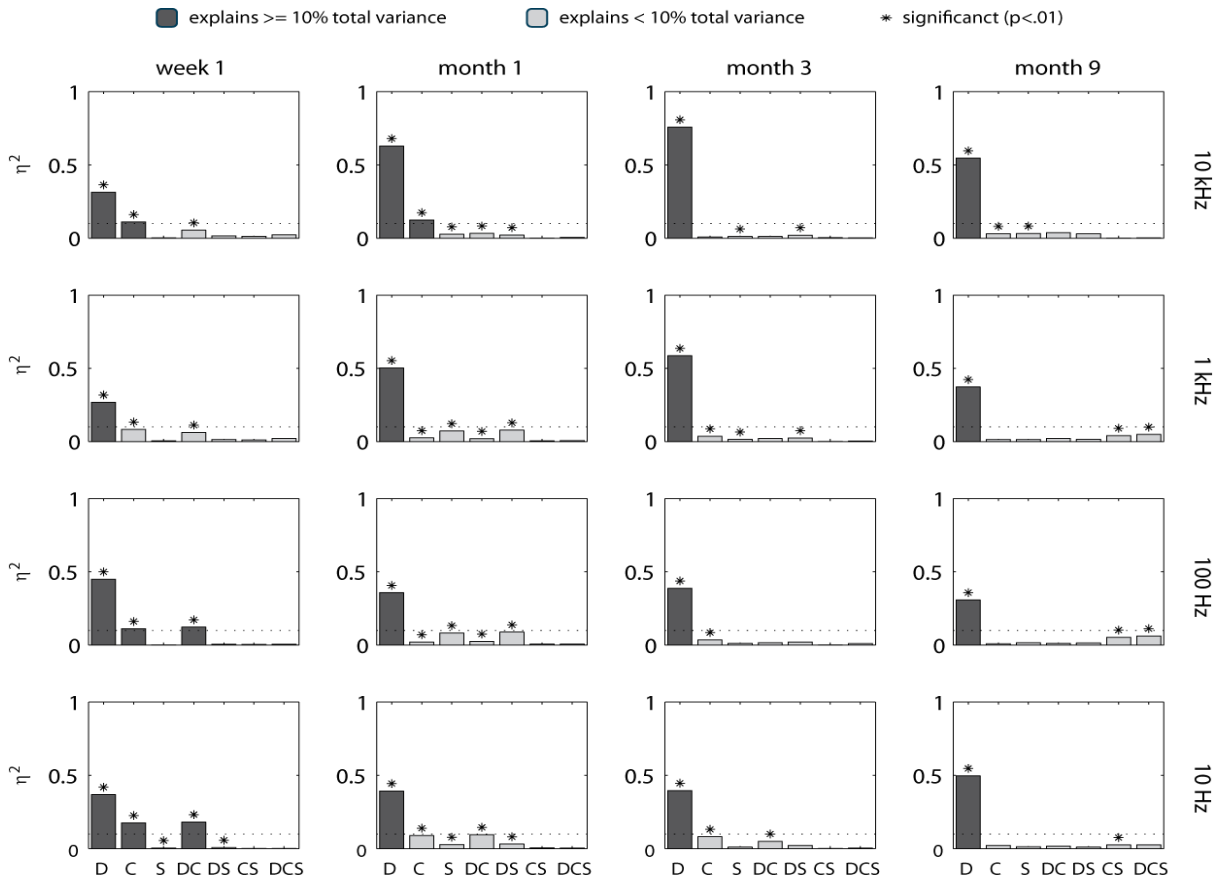

Figure 2.10: ANOVA Analyses for Impedances Related to Diameter, Coating, and Subject

Main and interaction terms in a 3-way ANOVA model: D = diameter, C = coating, S = subject (monkey). The results show that electrode diameter accounted for the largest significant difference in impedance for tested frequencies of 10 Hz, 100 Hz, 1kHz, and 10kHz. Coating was also significant, but accounted for less variance.

2.5.1 Coatings Provide Temporary Reductions in Impedance

Coated electrodes had lower impedance magnitudes and phase lags than uncoated electrodes for all contact diameters investigated, but the effects did not persist beyond three months post-implantation. As shown by the time courses of 100 Hz impedance magnitudes (Figure 2.11A) and phase lags (Figure 2.11B) profiles were closely matched across subjects for arrays with the same coatings, and all time courses converged at about 3 months. In Figures 2.11C-E, data from each of the pairs of coated arrays were combined across subjects and examined further to determine impedance effects across the entire frequency spectrum at week 1, month 3, and month 9. During the first week, the smallest diameter (300 μm) platinum, EIROF, and PEDOT electrodes had average 100 Hz impedances of 103.3 kΩ, 71.1 kΩ, and 11.1 kΩ, and average 100 Hz phase lags of -71.7 deg, -40.5 deg, and -19.9 deg, respectively. Similarly, the largest diameter (1200 μm) platinum, EIROF, and PEDOT electrodes had average 100 Hz impedances of 10.0 kΩ, 6.8 kΩ, and 3.5 kΩ, with phase lags of -53.3 deg, -20.6 deg, and -11.1 deg, respectively. During the first week, EIROF impedance magnitudes were only significantly lower than platinum below 100 Hz (interestingly, EIROF impedances were slightly higher than platinum at frequencies greater than 1 kHz), while PEDOT impedance magnitudes were significantly lower than platinum at all frequencies. The phase lags of coated electrodes during the first week were significantly lower than platinum below 10 kHz. By the third month, coating effects were greatly diminished for all electrode sizes, and by the ninth month coating effects were effectively gone, and only electrode size effects remained. Therefore, the subsequent analyses of size effects focus on platinum rather than coated electrodes.

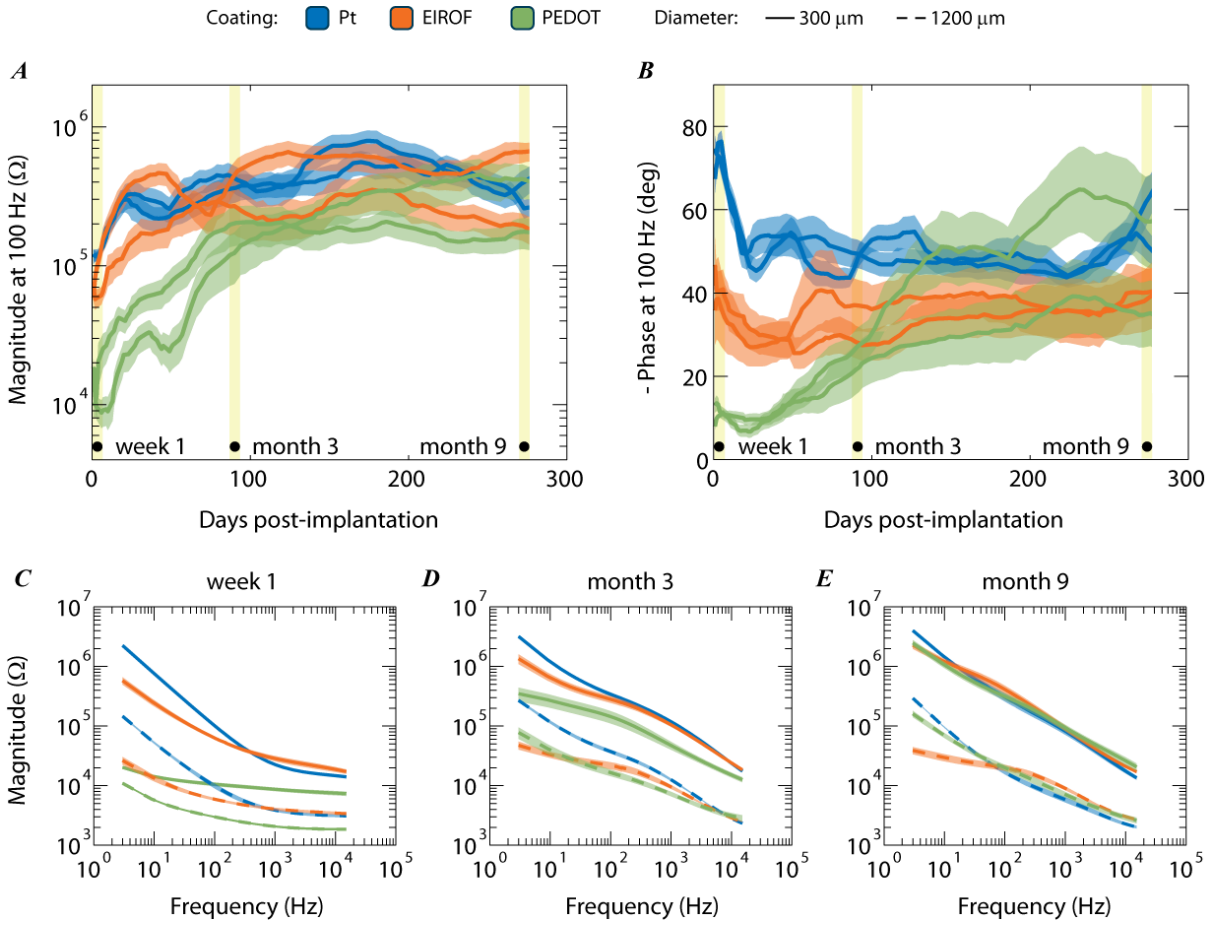

Figure 2.11: Chronic Changes in Electrode Impedances Dependent upon Coating

Impedance magnitudes **(A)** and phase lags **(B)** measured at 100 Hz are shown from 300 µm diameter electrodes on all six arrays over a 9 month period. Initially, coatings reduced both impedances and phase lags, but after 3 months the effect was greatly diminished. **C-E)** Impedance spectra combined across all arrays by coating and size are shown for the week 1, month 3, and month 9 time points highlighted in **A** and **B**. Colors indicate coatings, and solid and dashed lines represent the smallest (300 µm) and largest (1200 µm) electrode diameters. While all impedances were significantly different in week 1 (with the exception of platinum and EIROF at high frequencies), their differences were small at month 3, and no longer different by month 9 (with the exception of 1200 µm platinum and EIROF at extremely low frequencies). At month 9, coating effects were diminished to the point that impedances across all coatings simply grouped according to electrode diameter alone.

2.5.2 Impedance Effects of Electrode Size

Larger electrode contact sizes resulted in lower impedances throughout the duration of each implant, regardless of the electrode material. As shown in Figure 2.12A, the time courses of 100 Hz impedance magnitudes for the two platinum arrays followed similar profiles. Impedance magnitudes were clearly grouped by size, with only small variations between animals. Size effects were not present in phase lags, which were closely grouped across all electrode diameters (Figure 2.12B). In Figures 2.12C-E, data from both platinum arrays were combined across animals and complete spectral data are presented for the week 1, month 3, and month 9 time points. During the first week, the impedance spectra resembled pre-implantation profiles below 1 kHz, with only a 2-fold increase in magnitudes. However, the high-frequency asymptote was increased nearly 9 fold, resulting in a lower corner frequency between the $1/f$ behavior and frequency-independent behavior. At month 3, there was a large increase in impedances between 50 Hz – 1 kHz, likely caused by the accumulation of encapsulation tissue. By month 9, the increased mid-frequency bulge settled toward initial *in vivo* levels, with impedance magnitudes demonstrating slightly less than $1/f$ behavior.

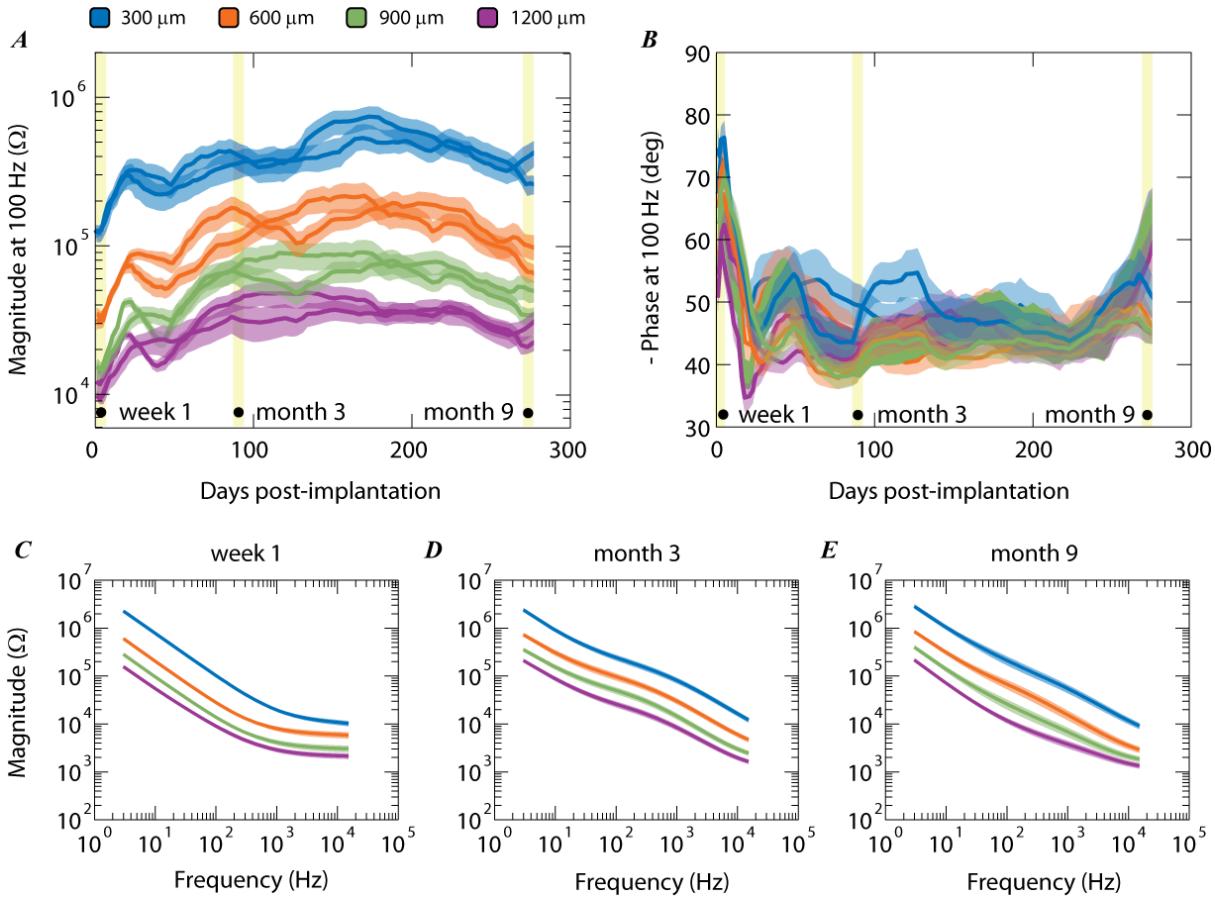

Figure 2.12: Chronic Changes in Electrode Impedances Dependent upon Size

Impedance magnitudes **(A)** and phase lags **(B)** measured at 100 Hz are shown for all electrode diameters from both of the platinum arrays over a 9 month period. Size effects on impedance magnitudes were significant and robust throughout the entire 9 months (and beyond) but were not significant for phase lags. **C-E)** Full impedance spectra combined across both arrays are shown for the week 1, month 3, and month 9 time points highlighted in **A** and **B**. Generally, all impedances aligned by electrode diameter, where larger sizes had consistently lower impedances.

2.5.3 A Shift in the Power-law Relationship Between Impedance and Electrode Radius

Throughout the duration of the implants, uncoated platinum electrodes demonstrated an approximate area-dependence at low frequencies and circumference-dependence at high frequencies, as was observed *in vitro*. During the first week post-implantation, the exponent of the power law describing the radius-impedance relationship shifted to circumference- dependence (from -2 toward -1). For example, the frequency where platinum electrodes showed behavior exactly between area- and circumference-dependence (exponent equals -1.5) shifted from about 3.5 kHz *in vitro* to about 250 Hz *in vivo*. Over the life of the implant, this mid-point frequency gradually shifted back to higher frequencies, and by month 9 was approximately identical to the *in vitro* frequency (Figure 2.13). This behavior is attributed to changes in the overall effective capacitance of the platinum electrode and tissue following implantation, which is supported by observed shifts in *in vivo*

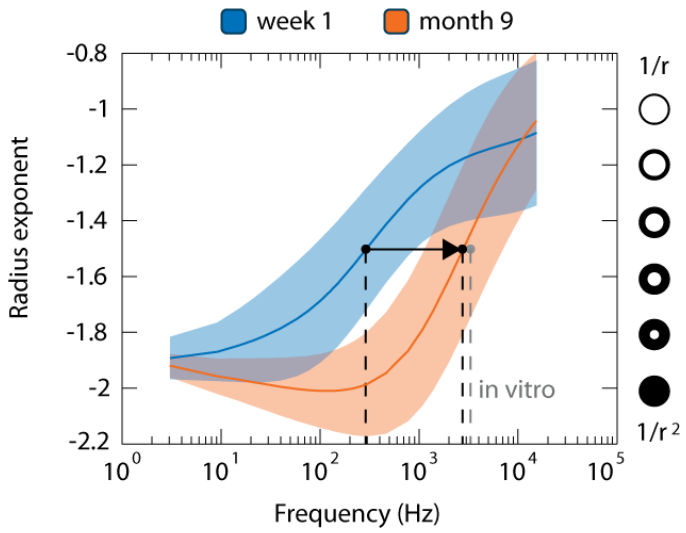

Figure 2.13: *In Vivo* Impedance Dependence on Radius

Shifts in the power law describing both early (week 1) and late (month 9) in vivo impedance dependence on radius in comparison to in vitro. In the first week post-implantation, the curve that indicates the transition between area-dependence and circumference-dependence was shifted toward lower frequencies. In the first week post implantation, the exponent (α) of the power-law relationship between impedance magnitude and the electrode radius ($1/r^{\alpha}$) of platinum electrodes shifted toward circumference-dependence compared to in vitro measurements in PBS. However, by month 9, the exponent curve transitioned to more closely align with in vitro values, where at 100 Hz, impedances were approximately area-dependent, and high frequencies above 3 kHz were circumference-dependent. (Shaded regions indicate 95% confidence intervals and dashed lines indicate frequencies corresponding to exponents equal to -1.5).

phase responses. During week 1 post-implantation, the phase responses of electrodes were leftward shifted toward lower frequencies (corresponding to higher capacitance), but steadily shifted to the right over following months toward levels similar to those observed *in vitro.*

2.5.4 The Stereotypical Impedance Response: Initial, Acute, Remodeling, and Chronic Phases

The impedance profiles of all electrodes (regardless of electrode size or material) followed a stereotyped 4-phase response in the first 100 days post implantation, consisting of an initial, acute, remodeling, and chronic period. Figure 2.14 shows the stereotyped 4-phase response for the 100 Hz impedances of all sizes on the two implanted platinum electrodes, which is centered within the mid- to high-gamma band commonly used in ECoG recordings. During the first 7 days,

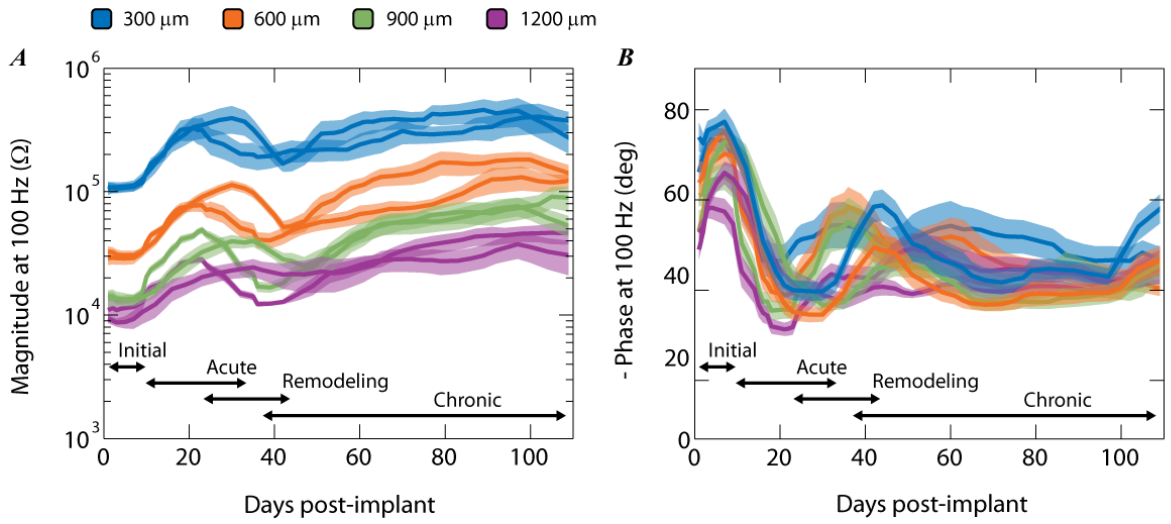

Figure 2.14: 4-Phase Chronic Impedance Response: Initial, Acute, Remodeling, and Chronic

The stereotypical 4-phase impedance response of all electrodes, characterized by an initial period (days 1-7), an acute period (days 7-30), remodeling period (days 25-45), and chronic period (beyond days 35-45) for both impedance magnitude **(A)** and phase **(B)**. During the initial period, impedance magnitudes were steady, but the phase lag increased. Following the initial period, impedance magnitudes increased, and phase lags decreased during both the acute and chronic periods, which were separated by a remodeling period in which both the magnitude and phase temporarily shifted back toward initial levels. This stereotyped response was observed across all electrodes regardless of size and coating.

electrode impedances demonstrated an initial response, where the impedance magnitude either decreased slightly or remained at a constant level as the phase lag increased. During the acute response in days 7-30, the impedance magnitude increased rapidly while the phase lag decreased. A remodeling phase occurred during days 25-45 where magnitudes dropped, and phase lags increased back toward initial impedance values. Finally, at about day 35, the chronic response began, during which time the impedance magnitudes and phases returned to levels previously observed in the acute response. After the second month impedances in the chronic phase remained mostly constant with only sporadic variations between subjects.

2.5.5 Constant Phase Element (CPE) and Cole Model for *In Vivo* Impedances

In vivo impedances involve electrical dispersions due to both the electrode-electrolyte interface and the surrounding tissue. For simplicity, the electrode is represented as a constant phase element (CPE), which is a generalization of a capacitive element that emerges from non-integer derivatives (fractional calculus). The CPE behavior of electrodes has been linked to adsorption, porosity, fractal surface roughness, and non-uniform current distributions (Brug, van den Eeden, Sluyters-Rehbach, & Sluyters, 1984; V. M.-W. Huang, Vivier, Frateur, Orazem, & Tribollet, 2007; McAdams, Lackermeier, McLaughlin, & Macken, 1995). The impedance of the tissue can be represented as a Cole model which is a generalization of the Randles model, where the capacitor is replaced by a CPE (Cole, 1940; Lempka et al., 2009; McConnell et al., 2009; Pliquett & Pliquett, 1999).

The following CPE-Cole model was used to model the electrode-tissue circuit and more accurately model *in vivo* impedance variations of the electrode and surrounding tissue. A constant phase element (CPE) was used to model the electrode, where the impedance is given by:

$$Z_e = \frac{K_e}{(j\omega)^{\alpha_e}} \tag{2.8}$$

Here, Z_e is the complex impedance of the electrode, K_e is a magnitude scaling factor, α_e is a normalized fractional exponent that determines the phase angle ($0<\alpha_e<1$), ω is the angular frequency (rad/s), and $j = \sqrt{-1}$.

The impedance spectra of tissue represented in the Nyquist plane appears as a semicircular arc with a locus positioned below the real-axis. Dispersive circuits that include capacitors result in similar arcs, but with loci positioned on the real axis. Based upon this observation, Cole proposed that tissue be represented with a model similar to the Randles circuit, but with the capacitor replaced by a CPE (Cole, 1940). The Cole tissue model provides added flexibility in fitting tissue impedance data by allowing the locus of the semicircle to drop below the real axis by adjusting the CPE exponent α. The Cole model used to represent the impedance of tissue is given by:

$$Z_t = R_\infty + \frac{\Delta R}{1 + (j\omega)^{\alpha_t}\Delta R/K_t} \tag{2.9}$$

Here, Z_t is the complex impedance of tissue,K_t and α_t are the magnitude and exponent of the parallel CPE, R_∞ is the resistance at infinite frequency, and ΔR is the difference between tissue resistance at DC (R_0) and infinite frequency (R_∞). In order to account for the shunt resistances

and capacitances of signal traces, impedances were measured from an array in PBS where each electrode contact was covered with a thick coating of insulating silicon. Shunt impedances were added in parallel to the CPE-Cole model during subsequent parameter fitting.

In order to determine how impedances associated with the electrode and with the tissue were changing over the first 100 days post-implantation, impedance data from platinum electrodes were fitted to the CPE-Cole model. Values for all six model parameters were determined for each electrode and day via minimization of a normalized loss function (Lempka et al., 2009). Parameter estimates for the model were calculated using the FMINCON function available in the MATLAB optimization toolbox (Mathworks, Natick, MA). A hybrid simulated annealing approach was used by performing 10 searches from randomized initial conditions in order to find the global minimum of the loss function:

$$J = \sum_{n=1}^{N} \frac{(Z_n' - \hat{Z}_n')^2}{{Z_n'}^2} + \frac{(Z_n'' - \hat{Z}_n'')^2}{{Z_n''}^2} \tag{2.10}$$

where n indicates the index of a given measured frequency, N is the total of measured frequencies, the superscripts $'$ and $''$ indicate the real and imaginary parts of the complex impedance, and $\hat{}$ indicates the estimated impedance from the model.

Parameters were estimated for each electrode and day in order to evaluate changes in impedances related to the electrode and tissue separately. Results of model-fitting show that initial changes in the overall impedance magnitudes were dominated by electrode effects, whereas all later changes were dominated by tissue effects. Early changes in the electrode model included increases in both the magnitude (K_e) and phase angle (α_e) of the electrode CPE. Thereafter, the

electrode model parameters were mostly constant, with only a slight decrease in phase angle (α_e) over time. Alternatively, tissue model parameters varied throughout the first 100 days, with ΔR showing the most size-specific distinctions. A key value in the Cole model is the P_y ratio

$$JP_y = \Delta R/(R_\infty + \Delta R) \tag{2.11}$$

which has been shown to be highly correlated with cell volume fraction of suspended cells (Pliquett & Pliquett, 1999) (due to increased cell density or hypertrophy) and also scar tissue around microelectrode implants (McConnell et al., 2009). Here, P_y increased both in the acute and chronic phases but decreased in the remodeling phase. This result supports the assertion that the acute and chronic phases were associated with cellular accumulation in the vicinity of the electrode, whereas, during the remodeling phase, cellular tissue was temporarily broken down or removed.

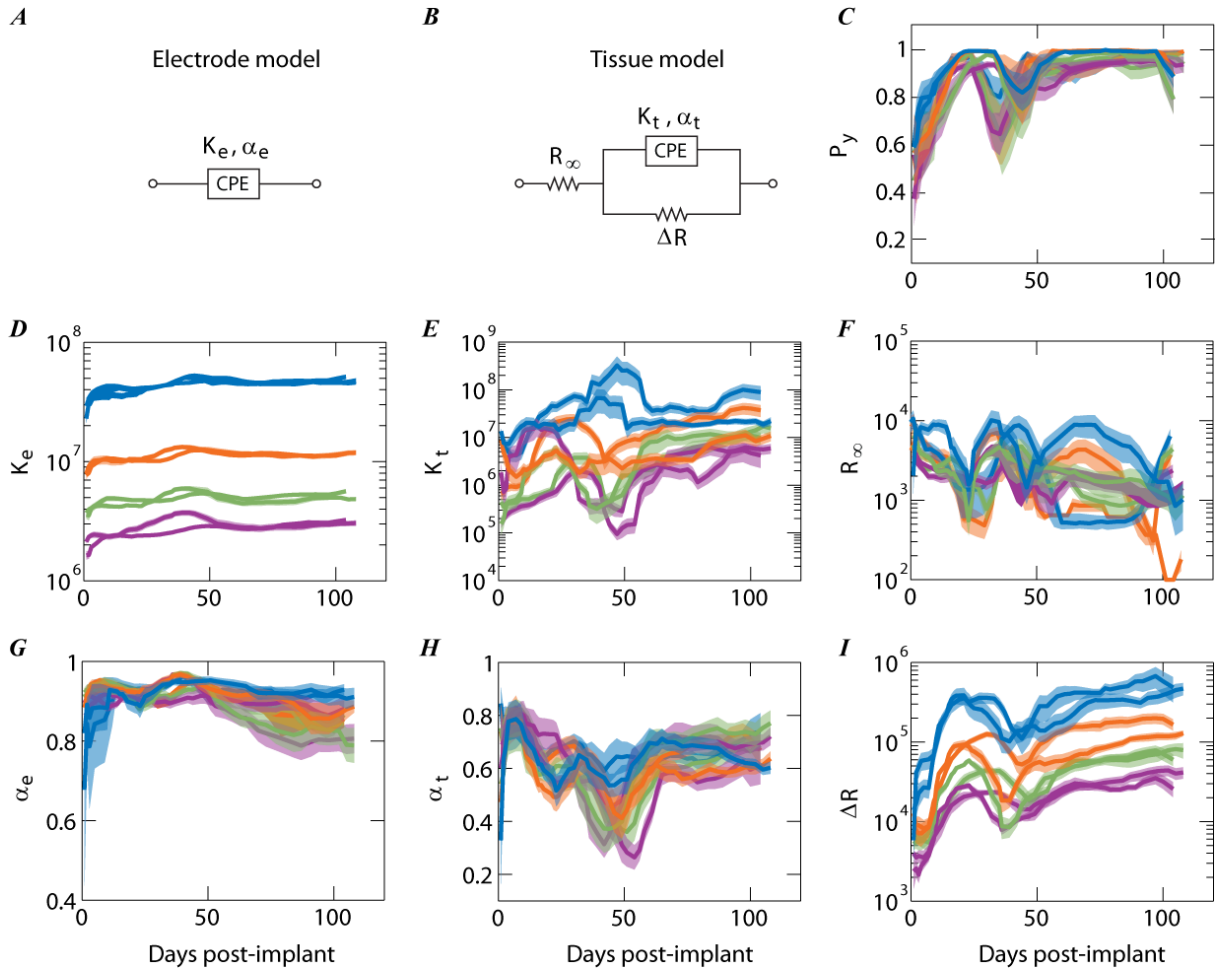

Figure 2.15: Modeling the Electrode-Tissue Impedance with Constant Phase Elements

Equivalent circuit models for platinum electrodes **(A)** and bulk tissue **(B)** along with their corresponding parameter values tracked over time. Time courses of electrode parameters **(D and G)** show an initial increase in CPE magnitude ($\boldsymbol{K_e}$) for all sizes along with an increase in the phase angle ($\boldsymbol{\alpha_e}$). Time courses of tissue parameters **(E, F, H, I)** show large variations throughout the first 100 days. The $\boldsymbol{P_y}$ ratio **(C)** indicates an increase in cell volume in both the acute and chronic phases, but a temporary dip in the remodeling phase.

2.5.6 Broad-spectrum Impedance Changes

Another way to look at impedance spectra is in the Nyquist plane where the imaginary (reactive) component is plotted against the real (resistive) component for all frequency points. Figure 2.16A shows Nyquist plots for an example 600 µm diameter platinum electrode at time points spanning the first 9 months following implantation. In these plots, each dot represents the impedance at a single measured frequency. Generally, impedances sweep from the upper right

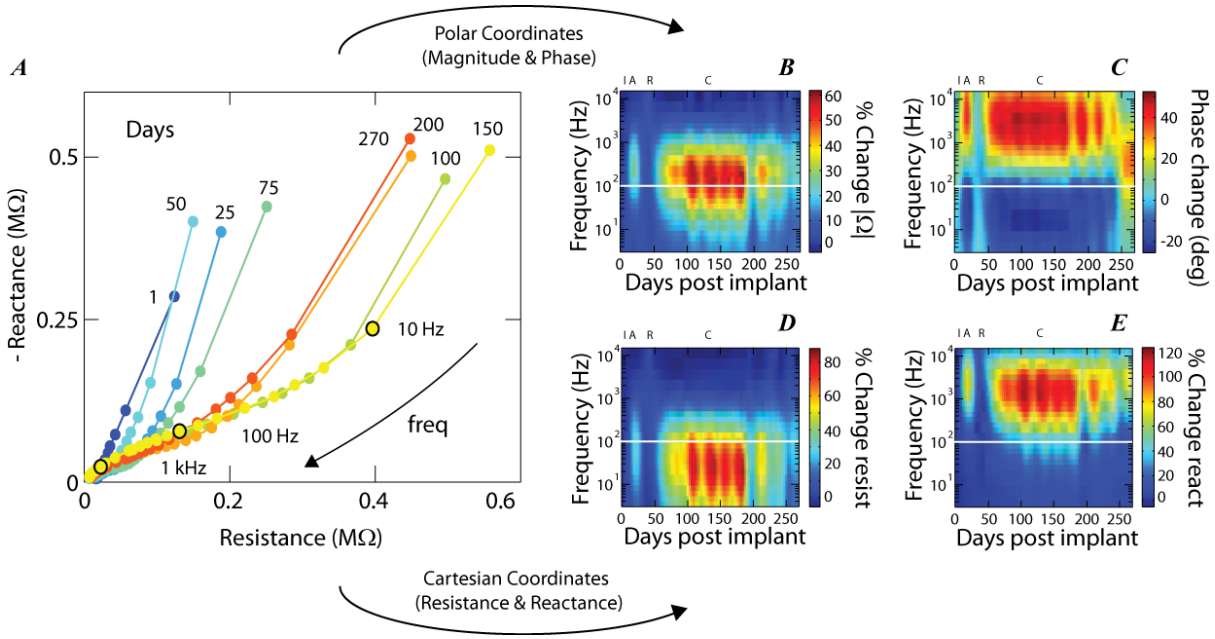

Figure 2.16: Broad-Spectrum Impedance Changes Observed in Nyquist Plots

Complex impedance data are shown in a Nyquist plot **(A)**, where the negative of the imaginary component (reactance) is plotted against the real component (resistance). Complex impedances recorded on days spanning the first 9 months post-implantation (each day is marked at the top and distinguished by color) are shown for each measured frequency (marked as dots, where low-frequency impedances appear in the upper right corner and high-frequency impedances appear in the lower left corner). During the initial period (and remodeling period), Nyquist traces appeared as straight lines, similar to a constant phase element (CPE). During the acute and chronic periods, low-frequencies were still dominated by CPE behavior, but mid- to high-frequencies (70 Hz to 1 kHz) showed the influence of a series semicircular arc. Temporal changes in spectral impedances are more clearly seen in polar coordinates (magnitude and phase) **(B-C)** or Cartesian coordinates (resistance and reactance) **(D-E)**. In polar coordinates, the largest change in magnitude occurred near the mid-gamma 100 Hz band often used for ECoG recordings, while the phase lag remained fairly constant in this frequency range. This large change in magnitude was a result of the overlapping effects of low-frequency increases in resistance and high-frequency increases in reactance. Note that in each of the spectral plots, the stereotyped impedance phases can be clearly distinguished.

corner down to the lower left corner with increasing frequency. In the Nyquist plane, impedances can be interpreted within two different coordinate systems: polar (magnitude and phase) or Cartesian (resistance and reactance). During the initial phase (e.g. day 1) and remodeling phase (e.g. day 25), impedances showed varying magnitudes, but constant phase angles, which is characteristic of CPEs. During the acute phase (e.g. day 25) and chronic phase (e.g. day 150), low frequencies continued to demonstrate CPE behavior, while high frequencies showed the appearance of a semicircular arc, which is characteristic of the tissue-related β-dispersion. The appearance and enlargement of this semicircular arc indicates an accumulation of cellular tissue around the electrode.

In order to determine the relative temporal changes in impedances across all measured frequencies, both the polar and Cartesian coordinates from the Nyquist plots were considered separately versus both frequency and time. Figures 2.16B-C show the relative changes in impedance magnitude across all frequencies (normalized by the average impedance in week 1) as well as the absolute change in phase angle. The greatest relative change in impedance magnitude occurred between 70 Hz – 700 Hz (about a 60 % increase), which includes the important mid- to high-gamma frequency band surrounding 100 Hz that is typically monitored in ECoG recordings. Conversely, the phase change was minimal in the mid- to high-gamma band range, which decreases in lower bands and increases in higher bands. These changes corresponded to large increases in resistance at low frequencies and reactance at high frequencies, as shown in Figures 2.16D-E.

2.5.7 A Variable-parameter RC Impedance Model

Impedances are complex numbers and are represented by the sum of a frequency-*independent* resistive (real) and frequency-*dependent* reactive (imaginary) component. Therefore, the impedance at any given frequency can be modelled by a series of a resistor and capacitor:

$$Z = R - j\frac{1}{\omega C} \tag{2.12}$$

where $j = \sqrt{-1}$ and ω is the angular frequency (radians/sec). This type of electrical model for the measured impedance can be referred to as a variable-parameter model, because the values of resistance and capacitance that model the impedance will vary with each measured frequency. (Fixed-parameter models tend to be more complicated and require parameter estimation, as demonstrated by the CPE-Cole model described previously). The value of the variable-parameter

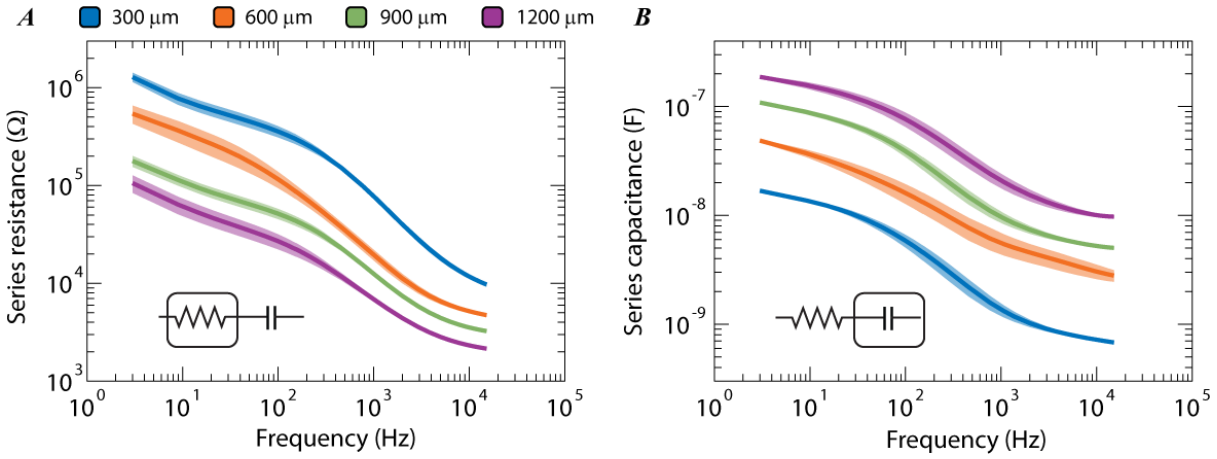

Figure 2.17: A Variable-Parameter RC Model of Electrode Impedance

Values for the variable-parameter series RC models for each of the platinum electrode sizes are given as a function of frequency. Each colored line indicates the equivalent series resistance **(A)** and capacitance **(B)** that can be combined in series to model an electrode's impedance at any given frequency. Values were calculated directly from impedances measured at 9 months, which is well into the chronic phase where impedances have generally plateaued. This model provides a valuable tool for designing and evaluating hardware that is intended to interface with chronic surface electrodes.

model is its simplicity—resistances and capacitances can be calculated directly, implemented with small electrical circuits, and easily interfaced with hardware (such as amplifiers and stimulators) to perform bench top tests with realistic electrode behavior.

The values of the equivalent series resistance and series capacitance for all four electrode diameters are provided in Figure 2.17 as a function of frequency. These values represent impedances of all diameters at 9 months post implantation. Both the series resistance and series capacitance decreased with increasing frequency. The largest diameter electrodes (1200 μm) had the lowest series resistances, but highest series capacitances. The combination of low resistance and high capacitance (which translates to low reactance due to the reciprocal relationship) results in an overall very low impedance magnitude. Alternatively, smallest diameter electrodes (300 μm) had the highest series resistance, and lowest capacitance, resulting in very high impedance magnitudes.

2.6 Discussion

2.6.1 Implications of Chronic Impedance Changes on the Biotic Response

This study represents the first detailed account of the time-varying impedance characteristics of electrode arrays implanted epidurally over cortex. However, the impedance response observed may be applicable to a broad range of applications involving similarly sized electrodes, such as deep-brain, cochlear, spinal, and cardiac implants. The time-varying impedances reflect changes occurring both at the electrode-tissue interface and within the surrounding tissue. Results from the CPE-Cole model show brief changes in the impedance

properties of electrodes during the initial response, which may be due to ion, protein, and cell adsorption to the electrode surface or changes in the ionic composition of the surrounding electrolyte. Similar behavior has been reported for deep-brain stimulator electrodes, but with a decrease in K_e rather than the increase observed here (Lempka et al., 2009). Thereafter, the impedance properties of electrodes remain stable and contact size-dependent. Conversely, tissue impedances did not change much during the initial response, but varied greatly in the acute, remodeling, and chronic phases. Based upon the correlation between the P_y value and cellular activity, the acute and chronic phases are likely associated with an increase in cellular presence whereas, the remodeling phase is likely associated with a brief reduction. The increase in cellular presence in the chronic phase may be due to the formation of a dense fibrotic sheath surrounding the array, which has been reported in a variety of non-CNS chronically implanted electrodes ranging from epidural spinal stimulators to cochlear implants (Cicuendez, Munarriz, Castano-Leon, & Paredes, 2012; Grill & Mortimer, n.d.; Nadol et al., 2001; Schmit & Mortimer, 1997) . The consistent deflection of P_y in the remodeling phase is not well-described in previous literature but may reflect a transition from primary to secondary healing or the formation of more permanent tissue associated with wound healing or encapsulation. The use of the term "remodeling" to describe this stereotyped phase of the impedance response reflects the assumption of cellular remodeling. However, impedances are indirect measures of the biotic response. Therefore, future work should focus on detailed histological analyses of the tissue response in this time period in order to form a more complete understanding of the cellular mechanisms that lead to the described impedance response.

2.6.2 Implications of Coatings for Chronic Implants

Platinum, IROX, and PEDOT are among the most recognized materials for electrodes, however direct side-by-side evaluations have been lacking, especially with respect to their behavior and stability in chronic implants. This study provides evidence that both EIROF and PEDOT coatings are highly effective for improving electrode characteristics for both stimulation and recording. However, the advantageous effects of EIROF and PEDOT were shown to quickly diminish beyond 3 months post implantation. Results from tissue and electrode modeling suggest that the diminishing effects of the coatings was likely due to degradation of the coatings themselves, not to the tissue response. However, further work (and histology) is required to confirm this conclusion. The durability of these coatings would likely have been further decreased if subjected to clinically-relevant levels of stimulation (often in the range of 1-5 mA) which is known to accelerate electrode degradation. Currently, these coatings are best suited for use in acute settings, rather than chronic long-term implants. While the properties of these coatings are highly desirable, future work should focus on conductive materials and coating techniques that provide long-term stability beyond several years in order to be relevant in chronic clinical applications.

2.6.3 Implications of Size Effects for Stimulation and Recording

The relationship between impedance magnitude and electrode radius was area-dependent at low frequencies and transitioned to circumference-dependence at high frequencies. For chronically implanted platinum electrodes, the mid-way transition occurs at approximately 3 kHz. This means that for recording, and likely most stimulation applications, focus should be placed on

the area rather than diameter of electrodes. Area-dependence means that impedances are very sensitive to changes in electrode diameter. This is a concern for micro-scale arrays, where diameters have been reported as small as 10-100 μm. As electrode diameters decrease, the impedances may become prohibitively large to allow passage of clinically-relevant currents within the safety limits of the water window. Additionally, decreased electrode size (and increased impedance) may lead to voltage-divider effects across the input resistor of the recording amplifier and devastatingly large noise that will significantly impact both the quality and bandwidth of signals. For example, an approximate 3 dB loss in signal will be observed from a 300 μm diameter platinum electrode with a typical 500 kΩ impedance at 100 Hz that is connected to an amplifier with a 1 MΩ input resistance versus a 0.3 dB loss from a 1200 μm diameter electrode with a 40 kΩ impedance. Compounding the problem, the noise floor of most commercially-available amplifiers attached to 300 μm electrodes severely limits the resolution of small signals (like ECoG) at frequencies above 100 Hz. This is in large part due to the fact that amplifiers are typically designed for macro-scale electrodes associated with EEG, EMG, or ECG. While noise from high-impedance electrodes can be reduced by averaging over repeated measurements, this is not an option for "smart" implantable devices and brain-computer interfaces that depend upon high-fidelity real-time recordings. For real-time high-fidelity ECoG recordings from chronically implanted arrays, 600 μm diameter platinum electrodes should be considered a practical lower limit.

Chapter 3

Characteristics of Chronic ECoG Recordings

3.1 Introduction

3.1.1 An Overview of Electrocorticographic (ECoG) Recordings

Electrocorticographic (ECoG) recordings have become an important means of monitoring electrophysiological activity of the brain in acute research and clinical settings, yet little is known about the characteristics of chronic ECoG recordings extending from several months to years. The proliferation of ECoG recordings in modern neuroelectrical methods stems from the pioneering work of Penfield and Jasper in the 1930s, which used epicortical recording and stimulation to map cortex and identify epileptogenic foci. In their seminal work, Penfield and Jasper utilized epidural electrodes, which were placed over the protective dural layer of the brain. Since then, subdural recordings have become standard in acute neurosurgical monitoring due to closer proximity to signal sources.

Advancements in neurotechnologies over the last several decades have spurred increased interest in chronic neural interfaces for treating a broad spectrum of disorders and diseases. Rapidly growing interest in chronic neural interfaces has led to a resurgence of epidural ECoG recordings, which may provide a desirable balance between high spatiotemporal signal resolution and minimal invasiveness for chronic use. A notable advantage of epidural electrodes is that they

avoid disruption of the dura that provides a protective barrier around the central nervous system. Penetration of the dura is associated with serious health risks including edema, infarction, hematomas, encephalitis, and infection, which may be exacerbated by cerebral spinal fluid (CSF) leakage (Fountas 2011).

3.1.2 Micro-ECoG Electrode Arrays and Effects on Non-physiological Noise in Recordings

Traditionally, both sub- and epidural ECoG have used surface electrodes constructed from Silastic-embedded platinum (Pt) metal disks ranging from 1 to 5 mm in diameter with interdiskal distances of 5-10 mm. However, advanced micro-fabrication techniques have enabled high-density milli- and micro-scale electrode arrays on thinner, more flexible substrates. These new electrode arrays have the potential to both provide higher resolution recording and stimulation capabilities and greatly reduce the implantable volume of electrode implants (Rubehn et al. 2009; Molina-Luna et al. 2007; Kim et al. 2007). However, while higher resolution ECoG recordings are desirable, decreased electrical contact size comes at the cost of smaller integrated neural signals and larger noise due to increased impedance.

Non-physiological noise in neural recordings originates from numerous dissipative processes, including thermal (Johnson-Nyquist) noise of the electrodes and tissue ($v_{thermal} = \sqrt{4k_B T B R_{electrode}}$), current noise from amplifier input currents imparted across electrode impedances ($v_{current} = i_{noise} R_{electrode}$), and voltage noise from the amplifier circuitry ($v_{voltage} = v_{noise}$). Here, k_B is Boltzmann's constant, T is absolute temperature, B is amplifier bandwidth, $R_{electrode}$ is the electrode resistance (real part of the impedance), and $v_{current}$ and $v_{voltage}$ are specifications of the amplifier. These noise sources are typically referred to the input

of the amplifier (prior to amplifier gain), are assumed to be uncorrelated, and, therefore, add as the sum of squares. While noise originates from dissipative processes and is linked to the real component of complex impedance, the imaginary component (due to capacitance) can shape the noise profile through signal filtering.

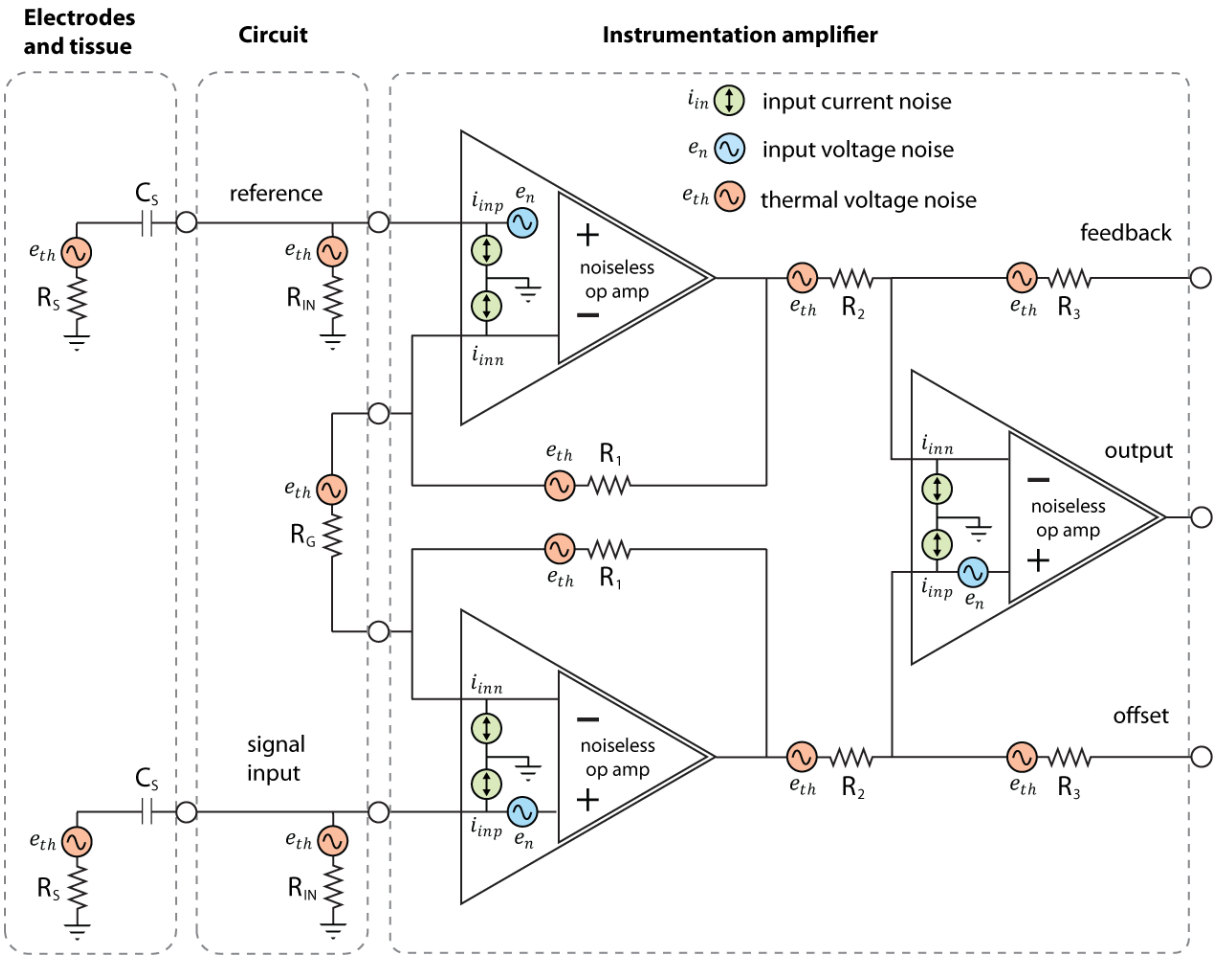

Figure 3.1: Noise Sources in Physiological Recordings

A generalized neural recording setup is illustrated with different dissipative noise sources that contribute to the overall non-physiological noise in recordings. Noise generators include the electrodes and tissue, passive circuit components, and active amplifiers. Noise from the electrodes and tissue is generated both by inherent thermal voltage noise, which is dependent upon the resistance of the tissue, and current noise from attached circuits that is driven through their resistance to create voltage noise. Electrode and tissue capacitance does not create noise but shapes it through filtering effects. Likewise, noise from passive circuit elements arises from both thermal and current noise driven through them. Active circuits, like amplifiers, have both current and voltage noise associated with them. Noise-reduction in a recording system is most important at the front-end stages and can be reduced by minimizing electrode impedance, minimizing passive resistor values, and using an amplifier technology that has appropriate current- or voltage-noise that is matched to electrode impedance.

3.1.3 Electrophysiological Origins of ECoG Signals

Electrical signals of the brain originate from the superposition of ionic currents originating from current flux into and out of electro-active cells distributed throughout the brain volume. Regional variations in extracellular current densities within the brain produce electrical potentials that can be measured between any two locations with a pair of electrodes. REDuction-OXidation reactions across the electrode-tissue interface transduce *ionic* currents in the tissue into *electrical* currents in the electrode so signals can be conditioned and recorded by electronic amplifier systems. The recorded time-varying signals are dependent upon 1) the proximity of each electrode to different cellular signal sources, 2) non-uniformities in source densities and tissue impedances, 3) the size of exposed electrode recording areas over which signals are integrated, and 4) the additive noise sources of the electrode-amplifier system.

ECoG signals are variants of local field potentials (LFPs) and are explicitly recorded from the cortical surface of the brain, either below (sub-) or above (epi-) the protective dural layer. Dominant sources of ECoG signals include slow synaptic currents from dendritic processes, both fast (< 2ms) and slow (10-100 ms) non-synaptic spikes from the neuronal somas, intrinsic resonant currents from oscillatory neurons, and relatively long-lasting (0.5-2s) afterhyperpolarization currents following neuronal bursting activity. The magnitude of ECoG scales with frequency, f, as $1/f^{n}$ in the range of n=1-2 and depends upon both the geometric alignment and temporal synchrony of sources. The origin of this power law is not well understood, but is believed to be linked to filtering properties of dendrites and complex network behaviors (Buzsáki et al. 2012).

Located further from signal sources than traditional LFPs, ECoG recordings utilize relatively larger-area electrodes in order to increase signal levels by integrating over regions of

synchronized activity. Subdural ECoG can achieve larger signals by placing electrodes closer to sources (Bundy et al. 2015), but, like all dura-penetrating electrodes, they present higher risks of infection and adverse reactive tissue response due to disruption of the protective blood-brain barrier. The spatial alignment of neurons along cortical folds affects signal levels at the surface. Dipoles aligned orthogonal to the surface in gyri will produce large potentials, whereas dipoles aligned parallel to the surface in sulci may cancel one another and produce smaller potentials. The highly-aligned apical dendrites of pyramidal cells in gyri produce large dipoles along their somatodendritic axes which are believed to contribute substantially to ECoG signals.

3.1.4 Signal Features of ECoG Recordings

Acute ECoG recordings have identified delta (1-3 Hz), theta (4-8 Hz), alpha (8-12 Hz), beta (12-30 Hz), and gamma (30-80 Hz) band power modulation as dominant signal features indicative of cortical processing. Recently, high-gamma (80-200 Hz) activity has been implicated as an additional important signal feature (Rouse & Moran 2009; Leuthardt et al. 2012; Miller et al. 2007; Crone et al. 2006). The precise mechanisms and dynamics that underlie the generation of these signal features is still not well understood. Some studies have linked beta rhythms to cortico-thalamic circuits, while gamma and high-gamma rhythms have been linked to local cortical spiking activity due to correlated gamma band power and firing rates (Heldman et al. 2006). Phase-amplitude coupling (PAC), where the phase of theta and alpha oscillations is coupled to the amplitude of high gamma oscillations, suggests that low-frequency oscillations may modulate local cortical activity.

3.1.5 ECoG for Chronic Neural Interfaces

ECoG recordings are an attractive high-resolution alternative to more invasive modalities like intracortical microelectrode recordings and subdural ECoG recordings for monitoring brain activity. Recent studies have used ECoG recordings to control motor neuroprosthetics (Rouse et al. 2013) and next-generation closed-loop neuromodulation devices capable of modulating therapies based upon real-time cortical activity (Rouse et al. 2011; Stanslaski et al. 2012; Wheeler et al. 2015). Both subdural and epidural ECoG BCI studies have shown beta and gamma band activity to be dominant control features (Wang et al. 2013; Rouse et al. 2013; Schalk et al. 2008). Characterization of these signal features through the initial, acute, remodeling, and chronic phases is critical for optimizing ECoG for chronic applications.

3.2 Purpose of the Study

ECoG presents a promising recording modality for chronic neural interfaces, but a comprehensive evaluation of signal quality, optimal electrode size, spacing, and reference techniques is needed. Optimal recording specifications for chronic ECoG recordings is dependent upon changes in electrode impedance and signal characteristics caused by reactive tissue responses to indwelling electrodes. Chapter 2 described chronic impedance changes of ECoG electrodes of varying size and material coatings. Distinct temporal changes in electrode impedances were characterized by a 4-phase reactive tissue response: an initial period (days 1-7), an acute period (days 7-30), remodeling period (days 25-45), and chronic period (beyond days 35-45). Here, this work is extended to include chronic changes in ECoG signals that coincide with the previous impedance study. This study combines theoretical, modeling, and electrophysiological data to

resolve unanswered questions regarding long-term signal quality and optimal recording techniques toward the goal of characterizing the viability of ECoG as a platform for a chronic neural interface.

3.3 Methods

3.3.1 An Analytical Recording Model

A two-stage analytic recording model is used to develop intuition about neural recordings. The model is formed by first considering the generation of potentials on the cortical surface below recording electrodes (Figure 3.2A), and second by considering the propagation of voltage signals through electrodes and amplifiers (Figure 3.2B).

In the first stage, which models signal generation, sources are approximated as a stationary dipole source with moment $I \cdot \boldsymbol{d}$ located some distance, *h*, below the cortical surface. For simplicity, the source is assumed to be located within a homogeneous conducting volume with bulk conductivity σ, so that the potential at a given radius $\boldsymbol{r}$ from the dipole center is given by:

$$\Phi = \frac{I\boldsymbol{d} \cdot \boldsymbol{r}}{4\pi\sigma r^3} = \frac{Id}{4\pi\sigma r^2}\cos\varphi \tag{3.1}$$

where φ is the angle between the vectors $\boldsymbol{r}$ and $\boldsymbol{d}$. The difference in potentials on the cortical surface is seen as a voltage between electrodes. The differential potential on the cortical surface below two electrodes is given by:

$$\Phi_{diff} = \frac{Id}{4\pi\sigma}\left(\frac{sin\theta_1}{r_1^2} - \frac{sin\theta_2}{r_2^2}\right) \tag{3.2}$$

where r_1 and r_2 are the distances between the dipole and electrodes and $sin\theta_1$ and $sin\theta_2$ are angles formed between the vectors $\boldsymbol{r}_1$ and $\boldsymbol{r}_2$ and cortical surface.

In the second stage, which models signal acquisition, the focus is placed on electrodes and amplifiers. The output of a differential neural amplifier is the difference between the two input voltages ($v_p - v_n$) compared to a common ground. Reduction of large common-mode signals (e.g. EMG, EOG, motion artifacts, stimulation artifacts, and 60Hz noise) is best achieved by matched-impedance electrodes with a low-impedance ground. When common-mode signals are not a problem and low noise is paramount, the reference can be tied directly to ground. Another common configuration is to tie the negative inputs of multiple amplifier channels to a single common reference electrode that is placed away from the signal sources. In all cases, voltage losses will occur between cortex and amplifier inputs due to voltage divider effects across the electrode impedance, Z_{ele}, (or Z_{ref} for the reference electrode) relative to the amplifier input impedance Z_{in}. Accordingly, the voltage output of the amplifier is given by:

$$V = \Phi_{diff_1} \frac{Z_{in}}{Z_{ele} + Z_{in}} - \Phi_{diff_2} \frac{Z_{in}}{Z_{ref} + Z_{in}} \tag{3.3}$$

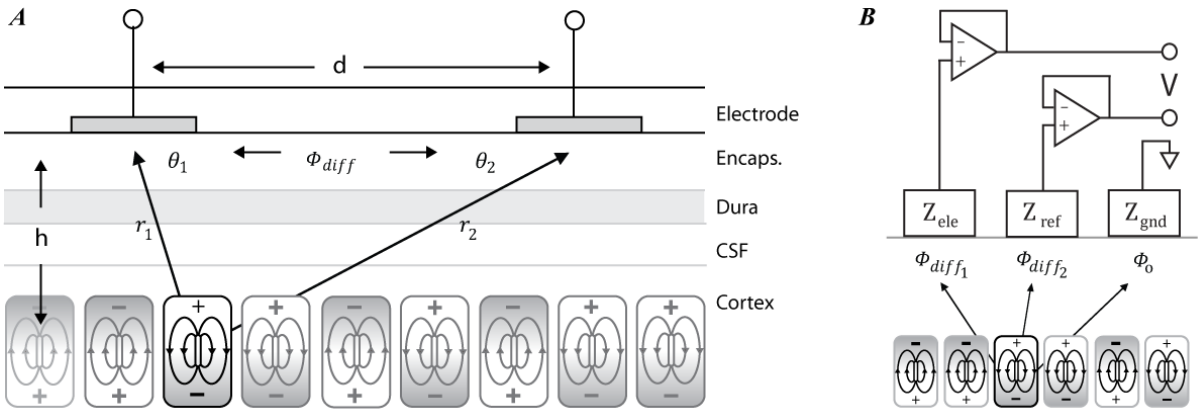

Figure 3.2: Analytical Recording Model

Analytical recording model consisting of tissue **(A)** and electrode sub-models **(B)**. In the tissue model, the potential at any given point is described by the dipole equation. The difference in potentials beneath two electrodes is a function of the electrode pitch, the height above the dipole source, and the bulk conductivity of tissue. In the electrode model, the potential described in the tissue model undergoes a voltage-divider effect due to the electrode and amplifier input impedances.

3.3.2 A Finite Element Recording Model

A finite-element recording model (FEM) was used to extend the previously described analytic recording model to account for interactions between the signal generation and acquisition stages, and explore more realistic conditions involving multiple non-homogeneous conducting layers and geometries. A 3D cortical slab model, similar to (Wongsarnpigoon & Grill 2008), was used to investigate the optimal electrode size and spacing (pitch) for epidural recordings. The modelled electrodes consisted of both a dural-facing recording electrode and skull-facing reference electrode embedded within an insulating substrate. Tissue layer thicknesses and electrical properties are summarized in Figure 3.3.

The model was built with COMSOL Multiphysics (version 3.4; Burlington, MA), and contained approximately 2.5M tetrahedral elements. Smaller elements were used to represent spaces nearest to electrodes and current sources in order to improve precision in these areas of interest. Average element sizes ranged from 7.7e-5 mm^3 in electrodes, 2.4e-4 mm^3 in encapsulation, 1.3e-2 mm^3 in dura, 4.6e-2 mm^3 in skull, 5.1e-2 mm^3 in CSF, 3.0e-1 mm^3 in gray matter, and 11.3 mm^3 in white matter. Reducing the mesh size of the model did not appreciably affect results, where potentials varied by less than 0.8%. Current flux continuity was preserved across internal

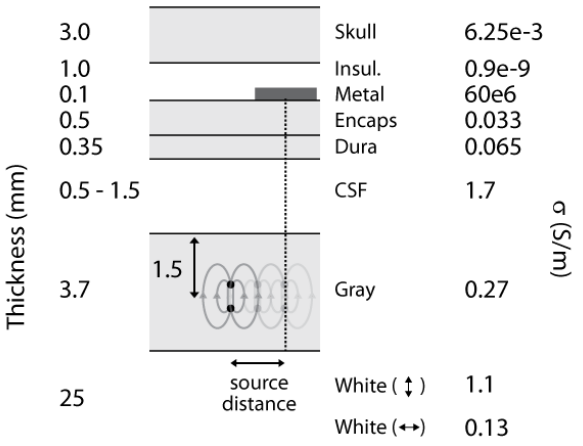

Figure 3.3: Finite Element Recording Model

An illustration of a finite element model (FEM) consisting of an epidural electrode, cortex, and dipole source is shown with corresponding layer thicknesses and conductivities.

boundaries and all external boundaries were set to ground (V=0), except for the top of the skull, which was set as an electric insulator (current density = 0).

Signals generated by cortical macro-columns were approximated as current source/sink pairs (dipoles) separated by 1 mm and centered 1.5 mm from the upper surface of the gray matter (Nunez, 2006). The potential difference between the recording and reference electrodes was measured as the source was moved outward radially from below the electrode center. The relative contribution of a source to the total recorded signal was determined by normalizing each of the measured potential differences by the maximum observed value (occurring when the source was directly below the electrode). The resulting 3D distribution, which represents a measure of the effective area of influence (or resolution) of the electrode, was used to determine optimal electrode spacing for electrodes with diameters of 300 µm, 1.2 mm, and 2 mm. Simulations were repeated for CSF thicknesses of 0.5 mm, 1 mm, and 1.5 mm to account for possible compression of the CSF layer by the overlaying electrode and surrounding encapsulation.

3.3.3 Electrode Array Design

Thin-film electrode arrays were constructed using MEMs fabrication techniques and consisted of three primary layers. The bottom and top insulation layers were constructed of 12 µm thick spin-coated polyimide (HD4110, HD Microsystems), and the middle layer of 50 µm wide interconnecting traces and electrode contacts was formed by photolithography and metal deposition of chromium (10 nm), gold (200 nm) and platinum (20 nm) for a total thickness of 230 nm. As shown in Figure 3.4, the flexible electrode arrays were based upon a folding design in which all electrode contacts faced downward *toward* the cortex and the references and ground faced upward *away* from the cortex. The purpose of the upward-facing references and ground was

to create "quiet" electrical references for ECoG recording, where signals generated by cortex would be largely silenced compared to global common-mode noise. The downward-facing electrodes consisted of 32 disc-shaped contacts arranged in rows of four interleaved diameters (300 µm, 600 µm, 900 µm, and 1200 µm). The two designated references were also disc-shaped contacts of 300 µm and 1200 µm diameter. A large-area (36.8 mm^2) "H"-shaped pad was used to both shield the references and provide a stable low-impedance electrical ground. The polyimide

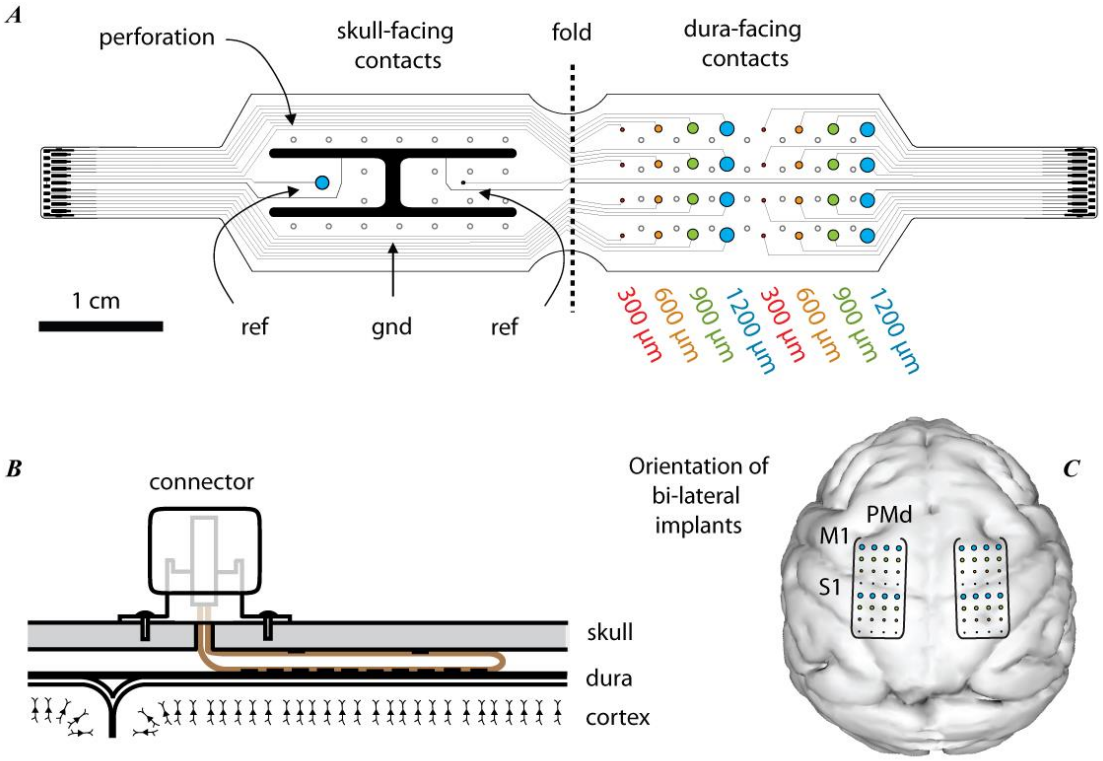

Figure 3.4: Thin-film Electrodes for Chronic Impedance Characterization

Thin-film polyimide arrays were constructed using MEMs fabrication processes and consisted of platinum disk electrode contacts printed onto a flexible polyimide substrate that was punctated by perforations for improved biological transparency **(A)**. Arrays were based upon a folding design where 32 electrode contacts of four different sizes faced downward toward the cortical surface and two references and a large-area ground faced upward toward the overlying skull as shown in **(B)**. Six arrays were implanted bilaterally into the epidural spaces of three macaque monkeys, covering primary motor (M1) and primary somatosensory (S1) cortex **(C)**. Two of the implanted arrays consisted of uncoated platinum electrodes, two with electrodes coated with EIROF, and two with coatings of PEDOT.

substrate was also punctated by rows of 500 μm perforations to improve the "biological transparency" of the implant by facilitating transport and signaling through the device.

3.3.4 Conductive Material Coatings

Electrode contacts on two of six implanted arrays were coated with activated iridium oxide, and another two arrays were coated with PEDOT:pTS. Electrodeposited iridium oxide films (EIROF) were formed from an aqueous solution of 4 mM $IrCl_4$, 40 mM oxalic acid, and 340 mM K_2CO_3 brought to a pH of about 10.3 that had rested in darkness for 48 hours. The iridium oxide film was formed by applying 50 cyclic voltage ramps between 0 V and 0.55 V (vs Ag/AgCl) at 50 mV/s followed by 1600 1 Hz pulses between the same voltage limits. (Yamanaka 1989; Marzouk et al. 1998; Meyer et al. 2001). PEDOT was electrochemically deposited and polymerized from an aqueous monomer solution of 0.1 M ethylenedioxythiophene (EDOT) and 0.05 M paratoluene sulfonate (pTS) dissolved in a 50% DI water and 50% acetonitrile. PEDOT:pTS coatings were formed by applying a galvanostatic current of 2 mA/cm^2 for 7.5 min. (Green et al. 2013). All electrodes were rinsed in deionized water, stored dry in sealed plastic containers, and sterilized in an ethylene oxide gas chamber prior to implantation.

3.3.5 Epidural Implantation of Electrode Arrays

Six electrode arrays were surgically implanted bi-laterally into three male juvenile macaque monkeys under anesthetic conditions and using aseptic surgical techniques. With the animal's head fixed on a standard stereotaxic frame, two 22 mm craniotomies were performed over each hemisphere. Through each craniotomy, surrounding dura was carefully detached from the overlying skull to produce a subcranial pocket into which the arrays could be easily placed without damage to the applied conductive coatings or underlying cortex. Each array was

positioned approximately parallel to the midline and spanned primary motor (M1) to primary sensory (S1) cortex. The arrays were pseudorandomly assigned to each monkey to ensure that each coating combination (Pt-EIROF, EIROF-PEDOT, and PEDOT-Pt) was represented within a monkey. Once the arrays were implanted and the craniotomies sealed, high-density zero insertion force (ZIF) connectors (Tucker Davis Technologies, Alachua, FL) were used to access each electrode channel for regular *in vivo* impedance measurements.

3.3.6 Neural Recordings

Baseline epidural ECoG activity was recorded from sensorimotor cortex of 3 juvenile macaque monkeys beginning 2-3 days post-implantation and continuing for a period of over 250 days. Approximately 10 minutes of baseline data were captured 2-3 times each week, after which electrochemical impedance spectroscopy (EIS) measurements were performed on all electrodes. During each session, the monkeys sat calmly within a custom plexi-glass primate chair with their heads fixed stationary but otherwise unrestrained.

Neural recordings from all 64 dural-facing electrodes (2 arrays x 32 channels per monkey) were acquired simultaneously using four 2-stage 16-channel TDT low-noise amplifiers (Tucker Davis Technologies, Alachua, FL) connected to electrodes through two high-density zero insertion force (ZIF) connectors . The first amplification stage was a customized TDT headstage built with a pass band of 3-500 Hz, gain of 5 V/V, and input impedance of 1 MΩ for low-noise operation. The second amplification stage was a standard TDT Medusa pre-amp with a pass-band of 0.5 Hz-7.5 kHz, gain of 10 V/V, 12-bit ADC sampled at 2,024 Hz, and a fiber-optic interface to transmit data to a monitoring station located outside of the recording room.

3.3.7 Physical Noise Model

The total non-physiological noise resulting from electrode impedances and amplifiers was estimated from a physical RC electrode impedance model, which consisted of a resistor and capacitor connected in series. Recordings were made across combinations of 7 resistance values (1 kΩ, 20 kΩ, 100 kΩ, 200 kΩ, 400 kΩ, 649 kΩ, and 2 MΩ) and 6 capacitance values (0.3 nF, 3.3 nF, 15 nF, 330 nF, 1.8 µF, and 10 µF), which spanned the range of complex impedances of electrodes measured with EIS. Noise recordings were analyzed similarly to neural recordings to yield power spectral densities for each of the resistance and capacitance combinations. Two-dimensional interpolation (MATLAB, interp2) across the R-C space could then be used to estimate the PSD of noise for any given electrode impedance and frequency.

3.3.8 Time-frequency Analysis, Signal Statistics, and SNR

Time-frequency analysis was applied to both neural and noise recordings to track the modulation of signal power over time using overlapping power spectral densities (PSD) of 500 ms sliding windows (epochs) sampled every 50 ms. The PSD of each 500 ms signal epoch was estimated by Thomson's adaptive multi-taper method (MATLAB, *pmtm*), which computes each epoch's periodogram using a sequence of orthogonal tapers. Resulting PSDs had a frequency resolution of 2 Hz and consisted of 512 frequency bins.

Statistical measures were calculated from distributions formed by the combined 500 ms epochs to produce signal power statistics for each of the 512 2-Hz frequency bins. Statistical measures included the mean, standard deviation, skewness, kurtosis, and 10^{th} and 90^{th} quantiles. The depth of modulation for a given contiguous frequency band was estimated as the difference between the integrated rms signal magnitudes derived from the 90^{th} and 10^{th} quantiles for all

included frequency bins. The mean, standard deviation, skewness, and kurtosis correspond to Pearson's first, second, third, and fourth moments about the mean. The general equation for the n^{th} moment about the mean is given by:

$$m_n = \frac{1}{N}\sum_{i=1}^{N}(x_i - \overline{x})^n \tag{3.4}$$

where $\overline{x}$ is the mean of all samples x_i. In this case, each sample x_i is an estimate of signal power within a given frequency band derived from the i^{th} 500 ms epoch of a particular day's recording. Qualitatively, the mean provides a measure of the center of the distribution, the standard deviation measures the distribution spread, the skewness measures the lopsidedness of the distribution, and kurtosis measures the peakedness. Each were calculated using MATLAB functions *mean, std, skewness,* and *kurtosis*.

Estimates of signal-to-noise ratios (SNR) were calculated as (*r*-*n*)/*n*, where *r* is the recorded signal and *n* is the estimated non-physiological noise. Signal characteristics tracked over time were smoothed with a 5-point moving average filter in order to emphasize global trends in the time-domain signals.

3.4 Modeling Results

3.4.1 Analytical Recording Model

Figure 3.5A shows the effects of varying electrode pitch, d, dipole depth, h, and bulk conductivity, σ, on potential differences on the cortical surface below two recording electrodes. First, as electrode pitch increases, the potential difference become larger and then plateaus, indicating that larger signals will result from electrodes spaced far apart. This is the motivation

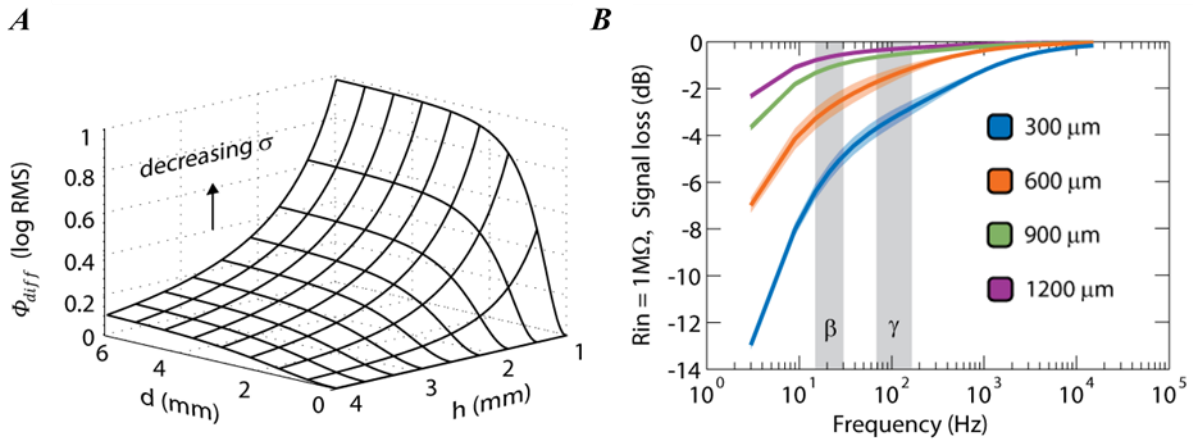

Figure 3.5: Expected Changes in Recorded Signals Based Upon Analytical Recording Model

Predictions of the tissue model **(A)** are that the potential difference will decrease with 1) increased height, 2) decreased electrode pitch, and 3) decreased impedance. A corollary of the 3rd factor is that spatial resolution will increase with increased bulk tissue impedance. The impedance model predicts that signals passing through high impedances electrodes will be subjected to larger attenuation. Signal attenuation due to typical impedances of platinum electrodes is shown in **(B)**.

behind using a distant ground located away from the signal source. Second, as the vertical distance between the electrodes and dipole source increases, the potential difference decreases as approximately$1/h^2$. This result supports arguments for subdural over epidural recordings, where electrodes are placed nearer to signal sources. Last, as bulk conductivity decreases, the potential difference increases. This result explains the shunting behavior of highly conductive media, like CSF, which reduces signal resolution by smearing potentials across the cortical surface. Additionally, this result predicts that the accumulation of resistive encapsulation tissue in the recording region (assuming no change in the vertical distance *h*) should lead to a simultaneous increase in signal strength and decrease in correlation between recorded signals.

Figure 3.5B shows the voltage divider effect of electrode impedance on recorded signal strength. Signal loss was calculated for a 1 MΩ amplifier input impedance using impedance values measured from each electrode size at day 250. Predicted signal attenuation was worse than -3 dB

(50% power) in the gamma-band (70-110 Hz) and nearly -6 dB (25% power) in the beta-band (15-30 Hz) for 300 μm electrodes. Alternatively, signal attenuation was smaller than -0.5 dB (90% power) in both beta- and gamma- bands for 1200 μm electrodes. For comparison, an amplifier input impedance of 5 MΩ would have resulted in approximately -1.8 dB (66% power) attenuation in the beta-band and better than -0.8 dB (83% power) attenuation in the gamma-band for 300 μm electrodes. An amplifier input impedance of 10 MΩ would have resulted in approximately -1 dB (80% power) attenuation in the beta-band and better than -0.4 dB (90% power) attenuation in the gamma-band for 300 μm electrodes. It is important to note that although signal attenuation is improved by increasing the amplifier input impedance, the overall noise contribution of the input impedance is also increased. The noise contribution of the 1 MΩ input impedance amplifier used here is considered in more detail in the following Noise Model.

3.4.2 FEM Recording Model

Simulations with the FEM confirmed the results of the analytic model previously described—specifically the combined effects of electrode pitch, dipole depth, bulk conductivity, and voltage-divider effects due to electrode impedance. In addition, the FEM was used to investigate how electrodes of varying size and pitch integrate signals from sources across the cortical surface. Figure 3.6 shows the normalized strength of dipoles at varying distances from electrodes of varying sizes, which can be thought of as a spatial distribution of influence on the recorded signal. Narrower curves correspond to more selective integration of nearby sources and, consequently, higher resolution, whereas wider curves correspond to the integration of signals across a larger area. CSF thickness was also varied to account for scenarios where the electrode array is in closer proximity to underlying gray matter. Generally, the spatial distributions of

influence of all modeled electrode diameters (300 µm, 1200 µm, and 2000 µm) were similar, although distributions of smaller electrodes were slightly narrower. Increased CSF thickness widened all distributions, resulting in larger areas of integrated signals. By defining the boundary of influence as the distance where a dipole's contribution falls below 10% of the maximum, it is observed that for a CSF layer of 0.5 mm, all electrode sizes integrate over approximately 1.1 cm^2 (radius of 6 mm). For a CSF layer of 1 mm, the integration area expands to 1.8 cm^2 (radius of 7.5 mm), and for a CSF layer of 1.5 mm, the area increases to 2.5 cm^2 (radius of 9 mm).

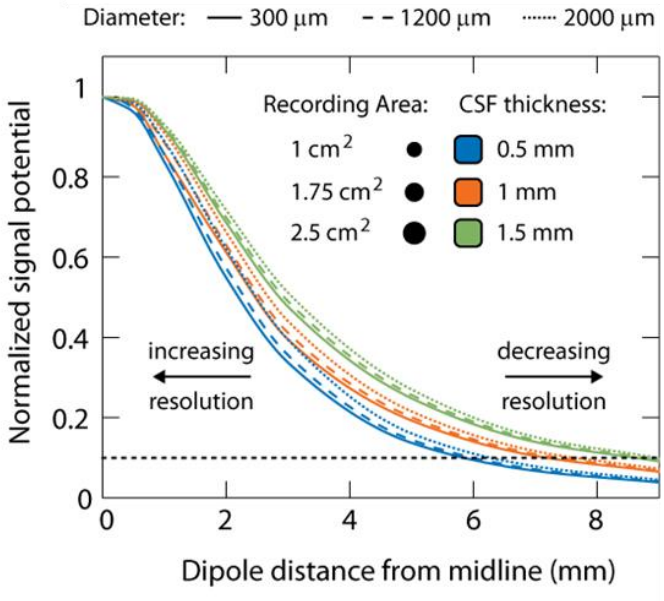

Figure 3.6: ECoG Spatial Resolution

The contributions from dipole sources located 1.5 mm below the surface of the gray matter are shown as a function of the horizontal radius from the electrode center. Normalization to the peak contributions (distance = 0) produces spatial distributions that are given as a function of electrode diameter and CSF thickness.

The combined spatial distributions of influence are shown in Figure 3.7A for different electrode packing geometries, each with a 6 mm pitch. When the distributions overlap, underlying sources will contribute to the integrated signals of multiple electrodes. The amount of common signal for each packing geometry within a unit area is shown in Figure 3.7B for electrode pitches of 3 and 6 mm. To determine the optimal electrode pitch for both hexagonal and rectilinear packing geometries, the amount of unique signal per unit area was calculated for varying electrode pitches. Assuming a uniform sheet of unity strength sources, the amount of unique signal could

be calculated by subtracting the total integrated common signal (shown in Figure 3.7B) from the total integrated signal (shown in Figure 3.7A).

Figure 3.7C shows the optimal electrode pitches for different electrode sizes, packing geometries, and CSF layer thicknesses. Results show about a 1 mm increase in optimal electrode pitch for 2 mm versus 300 µm diameter electrodes in all conditions, which are summarized by the bars at the bottom of each plot. Use of a hexagonal rather than square packing geometry produced slightly better unique signal per area, but optimal electrode pitches remained nearly the same. As expected, unique signal strength was greater for thinner layers of CSF which is predicted by analytic recording model. For 0.5 mm CSF thickness, optimal pitches ranged between 4.75 mm

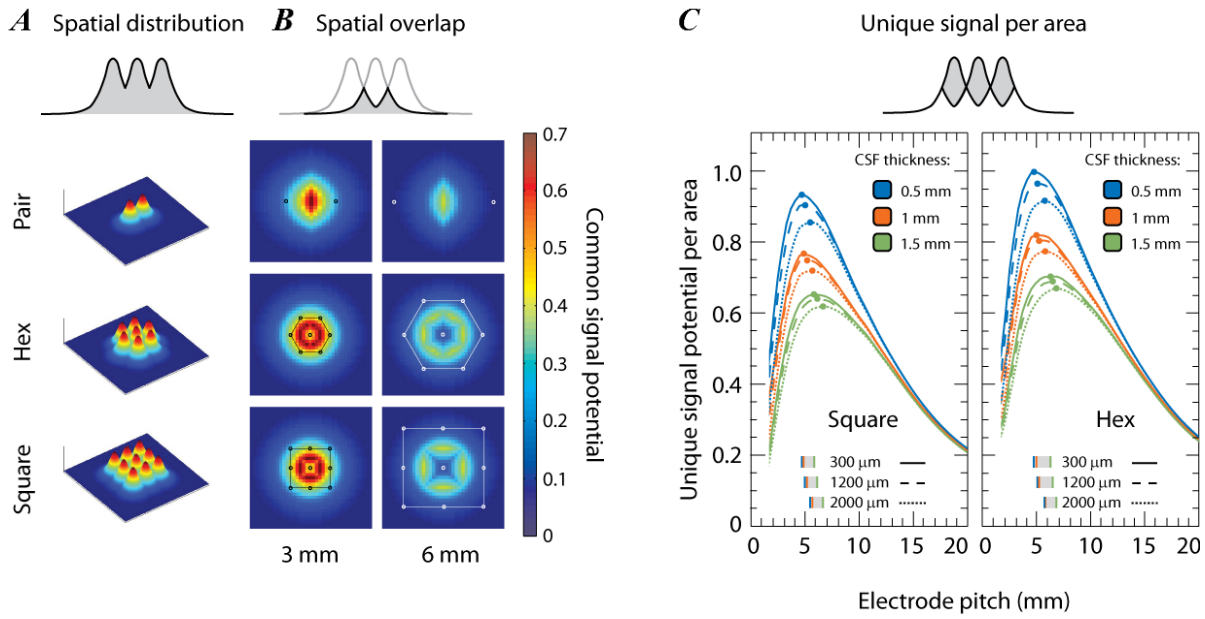

Figure 3.7: Optimal Spacing of ECoG Electrodes

A) The full spatial distributions of linearly-, hexagonally-, and rectilinearly- arranged electrodes are shown next to maps of the corresponding amount of common signal shared between electrodes for 3 and 6 mm electrode pitches within a unit area. **B)** The integrated unique signal remaining after subtraction of the overlapping signal is shown per unit area (circumscribed by a white line) for both rectilinear and hexagonal arrangements with varying electrode pitches. **C)** The peak values of unique signal per unit area and corresponding ranges of optimal inter-electrode distances are summarized at the bottom of each graph for each electrode size and CSF thickness.

to 5.75 mm; for 1 mm CSF thickness, optimal pitches ranged between 4.81 mm to 5.82 mm; and for 1.5 mm CSF thickness, optimal pitches ranged from 5.92 mm to 6.94 mm.

3.4.3 Noise Model

The construction of the amplifier-specific physical RC noise model is summarized in Figure 3.8. Two example power spectral densities for noise are shown in Figure 3.8A, which resulted from recordings from series RC combinations that represented the impedances of electrodes at a specific frequency. As illustrated in Figure 3.8B, the PSDs from each RC measurement were combined and organized by frequency to form stacked iso-frequency "noise surfaces". Given the impedance (or series RC equivalent) of an electrode at a given frequency, the associated non-physiological noise (from the amplifier and parallel combination of the electrode and input impedance) could be interpolated from the frequency-matched noise surface. Measured noise

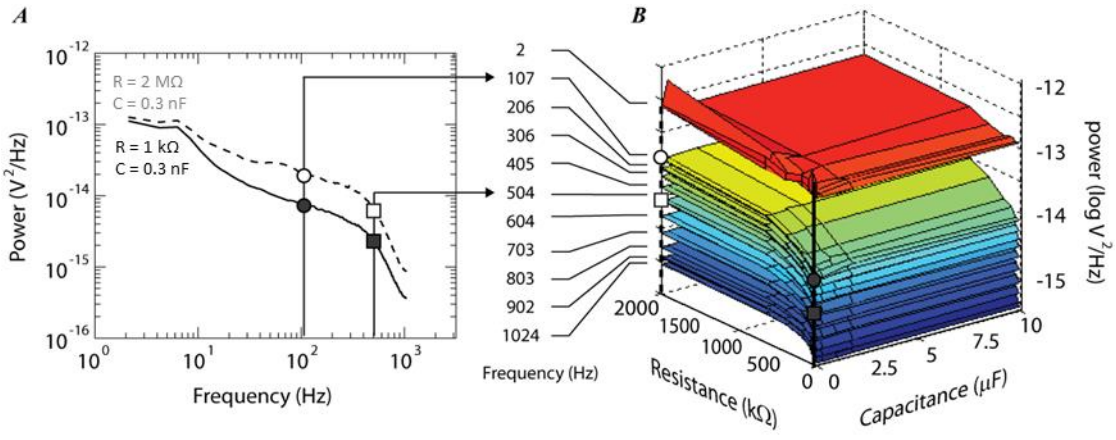

Figure 3.8: Physical Noise Model for ECoG Recordings

A) A physical noise model was formed by recording noise across a range of resistors and capacitors in series that matched the complex impedances previously reported for the same in vivo electrodes. **B)** The recorded power spectra were combined to form a three-dimensional noise model, where the noise produced by the amplifier attached to a given electrode impedance could be predicted, given the electrode's resistance, capacitance, and the frequency of interest.

plateaued with increasing series resistance due to the parallel input resistance at the amplifier front-end. Noise also increased with decreasing series capacitance, but this effect was only appreciable when both series resistance and series capacitance were very low. Because the series resistance and capacitance of electrodes were observed to be inversely related and beyond the region where capacitive effects became appreciable, noise estimates were dominated primarily by the resistance.

3.5 Chronic ECoG Signal Results

3.5.1 Effects of Electrode Material and Size

In Chapter 2, it was shown that conductive coatings significantly reduce electrode impedances in vivo, but effects became insignificant beyond 3 months compared to uncoated platinum electrodes of the same size. One of the goals in this study was to investigate how the coatings affect the quality of chronic signal recordings. However, a 3-way (subject, coating, and diameter) ANOVA (MATLAB, *anovan*) across subjects and 2-way (coating and diameter) ANOVA within subjects revealed that the variability of signal measurements between subjects was too large, and the coating effect size within subjects was too small to permit effective comparisons between arrays (Figure 3.9). Both ANOVAs showed a large and significant effect of electrode size, which persisted throughout the duration of the implants. Therefore, the remainder of this paper focuses on the chronic effects of electrode size within individual arrays, with an emphasis on uncoated platinum electrodes.

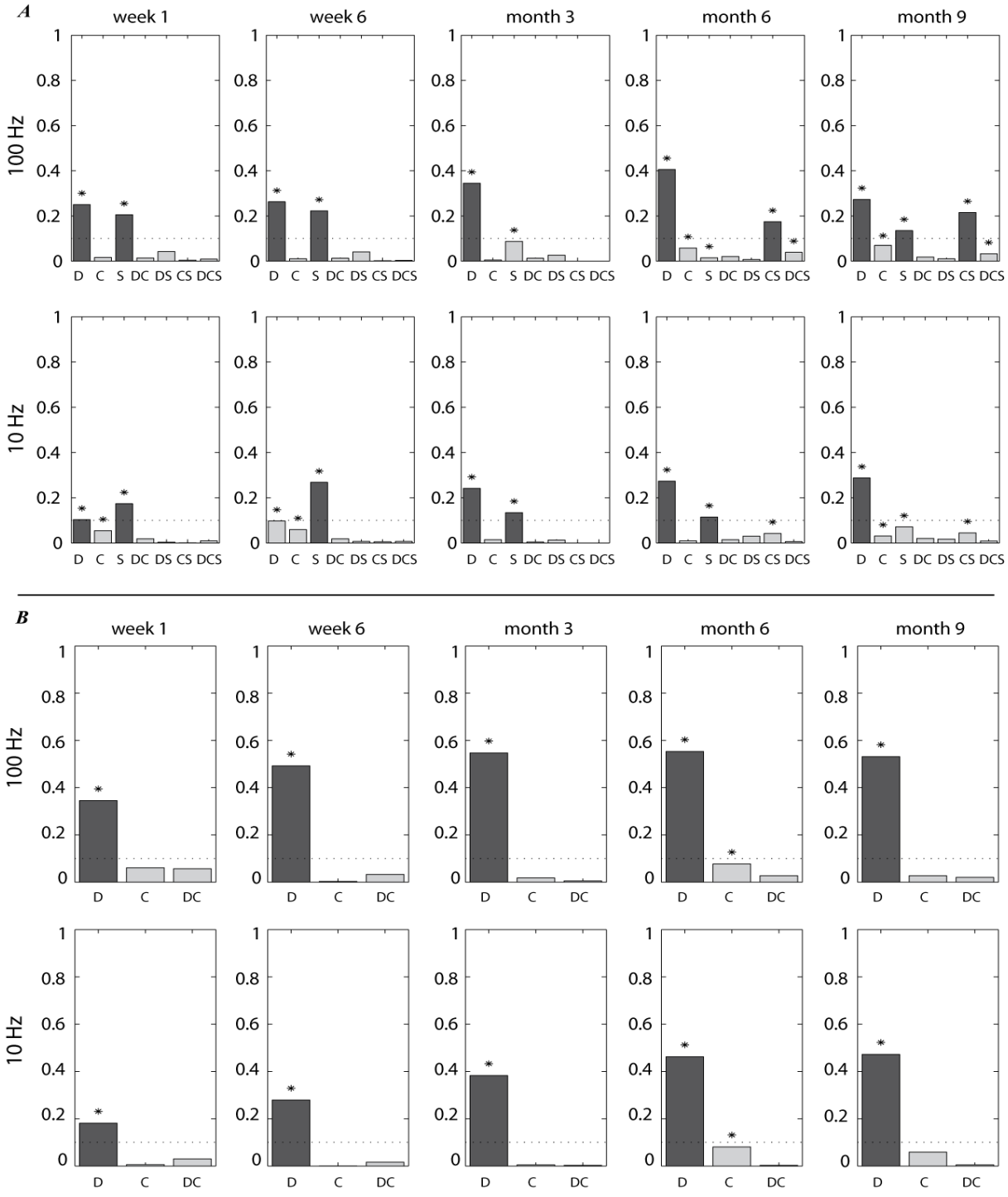

Figure 3.9: ANOVA Analyses for Signal Power Related to Diameter, Coating, and Subject

A) Main and interaction terms in a 3-way ANOVA model: D = diameter, C = coating, S = subject (monkey). The results show large and significant variations in signal power due to differences in subjects. **B)** Main and interaction terms in a 2-way ANOVA model within a single subject. The results show that the largest significant variation in signal power was due to electrode diameter. Therefore, subsequent analyses only compare signal effects associated with different electrode diameters within the same electrode array, and not effects of material coating and subject.

3.5.2 Recorded Signal Power, SNR, and Depth of Modulation

The PSDs of ECoG recordings from all 6 implanted arrays displayed characteristic $1/f^2$ fall-offs in power with increasing frequency throughout the implanted duration. An example PSD for a Pt array is shown in Figure 3.10A. The recorded signal power includes contributions from both physiological signals of interest and non-physiological noise resulting from the combined effects of the amplifier and electrodes. As shown by the traces at the bottom of Figure 3.10A, the non-physiological noise estimated from electrode impedances and the physical RC noise model was greater for smaller diameter electrodes across all frequencies. The SNR, which is a measure of the physiological signal compared to non-physiological noise, is shown for each electrode diameter in Figure 3.10B. The SNR decreased steadily with increasing frequency for all electrode sizes but

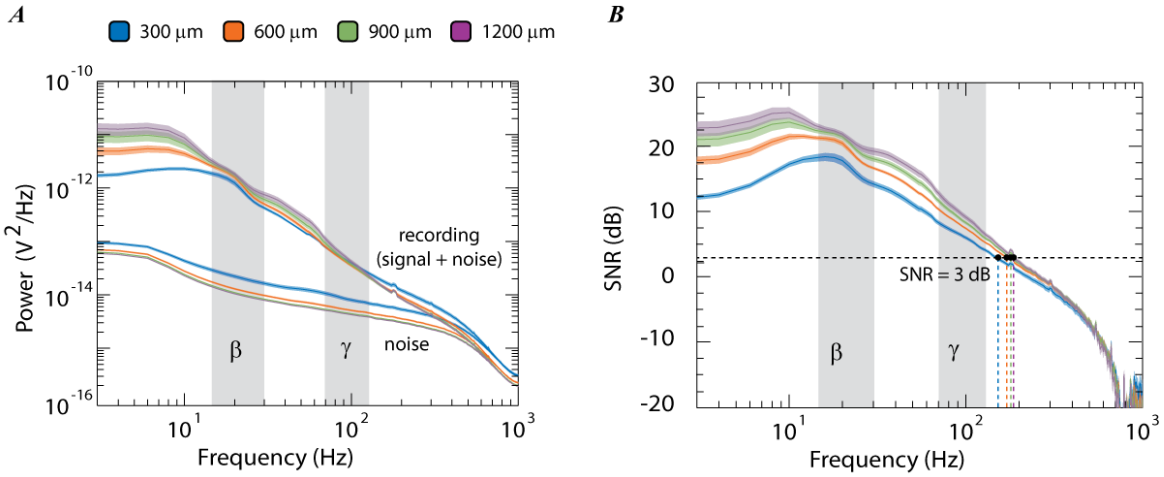

Figure 3.10: ECoG SNR Versus Electrode Size

A) The power of recorded signals on day 250, which include both physiological signals and non-physiological noise, are shown with the interpolated non-physiological noise from the physical RC noise model for each electrode size. **B)** The SNR (physiological Signal to non-physiological Noise Ratio) for each electrode size was estimated from the non-physiological noise interpolated from the physical RC noise model. The SNR decreased with increasing frequency and was highest for larger diameter electrodes. The SNR of 1200 um electrodes decreased to a level of 3 dB (where the power of the physiological signal was twice the non-physiological noise) at approximately 150 Hz for 300 µm electrodes and 185 Hz for 1200 µm electrodes.

was consistently higher for larger electrode diameters. The improved SNR of larger diameter electrodes was consistent for all 6 implanted arrays and equated to broadband enhancement of signal quality which diminished at higher frequencies near to the low-pass cutoff frequency of the amplifier. The 3 dB SNR level is marked in Figure 3.10B in order to illustrate the enhanced high-gamma band signal quality of recordings from larger diameter electrodes. 3 dB is the SNR level where the power of physiological signals is only twice the power of non-physiological noise.

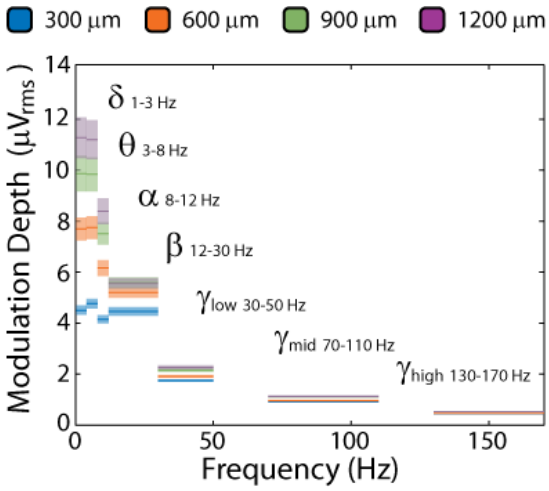

Figure 3.11: ECoG Depth of Modulation Versus Frequency Band and Electrode Size

The power of recorded signals on day 250, which include both physiological signals and non-physiological noise, are shown with the interpolated non-physiological noise from the physical RC noise model.

For SNR levels below 3 dB, signals become exceedingly more difficult to resolve above the noise floor. At day 250, the SNR of 300 µm electrodes decreased to 3 dB at about 150 Hz, whereas the SNR of 1200 µm electrodes decreased to 3 dB at about 185 Hz. At 150 Hz, the SNR of 1200 µm electrodes was nearly 6 dB, which corresponds to signal power that is 4 times larger than noise (a 2X improvement in signal quality over 300 µm electrodes).

The depths of amplitude modulation in frequency bands of interest were estimated from power distributions by integrating the upper (90^{th} quantile) and lower (10^{th} quantile) limits of power observed within each included frequency bin. The depth of modulation for each frequency band was defined as the rms signal difference between the 90^{th} and 10^{th} quantiles of the corresponding integrated power distributions spanning the entire band. Using this measure, the depth of modulation can be interpreted as the outer range of rms amplitude modulation within

which signals remained 80% of the time. Depths of modulation for various bands of interest are summarized in Figure 3.11, which are representative of levels observed for all electrodes. Larger electrode sizes were associated with larger depths of modulation for all frequency bands. For low frequencies, the depth of modulation was approximately 11 μV_{rms} for 1200 µm electrodes and about 5 μV_{rms} for 300 µm electrodes. The depth of signal modulation decreased rapidly with increasing frequency, such that modulation of mid-gamma was about 1 μV_{rms} and modulation of high-gamma was only about 500 nV_{rms}. Even at these higher frequencies, larger electrodes were associated with larger depths of modulation. For example, in mid- and high-gamma bands, the depths of modulation were 1.1 μV_{rms} and 525 nV_{rms} for 1200 µm electrodes, and 0.9 μV_{rms} and 467 nV_{rms} for 300 µm electrodes.

3.5.3 Chronic ECoG Signal Changes

Changes in recorded signal magnitude and SNR were tracked over a period of 250 days and were found to be similar across all 6 implanted arrays regardless of the subject, coating, and electrode size. Example time series from a Pt array are shown in Figure 3.12, where the stereotypical changes over time coincide with the impedance changes resulting from the 4-phase reactive tissue response previously described in Chapter 2. This 4-phase response is characterized by an initial period (days 1-7), an acute period (days 7-30), remodeling period (days 25-45), and chronic period (beyond days 35-45). During the initial period, the electrode impedance remained constant, while the signal magnitude decreased. During the acute period, both electrode impedance and signal magnitude increased. During the remodeling period, both impedance and signal magnitude decreased to values comparable to the end of the initial period. Finally, in the chronic period, signal magnitude remained generally constant, while the electrode impedance

slowly increased and leveled off to a steady level. This 4-phase response was observed across all electrode sizes and coatings with only minor variations in the onset and duration of each period.

Figure 3.13 shows the extended stereotyped responses of signal magnitude and estimated RMS from Pt electrodes in the beta (15-30 Hz) and gamma (70-110 Hz) bands up to 250 days. In the beta band, signal RMS was consistently greater for larger diameter electrodes across all time periods, as was the estimated SNR. This pattern was not as clear for signal RMS in the gamma band, where signal magnitude was mixed across electrode sizes. However, after accounting for the estimated non-physiological noise, the SNR showed the same separation between electrode sizes observed in the beta band where higher SNR was attributed to larger electrode diameter. For comparison, Figure 3.14 shows similar results for EIROF and PEDOT electrodes at 70-110 Hz.

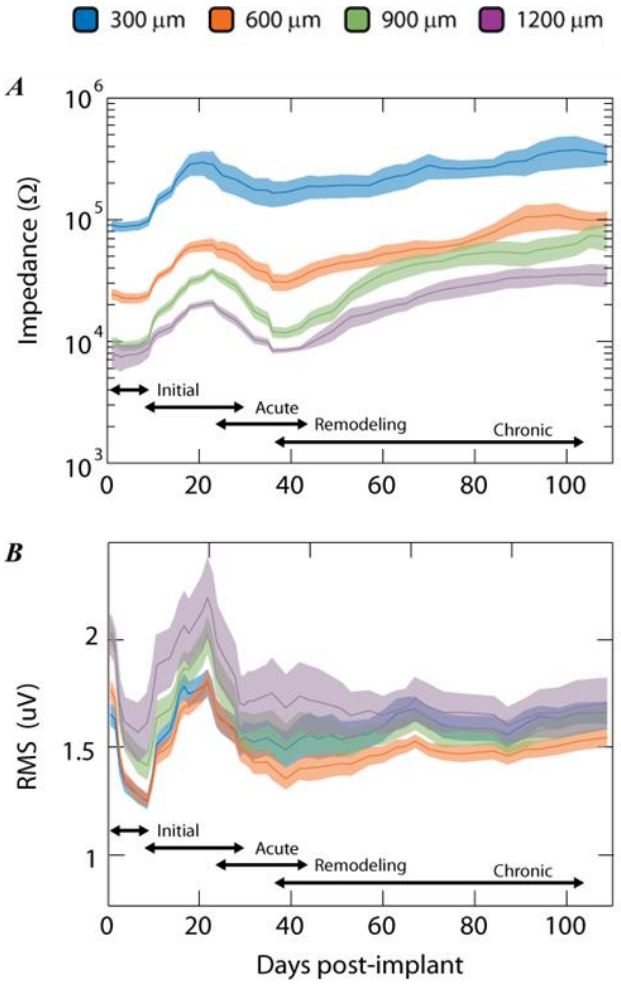

Figure 3.12: 4-Phase Chronic Signal Response: Initial, Acute, Remodeling, and Chronic

Comparison of the 4-phase responses observed both with changes in electrode impedances at 100 Hz **(A)** and recorded signal levels be 70-110 Hz **(B)** for a Pt electrode array.

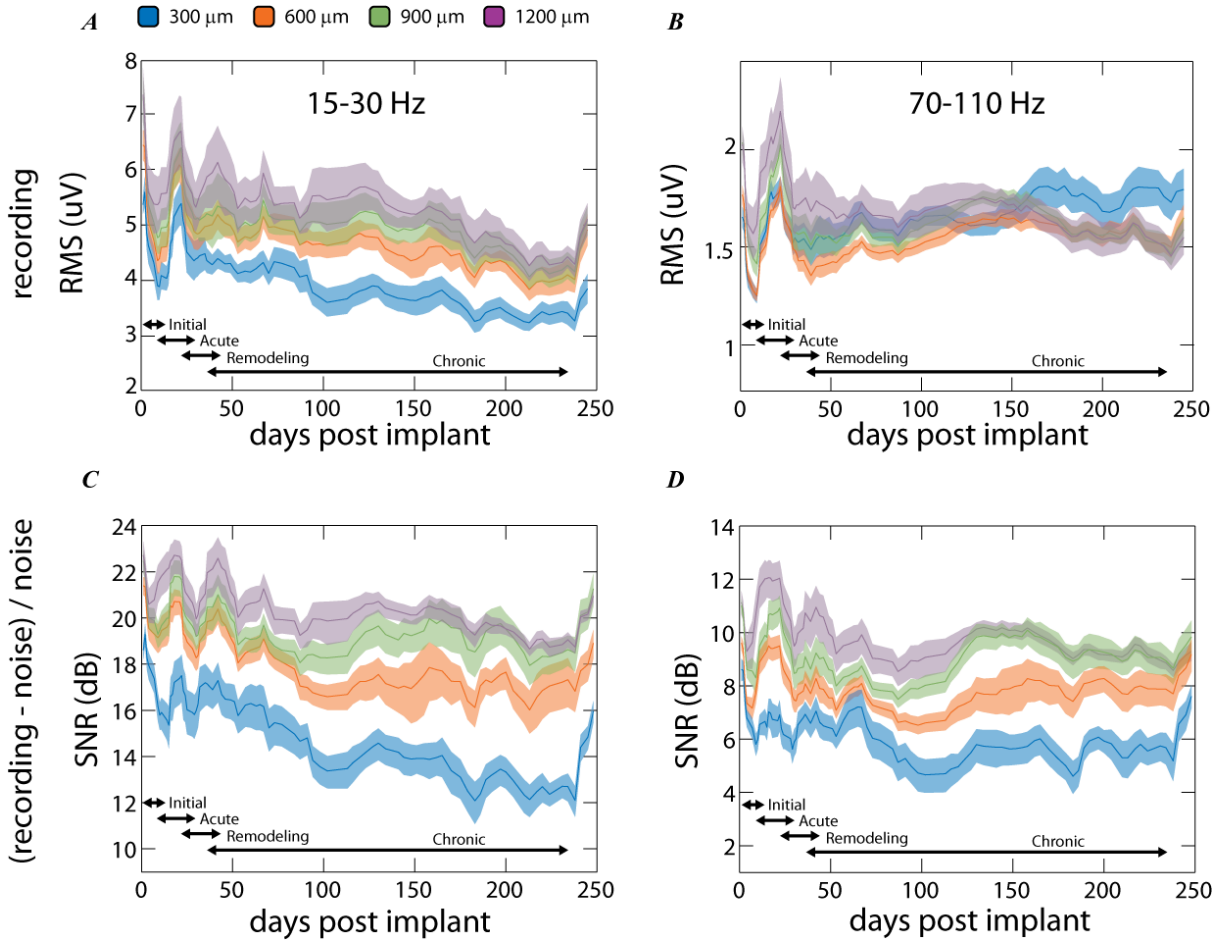

Figure 3.13: 4-Phase Chronic SNR Response Versus Electrode Size

A-B) The recorded signal amplitudes in beta (15-30 Hz) and gamma (70-110 Hz) bands, which include both physiological signals and non-physiological noise from the amplifier, are shown over the first 250 days post-implantation for all four Pt electrode sizes. Initially, larger electrodes had the largest signal amplitudes in both bands. However, in the gamma band, the smallest electrode had the largest signal amplitude after day 150. **C-D)** The non-physiological noise for each band was removed by subtracting the signal amplitudes of non-physiological noise interpolated from the physical RC noise model. The resulting signal was normalized by this noise to produce an estimate of the physiological SNR, which shows a clear separation between electrode sizes, where the largest diameters have consistently larger SNR.

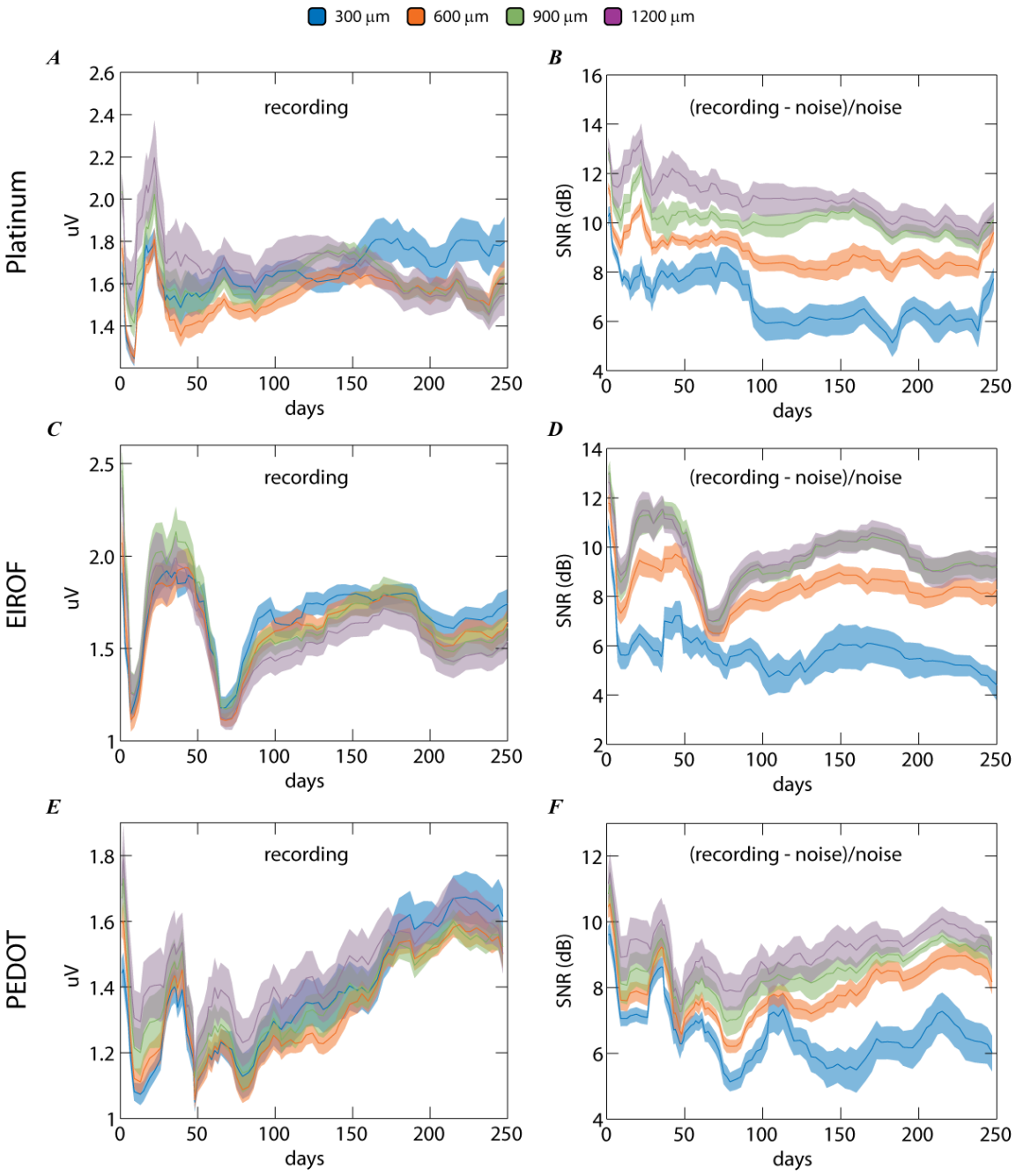

Figure 3.14: 4-Phase Chronic SNR Response Versus Coating

The recorded signal amplitudes and SNR in the gamma band (70-110 Hz) for Pt **(A,B)**, EIROF **(C,D)**, and PEDOT **(E,F)** electrodes. Each electrode array, regardless of material coating, shows the same reduction in SNR with smaller-diameter electrodes.

3.5.4 ECoG Signal Structure

While the previous results focus on chronic changes in the relative contributions of physiological signal and non-physiological noise, the following results focus on the structure of the physiological signal itself. Pearson's *moment statistics* corresponding to the mean, standard

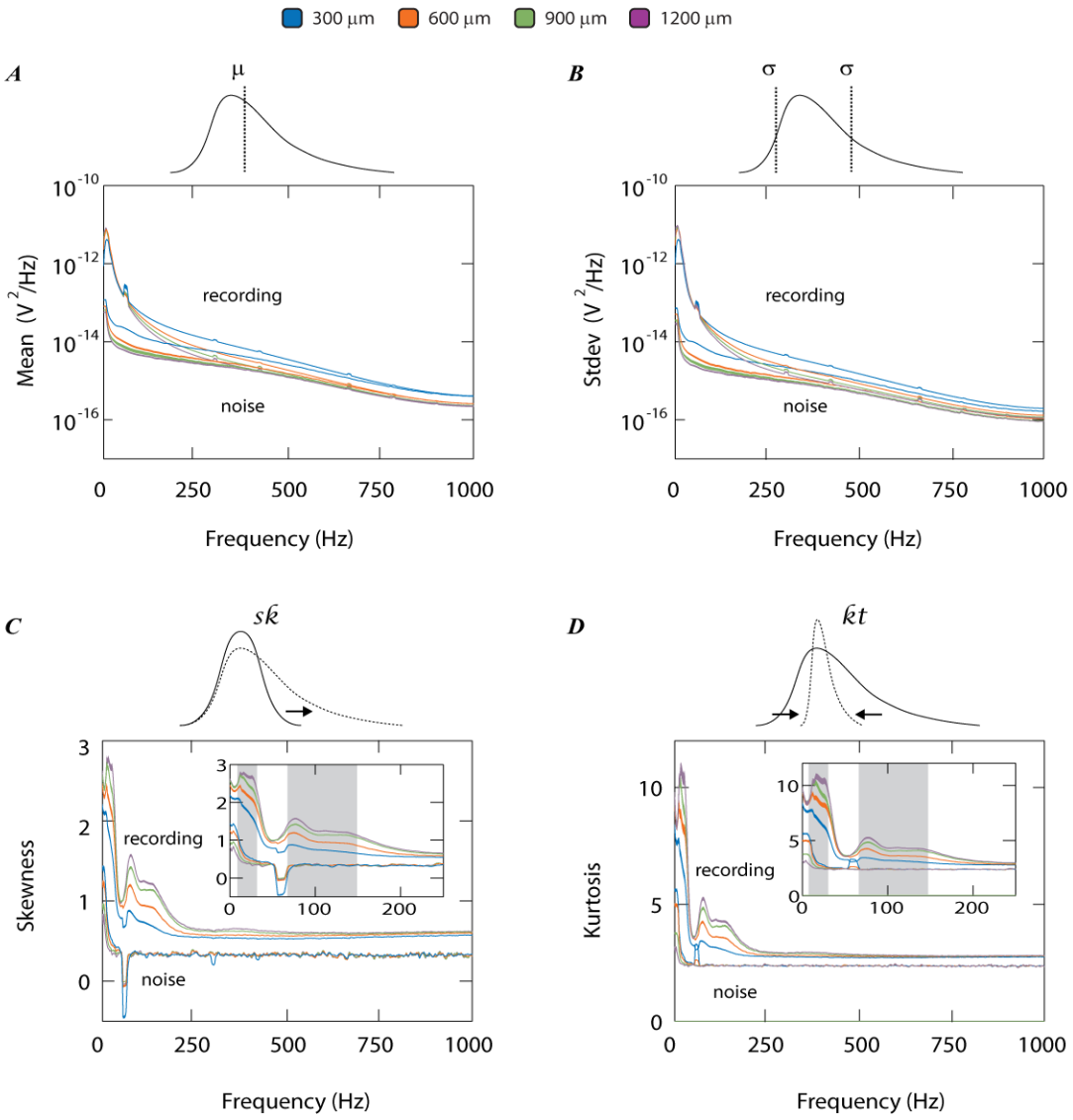

Figure 3.15: ECoG Signal Statistics: Mean, Stdev, Skewness, and Kurtosis

A separation of physiological noise from physiological signal at month 9 was conducted by assessing the first four moments of signal power (mean **(A)**, stdev **(B)**, skewness **(C)**, and kurtosis **(D)**). While the mean and stdev did not show anything, the skewness and kurtosis showed distinct peaks corresponding to the beta and gamma bands. The skewness and kurtosis of all other frequencies dropped to the level expected from Gaussian white noise.

deviation (stdev), skewness, and kurtosis were used to characterize the distributions of power observed within 2-Hz frequency bins. As shown in Figures 3.15A-B, neither the mean nor standard deviation of recordings showed any distinct structure that might indicate a separation between physiological signal and noise. However, both skewness and kurtosis showed distinct elevated deviations from noise in two broad bands, 8-35 Hz and 65-200 Hz with a deflection toward noise levels between 35-65 Hz, which was consistent across all recordings. Careful examination of the magnified views in Figures 3.15C-D shows that this deflection was not simply an artifact from 60 Hz line noise (which manifested as a narrow band notch), but instead was a consequence of some wider-band phenomenon. An inflection point in the high-frequency broad-band feature around 100 Hz suggests the possibility of two adjacent gamma band features spanning 65-100 Hz and

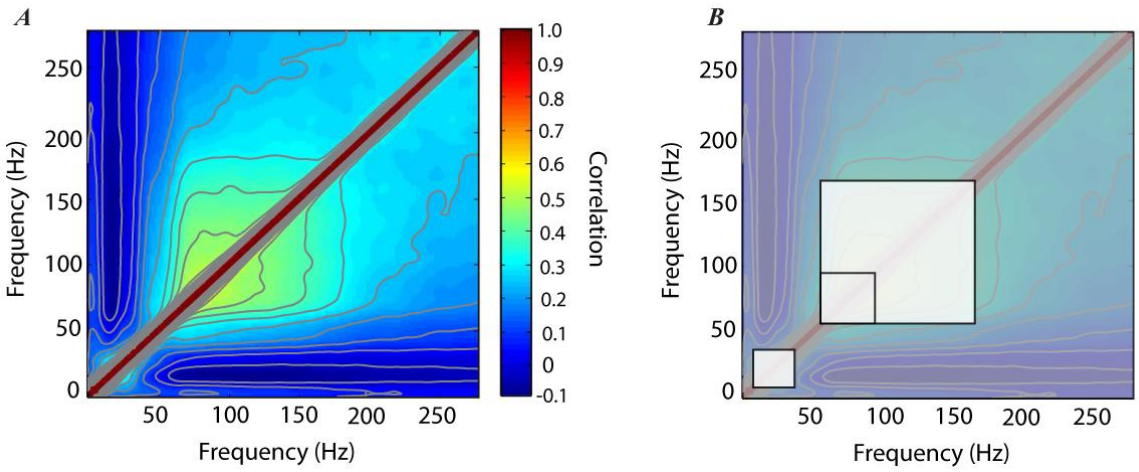

Figure 3.16: ECoG Correlation Structure Between Frequency Bands

(A) The correlation of power modulation between frequency bands was assessed for signals recorded on individual channels. The correlation structure shows two distinct bands: beta and gamma, as seen by the bulges near the diagonal. Gamma appears to be broadly correlated beyond several hundred hertz and slowly falls to flat low-level correlation levels expected from noise. Beta and Gamma are also slightly anti-correlated. **(B)** The correlation of power modulation between frequency bands was assessed between adjacent electrodes spaced 3 mm apart. Correlation decreased with increasing frequency and larger diameter electrodes resulted in larger correlations than smaller electrodes. This may not necessarily imply a higher spatial resolution of smaller electrodes, however, because increased uncorrelated noise (Gaussian white noise) on the smaller electrodes would produce the same effect—especially at higher frequencies where the noise floor is known to be higher for small-diameter electrodes.

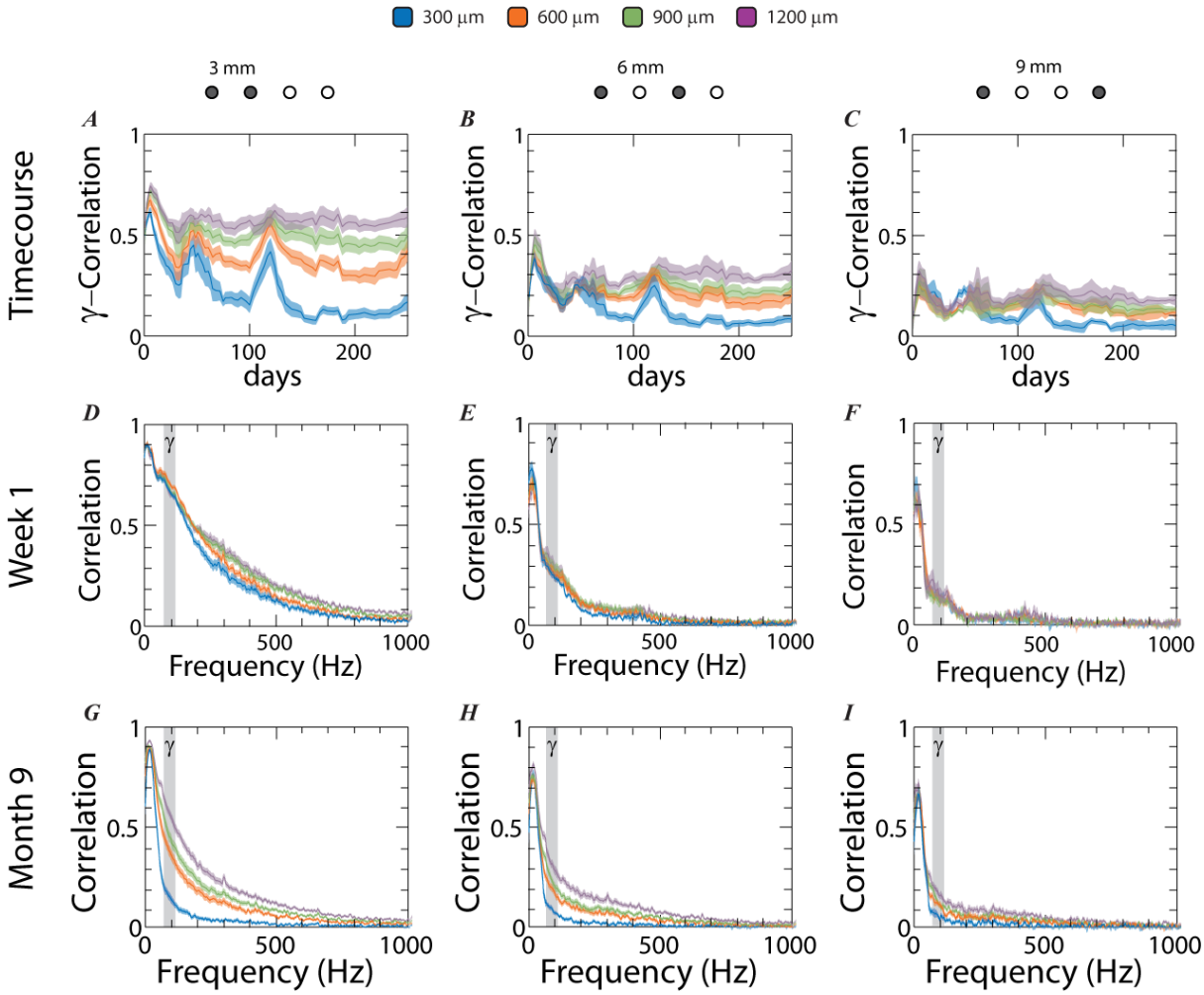

Figure 3.17: ECoG Inter-electrode Correlation Versus Distance and Size

Correlations between power modulation in the mid-gamma band (70-110 Hz) are shown over a 250-day period for each electrode size and for inter-electrode spacings of 3 mm **(A)**, 6 mm **(B)**, and 9 mm **(C)**. The mean correlation across all electrode combinations of the same size and distance is shown at 1 week **(D-F)** and at month 9 **(G-I)**. Overall, smaller electrodes diameters showed smaller inter-electrode correlation than larger diameters for all frequencies and across all time. However, it is not clear whether the reduced correlation is a consequence of reduced correlation in recorded physiological signal, or if the reduction in correlation was a result of larger uncorrelated noise due to the higher impedance and lower SNR. The observation that inter-electrode correlations were similar across all electrode sizes in week 1, gradually separated over time, suggests that the decrease in correlation observed with smaller electrodes may be due to noise, and not physiological signals.

frequency broad-band feature. Importantly, the magnitude of separation of these features from noise was enhanced for increasing electrode size, providing larger features at higher frequencies (up to nearly 200 Hz).

Signal structure was also evaluated by examining cross-frequency correlation of signal power on single electrodes. As shown in Figure 3.16A, the 8-30 Hz and 70-170 Hz features appeared as two distinct broad bands. Fluctuations in signal power within each band were highly correlated, as indicated by the wide-band increase in correlation along the diagonal. Correlated gamma activity was most concentrated within the 70-110 Hz band with diminishing broad-band correlation beyond 250 Hz. Activity *across* beta and gamma bands was slightly anti-correlated, and activity in the 30-50 Hz band between was generally uncorrelated with all bands. The dominant signal bands are highlighted in Figure 3.16B and correspond to alpha-beta (8-30 Hz), mid-gamma (70-110 Hz), and high-gamma (130-170 Hz).

The correlation of signal modulation between channels was tracked over time for inter-electrode distances of 3, 6, and 9 mm, as shown in Figure 3.17. As expected, correlations were higher for short inter-electrode distances, as predicted by greater overlap of areas of influence. Additionally, correlations between electrodes decreased rapidly with increasing frequency. Within the first several days post-implantation, the inter-electrode correlations for all electrode sizes were very similar but showed a distinct relationship between larger correlations and larger contact size following the first week. This effect was not observed as strongly for lower-frequency bands.

3.6 Discussion

3.6.1 Optimal Electrode Size and Spacing for ECoG

For epidural ECoG, electrodes were estimated to be located approximately 3-4 mm from signal sources in macaque monkeys and perhaps as far as 4-5 mm in humans, depending upon the thickness of CSF and dura. At these distances, the cortical areas over which signals are integrated are similar for electrode contacts in the range of 300-2000 μm, with smaller diameter electrodes achieving only slightly better performance in spatial resolution. This small improvement in resolution is countered by a large reduction in SNR due to higher impedances that 1) reduce the signal magnitude at the input to the amplifier, and 2) produce non-physiological noise that is added to the recorded signal. Based upon these findings, the recommended electrode contact size is in the range of about 1 mm diameter.

The optimal inter-electrode distances for hexagonally- and rectilinearly-arranged arrays ranged from 5-7 mm, depending upon the thickness of underlying CSF. The use of hexagonally-arranged electrodes is recommended to optimize the amount of unique signal that can be extracted per area. For the suggested 1 mm diameter electrodes, the optimal inter-electrode spacing is approximately 6 mm. This inter-electrode spacing is supported by electrophysiological results from chronic epidural electrodes used for motor BCI control, where performance decreased considerably when inter-electrode distances were less than 6 mm (Rouse et al., 2013).

The conductive CSF layer beneath electrodes has the largest effect on the area of integration, where thicker CSF layers shunt signals across larger areas, thereby reducing spatial resolution. Depending upon the thickness of implanted electrode arrays, the underlying CSF layer is expected

to be compressed in chronic implants, thereby reducing its shunting effect. Accumulation of insulative fibrous encapsulation around the implant may also serve to reduce shunting effects. Antectdotally, fibrous encapsulation surrounding chronic subdural electrode arrays has been observed to become highly integrated with adjacent dural tissue, suggesting that subdural implants may perform similarly to epidural implants under chronic conditions.

3.6.2 Effects of Noise on ECoG Signals

Bioelectrical recordings from electrodes can be decomposed into 1) physiological signals of interest, 2) physiological noise, and 3) non-physiological noise. The contributions of non-physiological noise can be greatly reduced through careful placement of electrodes (active, reference, and ground) relative to the signal source. For example, use of an upward skull-facing "quiet" reference and ground can minimize the amount of non-targeted neural activity picked up in neural ECoG recordings. Also, the use of a reference electrode with impedance matched to the recording electrode will maximize the common-mode rejection of the amplifier, which will reduce the presence of global common-mode signals like EMG, ECG, EOG, and 60 Hz line noise. Reduction of non-physiological thermal, current, and voltage noise can be achieved by use of low-impedance electrodes and low-noise amplifiers.

Estimations of non-physiological noise were facilitated by the combination of measured impedances and the RC noise model. By removing this layer of noise from recordings, physiological signals could be analyzed more accurately to determine differences in signal quality between electrode sizes and track changes in neural signals independent of the effects of electrode impedances. While smaller diameter electrodes produced larger total signal power at frequencies above 100 Hz, much of this signal power was due to non-physiological noise. Analysis of

physiological signal power vs non-physiological noise revealed that larger electrode diameters achieved higher SNR across all bands.

The use of low-impedance electrodes in combination with low noise amplifiers is critical for high-resolution measurements of ECoG. This is particularly important in the mid- and high-gamma bands where signal modulation depths fall below 1 μV_{rms}. For accurate recordings with SNRs above 3V/V (~10dB), combined non-physiological noise from the electrodes and amplifier should be less than 2 μV_{rms} in the alpha- (8-12 Hz) and beta-bands (12-30 Hz); less than 330 nV_{rms} in the mid-gamma band (70-110 Hz); and less than 160 nV_{rms} in the high-gamma band (130-170 Hz). For applications that do not require real-time decoding or control, SNR can be increased by a factor of $\sqrt{n}$ by averaging n trials together. However, for applications that rely on real-time analysis of ECoG and cannot benefit from averaging successive trials to improve SNR, use of low-noise amplifiers is critical.

3.6.3 Implications of Signal Changes for Chronic Implants

Until recently, ECoG recordings were only observed for acute periods extending no more than 30 days. Here, chronic changes in ECoG signals have been shown for up to 250 days post-implantation. Chronic changes in signal power and SNR were shown to coincide with the 4-phase reactive tissue response previously described in Chapter 2, consisting of an initial period (days 1-7), an acute period (days 7-30), remodeling period (days 25-45), and chronic period (beyond days 35-45). For acute recordings, the highest SNR occurs within the first several days. During this initial period, it is hypothesized that swollen tissues might press the electrodes closer to underlying signal sources to produce larger recordings. Throughout the first week, SNR will drop as swelling

reduces. In the second and third weeks, increased electrode impedances due to acute tissue encapsulation are observed. Signal SNR increases concomitantly during this period, possibly due to acute encapsulation tissue filling and compressing the conductive CSF layer. In the third and fourth weeks, tissue impedance decreases to near initial levels. During this remodeling period, encapsulation tissue from the acute response may be broken down allowing the shunting effect of CSF to decrease signal levels. Finally, during the chronic period, impedances once again increase, but signal SNR does not. The lack of SNR rebound may be due to either the formation of a denser permanent encapsulation layer that preserves the CSF shunting layer, or the formation of a thicker encapsulation layer that pushes electrodes further away from signal sources. Histological studies of these tissue responses is necessary to elucidate the precise mechanisms underlying these chronic changes.

Chronic SNR levels of ECoG remained high and relatively stable over the reported 250 days, with consistently higher levels associated with larger electrode diameters. The SNRs of the beta- and mid-gamma-bands were steady at approximately 10V/V (20 dB) and 3V/V (9.5 dB), respectively, for 1200 μm electrodes. High SNR and stable signals are of critical importance to chronic neural interfaces. This study validates the use of ECoG for chronic neural interfaces, which could supplement, or possibly replace single-unit recordings that are prone to signal loss over weeks to months.

The correlation of signal power modulation between electrodes was shown to decrease over time, with higher inter-electrode correlations associated with larger electrode diameters. This result is predicted by the analytical model and FEM simulations due to increased bulk impedance between the electrodes and signal sources. The increase in un-correlated non-physiological noise in recordings due to electrode impedances may also be responsible for this effect. While the

uncorrelated inter-electrode signals of smaller electrode diameters are desirable, the effect may be caused simply by their lower SNR, particularly in higher frequency bands where physiological signals are very small.

3.6.4 Implications of ECoG Signal Structure

The structure of ECoG signals was explored using statistical measures derived from distributions of power observed during baseline recordings. Measures of skewness and kurtosis revealed two broad frequency bands with distinct separations between signals and noise—specifically the alpha- and beta-bands (8-35 Hz) and the mid- and high- gamma-bands (65-200 Hz). Measures of skewness and kurtosis may be indicative of active modulation of neural activity, where positive deviations of signal power from baseline are more prevalent than negative deviations. Interestingly, the band between (35-65 Hz) displayed a deflection in skewness and kurtosis toward values expected from noise. Careful analysis within this deflection band showed that it was not a result from 60 Hz noise, but, in fact, an apparent node around which ECoG modulation appears to operate.

The same contiguous bands were also revealed within the cross-frequency correlation structure. The correlation structure showed that mid- and high-gamma bands are broadly correlated up beyond 300 Hz. These results suggest that while active modulation does occur up to 300 Hz, mid- and high-gamma bands may be better characterized as a single broad contiguous band. Cross-channel correlations showed that broad-band gamma modulation is more localized than alpha- and beta- modulation, which is consistent with gamma emerging from local cortical spiking activity, and alpha- and beta- modulations emerging from cortico-thalamic circuits. It is important to note that recordings were obtained while monkeys sat relatively still. Throughout the

period in which data for this study was being collected, the monkeys were not performing or being trained on any task, which could have biased their active modulation of signals. Therefore, while results from this study support a model for broad active modulation of gamma, slightly anti-correlated modulation of gamma with alpha and beta, and a fixed, non-modulated node around 35-65 Hz, results from trained behaving subjects may vary.

Chapter 4

A Motor BCI:

Multi-Dimensional Control using a

Co-adaptive Decoder

4.1 Introduction

4.1.1 An Overview of Motor BCIs

The discoveries that neurons in primary motor cortex (M1) encode intended movement direction (Georgopoulos et al.,, 1986) and velocity (Moran and Schwartz, 1999) resulted in development of motor neuroprosthetics to control cursors and later robotic arms. While invasive micro-electrode recordings have yielded the most advanced control (over 10 DOF in paralyzed individuals) (Wodlinger, 2015), chronic use of micro-electrode BCIs has been limited by immune responses. Non-invasive approaches using electroencephalography (EEG) and magnetoencephalography (MEG) have remained limited with sufficiently-good control of only 2 DOF. Significant challenges include weaker neural signals on the surface of the scalp for EEG and large external systems that are not readily mobile for MEG. ECoG-based BCIs are both minimally invasive and have the potential to capture high-fidelity signals. While ECoG-based BCIs are promising, they have yet to demonstrate dimensionality control on par with micro-electrode-based systems.

4.1.2 Decoding Algorithms for Motor Control

BCI decoding algorithms have been used to translate neural activity into the representations of distinct states (classifier decoders) or continuous control signals (analog decoders). The outputs of these decoders can be used in diagnostics (to identify something meaningful about the subject), as deciders (to choose between classes of responses), or as controllers (to drive system dynamics). For the most part, neural decoders have emerged from studies that aim to understand the relationships between neural activity and behaviors. This is often accomplished by observing neural activity and behavior concurrently and building statistical models to represent their relationships. Decoders can then be developed to predict, classify, and measure behavior indirectly through observations of the neural activity alone, and through extensions of the statistical models.

Generally, the development of a decoder starts by building a statistical model to link measured outputs (e.g., relevant behavior or states) back to observed neural activity, and then inverts the model such that desired outputs can be predicted by the neural activity alone. This approach works well when desired outputs are readily observed as the neural activity is recorded. However, observation of desired outputs is not always possible (e.g. neuropsychiatric state or movement with paralyzed individuals). In this case, proxies are required to estimate the desired output. Estimates of the desired outputs may be accomplished through psychometric tasks or imagined outputs (e.g., imagined movement or observed movements by others). For volitional control, where the subject can actively modulate activity to achieve a desired output, it is important to link the subject's intent back to the neural signals to be used with the decoder.

Several different types of decoders have been used in the past, some of which are listed below. These decoders vary in their statistical assumptions, their complexity in computation, and their performance in varying applications.

1) Population Vector Algorithm (PVA) (Georgopoulos et al, 1986)
2) Optimal Linear Estimator (OLE) (Salinas and Abbot, 1994)
3) Kalman Filter (Brown et al., 1998)
4) Laplace-Gaussian filter (Koyama et al., 2010)
5) Unscented Kalman Filter (Li et al., 2009)

As described by Zhang and Chase (2015), the performance of a decoder is also dependent both upon the dynamics of the system being controlled (i.e., the plant, using control systems terminology) and closed-loop error-correction achieved by the subject's ability to adapt modulation of their neural signals.

Careful co-design of the decoder, the plant, and feedback should be emphasized, when possible. For example, decoding position control for movement of a cursor will result in undesirable jerky movement and jitter caused by noise in the neural signals. Decoding velocity control of a cursor will provide smoother movement by integrating random noise but may slow movement, depending upon gain. Decoding of acceleration for control will result in even smoother movement but will require twice the control bandwidth as velocity control. Regarding closed-loop error-correction, a BCI inherently requires a subject to

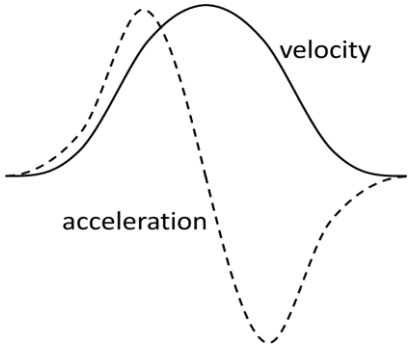

Figure 4.1: Control Bandwidth for BCIs

Velocity signals follow a well-characterized bell-shape curve as movement is initiated and then brought to rest. The associated acceleration (the derivative of velocity) modulates up and down twice as fast and needs approximately twice the bandwidth for BCI control.

be part of the control loop, and as such, feedback to the subject and their resulting adaptation should be carefully considered.

4.1.3 Co-adaptive Human-machine Learning

Coadaptation refers to the ability of both the subject and decoder to change their behaviors in order to improve the overall performance of the BCI. Shifts in neural tuning properties might occur due to adoption of new control strategies by the subject, changes in context or environment, competition with concurrent behavior or stimuli, or injury and disease. Coadaptive algorithms for motor BCIs enable the decoder to iteratively update parameters to track these neural changes over time, which may include inherent non-stationarities in the signals (Taylor et al., 2002; Orsborn et al., 2014). Challenges in implementing co-adaptation include 1) the need to estimate subject intent for training updates, 2) adjusting the learning rate of the decoder relative to subject learning, and 3) balancing the speed of decoder updates with time required to sufficiently sample the control space to avoid over-fitting.

4.2 Purpose of the Study

ECoG presents a promising technology for implementing a chronic BCI. One desirable benefit of ECoG is that surface electrodes are minimally invasive (particularly epidural ECoG arrays) compared to micro-electrodes. Other desirable benefits include stable recordings over extended periods and signal features that are rich with information (particularly the modulation of power in the gamma band), as described in Chapter 3. However, ECoG-based BCIs have not yet demonstrated multi-dimensional control on par with what has been achieved with micro-electrode

BCIs. Toward the goal of demonstrating multi-dimensional control, previous work that demonstrated 2 degrees-of-freedom (DOF) was extended by developing a new learning approach, called co-adaptation. Co-adaptive learning explicitly accounts for challenges in learning between both the BCI user and the machine, and it aims to optimize this concurrent adaptation to achieve higher multi-dimensional performance with less training time. Here, the focus was placed on the development of a co-adaptive framework for an ECoG-based BCI that provides error-correction to a naïve decoder based upon the inferred intended actions of the BCI user. This approach allows both the user and the decoder to converge on an optimal set of features for multi-dimensional control. This study combines signal processing and co-adaptive algorithm design with a hyperdimensional statistical framework to resolve unanswered questions regarding the optimal frequency bands and locations of ECoG signals for BCI control through two 4DOF behavioral tasks.

4.3 Methods

4.3.1 Task Designs for Single and Bimanual Multi-Dimensional Control

Two male, 6-10 kg monkeys (*Macaca mulatta*), I and K, were trained to perform behavioral tasks within a virtual environment displayed to them on a computer monitor. Each monkey was first trained to perform standard center-out tasks using a joystick. Monkey K was subsequently trained on 2DOF BCI tasks outside the scope of this dissertation, which focused on velocity- vs force-control. Following these studies, Monkey K learned to perform the Bimanual Out-to-Center task described below under brain control without any prior related training. Monkey I had never

performed a BCI task prior to participating in the Reach and Rotate task described below. Tasks were learned through operant conditioning with liquid rewards while sitting freely in a primate chair. Standard 17 inch LCD monitors positioned approximately 20 inches from the monkeys were used to display the tasks through a rendered 3D virtual environment.

Two BCI tasks were designed to demonstrate and evaluate 4DOF control, based upon the more traditional lower-dimensional center-out task. The first 4DOF task, Reach and Rotate, was focused on 4DOF control of a single cursor object within a virtual environment. The second task, Bimanual Out-to-Center, was focused on simultaneous control of two 2DOF objects within a virtual environment. In both tasks, cursors were moved via velocity control derived from neural signals. Each trial represented a movement to one of the possible targets, which was randomly chosen from a set, but not repeated until all trials had been completed. A maximum movement time to the target was enforced (typically less than 5 seconds) in addition to a minimum target hold time (1-3 seconds) when the cursor(s) reached their target(s). Successful trials were associated with a liquid reward. Unsuccessful trials were either not rewarded or associated with a reduced reward and were excluded from subsequent decoder updates using a co-adaptive leaning approach.

The Reach and Rotate task was designed to mimic similar translational and rotational movements required to insert a key into a keyhole. In this task, a controlled object and target object were represented as spherical bodies, each with a protruding stick to represent rotation. The cursor sphere-and-stick object could be translated in 3D and rotated in 1D (viewed as clockwise and counter-clockwise rotation) for a total of 4DOF. All movement was conducted within a large cube with semi-transparent walls. The cursor object was attached to the end of two 2-segmented arms with joints that resembled shoulders and arms. The purpose of the armature was to provide improved visualization of depth within the virtual environment that was displayed on a 2D

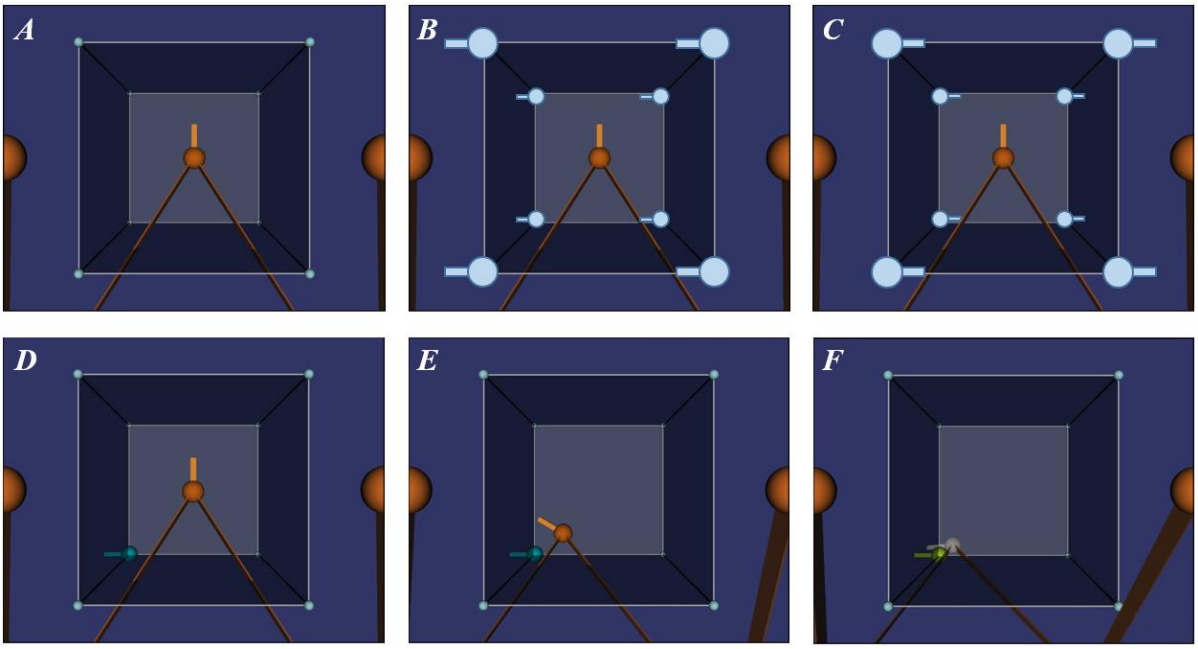

Figure 4.2: Behavioral Task for Single Object 4DOF Control: Reach and Rotate

Screenshots of the Reach and Rotate task designed for 4DOF control of a single object, shown in the center of a cube with "stick" oriented upward **(A)**. The cursor object is attached to two armatures intended to provide additional depth cues in the virtual environment. A total of 16 targets were possible, each located at a corner of the cube: 8 targets rotated counter-clockwise **(B)** and 8 targets rotated clockwise **(C)**. **D-F)** Task progression from target presentation, movement, and target acquisition is shown.

computer monitor. Depth cues were represented by linear perspective, relative size, overlap, angles of the armature's joints, and position of the armature links as they cut through the semi-transparent sides of the cube.

The Reach and Rotate task began with the cursor in the center of the cube with the stick pointed up. Next, a target appeared randomly in one of the 8 corners of the cube with either the stick pointing to the left (-90 degrees) or pointing to the right (90 degrees) relative to the cursor. This resulted in 8 corners x 2 rotations = 16 total perturbations to comprise a full set. Following completion of an entire set, the decoder was updated using the co-adaptive method described later. The gains for each translational DOF were equal. The rotational gain was normalized to the translational gains according to the maximum cube dimensions and rotational range (180 degrees).

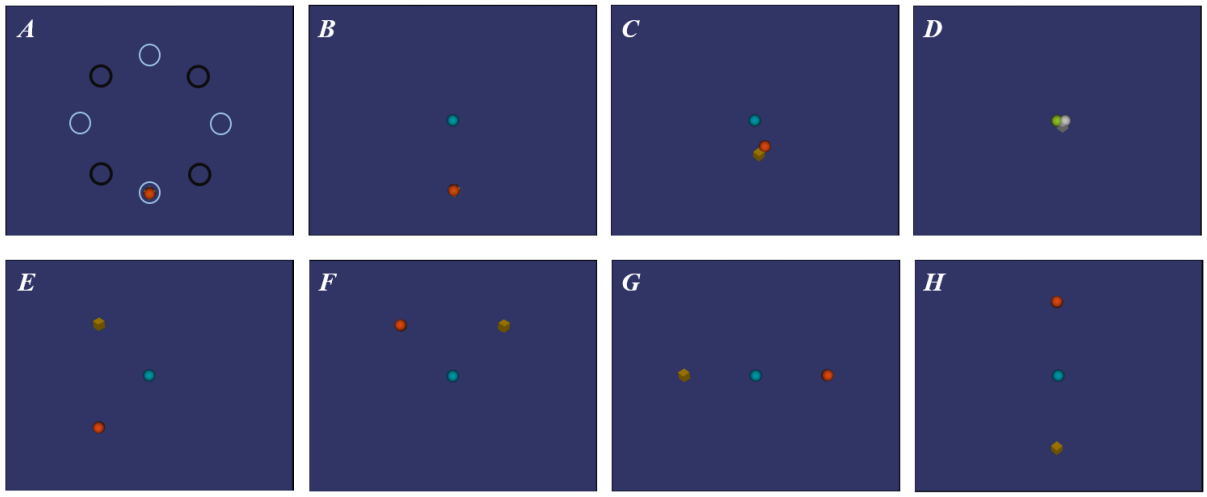

Figure 4.3: Behavioral Task for Multiiple Object 4DOF Control: Bimanual Out-to-Center

Screenshots of the Bimanual Out-to-Center task designed for 4DOF control of two separate 2DOF objects (represented as a cube and an orange sphere). **A)** For a given set of trials, the two cursors could start at any of the circled positions (black for one set of trials, and white for the next set, and so on). In some trials, the cursors would be opposite from each other, in others they may be adjacent to each other, and still others, they may be in the same location. **B-D)** A trial is shown in which both cursors appear at the bottom of the screen, the central target is presented, and the cursors are both moved to the target simultaneously. **E-H)** Screenshots of several starting configurations are shown, where **E** and **F** are from a common set, corresponding to the black circles in **A**, and **G** and **H** are from a common set, corresponding to the white circles in **A**.

Cursors could move outside of the cube, but not outside the field of view on the screen. Likewise, rotations were limited between -120 degrees to 120 degrees (30 degrees beyond each necessary maximum rotation).

The Bimanual Out-to-Center task was designed to mimic movement of two arms but constrained to only 2DOF (x- and y- translation) of each spherical cursor. Rather than moving two objects from the center to two peripheral targets (which follows the approach of the standard center-out task), the movement directions were reversed, from the periphery inward to a common central target. The rationale for this design was that it alleviated the cognitive load associated with spatial attention being spread across multiple areas of the screen. In the Out-to-Center task, it is possible to maintain generally focused attention near the center of the screen as both cursors move

inward. Different geometric shapes and colors were used to differentiate each cursor (a green cube, and an orange sphere).

The Bimanual Out-to-Center task began with each cursor positioned at a fixed radius from the center in one of four locations. In alternating sets, the four starting locations were rotated by 45 degrees to more thoroughly sample the space without requiring every combination per training set. For example, in the first set, the four locations were located North, East, South, and West from center. In the next set, the four locations were located North-East, South-East, South-West, and North-West from center. Within a set, the two cursors could start in the same location, 45 degrees apart, or at opposite locations (which could be flipped). This resulted in 4 starting locations for the first cursor x 4 locations for the second cursor = 16 total permutations to comprise a full set. Following completion of an entire set, the decoder was updated using the co-adaptive method described later. The gains for each translational dimension and each cursor were equal. Cursors were not outside the field of view on the screen.

4.3.2 Electrode Array Designs and Implantation

Monkey I was bilaterally implanted with two types of custom epidural ECoG arrays placed over sensorimotor cortex (M1 and S1) using standard stereotaxic methods. The first array, implanted over the left hemisphere, was fabricated by Ad-tech (Oak Creek, WI, USA). The second array, implanted over the right hemisphere, was fabricated by PMT (Chanhassen, MN, USA). Both Ad-tech and PMT electrode arrays had the same design, with the exception that the Ad-tech array consisted of 1.5 mm diameter Pt disk recording electrodes, and the PMT array consisted of

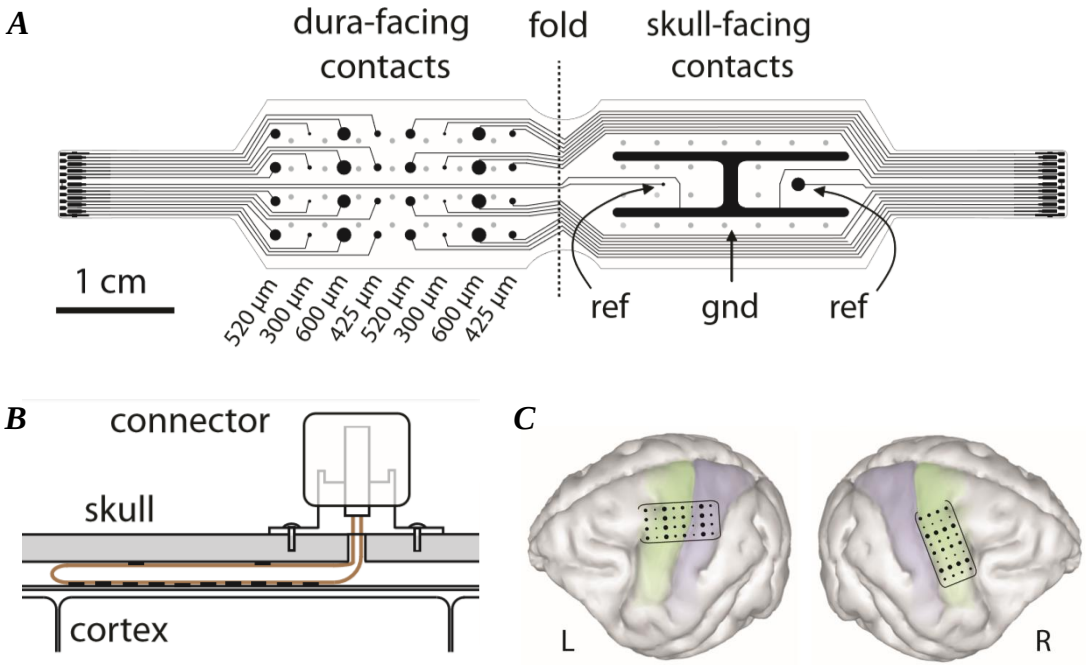

Figure 4.4: Thin-film Multi-Diameter Electrode Array

Thin-film polyimide arrays were constructed using MEMs fabrication processes and consisted of platinum disk electrode contacts printed onto a flexible polyimide substrate that was punctated by perforations for improved biological transparency **(A)**. Arrays were based upon a folding design where 32 electrode contacts of four different sizes faced downward toward the cortical surface and two references and a large-area ground faced upward toward the overlying skull as shown in **(B)**. Two arrays were implanted bilaterally into the epidural spaces covering primary motor (M1) and primary somatosensory (S1) cortex of the left hemisphere and M1 of the right hemisphere **(C)**.

2 mm diameter Pt disk recording electrodes. Both arrays contained 13 dura-facing recording

electrodes and 2 skull-facing reference electrodes. In addition, each array contained 3 mm diameter dura- and skull-facing ground electrodes. Each array was connected to a separate 18-channel miniature connector (Omnetics, Minneapolis, MN), which was housed and protected beneath a capped titanium chamber when not in use. The chamber assembly was permanently affixed to the skull with a standard acrylic headcap and bone screws.

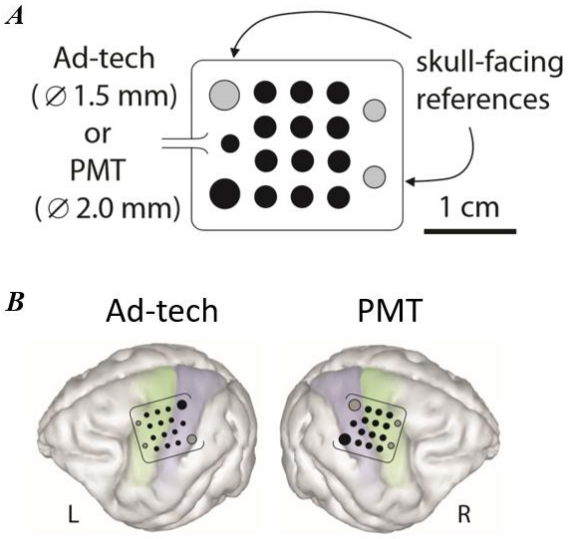

Figure 4.5: PMT and Ad-tech Electrode Arrays

A) Designs of the Ad-tech and PMT epidural ECoG arrays. **B)** Alignment of each array over sensorimotor cortex of Monkey I.

Monkey K was bilaterally implanted with two custom 32-channel thin-film arrays, similar to the arrays described in Chapters 2 and 3, but with Pt electrodes grouped in diameters of 300 µm, 425 µm, 520 µm, and 600 µm. The first electrode array was positioned over the left hemisphere to cover both M1 and S1. The second electrode array was positioned over the right hemisphere to cover only M1. Each flexible polyimide array was based on a folding design with 32 dura-facing recording electrodes, 2 skull-facing reference electrodes, and a large-area (36.8 mm^2) "H"-shaped ground pad. Each array was connected to miniature zero insertion force (ZIF) connector (Tucker-Davis Technologies, Alachua, FL) which was housed and protected beneath a capped delron chamber when not in use. The chamber assembly was permanently affixed to the skull with a standard acrylic headcap and bone screws.

4.3.3 Feature Selection and Motor Decoding using Optimal Linear Estimation

In order to obtain multidimensional control of a cursor, the spectral power modulation of recorded neural signals were transformed into multi-dimensional velocity control signals that drove the movement of a multi-dimensional cursor object. Visual feedback of the control was provided to the monkey by integrating the velocity signals and displaying the instantaneous position (and rotational orientation) of the cursor within a rendered virtual environment, presented on a computer monitor. The signal processing chain consisted of:

1) **Feature expansion**: The time series voltage recording from each ECoG electrode was expanded into five time-series features (power estimates within five separate frequency bands). Power estimation was accomplished with the combination of a filter bank implemented with 2^{nd}-order Butterworth bandpass filters followed by full-wave rectification (absolute value) and a final 2^{nd}-order Butterworth lowpass filter. Cutoff frequencies for bandpass filters were: 8-15 Hz (alpha), 15-30 Hz (beta), 30-55 Hz (low gamma), 70-115 Hz (mid gamma), and 130-175 Hz (high gamma). Spectral power near to 60 Hz harmonics, which result from mains power, were not included.

2) **Feature normalization**: First, a log transform was applied to each time series feature in order to decrease the skewness of its distribution (as described in Chapter 3) to approximate a Gaussian distribution, which is preferred for the regression model upon which the decoder is based. Next, each time series was normalized by subtracting its estimated mean and dividing by its estimated standard deviation. Normalization of features permitted subsequent analyses of decoder coefficients assigned for velocity

control signals to understand how features contribute to control. Estimates of both the mean (M) and standard deviation (S) were estimated online with the addition of each new time-series sample (k) using Knuth's computationally-efficient method:

$$M_k = M_{k-1} + (x_k - M_{k-1})/k \tag{4.1}$$

$$S_k = S_{k-1} + (x_k - M_{k-1})/(x_k - M_k) \tag{4.2}$$

This method can estimate M and S in a single pass and only requires memory for a counter (k), and the last estimate of M_{k-1} and S_{k-1}.

3) **Velocity Decode:** At each time step, each of the N normalized features, f_n, were multiplied by an assigned decoder coefficient, c_n, that represented the feature's contribution to the overall velocity control of a particular movement dimension. Coefficients were assigned by an OLE decoder model, which combined multiple regression models for each dimension of control. A final control signal for a dimension resulted from the summed weighted contributions from all features and a single constant, c_0, to account for fixed offsets in the regression model.

$$u[k] = \sum_n f_n[k] \cdot c_n + c_0 \tag{4.3}$$

This process was repeated for each dimension of control.

4) **Velocity Threshold:** Prior to applying the velocity control signal to movement, a thresholding function was applied to dampen spurious movements from small-signal noise. The threshold function was implemented by an arctangent function:

$$output = gain\left[\frac{1}{2} + \frac{1}{\pi}\text{atan}\big(slope(input - offset)\big)\right] \tag{4.4}$$

In this representation, parameters for *offset*, *slope*, and *gain* provide flexibility in tuning response characteristics of the thresholding function.

The coefficients for the velocity decoder were calculated by the OLE method, which combines regression models that link the normalized features to each dimension of control. Training data sets for the OLE consisted of two aligned time series data sets organized as matrices of T time samples, N numbers of normalized features, and D desired kinematic control signals:

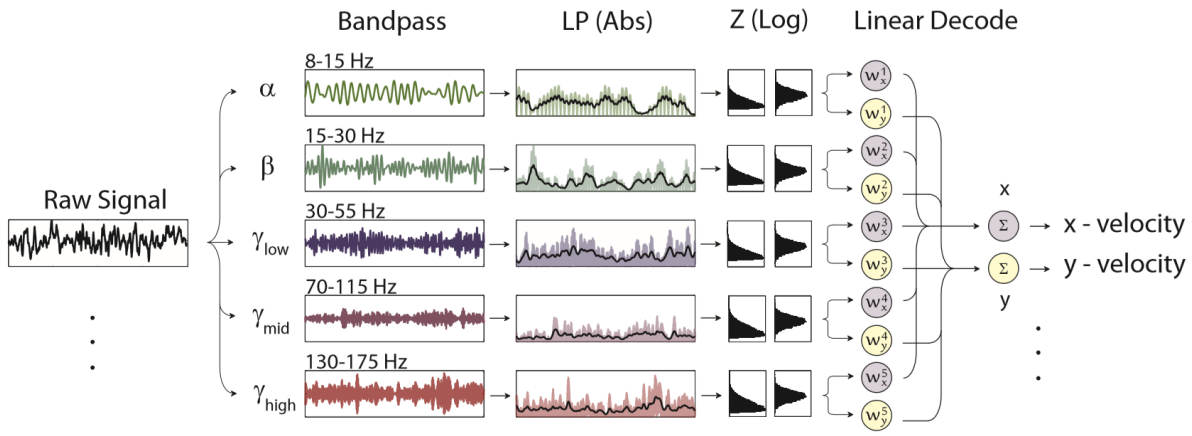

Figure 4.6: Signal Processing for Feature Extraction, Normalization, and Velocity Decode

The raw signal is first expanded into five frequency bands, and then the power within each band is estimated by a standard envelope-detection scheme that consists of full wave rectification and then low-pass filtering. The resulting estimate of power is then log transformed in order to approximate a Gaussian distribution. The signal is then z-scored by subtracting the mean and dividing by its standard deviation. Estimates of the mean and standard deviation are calculated by Knuth's method in a single pass. Velocity control signals for each dimension are then calculated by multiplying the signal by its unique coefficients for each dimension of control and summing its weighted contribution with all other channels. Finally, a thresholding function is used to dampen low-amplitude noise to improve the ability to hold the cursor still.

$$F: [T \times N] = \begin{bmatrix} f_{t_1}^{n_1} & f_{t_1}^{n_2} & \cdots & f_{t_1}^{N} \\ f_{t_2}^{n_1} & f_{t_2}^{n_2} & \cdots & f_{t_2}^{N} \\ \vdots & \vdots & \ddots & \vdots \\ f_{t_T}^{n_1} & f_{T}^{n_2} & \ldots & f_{T}^{N} \end{bmatrix} \tag{4.5}$$

$$K: [T \times D] = \begin{bmatrix} k_{t_1}^{d_1} & k_{t_1}^{d_2} & \cdots & k_{t_1}^{D} \\ k_{t_2}^{d_1} & k_{t_2}^{d_2} & \cdots & k_{t_2}^{D} \\ \vdots & \vdots & \ddots & \vdots \\ k_{T}^{d_1} & k_{T}^{d_2} & \ldots & k_{T}^{D} \end{bmatrix} \tag{4.6}$$

where F and K refer to features and desired kinematic control signals, respectively. The OLE assumes that K can be constructed by matrix multiplication of F by a matrix of regression coefficients C which represent the weighted contributions of each feature:

$$C: [N \times D] = \begin{bmatrix} c_{n_1}^{d_1} & c_{n_1}^{d_2} & \cdots & c_{n_1}^{D} \\ c_{n_2}^{d_1} & c_{n_2}^{d_2} & \cdots & c_{n_2}^{D} \\ \vdots & \vdots & \ddots & \vdots \\ c_{N}^{d_1} & c_{N}^{d_2} & \ldots & c_{N}^{D} \end{bmatrix} \tag{4.7}$$

$$K = FC \tag{4.8}$$

Therefore, C is estimated by the following:

$$C = F^{+}K = ((F^{T}F)^{-1}F^{T})K \tag{4.9}$$

Where F^{+} is the pseudoinverse of F. Note that in order to include a constant bias term, c_0, in the regression models, an additional column of 1's is added to the feature matrix such that $F: [T \times N + 1]$ and $C: [N + 1 \times D]$.

4.3.4 Co-adaptive Human-machine Training Algorithm

In order to train the OLE decoder, an estimate of desired control is required, in addition to the neural features occurring during the time of the desired control. In past approaches, the matrix K has been obtained from actual or imagined movements while neural data is recorded. Typically, these data sets include as many trials as possible and are very large to prevent over-fitting of the decoder model on trial-by-trial noise. However, this approach is slow and limits the ability of the decoder and subject to learn together.

The key idea behind co-adaptive learning is to approximate real-time error correction of the decoder through short and iterative updates. This approach allows the subject to quickly alter their control strategy based upon their observed real-time performance. It also provides a means by which the decoder can be iteratively refined to overcome over-fitting, drift, and new subject control strategies.

In the co-adaptive approach, only a minimum training set is desired in order to quickly provide a new update to the decoder. For the first training set, the cursor was controlled entirely by software, moving on its own from a central starting point to a set of targets that represented the full dimensional space while the subject observed. During this "watch-only" period, the cursor moved in a direct path such that the desired control signals were constant. As the cursor moved, a normalized multi-dimensional vector that represented the direction to the desired target was logged and used as the desired kinematic control signal K. Once a minimum set of targets were presented, the decoder was trained as described above.

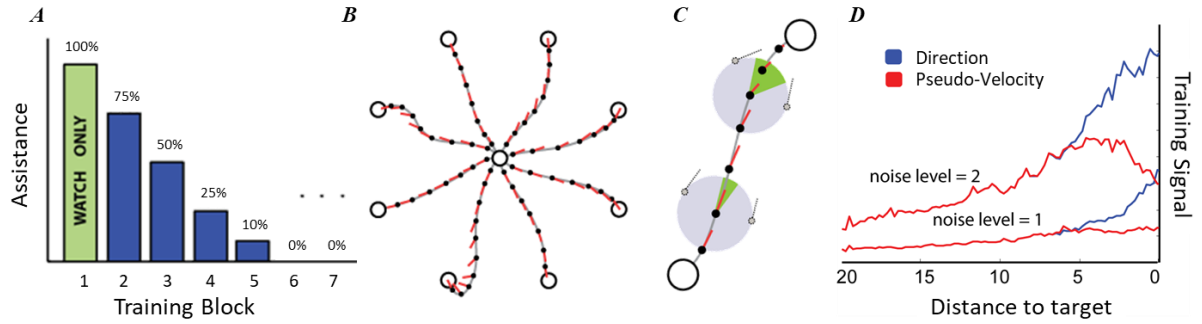

Figure 4.7: Co-adaptive Training Based Upon Estimated Pseudo-Velocity

A) The initial decoder model was based upon neural activity recorded during a "watch-only" period during which objects moved autonomously to each target within a complete set. As each training block progressed the monkey was given less assistance by the computer until block 6 when the monkey had full control of the cursor (no bias). **B)** Throughout each movement, instantaneous directions to the target (n-dimensional vectors) were recorded in addition to the observed neural activity. After each block of trials, weights from the linear decode model were updated via the OLE (least-squares regression) and assistance was decreased as the subject's control improved. **C)** A challenge with training the decoder based upon desired movement direction (a unit vector) is that as the cursor approaches the target, any undesirable noise in control (represented by the gray circle) results in larger jitter in the estimated desired direction to the target (highlighted in green). **D)** To overcome this challenge, a pseudo-velocity measure was used which forced the unit vector to zero as it approached and held its position at the target. Simulations are shown for different levels of noise in movement and the resulting jitter in the estimates of intended movement using both direction and the pseudo-velocity measure.

For the next training set, the gain on BCI control of the cursor was set at a low level and at each time step, the software calculated the optimal trajectory to the target and assisted movement in the correct direction. While moving under software assistance, the cursor was able to jitter due to initially poor BCI control, which could result in curved and meandering paths to the target. At each time step, the assumed optimal control was recorded as the normalized direction to the target. However, once the cursor reached a defined proximity to the target, the desired direction vector was attenuated linearly, such that all vector components approached zero as the cursor reached the target and was held momentarily to complete the trial. This desired control signal represented a "pseudo-velocity", intended to improve the ability of the decoder to allow the subject to hold the cursor stationary. Additionally, the attenuation limited noise in the training set caused by jitter in the cursor movement that is amplified by a direction vector as the cursor approaches the target.

Following collection of the full training set, a new set of regression coefficients were calculated. Rather than using the newly calculated regression weights alone for the updated decoder, memory of past weights was also included in the update through the implementation of a low-pass filter:

$$C_{new} = \alpha C_R + (1 - \alpha) C_{prev} \tag{4.10}$$

where C_{new} is the new decoder, C_{prev} is the previous decoder, C_R represents the newly calculated regression weights, and α is a smoothing coefficient that controls the relative contributions of old and new information into the decoder. At the extremes, when $\alpha = 1$, the decoder relies exclusively on new information, and when $\alpha = 0$, the decoder relies exclusively on old information and no longer learns. Based upon observed performance, a fixed value of $\alpha = 0.25$, was used for the studies described here, though this remains an interesting topic to explore further in future work.

Over subsequent trials, this process was repeated, the software assistance was reduced, and BCI control was increased. For a naïve monkey that had never performed a BCI task before, but was trained on the task using a joystick, BCI control was achieved in about 30 minutes. Although it only took 30 minutes for a naïve monkey to learn 2D the first time, full 4D control took a month of daily training to master. Once mastered, well-trained monkeys obtained 4D full control within three to four sets when starting with a zeroed-out decoder at the beginning of the day.

4.3.5 A Multi-Dimensional Statistical Framework for Analysis of Preferred Directions

For each 4DOF task, the OLE decoder was used to map neural features onto velocity control signals described within a 4-dimensional (4D) space. For a given control signal, this mapping is described by a summation of normalized features multiplied by their respective decoder coefficient that corresponds to a specific dimension (i.e., x-, y-, and z-translation with r-rotation). In this case, the combined coefficients for a feature can be described by a 4D vector, which has no restriction on the magnitude. Extending this representation, the 4D decode vector can also be described within the framework of a weighted preferred direction:

$$c = PD \cdot w = \begin{bmatrix} c_x \\ c_y \\ c_z \\ c_r \end{bmatrix} = \begin{bmatrix} PD_x \\ PD_y \\ PD_z \\ PD_r \end{bmatrix} \cdot w \tag{4.11}$$

where, here, *c* represents the features coefficients for each dimension. Under this framework, interesting questions can be investigated through the analysis of the weights, w, that provide an indication of *how much* features contribute to control, but also through the analysis of preferred directions, PD, that provide an indication of *how aligned* features are in their contributions to multi-dimensional control. In order to understand the importance of features being assigned similar or different PDs, a statistical

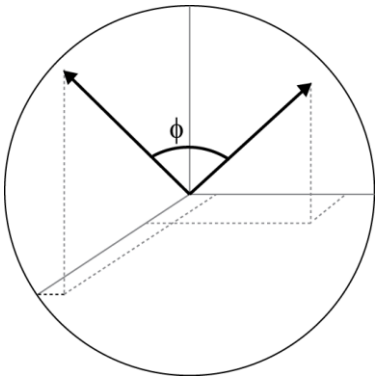

Figure 4.8: Alignment Between PDs

The angle $\boldsymbol{\phi}$ describes the alignment between PDs assigned to separate features. For the 4DOF tasks, the goal is to similarly compare the alignment of PDs in a hyperdimensional space greater than 3D.

framework is needed to describe how the PDs of multiple features should be expected to align if assigned at chance.

The following provides a generalized mathematical analysis of the expected likelihood of finding PDs aligned by angle for multi-dimensional spaces. First, to orient to multi-dimensional mathematical notation, concepts of an *n*-sphere and *n*-ball are defined, which is a generalization of the ordinary "sphere" and "ball" to spaces of arbitrary dimension. For any natural number *n*, an *n*-sphere of radius *r* is defined as the set of points in (*n*+1)-dimensional Euclidian space, all located a distance *r* from the center, *c*.

0-sphere: is a pair of points {c-*r*, *c*+*r*} and is the boundary of a **1-ball** (line segment)

1-sphere: is a circle of radius *r* centered at *c*, and is the boundary of a **2-ball** (disk)

2-sphere: is an ordinary 2-dimensional sphere in 3-dimensinal Euclidean space, and is the boundary of a **3-ball** (ordinary ball)

3-sphere: is a sphere in 4-dimensional Euclidean space and is the boundary of a **4-ball**

The set of points in (n+1) space: (x_1, x_2, x_3, …, x_{n+1}) that defines an n-sphere (S^n) is represented by:

$$r^2 = \sum_{i=1}^{n+1} (x_i - c_i)^2 \tag{4.12}$$

where *c* is a center pint and *r* is the radius. This *n*-sphere (S^n) exists in (n+1)-dimensional Euclidean space and is an example of an *n*-manifold.

Measures of *n*-spheres and *n*-balls are defined as follows:

$S_1(R) = 2\pi R$: 1-dimensional measure of a 1-sphere of radius R, which is the circumference of a circle of radius R in the Euclidean plane

$V_2(R) = \pi R^2$: 2-dimensional measure of a 1-sphere. This is the region enclosed by the 1-sphere, which is a disk of radius R in the Euclidean plane (The "volume" of a 2-ball)

$S_2(R) = 4\pi R^2$: 2-dimensional measure of a 2-sphere. This is the surface area of a normal sphere

$V_3(R) = \frac{4}{3}\pi R^3$: 3-dimensional measure of a 2-sphere. This is the volume of a normal sphere (3-ball)

In general, the volume in *n*-dimensional Euclidean space of an *n*-ball of radius R is:

$$V_n(R) = C_n R^n, \text{ where } C_n = \frac{\pi^{n/2}}{\Gamma\left(\frac{n}{2}+1\right)} \tag{4.13}$$

if *n* is even: $C_n = \frac{\pi^{n/2}}{\left(\frac{n}{2}\right)!}$ since $\Gamma\left(\frac{1}{2}\right) = \sqrt{\pi}$

if *n* is odd: $C_n = \frac{2^{\frac{n+1}{2}}\pi^{\frac{n-1}{2}}}{\text{n!!}}$

The "surface area", or, properly, the (*n*-1)-dimensional volume of the (*n*-1)-sphere at the boundary of the *n*-ball is:

$$S_{n-1} = \frac{dV_n}{dR} = \frac{nV_n}{R} = nC_n R^{n-1} \tag{4.14}$$

With the previous description of the concepts of *n*-dimensional "volumes" and "surface areas", the next step is to translate the formulations above into Euclidean space. An *n*-dimensional Euclidean space analogous to the *n*-dimensional spherical coordinate system consists of a radial coordinate, r, *n*-1 angular coordinates ranging from [0, 2π) radians, and one angular coordinate ranging from [0, π):

$$\begin{aligned} x_1 &= r\cos(\phi_1) \\ x_2 &= r\,\sin(\phi_1)\cos(\phi_2) \\ x_3 &= r\,\sin(\phi_1)\sin(\phi_2)\cos(\phi_3) \\ &\vdots \\ x_{n-1} &= r\,\sin(\phi_1)\cdots\sin(\phi_{n-2})\cos(\phi_{n-1}) \\ x_n &= r\,\sin(\phi_1)\cdots\sin(\phi_{n-2})\sin(\phi_{n-1}) \end{aligned} \tag{4.15}$$

The inverse transformations are unique, except for some special cases described below:

$$r = \sqrt{x_n^2 + x_{n-1}^2 + \cdots + x_2^2 + x_1^2} \tag{4.16}$$

$$\begin{aligned} \phi_1 &= arccot\left(\frac{x_1}{\sqrt{x_n^2 + x_{n-1}^2 + \cdots + x_2^2}}\right) \\ \phi_2 &= arccot\left(\frac{x_2}{\sqrt{x_n^2 + x_{n-1}^2 + \cdots + x_3^2}}\right) \\ &\vdots \\ \phi_{n-2} &= arccot\left(\frac{x_{n-2}}{\sqrt{x_n^2 + x_{n-1}^2}}\right) \end{aligned} \tag{4.17}$$

$$\phi_{n-1} = 2arccot\left(\frac{\sqrt{x_n^2 + x_{n-1}^2} + x_{n-1}}{x_n}\right)$$

If $x_k \neq 0$ for some k but all of $x_{k+1}, \ldots, x_n$ are zero, then $\phi_k = 0$ when $x_k > 0$, and $\phi_k = \pi$ when $x_k < 0$. Also, ϕ_k for any k will be ambiguous whenever all of x_n are zero; in this case ϕ_k may be chosen to be zero also.

A hyper-spherical volume element and its hyper-spherical volume integral are given as:

$$d_{\mathbb{R}^m}V = r^{m-1}\, sin^{m-2}(\phi_1)\, sin^{m-3}(\phi_2) \cdots sin(\phi_{m-2})\, dr\, d\phi_1\, d\phi_2 \cdots d\phi_{m-1} \tag{4.18}$$

$$V_m = \int_{r=0}^{R}\int_{\phi_1=0}^{\pi}\cdots\int_{\phi_{m-2}=0}^{\pi}\int_{\phi_{m-1}=0}^{2\pi} d_{\mathbb{R}^m}V \tag{4.19}$$

Recalling that $S_{n-1} = \frac{dV_n}{dR} = \frac{nV_n}{R}$, the hyper-spherical surface integral is give as:

$$S_{m-1} = \frac{m}{R}\int_{r=0}^{R}\int_{\phi_1=0}^{\pi}\cdots\int_{\phi_{m-2}=0}^{\pi}\int_{\phi_{m-1}=0}^{2\pi} d_{\mathbb{R}^m}V \tag{4.20}$$

For a 3-sphere (4D):

$$d_{\mathbb{R}^4}V = r^3\, sin^2(\phi_1)\ \sin(\phi_2)\ dr\, d\phi_1\, d\phi_2\, d\phi_3 \tag{4.21}$$

$$V_4 = \int_{r=0}^{R}\int_{\phi_1=0}^{\pi}\int_{\phi_2=0}^{\pi}\int_{\phi_3=0}^{2\pi} r^3 \sin^2(\phi_1)\sin(\phi_2)\, dr\, d\phi_1\, d\phi_2\, d\phi_3 \tag{4.22}$$

$$S_3 = 4\int_{r=0}^{R}\int_{\phi_1=0}^{\pi}\int_{\phi_2=0}^{\pi}\int_{\phi_3=0}^{2\pi} r^2 \sin^2(\phi_1)\sin(\phi_2)\, dr\, d\phi_1\, d\phi_2\, d\phi_3 \tag{4.23}$$

For a unit 3-sphere, R = 1 and ϕ_3 integrates out to 2π, such that:

$$V_4 = \frac{2\pi R^4}{4}\int_{\phi_1=0}^{\pi}\int_{\phi_2=0}^{\pi}\sin^2(\phi_1)\sin(\phi_2)\ d\phi_1\, d\phi_2 \tag{4.24}$$

$$V_4 = \frac{2\pi R^4}{4}\int_{\phi_2=0}^{\pi}\sin(\phi_2)\ d\phi_2\left[\frac{1}{2}\phi_1 - \frac{1}{4}\sin(2\phi_1)\right]_0^{\pi} \tag{4.25}$$

$$V_4 = \frac{\pi^2 R^4}{4}\int_{\phi_2=0}^{\pi}\sin(\phi_2)\ d\phi_2 \tag{4.26}$$

$$V_4 = \frac{\pi^2 R^4}{4}[-\cos(\phi_2)]_0^{\pi} = \frac{\pi^2 R^4}{2} \tag{4.27}$$

While arduous, the previous derivations provide the mathematical basis for determining the likelihood of two randomly assigned PDs should be aligned by an angle ϕ. Toward this goal, suppose that two random unit vectors within an *n*-sphere are chosen from a uniform distribution such that there is a uniform probability that they each may point to any location on the surface of the n-sphere. The goal is to determine the probability density function for the angle, ϕ, that is formed between the two unit vectors, which must lie within the bounds of [0 π].

First consider the case of a 2-sphere (normal sphere) since it is easiest to visualize. Once the first unit vector is chosen, imagine a circle on the surface of the sphere that is oriented normal to the first unit vector. Given an angle ϕ, this circle represents all points on the sphere's surface where a second unit vector may point, such that all angles formed between the two vectors must equal ϕ. As ϕ increases, so does the circumference of the circle, until $\phi = \frac{\pi}{2}$, at which point the circle begins to close again. In this way, the circumference of the circle represents the probability that the second randomly chosen vector will be an angle of ϕ from the first vector. It is important to note that the angle between the vectors can be described by a rotation through a single spherical dimension by orienting the axes appropriately. Therefore, to consider the probability of obtaining

an angle of ϕ across a single dimension between any two vectors, the relationship between ϕ and the *n*-sphere's surface measure must be defined.

The distribution over ϕ for a 2-sphere (normal sphere) is given by:

$$f(\phi) = \mathrm{C}\sin(\phi) \tag{4.28}$$

where C is a constant, since all other variables are integrated out. In order to be a proper distribution, the integral over ϕ $[0\ \pi)$ must be equal to 1:

$$f(\phi) = \mathrm{C}\sin(\phi) \tag{4.28}$$

$$f(\phi) = \int_{\phi=0}^{\pi} C\ sin(\phi)d\phi = C[-\cos(\phi)]_0^{\pi} = 2C = 1, \qquad \therefore C = {}^{1}/_{2} \tag{4.29}$$

$$f(\phi) = \frac{1}{2}\sin(\phi), \qquad \phi: [0\ \pi] \tag{4.30}$$

The distribution over ϕ for any *n*-sphere where *n* >1 will be the same as derived above since the surface integral will always depend upon $sin(\phi)$ and must always integrate to a value of 1 (so C=1/2). This also means that for a unit 0-sphere (a circle), the distribution over ϕ is uniform: $f(\phi) = \frac{1}{2\pi}$, which can be more easily rationalized.

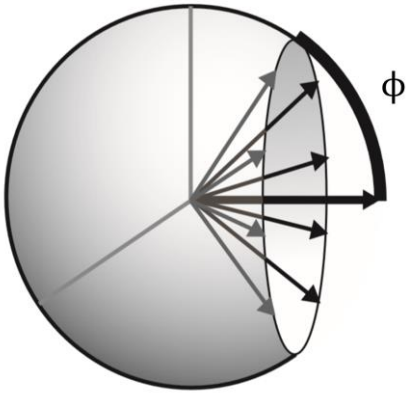

Figure 4.9: Distribution of PD Alignment Angles in 3D

Illustration of why the uniform probability density function for the alignment of two vectors in a 3D space is proportional to $\boldsymbol{sin(\phi)}$. As $\boldsymbol{\phi}$ increases, the circumscribed circle of all points that correspond to different vector possibilities grows with a radius equal to $\boldsymbol{sin(\phi)}$. The proof for equation 4.30 shows that the same distribution applies to all hyperdimensional spaces greater than 3D

To summarize, these derivations provide a mathematical proof for why it is expected that the distributions between PDs assigned by the OLE decoder should be described by equation 4.30, if they are assigned at random. The resulting distribution can also be conceptualized graphically by observing that the circumference of the circle (representing all points that could be formed on the surface of a normal sphere at a given angle ϕ) is dependent upon the inner radius formed by $\sin(\phi)$. This distribution is also applicable for control of higher dimensional control beyond 4DOF.

4.4 Results

4.4.1 4DOF Task Performance

Both monkeys became proficient at their respective tasks within about a month of daily training. Following a month, performance on the tasks was related more to motivation than to task difficulty. On a typical day, monkeys performed between 25-40 sets (consisting of 16 correct trials each). Movement to targets was smooth and minimum hold times on the target were increased to as much as 5 seconds, to demonstrate the ability to both move and stop. Typical movement times to targets were about 5 seconds, and both monkeys were able to skillfully moved in each dimension simultaneously, resulting in the most efficient paths to the targets. Representative averaged movement paths for the Reach and Rotate task are shown in Figure 4.10.

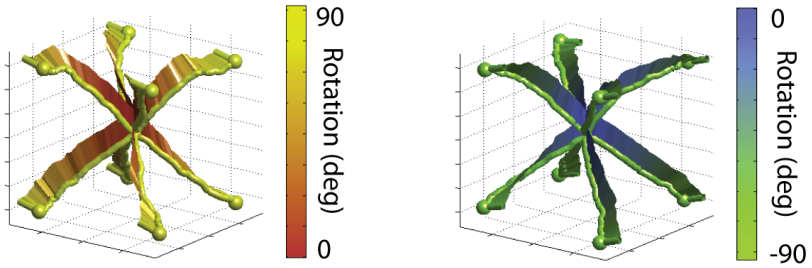

Figure 4.10: Average Reach and Rotate 4D Trajectories

Average movement paths for the Reach and Rotate task showing smooth and continuous movements in all dimensions from the center to targets located at the corners of the cube

4.4.2 Uniqueness of Frequency Bands for Control

The description of coefficients as weighted PDs by Equation 4.11 means that PDs can be compared between frequency bands on a given electrode to examine how similar their contributions are to control. Equation 4.30 shows that if PDs are randomly and uniformly assigned

to features on an electrode, then the expected distribution of angles between PDs should follow a (half-)sinusoid distribution.

For a given electrode and raw decoder update (the regression coefficients prior to smoothing by the co-adaptive filter), angles were measured between each frequency band's assigned PD. These measured angles were then grouped into pair-wise bins, corresponding to all possible combinations of frequency bands: alpha vs alpha, alpha vs beta, … beta vs beta, beta vs low-gamma, … low-gamma vs low-gamma, low-gamma vs mid-gamma, … etc. This was repeated for each electrode and raw decoder update (pre-smoothing). Bins were then combined across all electrodes and decoder updates, and the resulting distributions of PD-angles appearing within each bin were compared against the distribution from Equation 4.30. As shown in Figure 4.11, the mid- and high-gamma

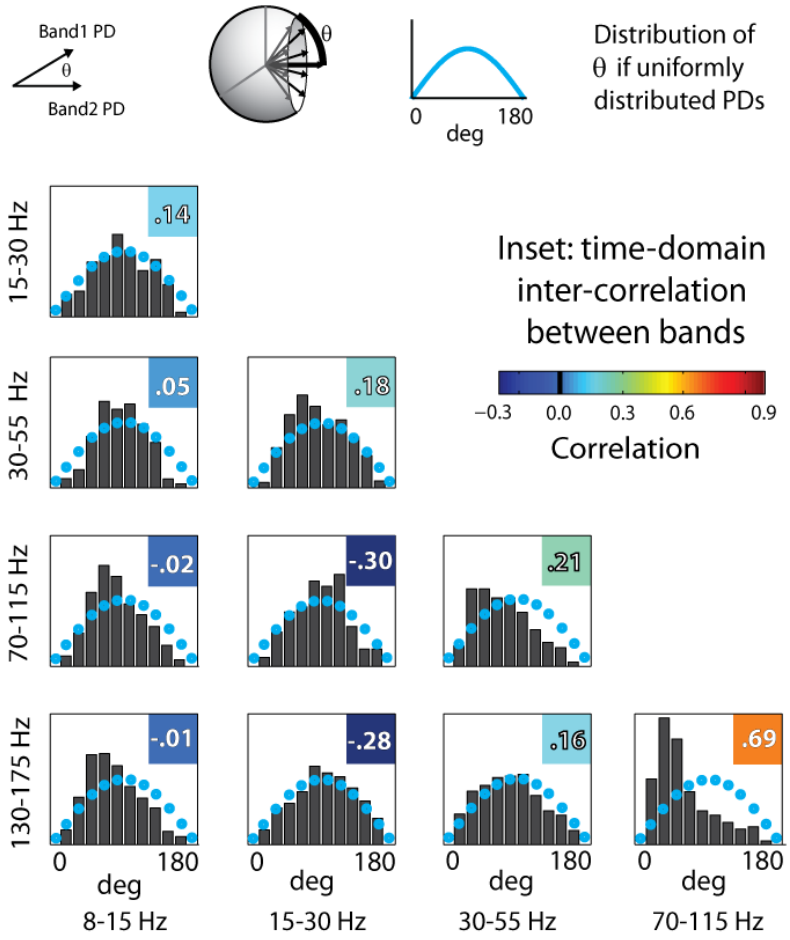

Figure 4.11: Alignment of PDs Assigned to Frequency Bands

Distributions of PDs between frequency bands. The distribution for mid- and high-gamma shows a significant deviation from what would be expected if the PDs had been assigned randomly. The mean correlation between each frequency band's signals is also shown for each pair-wise combination. The correlation between mid- and high-gamma and assignment of closely aligned PDs indicates that these two bands were carrying similar information and contributing to control in a similar way.

had the highest alignment of assigned PDs, as indicated by the peak in the distribution that is shifted toward 0 degrees.

Following a similar approach as was taken with the PDs, correlations between feature time series that were used to train the decoder were also calculated and compared across each bin. The mean correlations between features was highest between mid- and high-gamma (r=0.69) and lowest between beta and mid-gamma (r=-0.30) and beta and high-gamma (r=-.28).

4.4.3 Optimal Frequency Bands for Control

As described by Equation 4.11, the coefficients assigned by the OLE decoder can be interpreted as a weighted PD. In order to examine the relative contributions of each frequency band to control, weights from each training set (16 successful trials to each target) were grouped by frequency band and normalized by the total sum of all weights in order to calculate a distribution. Figure 4.12 shows that the resulting distribution of weights across bands on representative days for both monkeys. Lines and error bars represent the mean and standard error of the mean as calculated across the full number of training sets. Results show that beta (15-30

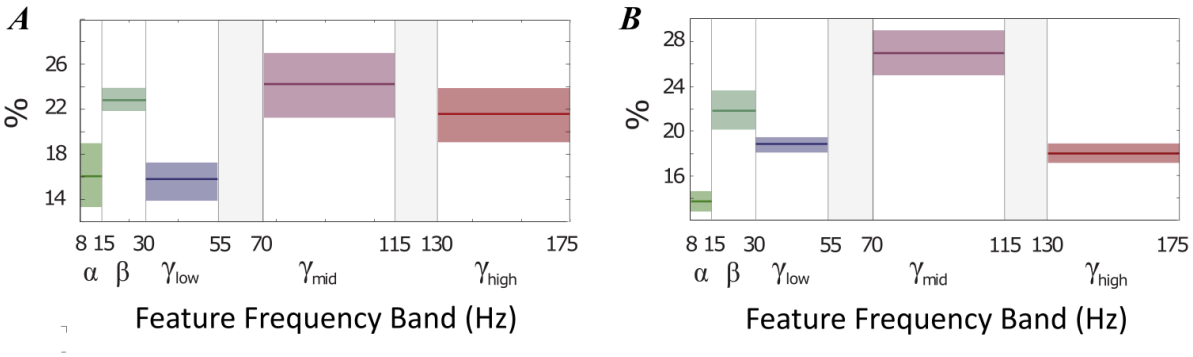

Figure 4.12: Optimal Frequency Bands for BCI Control

Distribution of weights are shown by band for Monkey I, who performed the Reach and Rotate task **(A)** and for Monkey K, who performed the Multi-object Out-to-Center task **(B)**. Both beta and mid-gamma received the greatest amount of weights.

Hz) and mid-gamma (70-115 Hz) received the greatest amount of weights. This result is consistent with the observation from Chapter 3 (Figure 4.13), that distributions of power in these bands are more skewed, which further suggests that skewness is a measure of the ability to actively modulate signal power. Interestingly, high-gamma (130-175 Hz) was also assigned a large percentage of weights for Monkey I, but not Monkey K. Again, referring to results from Chapter 3, this may be explained by poorer SNR from Monkey K's smaller-diameter electrodes.

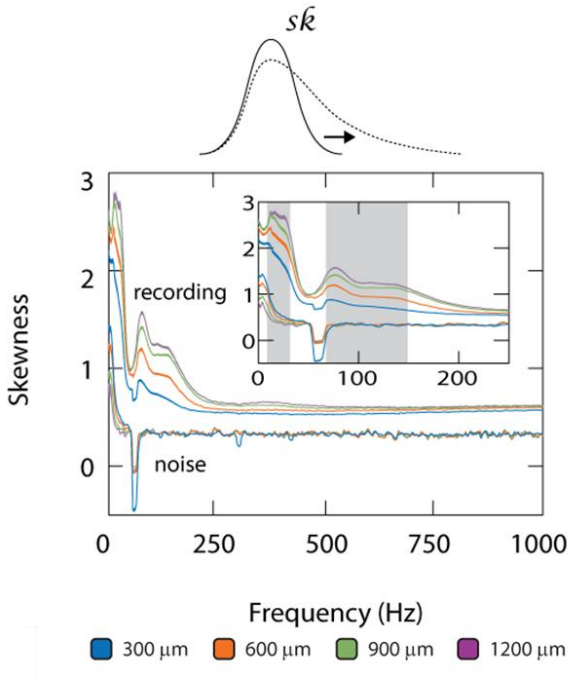

Figure 4.13: Skewness Related to Active Modulation

An analysis of signal statistics from Chapter 3 shows an increase in skewness in the same bands that were most heavily weighted by the OLE decoder. Smaller diameter electrodes were associated with less skewness and were shown to have lower SNR.

4.4.4 Depth of Modulation

Features were further examined by considering how well their activity was described by a traditional cosine-tuning model. Time series data for each feature during successful movement periods were fit to cosine tuning functions and the fit was quantified by an R^2-measure. As may be expected, a cosine tuning model best described features in bands that were assigned the highest weights by the decoder. An example is shown in Figure 4.14 for Monkey I, with mean R^2 values of about 0.6 and 0.7 for mid- and high-gamma, respectively. Beta was not as well-described by cosine tuning, with a mean R^2 value of 0.45.

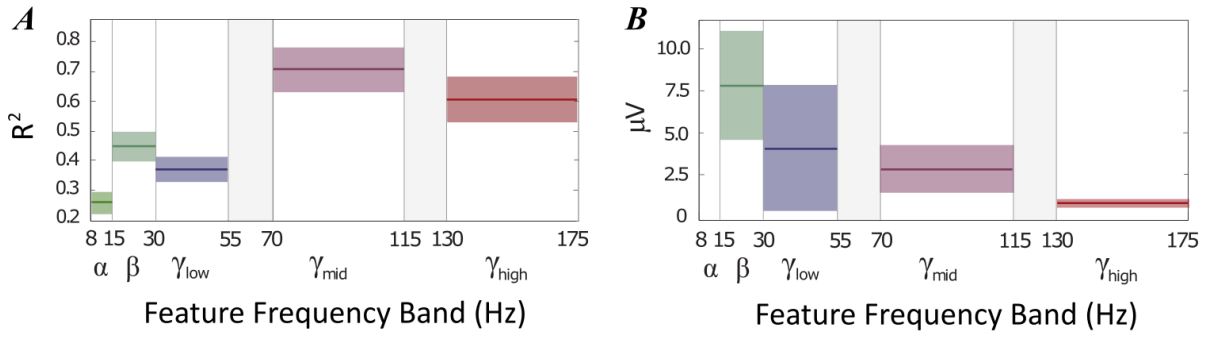

Figure 4.14: Depth of Modulation Versus Frequency Band During BCI Control

A) The fit of cosine tuning function to features and the corresponding goodness-of-fit for each frequency band. **B)** The depth of modulation of fitted cosine tuning functions, where only functions with a fit better than $R^2 > 0.4$ were included. The depths of modulation here correspond well to estimates from Chapter 3.

The depth of modulation of fitted cosine-tuning functions was also examined for well-fitted features determined by $R^2 = 0.4$ or higher. Again, using the same dataset from Monkey I, depths of modulation were 7.8 μV for beta, 4.1 μV for low-gamma, 2.8 μV for mid-gamma, and 1 μV for high-gamma. Analyses from Chapter 3 estimated modulation for 1.2 mm diameter electrodes to be 5.7 μV for beta, 2.1 μV for low-gamma, 1.1 μV for mid-gamma, and 525 nV for high-gamma. The increase in modulation calculated in this current analysis, may be due to: 1) here signals were combined from 1 mm and 2 mm electrodes here versus 1.2 mm electrodes in Chapter 3, and 2) here signals were recorded during an active task versus signals recorded while monkeys sat calmly in Chapter 3.

4.4.5 Preferred Cortical Regions for Control

Preferential electrodes and cortical regions that were used for control were also analyzed by summing the decoder weights across all frequency bands for each electrode, normalizing its total weight by summation of all electrode weights, and mapping the electrode to the estimated region of cortex over which it was implanted. Monkey I did not show any preferential assignment

of weights to electrodes within any given region of the electrode array or cortex. However, a unique distribution was observed with Monkey K. Figure 4.15 shows the distribution of normalized electrode weights specific to each controlled DOF (the number indicates the object and letter indicates the X-Y dimension). It is possible to see that there is a preferential weighting of electrodes located on the leftmost (frontal) region of the left-hemisphere array. The weighting appears to be more spread out on the right-hemisphere array. When the total summed weights of all electrodes on the left hemisphere are compared against the total summed weights of all electrodes on the right hemisphere, a pattern emerges. As shown in Figure 4.15, the left hemisphere accounted for approximately 1/3 of the total weights, and the right hemisphere accounted for approximately 2/3 of the total weights. This was consistent across all controlled DOF.

Considering the regions over which the electrode arrays were implanted, roughly ½ of the left hemisphere array covered M1, whereas all of the right hemisphere array covered M1. The result suggests that the majority of control came from M1, not S1. As such, 1/3 of the total amount of M1 cortex (combined across hemispheres) was aligned under the left hemisphere array, and 2/3 of the total amount of M1 cortex was aligned under the right hemisphere array. This indicates that while S1 can be used to contribute to control, M1 is preferred.

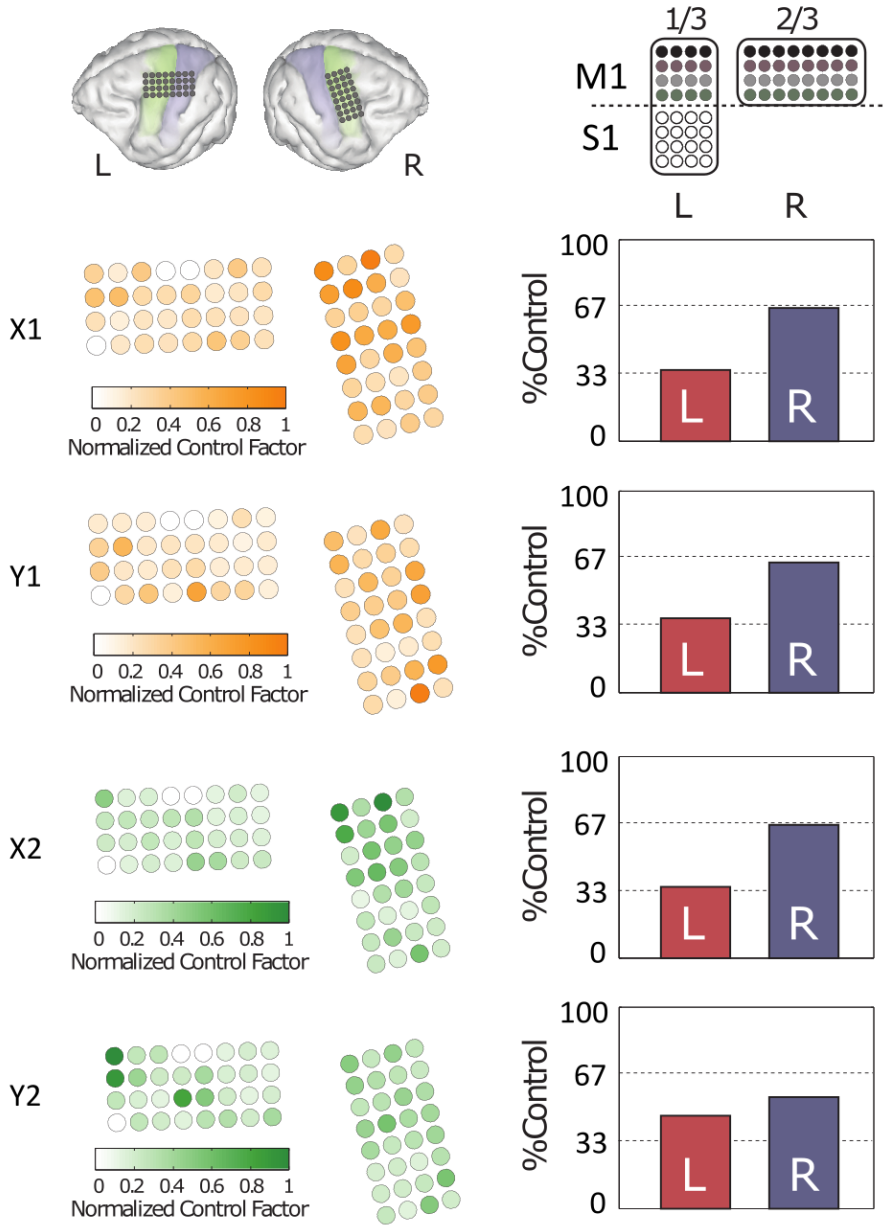

Figure 4.15: Preferred Cortical Regions for BCI Control

Normalized weights for each dimension of control are shown superimposed on each electrode. The relative total amount of weights on the left versus the right electrodes is approximately 1

4.4.6 Learning Rate for Co-Adaptive Training

The co-adaptive learning rate, α, sets the speed at which decoder coefficients change with each update. It also controls the amount of memory in the system by adjusting the relative contributions of newly calculated coefficients versus coefficients that were used in the past. Setting α=1 means that there is no memory in the system and each update to the decoder will equal the raw regression coefficients from the OLE decoder. Alternatively, setting α=0 means that there is no learning of new information and each update to the decoder will be equal to the previous coefficients. The goal is to adjust the learning rate such that the decoder can balance rapid learning with consistent de-noised weights from the past.

As shown in Figure 4.16A, the raw regression coefficients from the OLE decoder were noisy from update to update, but general trends in the weights can be seen. Figure 4.16B shows the smoothed weights from the co-adaptive filter corresponding to a single degree of freedom controlled during the 4DOF BCI task. In the dataset shown, the learning rate was chosen based upon previous experience (α=0.25). The decoder began without any prior knowledge of weights to use, which can be seen by the top row of white (zeros across all features). Over time, the consistent weights were emphasized while spurious noisy weights were zeroed. Additionally, some features

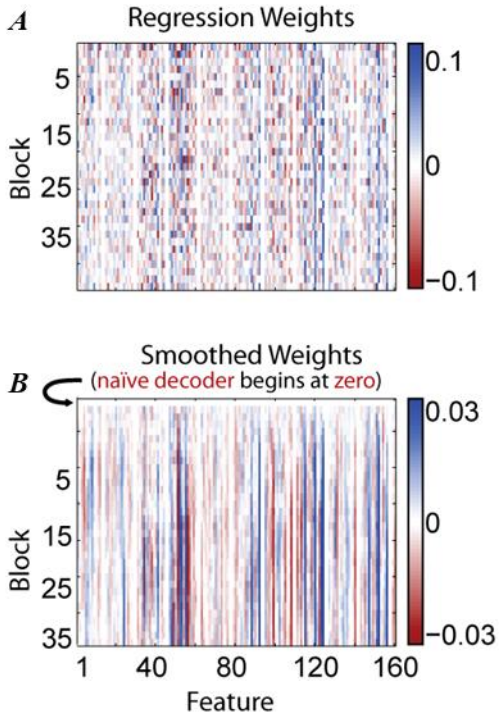

Figure 4.16: Effects of the Co-adaptive Learning Algorithm on Decode Weights Over Time

Raw regression weights **(A)** and smoothed decoder weights **(B)**

were emphasized temporarily but went away (e.g., features 1-10 between blocks 10 and 20). This may indicate a change in the control strategy being used by the monkey. It is difficult to predict how performance may have been changed due to variations in the learning rate parameter. Optimization of the learning rate, which could be variable over time, remains an interesting topic for future work.

4.5 Discussion

4.5.1 Optimal Features for Decode

Beta, mid-gamma, and high-gamma bands were most heavily weighted by the naïve decoder for control. However, mid- and high-gamma were not observed to be distinct in the information they carried. The similarity in information was shown both by their correlation and their assigned PDs for control, which were highly aligned. This suggests that the two bands could be combined into one single band, or that high-gamma could be excluded from the BCI, such that control would be derived from signals less than 115 Hz. Reducing the bandwidth required for control could be advantageous for a bi-directional BCI with low-frequency bands for control and high-frequency bands for stimulation. While this result is specific to recordings over sensorimotor cortex used for neuroprosthetic control, it would be interesting to investigate if the result holds for other cortical areas, including deep-brain local field potentials (LFP), which may be more relevant to other closed-loop therapies.

Greater use of beta, mid-gamma, and high-gamma for control also aligns with predictions from Chapter 3. In Chapter 3, these bands showed the greatest amount of skewness and kurtosis, which were interpreted as active modulation. The skewness and kurtosis analyses also showed

little modulation of low-gamma (30-55 Hz) which did not contribute to control in the motor BCI tasks here. Mid-gamma (70-115 Hz) contributed the most to control in both monkeys, but high-gamma (130-175 Hz) contributed less in Monkey K. This result is consistent with the reduced SNR that was observed in Chapter 3, due to the smaller electrode size. As shown in Figure 3.10, the SNR dropped to 3 dB at approximately 150 Hz for 300 μm diameter electrodes, and at approximately 185 Hz for 1200 μm diameter electrodes. This suggests that for real-time BCI applications, where signal averaging isn't an option to lower noise, larger electrodes (with lower impedance and higher SNR) may be ideal. For applications in which multiple measures can be made and averaged, which reduces noise by a factor of $1/\sqrt{n}$ (where n is the number of measurements), electrodes with diameters less than 600 μm may work well. However, for real-time applications where averaging is not possible, electrodes greater than 600 μm appear to be best.

4.5.2 Challenges with Multi-Dimensional Control

More than one strategy could be employed to teach a user multi-dimensional control with a BCI. One strategy could be to teach them one DOF first, then two, and three… and so on. Another strategy could be to teach them to control every DOF at the same time, but with assistance that is gradually reduced. While the results from this study cannot suggest which of the approaches is optimal, it does highlight several challenges in learning control. For example, using the analogy of local minima from optimization problems, teaching one DOF at a time could lead to biases that are difficult to overcome as more dimensions are added – resulting in sub-optimal performance around a local minimum. Alternatively, training on all dimensions at the same time, might allow the user to overcome biases with prior learning, but could also be more challenging.

Feedback was observed to be of critical importance in early learning. In this task, monkeys relied upon visual feedback in order to make movement corrections. In the Reach and Rotate task, feedback was less clear for movement in depth (into the screen) than left-right, up-down and rotational movement. This was the reason for adding additional depth cues like the jointed arms and semi-transparent cube sidewalls. Upon early learning, the monkey adopted a strategy of moving quickly first in the dimensions with greatest feedback and then slowly pushed the cursor forward or backward until the target was hit, such that more time was spent moving in depth than the other dimensions. The result was that when this training data was used in the next decoder update, regression weights became preferentially larger for the depth dimension. This effect makes sense because the depth component of the pseudo-velocity signal remained closer to ±1 for a longer duration, resulting in a larger rms signal to be fit by the decoder. With practice, this bias was reduced and decoder weights became normalized. How feedback and biased training affects learning rate and performance over time remains an interesting topic for future study. For example, it would be interesting to study how augmented feedback may improve learning and performance. Additionally, these issues emphasize the importance of co-designing both the controller and system to be controlled, with special attention to control bandwidth and subject feedback.

Other challenges with multi-dimensional control are the size of training sets required to fully sample the space for decoder development and the size of verification movements required to demonstrate independent control of each DOF. For a 2 DOF task, there are 4 permutations on movement; for a 3 DOF task, there are 6 (though in this study, using the corner of the cube created 8), and for a 4 DOF task, there are 8 (though in this study, using the cube and rotation created 16); and so on. Ideally, these movements should be relatively straight and equal in time in order to avoid training data set biases previously discussed. As the dimensionality grows, so too does the

time required to train. Additionally, demonstrating independent control of all dimensions requires a similarly growing set of trials. For small dimensional control, this may not be an issue, but for much larger dimensionality, this brute-force method may prove to become more challenging. An area of future study could be to reduce the size of these sets through approximations of a fully-sampled space, or by rotating through sub-sets of the space for each decoder update and adjusting the memory of a co-adaptive decoder to include previous training.

4.5.3 Co-adaptive Algorithms

The use of co-adaptive training was observed to accelerate learning and performance with the BCI, which enabled an increase in the number of dimensions that could be controlled. Anectodelly, past methods that updated decoders once a day based upon a previous day's data would require roughly a month to train a monkey to achieve proficient control of 2 DOF. The first time that the co-adaptive decoder was used was with an untrained monkey who had never performed a BCI task. The time it took to achieve equivalent performance was less than an hour. The effect of the co-adaptive decoder had on performance was clear, but how exactly it improved learning and performance was not as well-studied and remains an interesting topic for future work.

The fundamental idea behind the co-adaptive algorithm is to provide approximate real-time error-correction to the decoder, similar to the way feedback in a control system corrects for output errors. In order to provide a measure of the error, an estimate of the desired output must be determined. For the tasks described here, the desired output was known because the monkeys were trained to move the cursor to the target for a liquid reward. Within a controlled-environment this works well, and error-correction can be provided to the decoder. However, if a subject were to be allowed to use the BCI unsupervised in a free-play mode, then it would be difficult to know

what their intent is and error-correction would no longer be possible. Therefore, the key to co-adaptation is to accurately estimate subject intent and provide error-correction as quickly as possible.

Estimating user intent is an exciting area of study with broad applicability in human-machine interfaces. In fact, neural signals used for control should also be considered to be estimates of user intent. Future work may seek to combine multiple methods of estimating user intent with BCIs in order to provide enhanced cooperative control. For example, estimates of user intent could be derived from eye-tracking: if a subject is fixated on objects in their environment, they are likely intending to interact with them. Cognitive load and attentional signals could also be used to inform a cooperative BCI: perhaps providing an indication of subject interest in objects in the environement or signaling a need to shift relative contributions over control to other signals when the users attention is challenged. Additionally, context-dependent behavioral models could also provide predictions of the user's intent based upon previous experiences. By combining multiple estimates of user intent, a more accurate prediction of intent might be possible that could enable error-correction of the decoder outside of constrained tasks and in real-world use.

Like feedback in a control system, the gain on error-correction must also be carefully adjusted such that the subject and decoder do not become unstable. For the co-adaptive algorithm described in this work, decoder updates were provided after the completion of an entire training set, but updates could have been provided more often. One of the benefits of the OLE decoder is that coefficients can be quickly calculated. Recent interest in deep learning has shown promising results for neural decoders, but training large multi-layer networks can be time-consuming. Future work might explore how these advanced decoding techniques might be accelerated such that they could be included in a co-adaptive feedback loop. In this study, the parameter α controlled the

learning rate (or amount of memory) of the decoder. Future work might investigate optimal learning rates, or even adaptive learning rates, to enhance performance in the context of BCIs, but also in broader applications involving human-machine interactions.

Chapter 5

A Bi-directional BCI:
Control with Sensory Feedback

5.1 Introduction

5.1.1 An Overview of Bi-directional BCIs

A bi-directional BCI combines the ability to both record and stimulate neural tissue, which enables advanced closed-loop functionality beyond what can be achieved with record-only or stimulate-only technologies. Examples of potential closed-loop applications include: 1) providing more effective therapies for disease and disorders through responsive stimulation, 2) repairing or re-organizing neural connectivity through induced neuroplasticity, 3) improving learning, memory, and sleep through event-triggered stimulation, and 4) restoring or augmenting sensorimotor functionality through motor control and sensory feedback. In the past, open-loop stimulation therapies, like deep brain stimulation (DBS) have required manual titration and fine-tuning through multiple visits to clinicians, likely resulting in sub-optimal effects. Open-loop motor prosthetics have relied upon visual feedback and suffered from lack of refined gripping force and of loss of control when subjects aren't visually attending to the prosthetic. Despite the need for closed-loop BCIs, work in this area has only recently emerged and has been limited.

Work on micro-electrode motor BCIs has recently been extended to include microstimulation for sensory feedback by interleaving recording and stimulation (O'Doherty, 2011). In order to reduce the latency of recording post-stimulation, advances in amplifier design have included "fast-settle" functionality that effectively zeroes the output of the amplifier to quickly recover from ringing caused by stimulation artifacts exceeding the input dynamic range. (Harrison, 2003). Using communications nomenclature, this approach uses time-division multiplexing, which requires separate non-overlapping time slots for recording and stimulation. This approach has been used to demonstrate a closed-loop sensorimotor BCI, but suffers from lost control information while stimulating. For chronic applications, loss of motor control signals is exacerbated by immunoreactive responses and signal degradation common with all micro-electrode systems.

Other work has focused on recording low-frequency local field potentials (2-40 Hz) during DBS by filtering out stimulation artifact with a high-order low-pass filter (Rossi, 2007). Using communications nomenclature, this approach uses frequency-division multiplexing, where recording and stimulation are allocated non-interfering frequency bands. Use of separable bands has the advantage that recording and stimulation can occur simultaneously, which could improve BCI performance and reduced closed-loop response time. While promising, real-time closed-loop control has yet to be demonstrated using this approach. Additionally, it remains unknown whether or not high-frequency stimulation can provide perceivable sensory feedback without interfering with recordings of mid-gamma (70-115 Hz) which was previously shown to be important for control.

5.1.2 Separable Bandwidths for Recording and Stimulation

The strategy employed here for a bi-directional BCI with cortical surface electrodes is to use frequency-division multiplexing with frequency bands assigned to recording and stimulation. This approach is similar to spectrum allocation by the FCC to limit interference between different radio communication technologies.

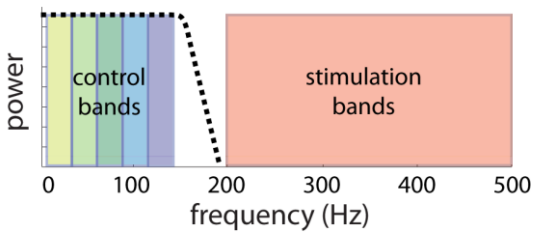

Figure 5.1: Separable Bands for a Bi-directional BCI

The dotted line represents a low-pass filter to remove stimulation artifacts from recordings.

Results from previously described studies showed that beta (15-30 Hz) and gamma (75-115 Hz) are ideal for BCI motor control. These bands showed the greatest apparent active modulation of power, as measured by skewness and kurtosis, and received the greatest influence over multi-dimensional control from a naïve decoder, as measured by assigned regression weights. Therefore, a reasonable spectrum allocation for a bi-directional BCI is to assign frequency bands below 120 Hz for control and frequency bands above 120 Hz for stimulation. Unlike time-division multiplexing of data, in which recording and stimulation periods must be interleaved in time, this frequency-division multiplexing approach allows for simultaneous recording and stimulation without interference.

5.1.3 Stimulus Waveforms

Considerations for stimulus waveforms include: 1) safety, 2) threshold current levels, and 3) spectral overlap with frequency bands used for control. Pulse trains are the most common waveforms used for neural stimulation, although sinusoids, Gaussians, and other types of

waveforms have also been explored. (Reilly, 1998). Non-pulsatile waveforms have been shown to provide desirable low-energy characteristics that are less damaging to electrodes and can potentially extend the battery lifetime of implantable neuromodulation systems (Wongsarnpigoon, 2009). Sinusoids are attractive at first glance for limiting spectral overlap with recording bandwidths due to their narrow spectral bandwidth compared to pulses (this is discussed more later). In all cases, the waveforms are typically biphasic, with equal charge in both the anodic and cathodic phases. Charge-balanced waveforms help to mitigate the accumulation of electrochemical products that mediate charge transfer across the electrode-tissue interface (which are discussed in Chapter 2). Unbalanced waveforms can lead to degradation of both the electrode and surrounding tissue over time.

In addition to balanced charge, both the total amount of charge per phase and charge per electrode area should be limited to avoid tissue damage. An empirical formula for determining safe levels of stimulation was provided by Shannon (1992) and is often referred to as the "Shannon Criteria". Shannon developed a model for describing thresholds for unsafe stimulation based upon stimulation parameters and histology collated from a large body of experimental reports. This model is dependent upon both the total injected charge within a phase, Q, the area of the electrode, A, and the normalized charge per area, D. The parameter k represents a threshold for tissue damage. Stimulation parameters near k=2 resulted in tissue damage, whereas parameters near k=1, did not. Therefore, a value of k=1.5 is the generally accepted threshold over which stimulation parameters are considered unsafe. Shannon's Criteria relates these parameters as follows:

$$\log(D) = k - \log(Q) \tag{5.1}$$

For pulses with a phase duration T and peak current I the integrated charge per phase is:

$$Q = IT \qquad \text{(pulse)} \tag{5.2}$$

For sinusoids, the corresponding phase duration, T, can be related to frequency, f, by $T = 1/(2f)$. Again, with peak current I, the integrated charge per phase is:

$$Q = \frac{I}{2f} \qquad \text{(sine)} \tag{5.3}$$

Assuming the electrode is a disk with diameter, d, and area, $A = \pi d^2/4$:

$$D = \frac{Q}{A} = \frac{4IT}{\pi d^2} \qquad \text{(pulse)} \tag{5.4}$$

$$D = \frac{Q}{A} = \frac{2I}{\pi f d^2} \qquad \text{(sine)} \tag{5.5}$$

For a given electrode diameter and pulse width (or frequency for sinusoids), the maximum safe current can be calculated by:

$$I_{max} = \frac{d}{2T}\sqrt{\pi k} \qquad \text{(pulse)} \tag{5.6}$$

$$I_{max} = \frac{\pi f d}{2}\sqrt{\pi k} \qquad \text{(sine)} \tag{5.7}$$

Figure 5.2 shows corresponding maximum safe currents for a range of pulse widths and frequencies of interest for the implementation of the bi-directional BCI under consideration. For

a 2 mm diameter electrode driven by sinusoids in the frequency range of 200-500 Hz, safe current amplitudes are about 1-1.5 mA. Pulse stimuli can be driven at the same frequencies, but with shorter phase durations, typically in the range of 200 µs -1,000 µs. Within this pulse width range, safe current amplitudes increase to a range of 1-5 mA.

Both simulations and behavioral experiments have been used to study the differences between waveforms to elicit responses. For example, Reilly used a computational model of an electrode and axon to investigate differences between monophasic pulses, biphasic pulses, and biphasic sinusoids. Results are reconstructed in Figure 5.3, which shows both the threshold current

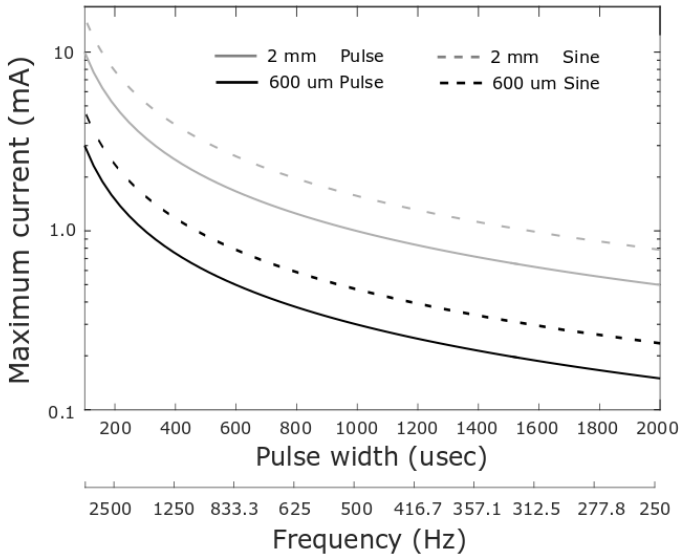

Figure 5.2: Maximum Safe Currents Based Upon Shannon's Criteria

Maximum currents are plotted based upon Shannon's Criteria (k=1.5) for pulses and sinusoids through electrodes of either 600 µm or 2 mm diameter. The phase duration and frequency of pulse waveforms are not linked the way that they are for sinusoids, allowing for narrow pulse widths and larger currents for a given frequency. The lower frequency axis maps the frequency of stimulation onto the corresponding pulse width for comparison between pulse and sinusoidal waveforms.

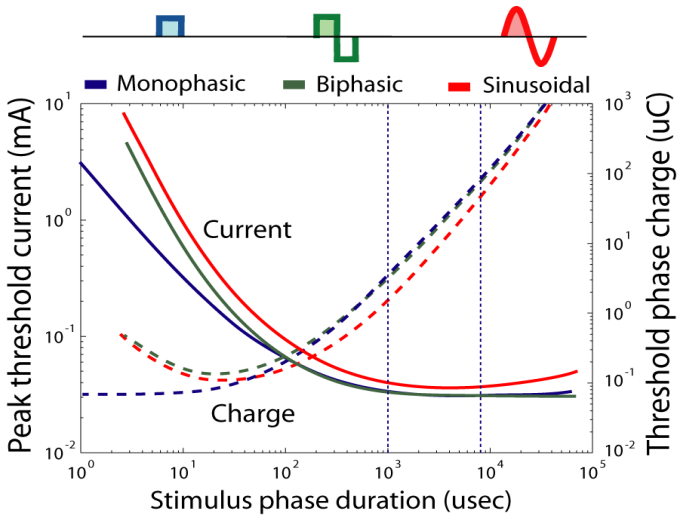

Figure 5.3: Threshold Currents for Pulses and Sinusoids

Adapted from Reilly (1998). Threshold activation current levels for monophasic, biphasic, and sinusoidal waveforms are plotted against stimulus phase duration for a simulated point electrode and axon model.

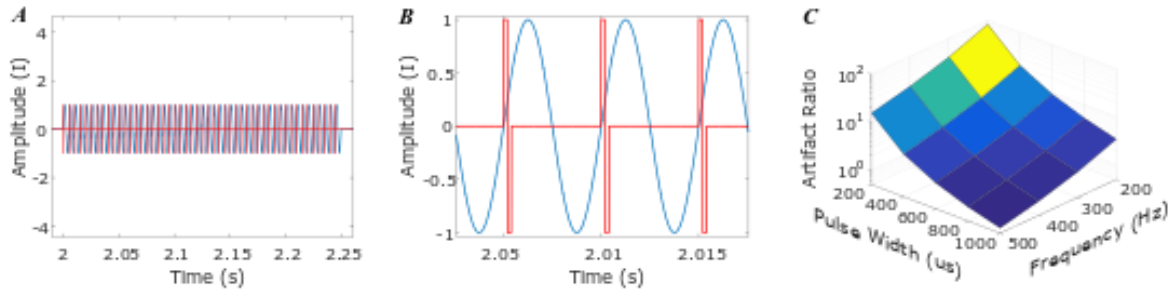

Figure 5.4: Comparison of Spectral Power from Pulse and Sinusoid Waveforms

A) Simulations of pulse trains and sinusoids were conducted to explore the spectral overlap with recording bands (less than 115 Hz). **B)** Closer view of pulses and sinusoids that emphasizes the dependence of phase duration and frequency for sinusoids. Pulse trains of the same frequency can have shorter phase durations that result in reduced injected charge per phase. **C)** The stimulation waveforms were LP filtered at 115 Hz, and bandpass filtered into 5 bands of interest for recording: 8-15 Hz, 15-30 Hz, 30-55 Hz, 70-90 Hz, and 90-115 Hz. The maximum peak-to-peak amplitudes within each band were calculated for a range of pulse widths and stimulation train frequencies. Results were similar across all bands. The relative increases in artifacts resulting from sinusoids ($sine_{p\text{-}p} - pulse_{p\text{-}p}$)/$pulse_{p\text{-}p}$ for various pulse widths and frequencies is shown for the 70-90Hz range. The relative size of artifacts was best for pulse trains with small pulse widths and low frequencies. For large pulse widths and high frequencies, pulses and sinusoids became more similar.

and corresponding charge of multiple waveforms plotted against their phase duration. Threshold currents for biphasic waveforms are greater than for monophasic waveforms, though they converged to the same level for pulse durations exceeding several hundred microseconds. Though it is difficult to translate the threshold stimulation values from Reilly's simulation results for micro-stimulation to cortical surface macro-stimulation, it is informative to note the general trend that thresholds for sinusoids are greater than both monophasic and biphasic waveforms.

Stimulation artifact in recording bands must also be minimized to ensure high-fidelity and uninterrupted control from the BCI. Stimulation artifact can result from two dominant sources: 1) saturation of the recording amplifier due to the large dynamic range of stimulation signals relative to neural signals of interest, and 2) spectral power overlap from stimulus waveforms into the recording frequency bands used for control. Regarding the first source of artifact, just as neural recordings can be described by electrical potentials arising from current sources within the volume-

conducting body (as described in Chapter 3), artifacts in recordings caused by stimulation are proportional to the stimulation current. Therefore, currents should be kept to a minimum possible level, and the amplifier should be designed to not saturate at the resulting voltage levels. Regarding the second source of artifact, waveforms should have minimal spectral overlap with the recording bands.

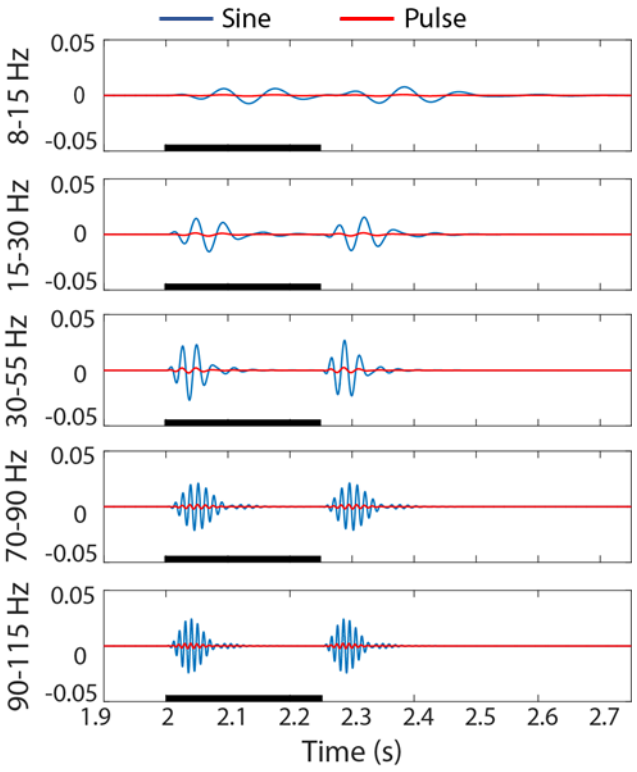

Figure 5.5: Simulated Artifacts from Pulses and Sinusoids in Control Bands

Time-domain stimulation artifacts are shown in each recording band caused by sinusoidal and pulse waveforms of equal amplitude (frequency = 200 Hz, pulse width = 300 µs). Stimulation is marked by the black bar. The dominant artifact occurs at the onset and offset of stimulation. This effect is due to spectral spreading caused by the time-domain multiplication of each stimulus waveform by a pulse (with duration equal to the length of the stimulation train), which is equivalent to convolution of a wide-spectrum sync function with the stimulus waveform's spectral power distribution in the frequency domain. Onset/offset artifact can be reduced by smoothly transitioning into and out of the onset and offset (e.g., using a ramp, Gaussian, or sinusoid).

While sinusoids may appear to be desirable due to their very narrow bandwidth (a single frequency), the onset and offset of the stimulus (which is a pulse function) also has an associated bandwidth that is convolved with the stimulus waveform in the frequency domain. The frequency response of a pulse is described by a sync function that spreads spectral power over a wide range. Compared to short repetitive biphasic pulses, sinusoids have more power located at the stimulation frequency. When that concentrated power is convolved with the onset/offset pulse function, much of it is shifted into the nearby recording frequency bands. On the other hand, biphasic pulse trains also have peak power at the given stimulation frequency, but the overall power is much lower (due to the smaller pulse

width) and spread out over much higher frequencies. When spectral power of the pulse train is convolved with the onset/offset pulse function, much less power ends up in the recording bands. This explains the larger peak-to-peak artifact summarized in Figure 5.4A, which is further detailed in Figure 5.5. Here, you can see that the largest artifacts from stimulation do not occur during the stimulation train, but, instead, at the onset and offset of stimulation. This effect is analogous to windowing in spectral power estimation (e.g., Hamming, Hann, and multi-taper).

To summarize, sinusoids are associated with reduced maximum safe currents, potentially higher thresholds for eliciting responses, and have greater artifact than bi-phasic pulses. Therefore, this study restricted stimulation to the use of biphasic pulses. The design of optimal waveforms remains a topic beyond the scope of this work.

5.2 Purpose of the Study

Implementation of a bi-directional BCI using separable control and stimulation bandwidths requires the design of a low-frequency artifact-suppressing amplifier for control and the design of stimulus waveforms to limit spectral interference in low frequencies. Again, using the analogy of radio communications, a spectral mask (or channel mask) defines limits on power in adjacent bands in order to limit adjacent-channel interference. Likewise, the aim here is to create a spectral mask by implementing a sharp low-pass filter in the artifact suppressing amplifier to limit the unwanted stimulation power modulation in the control bands. Similarly, low-frequency components of stimulation spectral power can be limited by designing high-frequency pulse trains with smoothed onset and offset ramping functions. This study combines signal processing theory, analog electronics design, and a psychometric task to demonstrate the feasibility of a bi-directional BCI that combines ECoG control with electrocortical stimulation feedback.

5.3 Methods

5.3.1 Electrode Array Designs and Implantation

A 32-channel epidural ECoG array was fabricated from an array of 600 µm Pt/Ir micro-wires embedded in an insulative acrylic mold formed from poly(methyl methacrylate). Micro-wires were arranged in a hexagonal pattern with 3 mm inter-electrode pitch at the lower surface of the array where contact was made with the epidural surface of the brain. Microwires were soldered to a PCB that provided a breakout to two Omnetics connectors (18 Position Nano-Miniature Connector, Omnetics Connector Corp) for ease of connection to the amplifier via a connector

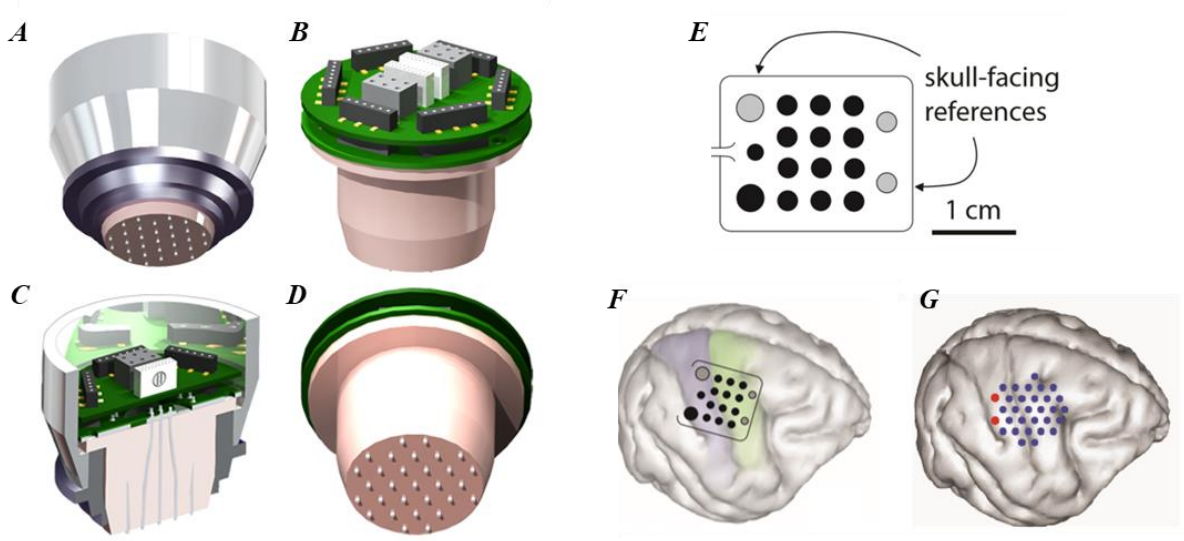

Figure 5.6: Electrode Array Designs Used In Stimulation Studies

A-D) An array of 600 µm diameter Pt/Ir electrodes with 3 mm hexagonal spacing fabricated from micro-wire embedded in an acrylic substrate. Attached PCBs provided a re-distribution layer to break out electrodes to jumpers for selecting references and miniature Omnetics connectors. The acrylic sub-assembly was sealed within a titanium chamber with a stainless steel lower ring that aligned to a standard craniectomy. The electrodes protruded slightly to make contact with the dura through the craniectomy. **E)** A PMT electrode array with 1 mm diameter contacts (similar to the arrays described in Chapter 4). Monkey G was implanted unilaterally with the 1 mm electrode array placed subdurally above S1 and M1 **(F)** and Monkey L was implanted unilaterally with the 600 µm electrode array placed epidurally above S1 and M1 **(G)**.

cable. In addition, six of the electrodes were broken out to headers such that any two could be used as a recording reference for two 16-channel amplifiers. The electrode was fashioned to fit within a stainless steel recording chamber that was attached to an 18-mm diameter titanium collar designed to sit atop a standard 18-mm craniotomy. The metal chamber assembly served both to shield the electrodes and connector PCB as well as provide a body ground for the recording system. The bottom surface of the electrode protruded slightly from the bottom of the assembly and was polished to ensure a smooth interface with underlying tissue. The array was aligned over both primary motor (M1) and primary somatosensory (S1) cortex and the assembly was permanently affixed to the skull with a standard acrylic headcap and bone screws. A removable cap was placed on the top of the assembly to protect the underlying connectors when the animal was not conducting experiments.

5.3.2 Task Design for Evaluating Stimulus Thresholds

Two male, 6-10 kg monkeys (*Macaca mulatta*), G and L, were trained to perform a psychophysical stimulus detection task within a virtual environment displayed to them on a computer monitor. Monkey G received subdural electrocortical surface stimulation from 2 mm diameter electrodes, and Monkey L received epidural electrocortical stimulation from 600 µm diameter electrodes. The task was learned through operant conditioning while sitting freely in a primate chair. A standard 17-inch LCD monitor positioned approximately 20 inches from the monkey was used to display the task through a rendered 3D virtual environment. A joystick (APEM 9000 Series, www.digikey.com) was used to move a cursor to perform the task. Sensory stimulation from a miniature vibrating disk motor (VPM2, www.robotshop.com) taped to the arm

was used during training and was replaced by electrical stimulation applied to cortical electrodes over S1 during actual experiments.

The stimulus detection task was based upon a conditioned avoidance behavioral paradigm first described by Heffner and Heffner (1995). In their original task, a water-scheduled animal initiates a detection trial as soon as they make contact with a metal drink tube. Following a random time interval, a stimulus is presented as a warning, and soon after a mild electrical shock is applied through the drink tube. By exploiting the natural tendency of animals to avoid aversive stimuli, the animal quickly learns to break contact with the drink tube as soon as the warning stimulus is detected. Stimuli which do not result in a break with the drink tube may be considered sub-threshold.

In the task used here, monkeys were trained to use a joystick to move a cursor on a computer screen to interact with displayed targets in order to both initiate trials and indicate when they detect the presence of electrocortical stimuli. Rather than using negative reinforcement, monkeys were motivated with liquid rewards for correctly indicating whether or not a stimulus was presented. Trials were initiated at the monkey's leisure by moving a cursor to a target sphere located on the center of the screen. Upon acquiring the central target, a ring appeared around the cursor. The monkey was trained to quickly move the cursor to touch the ring only following the presentation of a stimulus. After a random period of 0.5-4 seconds following initiation of a trial, an electrocortical stimulus pulse train was initiated. Following the stimulus, the monkey was given 2 seconds to respond by moving the cursor to the ring. Using the terminology of signal detection theory, correct responses to stimulation are considered "hits" and incorrect responses are "misses". Sham trials, in which no stimulation was presented, were interleaved randomly with stimulation

trials. If the monkey incorrectly touched the ring during a sham trial, the response was considered a "false alarm". If the monkey correctly remained within the ring during a sham trial, the response was a "correct rejection". The inclusion of sham trials helped to mitigate the bias of guessing that would occur if stimulation was provided in every trial, since there would be little to lose for guessing incorrectly and much to gain if the guess was correct.

Stimulus parameters were presented according to the adaptive staircase method (Koivuniemi, 2011) which is more susceptible to subject biases than the method of constant stimuli but can be conducted in less time. In the method of constant stimuli, a fixed number of parameter values are tested by randomly presenting them to the subject repeatedly. The detection

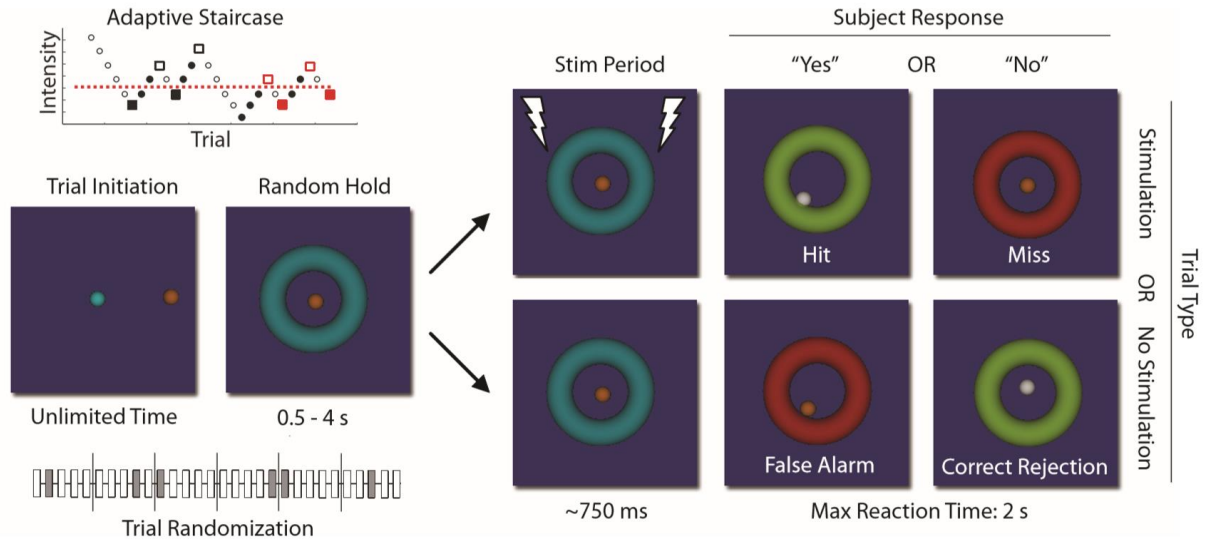

Figure 5.7: Behavioral Task for Determining Threshold Current Levels for Detection

A psychometric stimulus detection task was used to determine threshold current amplitudes corresponding to detection of the stimulus 50% of the time. A joystick-controlled cursor (orange sphere) was moved to the central target to initiate a trial. After initiation, a ring appeared around the cursor. Upon stimulation, the monkey was trained to quickly move the cursor to touch the ring, but otherwise hold the cursor still. Stimulus trials were interwoven with sham trials in a ratio of 1:5 to mitigate "guess" trials. Thresholds were investigated for a number of stimulus pulse train patterns ranging in frequency and pulse width. This paradigm is based upon Heffner and Heffner (1995), but without negative reinforcements. It also readily lends itself to signal detection theory through the Trial-Type and Subject-Response categories shown. An adaptive staircase method was used to decrease the amount of time required for threshold estimation (Koivuniemi et al., 2011).

probabilities are often corrected for guessing and fit by a psychometric curve. Through extrapolation, the threshold and sensitivity can be calculated. While this method provides a good estimate of both the threshold and sensitivity, experiments can be long due to the large number of repetitions necessary for accurate measurements of detection probabilities. The adaptive stair-case method is designed to decrease the number of trials necessary for estimating thresholds by adjusting the tested parameter values based upon previous performance (Leek, 2001). For example, the parameter value is increased following incorrect responses and decreased following incorrect responses so that the test values are concentrated near threshold levels.

In a given test series, the amplitude current of biphasic pulse trains was varied between trials (according to the staircase method) while pulse width, pulse frequency, and pulse train duration were kept constant. A series of detection trials would run until 9 reversals were observed, and the threshold was estimated by averaging an even number of previous values at which reversals occurred. The resulting threshold estimate corresponds to the value in which the stimulus is detected 50% of the time. Sham trials, in which no stimulation occurred, were included to reduce guessing. Blocks of trials in which the false alarm rate exceeded 20% were excluded from analyses and repeated later. Current amplitude thresholds were determined for a range of high frequency pulses (between 200 Hz and 500 Hz) and pulse widths (between 200 μs and 1 ms). These ranges of frequency and pulse width were chosen based upon their candidacy for later use in the a bi-directional BCI, where limited low-frequency spectral components was desired.

5.3.3 Artifact-suppressing Amplifier Design

A front-end amplifier was designed to replace an existing pre-amplifier module commercially available from Tucker Davis Technologies (TDT). The TDT 2-stage amplifier system consists of 1) a low-noise pre-amplifier module that provides an initial 5X gain on input signals, and 2) an RA16PA Medusa digitization module that provides an additional 10X gain on input signals prior to digitization using a 16-bit analog-to-digital converter (ADC). The two modules connect to each other via a standard DB25 connector and are powered by lithium ion batteries in order to provide electrical isolation from potential 60-Hz mains electrical noise. Additional electrical noise immunity is achieved by an electro-optical converter in the RA16PA for optical communication back to a Base Station that contains DSPs for signal processing. For the bi-directional BCI recording system, the TDT digitizer and Base Station were used un-modified, but the analog pre-amp was replaced with a custom artifact-suppressing amplifier with a larger dynamic input range (+/- 6V), lower bandwidth (2-120 Hz), and higher-order low-pass filter (8^{th}-order). Specifications for the TDT pre-amp, TDT digitizer, and custom amplifier are provided in Table 5.1.

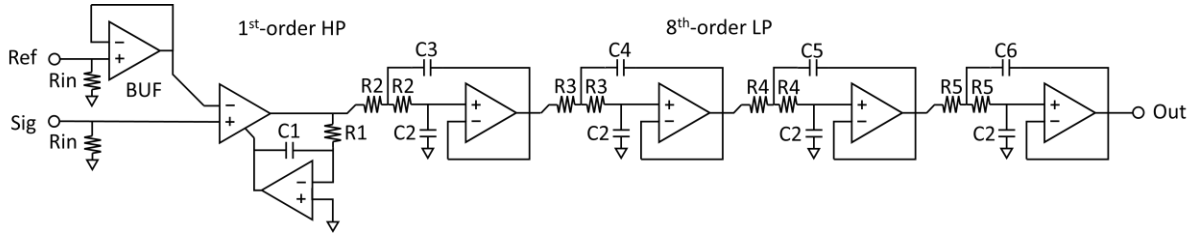

Figure 5.8: Circuit Topology of the Artifact Suppressing Amplifier

General circuit design for each amplifier channel. The reference was buffered and shared as the inverting input to all INAs. A first-order high-pass filter was implemented by an active integrator that provided feedback to the reference of the INA. An 8^{th} order low-pass filter was implemented by four 2^{nd}-order cascaded filter stages designed in a Sallen-Key configuration.

The custom amplifier was designed for single-ended recording and consists of multiple stages: an initial unity-gain buffer stage for the reference signal, an INA stage with 5V/V gain, an active 1st-order high-pass filter stage implemented as a feedback reference to the INA, and four 2nd order low-pass filter stages. This active filtering topology was chosen over a front-end passive filter due to the signal loss and noise performance associated with the passive elements. Passive front-end filters elements can add noise and reduce signals through voltage-divider effects which lowers the signal-to-noise ratio (SNR). The topology was replicated for a total of 16 channels which were all referenced to a common reference channel.

Input impedances to signal channels and the reference channel were matched with a 5 MOhm resistor (+/- 1%) for optimal common-mode rejection ration (CMRR). A value of 5 MOhm was chosen to balance low noise operation with voltage divider effects caused by chronic electrode

Specification	**TDT Pre-amplifier**	**Custom Amplifier**	**Medusa Digitizer**
Input Impedance	1 MOhm	5 MOhm	100 kOhm
High-pass	0.1 Hz 1st-order	2 Hz 1st-order	2.2 Hz 1st-order
Low-pass	500 Hz 2nd-order	120 Hz 8th-order	7.5 kHz 1st-order
Gain	5 V/V	5 V/V	10 V/V
Input Range	+/- 4 mV	+/- 6V	+/- 4 mV

Table 5.2: Specifications of the TDT and Custom Amplifier Systems

Rin	**R1**	**R2**	**R3**	**R4**	**R5**
5 MOhm	27 kOhm	2.87 kOhm	2.43 kOhm	1.65 kOhm	576 Ohm
C1	**C2**	**C3**	**C4**	**C5**	**C6**
2.2 µF	500 nF	470 nF	680 nF	1.5 µF	10 µF

Table 5.1: Resistor and Capacitor Values for the Artifact Suppressing Amplifier

impedances on the order of 30-300 kOhm at 100 Hz (as reported in Chapter 2). While each signal channel was connected directly to the non-inverting input of an instrumentation amplifier (INA111, Texas Instruments, USA), the reference channel was first buffered (OPA140, Texas Instruments, USA) before splitting to the multiple inverting inputs of the INAs. This configuration overcomes voltage divider effects and reduced CMRR that could occur if the reference was directly fed into multiple parallel input resistors on the INAs, which would collectively result in an effective input resistance of 5/16 MOhms to the reference.

A high-pass filter was implemented by an active feedback integrator that fed differential and common dc signals back into the INA's reference pin. A gain of 5 V/V from the INA was set by an external resistor (Rg = 12 kOhm), according to the INA's datasheet. Subsequent low-pass filter stages were cascaded in a Sallen-Key configuration to approximate an 8^{th}-order Butterworth filter. All active filters were implemented with low-noise precision amplifiers (AD8674, Analog Devices, USA). Implementation of a Butterworth filter with Sallen-Key topology was chosen for its maximally flat passband and ease of implementation with minimal components. However, the same topology could have implemented a Chebyshev filter, which would have provided a steeper low-pass roll-off, but more ripple in the passband. Resistor and capacitor values for the filter stages are provided in Table 5.2.

A conservative supply voltage of 12 Vpp was chosen in order to allow enough dynamic range to record stimulation artifacts, which were estimated to be less than +/- 1V at the input to the amplifier. A 12 V DC external re-chargeable battery was used in conjunction with a virtual

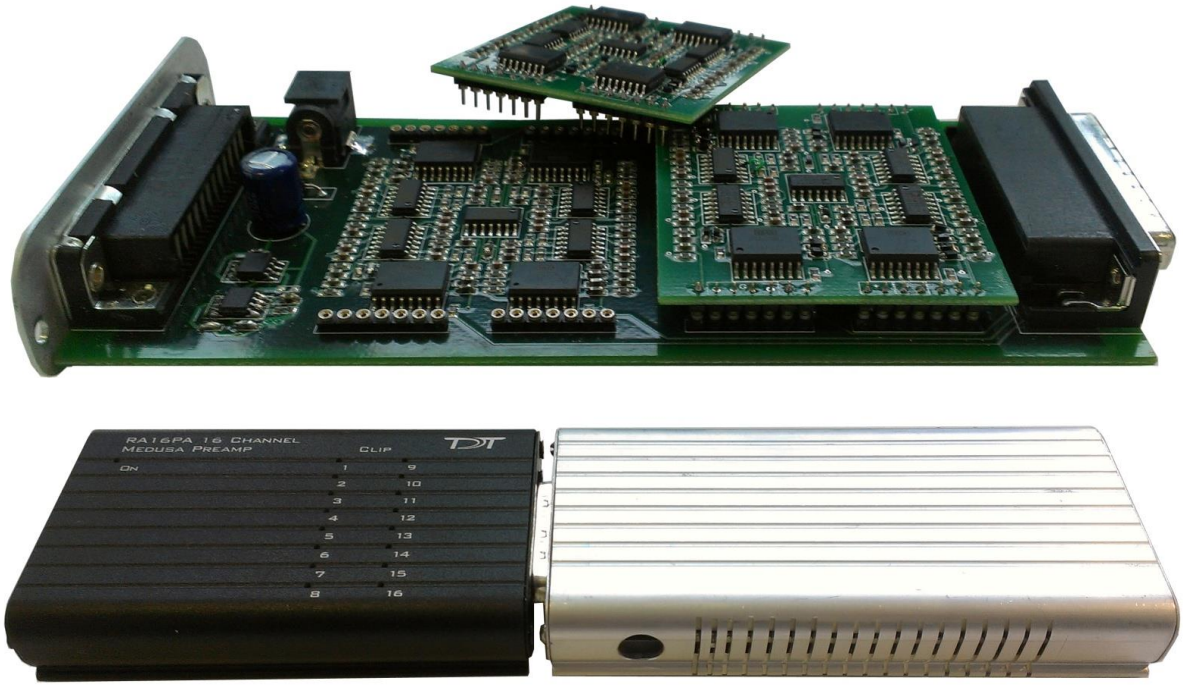

Figure 5.9: Photographs of the Artifact Suppressing Amplifier

The electronics assembly consisted of a mother board with 16 channels, power conditioning, and connectors. Two additional daughter boards could be attached for 16 additional amplifier channels. The electronics assembly was housed within an extruded aluminum frame designed to attach directly to the TDT Medusa digitization stage.

ground circuit (TLE2426, Texas Instruments, USA) to provide a stable midpoint for system ground at ½ of the supply voltage. A diode protection circuit was used to protect the amplifier from potential reverse currents caused by incorrect connection of the battery, and a large capacitor was used to buffer large spurious currents for a stable system ground. This resulting virtual ground ensured that the amplifier was always capable of a maximum symmetric swing even as the battery discharged. The amplifier was housed in an extruded aluminum enclosure that provided EMI shielding for immunity to external noise. Two DB25 connectors on either end of the enclosure allowed easy connection to electrodes at the input and to the TDT Medusa digitization stage at the output.

5.3.4 *In Vivo* Measurement of Stimulus Artifact

In order to investigate the recorded voltage levels of typical stimulus artifacts, stimulation from a current-controlled stimulus isolator (MS16, Tucker-Davis Technologies, USA) was applied between two electrodes while recordings were obtained from nearby electrodes. For this experiment, only the front end of the custom amplifier was used (without the 8th-order LP filter) and signals were digitized using an ADC integrated into the TDT Base Station (~250 kHz and 24-bit resolution). Biphasic pulse trains with a magnitude of +/-750 µA and 1 ms durations were driven between two electrodes spaced ~5.2 mm apart. Peak-to-peak measurements of the resulting recorded artifact were recorded for each electrode.

Stimulus artifacts were also recorded with the complete custom amplifier (including the 8th-order LP filter) to investigate the effects of stimulation waveforms on recorded signals. Stimulus waveform shapes were varied by adjusting the frequency of pulses and the use of a linear gating functions (ramps) to smooth onset and offset. Spectral power was estimated in multiple frequency bands from the recorded signals in both stimulation and non-stimulation trials. A two-sample Kolmogorov-Smirnov test was used to test the null hypothesis that the data from both sets came from the same continuous distribution—the alternative hypothesis being that stimulation artifact caused a significant variation in the recorded signal power.

5.3.5 Decoding Algorithms for Motor Control

Decoding algorithms for the bi-directional BCI are described in detail in Chapter 4. To summarize, an optimal linear estimator (OLE) decoder was used in conjunction with co-adaptive

learning methods to train the decoder. Time series signals from each electrode were expanded into features comprising power modulation in four frequency bands: 8-15 Hz (alpha), 15-30 Hz (beta), 30-55 Hz (low gamma), 70-115 Hz (mid gamma). Features were log-transformed and normalized by estimates of the running mean and standard deviation using Knuth's method. Co-adaptive decoder learning was only used during an initial center-out training period, and the decoder was held fixed for the subsequent bi-directional task. Neural signals were transformed into 2DOF velocity control signals, thresholded using an arctan function, and applied to cursor movement.

5.3.6 Task Design for Closed-loop Sensorimotor Control

One male, 6-10 kg monkey (*Macaca mulatta*), *L*, was trained to perform a two-alternative forced-choice task (2AFC) within a virtual environment displayed to them on a computer monitor. The task was learned through operant conditioning with liquid rewards while sitting freely in a

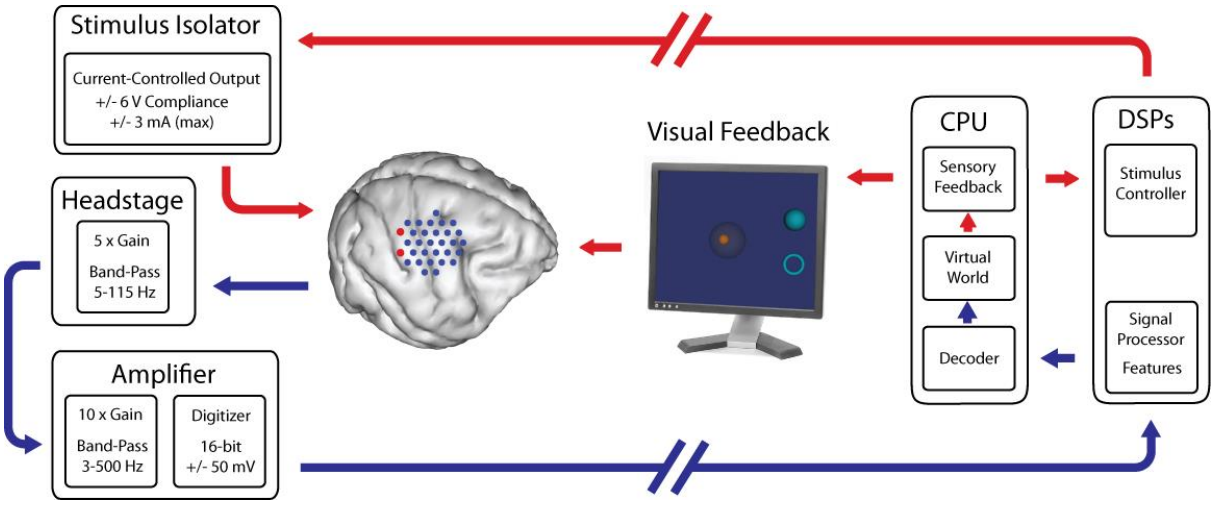

Figure 5.10: Closed-loop Diagram of the Bi-directional BCI Setup

Velocity control of a cursor was obtained during stimulation through the use of the custom artifact-suppressing amplifier. Signals were digitized and fed to a bank of DSPs to perform feature extraction. Signals were then converted to control by a decoder on a PC. Feedback to the monkey included the visual display of the virtual environment and real-time electrocortical stimulation through current-controlled electrostimulation.

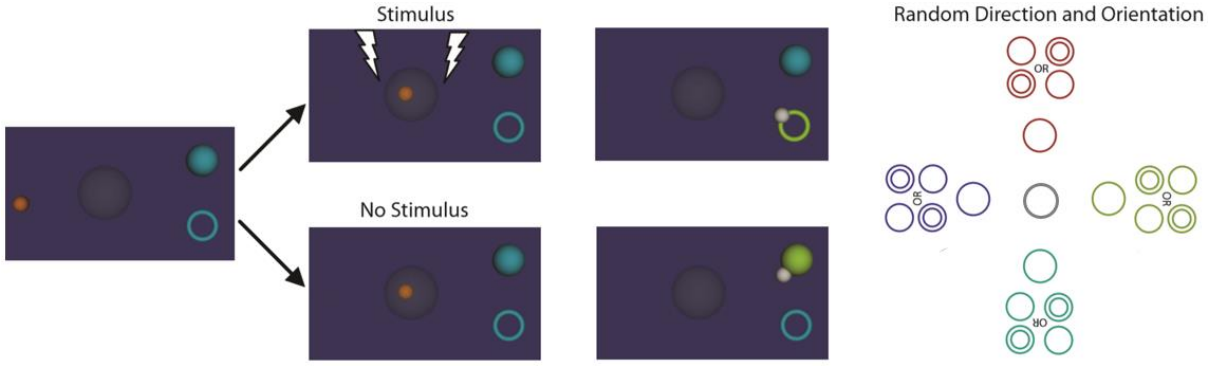

Figure 5.11: Behavioral Task for Demonstrating a Bi-directional BCI

A closed-loop 2AFC BCI task was used to assess the ability to simultaneously control cursor movement in the presence of electrocortical stimulation. In this task, the monkey moved the cursor under brain control. Once a trial was initiated, the monkey was trained to move through a central "test" object. In some trials, the monkey would receive suprathreshold stimulation and would indicate the presence of stimulation by moving to the ring target. In other trials, no stimulation would be provided, and the monkey would indicate that no stimulation was present by moving to the sphere target. The direction of movement, from trial start to target selection, was rotated pseudo-randomly in 4 different orientations in order to eliminate biases in target selection based upon ease of movement in specific directions. Additionally, the relative sphere and ring positions were switched, resulting in 4 directions x 2 ring-sphere orientations = 8 possible trials within a set.

primate chair. A standard 17-inch LCD monitor positioned approximately 20 inches from the monkey was used to display the task through a rendered 3D virtual environment. The monkey was first trained to perform the task using a joystick (APEM 9000 Series, www.digikey.com) to move the cursor and with sensory stimulation from a miniature vibrating disk motor (VPM2, www.robotshop.com) taped to the arm. Next, the vibrating disk motor was replaced by electrical stimulation applied to cortical electrodes over S1 (MS16 isolated current-controlled stimulator, Tucker-Davis Technologies, USA). Finally, the joystick was replaced by full BCI control.

The 2AFC task was designed to demonstrate a bi-directional BCI and included both neural control of cursor movement and virtual sensory feedback via direct electrocortical stimulation. In order to initiate a trial, the cursor would need to move to a "start" target pseudo-randomly positioned at any of 4 locations on the screen. Each start target location was positioned a fixed

distance away from the screen center. Upon successful movement to the start target, the start object would disappear, and 3 new objects would appear: a large semi-transparent "test" target in the center of the screen, and two "decision" targets on the opposite side of the screen. The subject learned to move through the test target, at which time they would either receive stimulation (stim trial) or receive no stimulation (no stim trial) and then proceed to one of the decision targets to indicate whether stimulation was given or not. The decision target objects consisted of a ring to indicate that stimulation was detected, and a sphere to indicate no stimulation was detected. A given trial was aborted if the start target was not engaged within a minimum amount of time (about 30 seconds), if the test target was not engaged, and if neither decision target was chosen within a minimum amount of time (about 30 seconds). Additional stimulation could be triggered by re-engaging with the test object without penalty. The flow of movement was designed from one side of the screen to the other but was rotated in 4 different directions to remove bias associated with movement in a particular direction. Each trial was associated with a different direction, randomly chosen, and not repeated until all trials within set had been completed.

5.4 Results

5.4.1 Stimulus Detection Thresholds

Stimulation thresholds determined from the adaptive staircase method are shown in Figure 5.12 for both Monkey G (subdural implant with 2 mm diameter electrodes) and Monkey L (epidural implant with 600 µm diameter electrodes). Threshold levels of stimulation were all within safe levels estimated by the Shannon Criteria for Monkey G, but not Monkey L. For Monkey L, thresholds for short pulse widths near 200 µs were observed to be approximately 700 µA, which is below the estimated safe maximum of about 1.4 mA. However, thresholds for pulse widths exceeding 600 µs were observed to exceed safety levels predicted by the Shannon Criteria. The elevated levels for Monkey L could have been due to a thin layer of bone regrowth observed below the epidural array post-explanation. Additionally, shunting effects of the CSF may have led

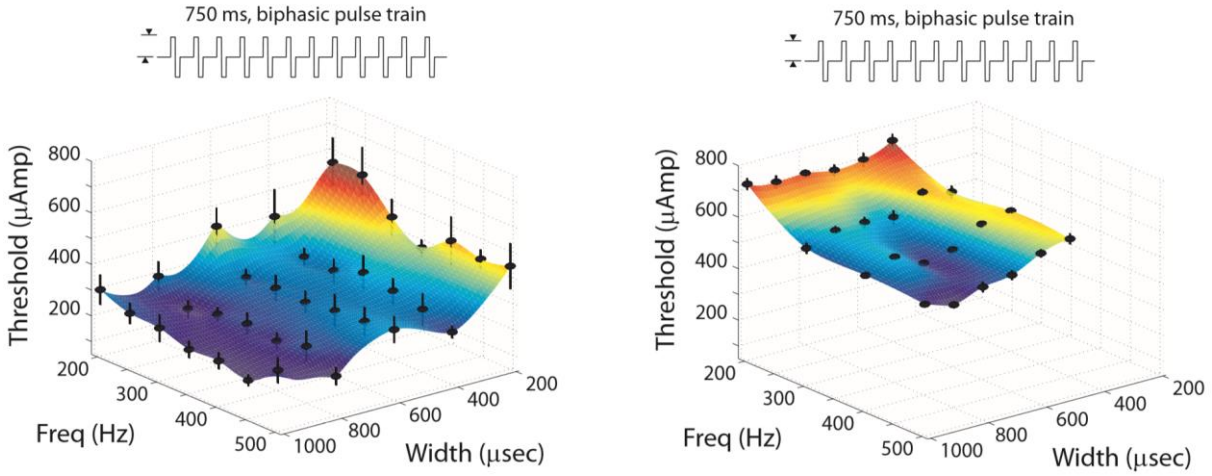

Figure 5.12: Stimulus Detection Thresholds for Subdural (left) and Epidural Electrode Arrays (right).

Stimulus thresholds for Monkey G (subdural 1 mm electrodes) and Monkey L (epidural 600 µm electrodes). Black spheres represent the mean of 5 trials and the bar represents the standard error of the mean. In general, lower frequencies and smaller widths required the largest currents. Thresholds for subdural stimulation with 1 mm electrodes were roughly 400 µA less than epidural stimulation with 600 µm electrodes).

to greater dispersion of current from the epidural electrode across the cortical surface. While direct comparisons between the two monkeys are difficult due to their differences in electrode size and location, the results demonstrate that stimuli can be detected below 1 mA.

5.4.2 *In Vivo* Artifact Size

Based upon the result that threshold amplitudes for stimulation detection are near or below 1 mA, a stimulus amplitude of 750 µA was chosen to assess the size of artifact observed in cortical surface recordings. Stimulation was driven between two electrodes spaced approximately 5.2 mm apart at the edge of the array while recordings were taken from all remaining electrodes. Signals were referenced to an electrode located on the opposite side of the array and lying near to the isopotential line formed between the stimulation electrodes. The resulting map of peak-to-peak voltages show a pattern similar to what would be expected from a dipole source. The maximum artifact occurred closest to the electrodes and off of the predicted isopotential line. The maximum value observed was approximately 70 $\mu V_{p\text{-}p}$. Artifacts remained

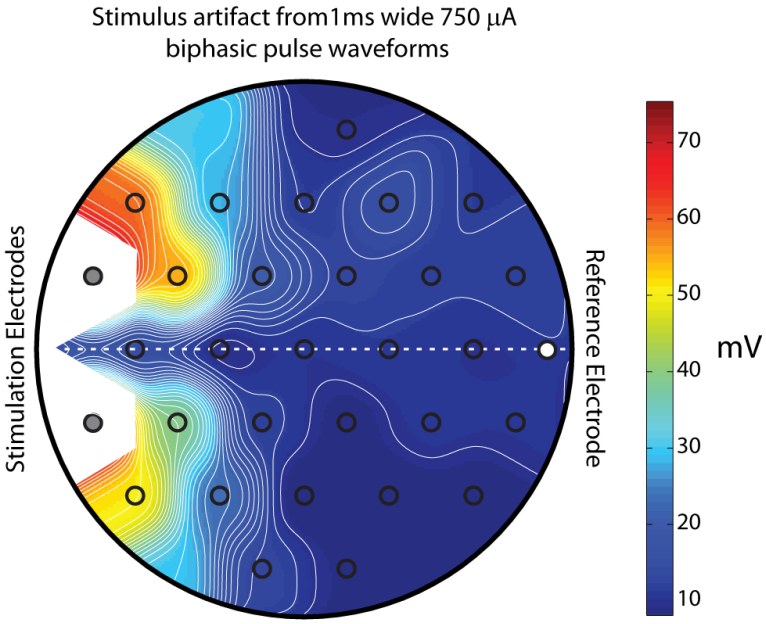

Figure 5.13: *In Vivo* Measurements of Artifact Size

A map of peak-to-peak stimulation artifact size was created by recording signals while stimulating nearby with 750 µA biphasic pulses. The resulting map corresponds well to the potential distribution predicted by bipolar stimulation.

below 25 μV_{p-p} beyond 6 mm perpendicular from the stimulation electrodes. This result confirms that the optimal placement of recording electrodes is along the ispotential line formed perpendicular and through the center of the stimulation dipole. In many cases, however, placement of electrodes may not be as easily controlled relative to stimulation. For these scenarios, amplifiers must be designed with an appropriately wide dynamic range to permit the large artifacts without saturation. The resulting map can also be used to estimate the size of artifact for other levels of stimulation by scaling the artifact proportionally to the change in stimulation size.

5.4.3 Amplifier Performance

Performance of the amplifier was determined by measuring the frequency response, phase lag, group delay, and noise referred to input. As shown in Figure 5.14, the amplifier has a passband gain of 14 dB (or 5V/V) with corner frequencies of 5 and 120 Hz. The filter rolls off at high frequencies at approximately -160 dB/decade. This is expected performance from the 8th-order Butterworth filter. A harder corner could have been achieved with a Chebyshev filter, but at the expense

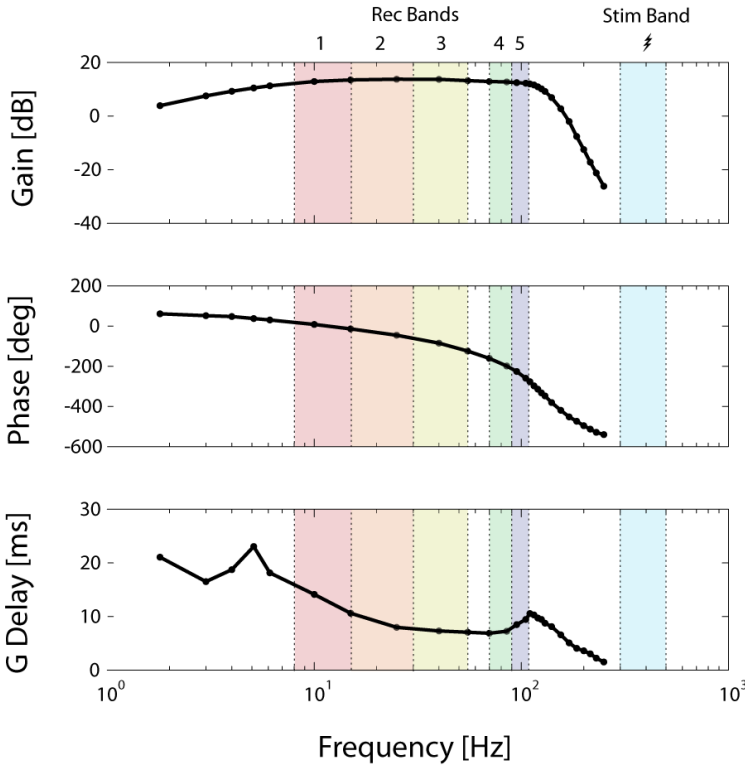

Figure 5.14: Amplifier Frequency Response

The response shows a 1st order high pass at 5 Hz, pass-band gain of 14 dB, and 8th-order low pass at 120 Hz.

of more ripple in the passband. Phase delay also showed expected behavior, transitioning from a 90° lead at low frequencies (due to the 1st-order high-pass filter) to -630° lag at high frequencies (due to the 8th-order low-pass filter). While phase delay describes the lag in time of the phase at a given frequency, group delay describes the lag in time of the amplitude envelope at a given frequency. This is particularly important because control signals are derived from estimates of the envelope around each band. The group delay was measured to be approximately 10 ms, with greater delays near the corner frequencies.

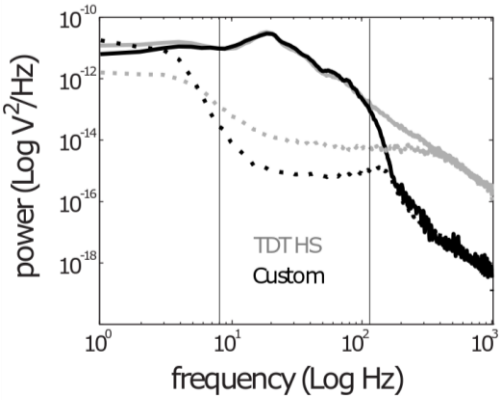

Figure 5.15: Amplifier Noise Performance

Noise performance (referred to input) is shown compared to the TDT system (dotted lines).

The common-mode rejection ratio (CMRR) of the amplifier was 74 dB. CMRR was determined by driving both recording channels and reference with the same input signal (70 Hz, $1V_{p\text{-}p}$) and comparing the common-mode gain G_{cm} to the differential gain G_d observed when the reference was grounded ($CMMR = 20\log[G_d/G_{cm}]$). The noise performance of the artifact-suppressing amplifier was measured with inputs shorted together, which provides a measure of the voltage-noise of the system. As described by the physical noise model in Chapter 3, measurements that include current and thermal noise can be achieved by tying the amplifier input to resistor and capacitor values that approximate electrode impedances. Noise measurements were divided by the gain of the amplifier, resulting in noise referred to the input of the amplifier. Figure 5.15 shows the spectral power density of input-referred noise compared to the original TDT system. As can be seen, the noise performance is improved by the custom amplifier. Integrated input-referred

noise in each recording band was measured to be: 149 nV (8-15 Hz), 122 nV (15-30 Hz), 126 nV (30-55 Hz), 126 nV (70-90 Hz), and 157 nV (90-115 Hz). The corresponding spot noise is: 56.3 $nV/\sqrt{Hz}$ (at 11.5 Hz), 31.5 $nV/\sqrt{Hz}$ (at 22.5 Hz), 25.2 $nV/\sqrt{Hz}$ (at 42.5 Hz), 28.2 $nV/\sqrt{Hz}$ (at 80 Hz), and 31.4 $nV/\sqrt{Hz}$ (at 102.5 Hz). The spectral power of recorded neural signals was also compared between systems. As shown in Figure 5.15, recorded signal power was equivalent. However, SNR was improved with the custom amplifier due to the lower noise floor.

5.4.4 Recording through Stimulation

The ability to record ECoG signals during stimulation was evaluated for a variety of stimulus frequencies, pulse widths, and amplitudes. For each set of parameters, 50 trials were performed with stimulation, and 50 "sham" trials were performed without stimulation. Recorded signals were divided into the five frequency bands allocated for control. The difference between stim vs sham trials was determined by a non-parametric two-sample Kolmogorov-Smirnov test ($p<0.01$) that compared the distributions of stim vs sham trials within a sliding 50 ms window. The results show that stimulation as low as 150 Hz did not produce an effect on recordings in any of the control bands. Interestingly, some higher frequencies (e.g. 400 Hz) did produce a significant effect at the onset and offset of stimulation. This result was predicted by the simulations shown in Figure 5.5. The onset/offset artifact was effectively removed by applying a 250 ms linear ramp gating function both at the beginning and end of the stimulation train. This gating function acted as a simplified windowing function, similar in effect to a Hamming or Hann window.

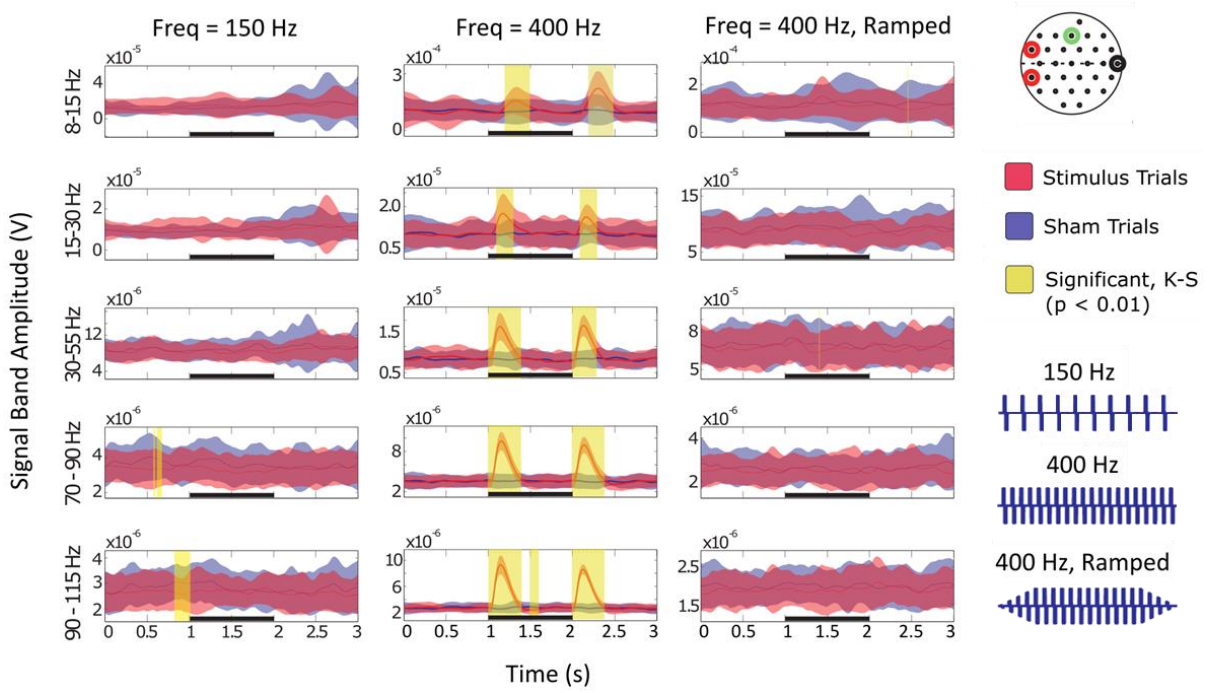

Figure 5.16: ECoG Recordings During Simultaneous Stimulation

Examples of signals recorded through stimulation are shown for various stimulation parameters (columns) and in different recording bands (rows). Each plot shows the mean and standard error of the mean corresponding to 50 stimulus trials and 50 sham (no stimulus) trials. Stimulation is marked by the black bar at the bottom of each plot. Regions of time when stimulus trials were significantly different from sham trials are highlighted in yellow. Significance was determined by a two-sample Kolmogorov-Smirnov test ($p<0.01$). The first column shows that 150 Hz stimulation did not have a significant effect on recordings (highlighted regions precede stimulation and likely occurred due to chance). The second column shows that increasing the frequency of stimulation moved the associated dominant power further away from the amplifier cutoff but created onset/offset artifacts. The third column shows that artifacts were removed by linearly ramping the amplitude of stimulation for 250 ms at the onset and offset of the pulse train. Recordings were taken from an electrode located approximately 9 mm away from the stimulation electrode pair and off of the predicted isopotential line. The stimulation (red), recording (green), and reference (black) electrodes are marked on the electrode array map in the upper left-hand corner.

5.4.5 Bi-directional BCI Performance

Monkey L trained for more than 6 months on the 2AFC task, first using joystick control with vibrotactile stimulation applied to the forearm and later with brain control and electrocortical surface stimulation. The 2AFC task combined aspects of both the center-out and stimulus detection tasks, requiring selection of one of two targets based upon whether or not stimulation was detected. As such, this task was found to be more challenging than previous tasks and required a longer training period to learn. Under joystick control with vibrotactile stimulation, typical performance was around 80%. Under brain control with electrocortical surface stimulation, typical performance was lower, around 70%. For the 2AFC task, chance performance was 50%, so the monkey's performance indicates that, although challenged, they were not simply guessing, but were engaged and attempting to respond to stimulus cues.

Suprathreshold parameters were used for electrocortical stimulation to help ensure that the monkey detected the stimulation. All stimulation patterns consisted of symmetric biphasic pulse trains without an inter-phase interval. Typical stimulation parameter ranges include: amplitude (750-2200 μA), pulse width (400-750 μs), frequency (300-450 Hz), duration (1.5-4 seconds), ramp onset/offset (250-1500 μA). Parameters were adjusted to balance detectability with minimal interference with simultaneously recorded control signals.

Cursor movements obtained under brain control are shown in Figure 5.17 from a session that took place after approximately 8 months of training. In this session, the monkey performed 172 trials and achieved 67% performance. Once a trial was initiated by the monkey, the time to interact with the "test" object and make a decision, took 5.9 ± 2.6 seconds for stim trials and 5.6 ± 2.4 seconds for no-stim trials. As shown by the comparison between stimulation and no-

stimulation trials, cursor trajectories were not noticeably affected by the presence of stimulation. For comparison, Figure 5.17 also shows cursor movements obtained under joystick control. For the joystick-controlled data set, the monkey achieved a performance of 78% over 124 trials. As shown, movements are similar, though cursor trajectories were slightly smoother and a bit faster under joystick control than brain control. Under joystick control, the movement time for stimulation trials was 5.6 ± 1.0 seconds and 5.3 ± 1.0 seconds for no-stim trials.

5.4.6 Optimal Features for Bi-directional Control

Only 16 of the 32 electrodes were used for brain control for the bi-directional task. The electrode array was split into two connector ports, where electrodes located proximal to sensory cortex (1-16) were used for stimulation, and electrodes located proximal to motor cortex (17-32) were used for recording. Stimulation was provided between two electrodes located on the opposite side of the array from recording electrodes in order to limit stimulation artifact. All recordings were referenced to designated 600 μm diameter electrode located along the theoretical isopotential line created by the stimulation electrodes and on the opposite side of the electrode array.

Prior to initiating the 2AFC task under brain control, a naïve OLE decoder was trained over approximately 10-20 sets of a standard 2-D center-out task using the co-adaptive method described in Chapter 4. Once satisfactory brain control was achieved, the decoder was fixed for the remainder of subsequent 2AFC task. Importantly, the decoder was not trained during stimulation, though this remains an interesting topic for further investigation.

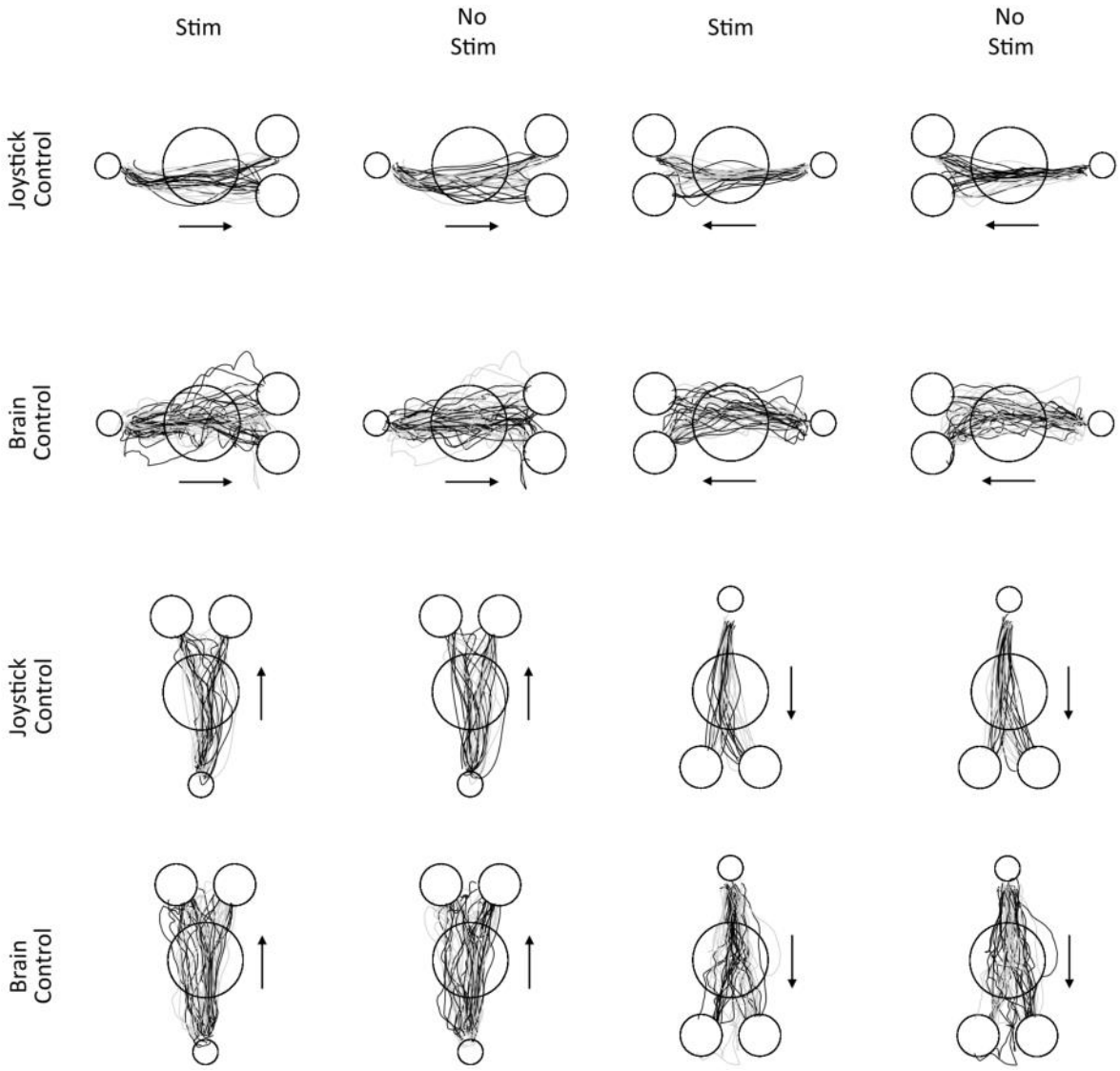

Figure 5.17: Cursor Movements in Bi-directional Task

Cursor trajectories are shown for each direction of movement. Movements are organized by stimulation versus non-stimulation trials (columns) and by joystick control versus brain control (rows). Under Stim columns, corresponding stimulation trajectories are shown in black and overlay light gray non-stimulation trajectories. In the adjacent No Stim column, corresponding non-stimulation trajectories are shown in black and overlay light gray stimulation trajectories. The center circle represents the "test" object and the two adjacent circles represent the "decision" targets. During the actual task, one decision was a ring, corresponding to stimulation, and the other was a sphere, corresponding to no stimulation.

Chapter 4 described the theoretical background and analysis of interpreting coefficients assigned by the OLE decoder to each feature as a weighted preferred direction. In order to examine the relative contributions of each frequency band to control, weights from each center-out training set were grouped by frequency band and normalized by the total sum of all weights in order to calculate a distribution. Figure 5.18 shows the distribution of weights assigned across bands, where lines and error bars represent the mean and standard error of the mean as calculated across the full number of training sets. Results show that beta (15-30 Hz) and mid-gamma (70-90 Hz and 90-115 Hz) received the greatest amount of weights. This result supports similar findings from 4DOF tasks (Chapter 4) and predictions from signal statistics (Chapter 3).

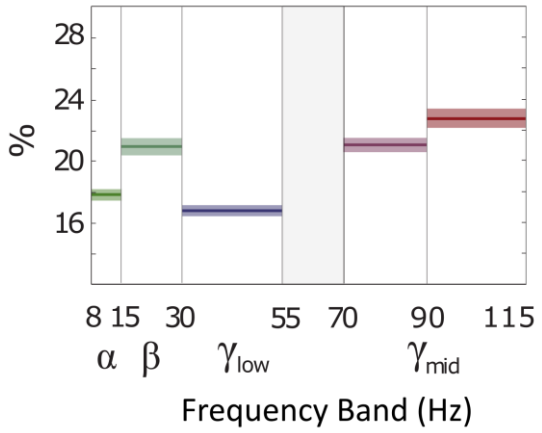

Figure 5.18: Optimal Frequency Bands for Bi-directional BCI Control

Both beta and mid-gamma received the greatest amount of weights.

The relative contribution of individual electrodes was also analyzed by summing the decoder weights across all frequency bands for each electrode and normalizing its total weight by the maximum observed value. As shown in Figure 5.19, control was distributed across all of the electrodes used for recording. The amount of stimulation artifact observed on electrodes was analyzed by comparing the average signal power observed in each control band during movements grouped by trials either with or without stimulation. Stimulation parameters for the dataset shown are: amplitude = 1.5 mA, pulse width = 400 μs, frequency = 400 Hz, duration = 4 s, ramp onset/offset = 1.5 s. Figure 5.20 shows the absolute change in power between stimulation and non-stimulation conditions for each control band and mapped onto each electrode position. Here,

it can be seen that the greatest changes in signal power occurred off of the theoretical isopotential line, as predicted by Figure 5.13. More detailed plots are shown in Figures 5.21-5.25, which show the calculated mean power for each condition along with the standard error of the mean. Results show that changes in signal power were small. In the lower control bands, stimulation trials tended to show slightly more power than non-stimulation trials, but this pattern was reversed in upper control bands.

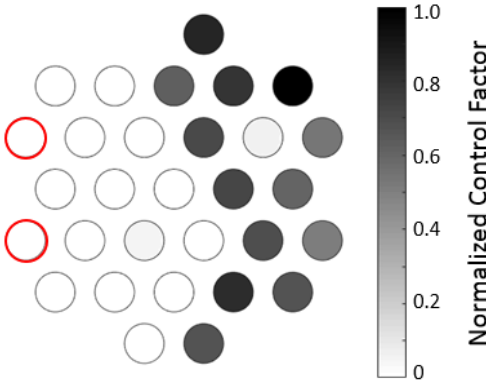

Figure 5.19: Electrode Locations for Bi-directional BCI Control

Control is distributed across all electrodes used for recording on the right side of the array. The left side of the array was used for stimulation. In all sessions, stimulation was through the electrodes marked in red.

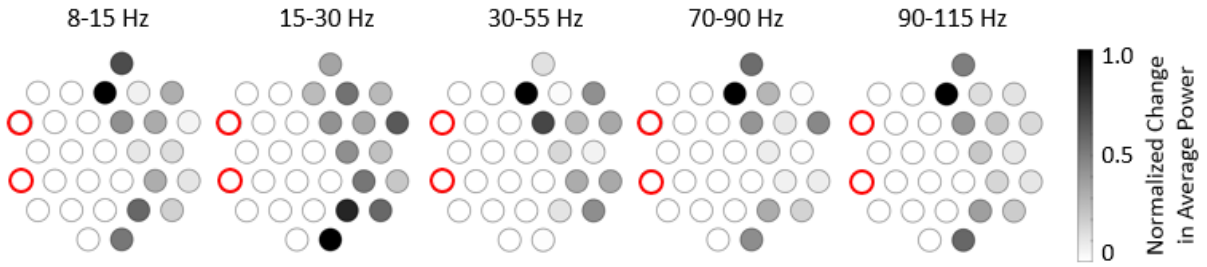

Figure 5.20: Absolute Change in Power Between Stim and No-Stim Trials

Normalized signal power from recording channels are shown on the right half of the array. The left of the array was used for stimulation. The stimulation electrodes used are shown in red. While changes in signal power were small, electrodes at the top and bottom edges of the array (off of the theoretical isopotential line) showed the largest changes.

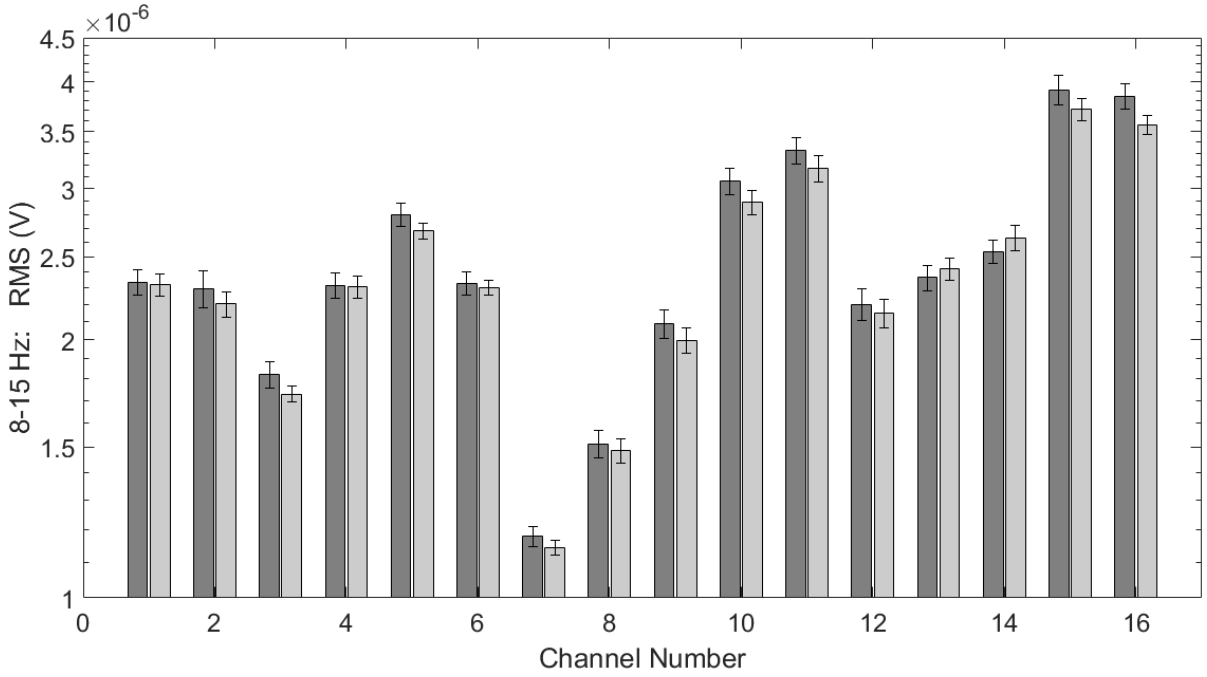

Figure 5.21: Alpha (8-15 Hz) Changes in Power Between Stim (Dark) and No-Stim (Light) Trials

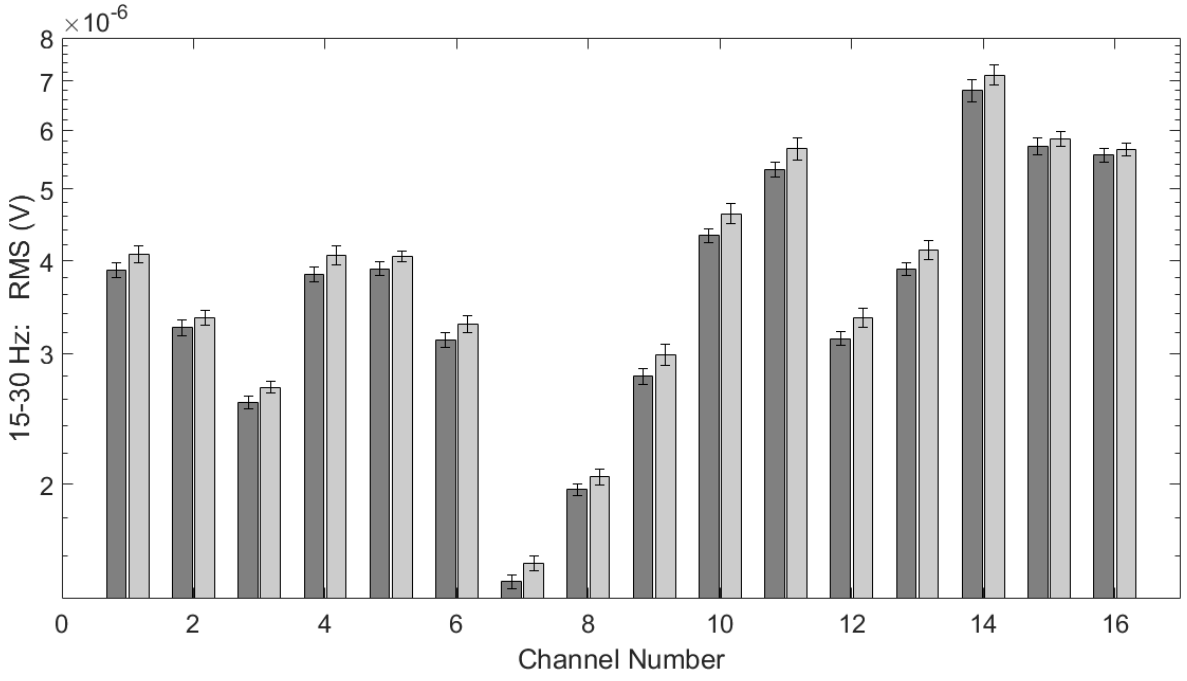

Figure 5.22: Beta (15-30 Hz) Changes in Power Between Stim (Dark) and No-Stim (Light) Trials

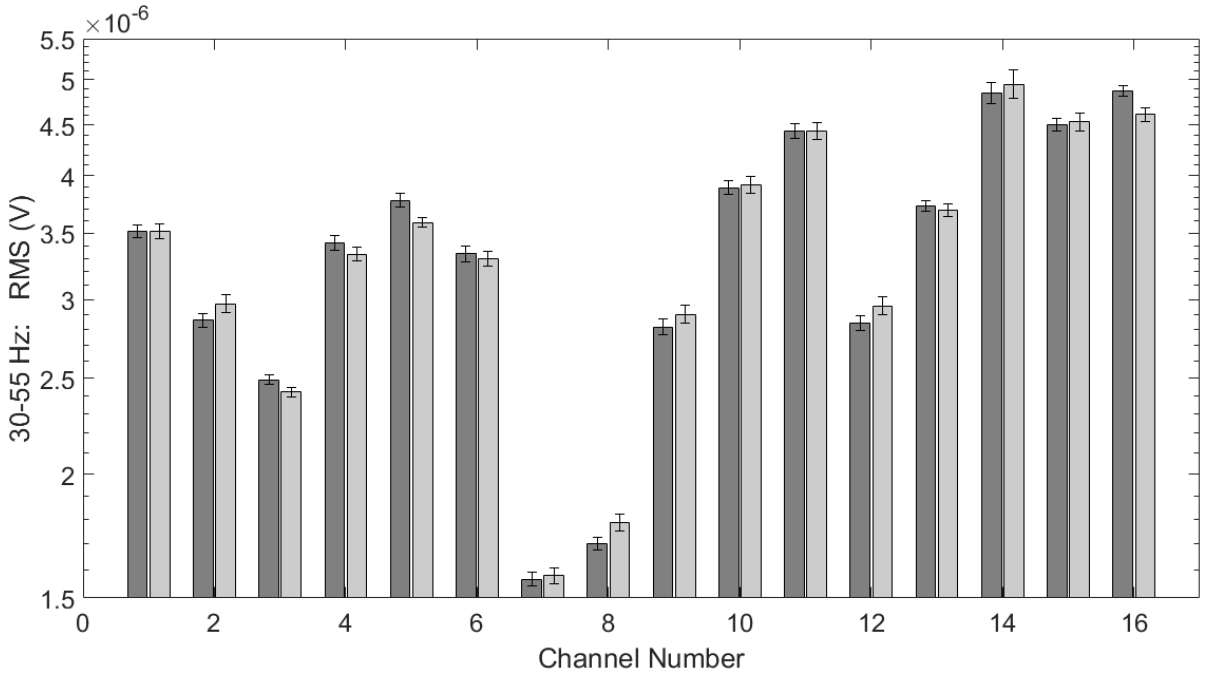

Figure 5.23: Low-gamma (30-55 Hz) Changes in Power Between Stim (Dark) and No-Stim (Light) Trials

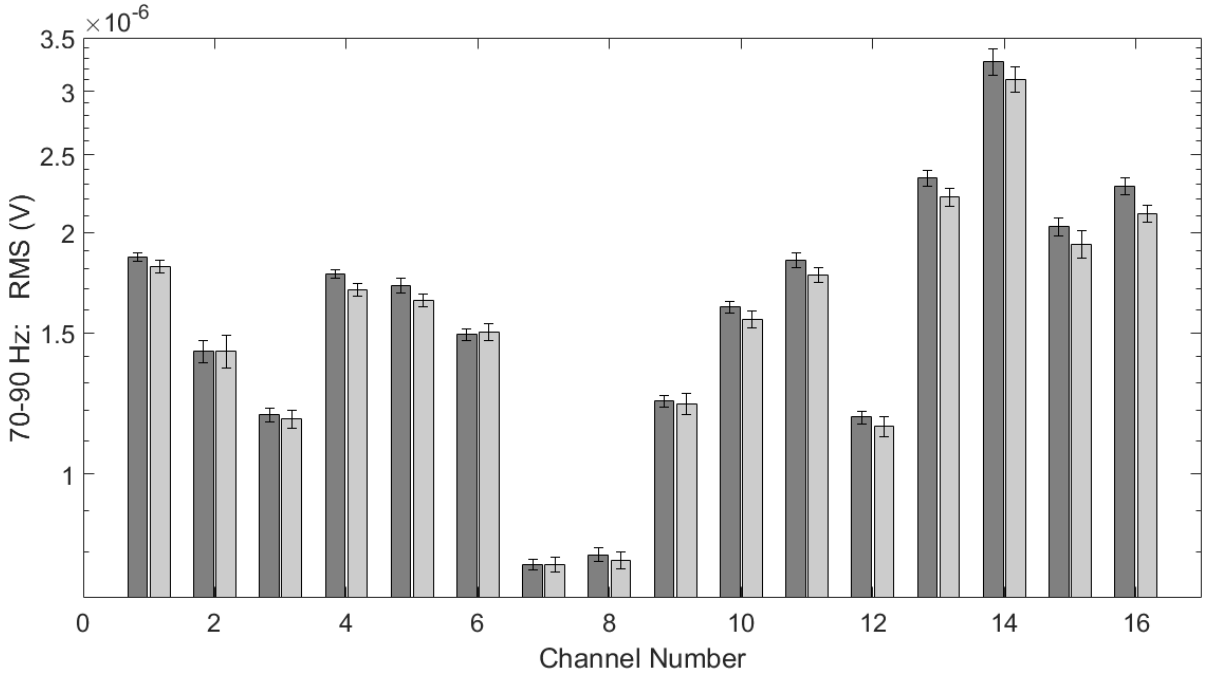

Figure 5.24: Mid-gamma (70-90 Hz) Changes in Power Between Stim (Dark) and No-Stim (Light) Trials

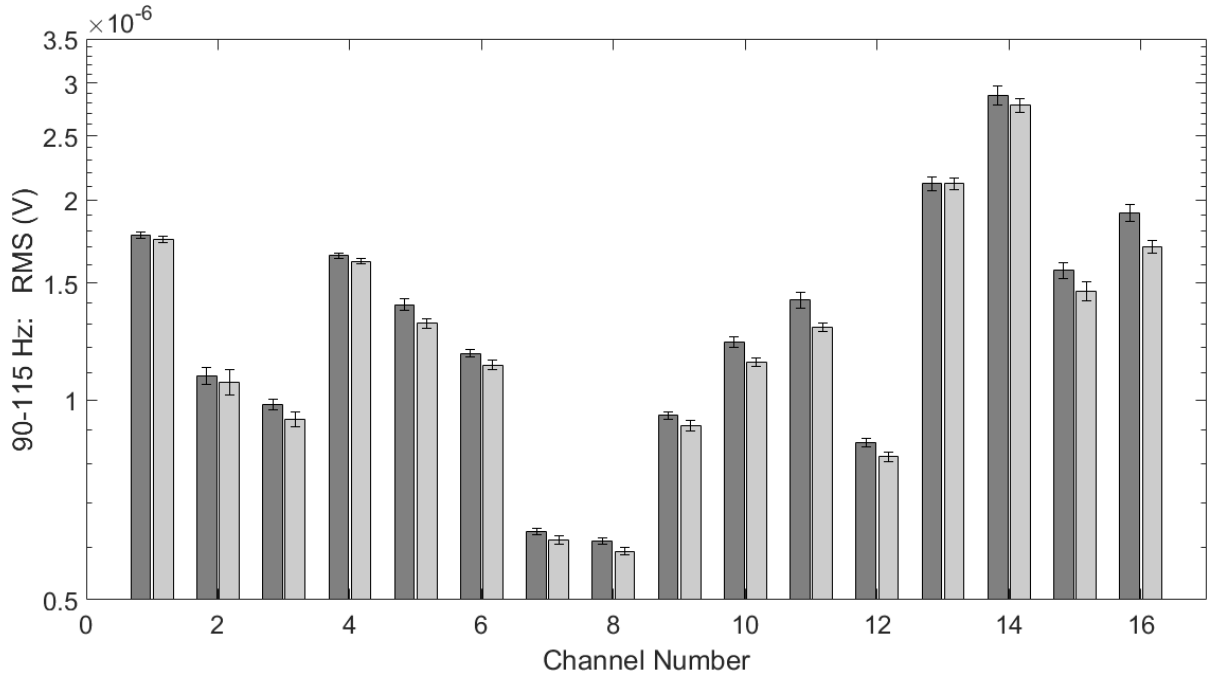

Figure 5.25: Mid-gamma (90-115 Hz) Changes in Power Between Stim (Dark) and No-Stim (Light) Trials

5.5 Discussion

5.5.1 Multi-layered Approach to Artifact Rejection

This study demonstrates the feasibility of recording high-quality ECoG recordings while simultaneously providing electrocortical surface stimulation. Unlike other modalities that depend upon time-domain analyses of signals with large bandwidths (e.g. multi-unit recordings), the ability to capture information from relatively narrow frequency ECoG bands enables frequency-multiplexed bi-directional information to and from the brain. In order for this separable-band scheme to work, a multi-layered approach to artifact rejection was employed through the co-design of the amplifier, signal processing chain, and stimulus waveforms. This systems-level method of

development aimed to balance design specifications such that recorded signals could be effectively used for control while stimulation patterns could be readily detected as sensory feedback.

The electronics development for stimulus artifact rejection included the design of a wide dynamic input range amplifier that could pass large-signal stimulus artifacts without saturating. The custom amplifier was designed to achieve low-noise performance while filtering out high-frequency stimulation artifacts without constraints on power consumption or size. Chapter 2 presented the upper limits on noise required to achieve an SNR of 3V/V for each band: noise was specified to be less than 2 μV for beta (15-30 Hz) and 330 nV for mid-gamma (70-115 Hz). The custom amplifier exceeded these noise specifications and achieved estimated SNRs of 50V/V for beta and 6V/V for mid-gamma. The custom amplifier is well-suited for percutaneous use outside of the body, but for implantable applications, alternative amplifier architectures will be required and likely involve an ASIC design. A JFET input stage was used for the custom amplifier, which provided balanced low 1/f voltage and current noise, each matched to the electrode impedances and signal bandwidth. However, CMOS is a more popular choice for mixed-signal applications that incorporate analog-to-digital converters (ADC) and registers for programmable recording parameters (e.g., bandwidth, gain, channel shut-down). CMOS is also more readily scalable to high-channel counts with miniaturized feature sizes. Future work may seek to develop CMOS amplifier architectures that can balance low 1/f noise with low-power operation and miniaturized size. Based upon the artifacts observed here, a dynamic range of ±40 mV is sufficient to permit recording within 1 cm of surface stimulation electrodes with currents as high as 1.5 mA. For deep-tissue stimulation where conductivities around the electrodes are more isotropic compared to surface electrodes placed right under the skull, current will spread more uniformly and artifacts

may be smaller in magnitude than observed here. Therefore, for most neuromodulation applications, a dynamic range of ±20 mV should be sufficient.

Provided that the amplifier performance is sufficient to pass large-signal stimulation artifacts, subsequent filtering stages can be used to reduce unwanted signals. Here, an 8^{th}-order low-pass filter was used to reduce high-frequency artifacts prior to signal digitization. A consequence of using a high-order hardware filter is that increased phase lag and group delay can lead to unwanted signal distortion and envelope delays. In many cases, hardware filters can be implemented with lower power consumption than digital designs. However, digital designs often provide more flexibility in signal processing—for example, filters with zero lag. In a multi-stage mixed-signal design, artifacts only need to be reduced sufficiently to avoid saturation of secondary amplifier stages and the dynamic range of the ADC. Once the signal is digitized, a wide variety of signal processing techniques may be employed, including template subtraction. Future work may seek to develop signal processing designs that span both analog and digital domains and optimize for power consumption for use in implantable systems.

Stimulation waveforms must be designed carefully in order to shape artifacts such that they can be rejected during recording but without compromising the stimulation effect. Here, stimulation waveforms needed to be detectable but not interfere with the low-frequency recordings bands. Attention must be paid not only to the pulse shape (or alternative shapes like sinusoids or Gaussians), but also ramping functions at the onset and offset of stimulus trains. Here, a simple linear ramp function was used at the onset and offset of pulse trains, but other functions may further improve performance. While this work focused on bi-polar stimulation from a single pair of electrodes, other applications may require stimulation on many more channels. The resulting artifacts from multi-channel stimulation in recorded signals will be equal to the superposition of

artifacts from each individual stimulation source. Therefore, in scaled-up applications, stimulation waveform shaping must take into account the total effect of all stimulation channels. Future work may seek to optimize waveforms for balanced activation efficacy, power consumption, and artifact rejection, and may also seek to develop stimulus waveform shaping algorithms for multi-channel applications.

5.5.2 Implications for Sensorimotor BCIs

This study demonstrated both motor control and sensory feedback through a bi-directional BCI, which could be used to restore sensorimotor function to people with paralysis or an amputation. Unlike other bi-directional BCI approaches that must interleave recording and stimulation in time, the approach presented here was able to achieve both simultaneously and without interruptions. Additionally, the bi-directional BCI was achieved without penetrating the dura, which reduces risks to the subject. Based upon the stability of epidural ECoG signals presented in Chapter 3, this type of minimally-invasive BCI could be well-suited for chronic applications extending beyond time periods currently achievable using more invasive penetrating electrode technologies.

Sensory information was encoded by electrocortical surface stimulation, and threshold amplitudes for detecting the stimulation were shown to vary with stimulation frequency and pulse width. Subdural stimulation produced lower thresholds than epidural, as expected, but results were confounded by different electrode diameters. Epidural stimulation might have resulted in activation of small-diameter pain fibers in the dura rather than the underlying sensory cortex, although this seems unlikely. Studies using epidural motor cortex stimulation (MCS) have reported that patients can tell when and over which associated body part stimulation occurs, which

indicates that underlying cortical neurons are being activated (Fujioka et al., 2018). Future studies with human subjects could more easily investigate the subjective experience associated with different patterns of stimulation. Future studies may also explore the discriminability between sensory stimulation patterns in order to understand how much stimulation parameters must be modulated in order to create a "just noticeable difference" to the subject. Similar to Weber's Law, the relationship between stimulation parameter change and perceptual change could be nonlinear. Understanding this mapping will help to establish the bandwidth required to encode diverse sensory perceptions.

Similar to results from motor BCI studies in Chapter 3, the optimal frequency bands for control with the bi-directional BCI included beta (15-30 Hz) and mid-gamma (70-115 Hz). However, the current study further demonstrates that BCI control can be achieved with as few as 16 electrodes and narrower bandwidth. The decoder was trained based upon data from a center-out task that did not include stimulation. In the future, the decoder training paradigm might be adjusted to also include stimulation. Decoder optimization could be designed to minimize the weights on features that contain artifact so that they have less effect on control. Alternatively, the decoder could be trained to recognize artifact and adjust control accordingly, and in real-time. Finally, the co-adaptive approach to training the decoder might also be adapted to train a stimulation encoder. By providing real-time error correction to the encoder based upon the discriminability of stimuli or subjective perception, the encoder could be tuned to optimally adjust stimulation patterns to enhance the SNR of encoded information. Similarly, co-adaptive algorithms could be used to optimize many other aspects of closed-loop performance with the bi-directional BCI to improve human-machine interactions.

5.5.3 Implications for Broad Closed-Loop Applications

The results of this study extend beyond sensorimotor BCIs and are relevant to a wider range of applications that involve closed-loop therapies. Future applications may include medical therapies as well as augmented or enhanced performance. Epidural (and even subdural) ECoG is an attractive alternative to penetrating electrodes for chronic applications. In many ways the low-frequency content of ECoG signals is similar to local field potentials (LFP) recorded from micro- and macro-electrodes both in cortical and deep-brain regions. LFP and other relatively low-frequency signals in the body, including electromyography (EMG), may also be suitable for closed-loop systems that employ a similar separable band strategy. By enabling simultaneous sensing and stimulation through the techniques described here, responsive therapies can not only be tuned to individual patients, but also provide precision therapies at exactly the right place and time. This has the potential to improve targeted outcomes while reducing undesirable side effects.

Appendix

A.1 Electrical Conduction Within Electrodes

In solid metal conductors, atoms align in three-dimensional lattices and their atomic orbitals merge to form molecular orbitals which can be traversed by electrons as their energy levels change. Electrons in the energetically lower valence band are less mobile than the energetically higher conduction band. At normal temperatures above T=0 Kelvin, electrons move stochastically between levels as they are excited by thermal energy. Higher temperatures excite electrons into higher energy orbitals as described by the Fermi-Dirac distribution that links the energy of electrons to thermal energy by the Boltzmann constant. Electrical conductivity of metallic solids decreases with increasing temperature because of random thermal motion which makes electrons less efficient in transporting charge due to increased collisions with neighboring atoms. This phenomenon results in thermal-electrical noise referred to as Jonhson-Nyquist noise. (Andreas Elschner et al., 2011).

In saturated polymers like polyethylene, all valence electrons are used in covalent σ-bonds which results in a large energy gap between the valence and conduction bands, and the material shows insulating properties. However, in conjugated polymers, a π system is formed along the polymer backbone where electrons not involved in σ-bonds reside in π bands that are either completely filled or completely empty. Since there are no partially filled bands, pure conjugated polymers behave as semiconductors. Unlike doping in semiconductors, where a foreign atom is introduced into the host's lattice, doping in conductive polymers refers to a chemical reaction (oxidation or reduction) that alters the number of available charges in the polymer's chain. The

relationship between temperature and conductivity in intrinsically conducting polymers follows the pattern of normal semiconductors. (Andreas Elschner et al., 2011).

A.2 Electrical Conduction Across Electrodes

In a bioelectric interface, the total flow of current between the electrical device and surrounding tissue results from both faradaic and non-faradaic (capacitive) processes. Faradaic currents involve the movement of electrons across the electrode-electrolyte interface due to electro-chemical redox reactions at the electrode surface. Non-faradaic currents result from the coupled movement of electrons in metal and charged ions and molecules in solution toward and away from a capacitively charged electrode-electrolyte interface without an exchange of electrons across the electrode surface. Within a metal electrode, current is passed by the movement of free electrons in the molecular conduction band relative to the fixed atomic lattice. The bulk of biological tissue is an electrolytic solution and electrical current arises from the flow of free electrons, ions (anions$^-$ and cations$^+$), and charged molecules. Charge transfer *across* the electrode-tissue interface is mediated by redox (***RED***uction-***OX***idation) reactions through which the reactants change their oxidative state by accepting (reduction) or donating (oxidation) electrons. Therefore, the movement of negatively charged electrons is responsible for electrical current flow in the metal electrode *and* across the electrode-electrolyte interface, and the movement of both positive and negative charges is responsible for electrical current flow in the bulk electrolytic solution. In a two electrode electro-chemical configuration, reduction reactions take place at the cathode$^-$ which attracts cations$^+$ in the electrolyte solution. Oxidative currents occur at the anode$^+$ which attracts anions$^-$ in the solution. Using the definition of *convention electrical current flow*

(the direction of positive charge movement) current flows out into the electrolyte solution from the anode and returns through the cathode.

A.3 Faradaic (Non-capacitive) Currents

Oxidation and reduction currents are *faradaic*, which requires the movement of electrons across the electrode-electrolyte interface via changes in valency of surface-bound reactants. Reactants may include metal ions from the electrode itself, or dissolved analytes in the surrounding solution. The impedance to faradaic current flow at the electrode-electrolyte interface is dependent upon the availability of conduction electrons in the metal electrode, the associated redox reaction rates, and the mass transport of reactants and products to and from the interface. Impedances that arise from each of these limiting factors result in over-potentials that polarize the electrode-electrolyte interface when current is actively driven. Over-potential refers to any potential beyond the equilibrium resting potential (E_{eq}) that naturally exists at the interface between any dissimilar materials when current is not actively driven.

The activation overpotential (η_a) is the voltage drop at the electrode-electrolyte interface necessary to maintain current flow due to redox reactions and is described by the Butler-Volmer equation: (Bard & Faulkner, 2001)

$$I = A \cdot i_0 \left[\frac{C_{ox}(0,t)}{C_{ox}^*} e^{-\frac{\alpha n F \eta_a}{RT}} - \frac{C_{red}(0,t)}{C_{red}^*} e^{\frac{(1-\alpha) n F \eta_a}{RT}} \right] \quad \text{(A.1)}$$

Here, I is current (amps), A is the electrochemical surface area (meters^2), α is a charge transfer coefficient (dimensionless), n is the number of electrons involved in the reaction, F is Faraday's constant, R is the universal gas constant, and T is absolute temperature (Kelvin). i_0 is the exchange

current density (A·meters^{-2}) that reflects the intrinsic electron exchange rate between an analyte and electrode at equilibrium. Although the equilibrium net current is equal to zero, faradaic activity is still in progress at the electrode surface, with equal magnitudes of anodic and cathodic currents. The exchange current is an important kinetic parameter, where a large exchange current facilitates fast reaction kinetics. $C_{ox}(0,t)$ and $C_{red}(0,t)$ represent the time-dependent concentrations of the oxidized and reduced species at zero distance from the electrode surface, and C_{ox}^{*} and C_{red}^{*} are the bulk concentrations. When recording bioelectric potentials, η_a is very small and the concentrations of the oxidized and reduced species at the electrode surface are equal to the bulk concentrations. Under these conditions, the Butler-Volmer equation simplifies to linear relationship: (Bard & Faulkner, 2001)

$$I = A \cdot i_0 \frac{nF}{RT} \eta_a \tag{A.2}$$

From this linear relationship, the charge transfer resistance R_{ct} can be defined, which is a useful parameter for modeling electrochemical impedance spectroscopy (EIS) data: (Bard & Faulkner, 2001)

$$R_{ct} = \frac{\eta_a}{I} = \frac{1}{A} \cdot \frac{RT}{i_0 nF} \tag{A.3}$$

When stimulating tissue, η_a is very large and the net current is dominated by either the anodic or cathodic reactions so that one of the terms in the Butler-Volmer equation goes to zero. Under these conditions and ignoring mass transport effects, the Butler-Volmer simplifies to the logarithmic Tafel Equations: (Bard & Faulkner, 2001)

$$\eta_a^{red} = \left(-\frac{RT}{\alpha nF}\right)\ln(I_{red}) + \left(\frac{RT}{\alpha nF}\right)\ln(Ai_0) \tag{A.4}$$

$$\eta_a^{ox} = \left(\frac{RT}{(1-\alpha)nF}\right)\ln(I_{ox}) - \left(\frac{RT}{(1-\alpha)nF}\right)\ln(Ai_0) \tag{A.5}$$

The Tafel equation for oxidation (or reduction) is only valid when currents attributed to the reverse reaction contribute less than 1% to the total current.

Tafel behavior assumes that reactions are not transport limited, but this assumption is not valid when large prolonged currents deplete the electroactive species at the electrode surface. In this case, the redox reaction rates (and necessarily current) will depend upon diffusion of reactants between the electrode surface and the bulk solution. When a specific redox reaction is mass-transport limited, the current *associated with that reaction* will become independent of the applied potential. Independence of current and voltage for a particular redox reaction does not mean that an increase in potential will not result in more net faradaic current, however, as the redox potentials for other reactions may be reached and result in an additional source of charge transfer. The movement of an electroactive species under diffusion control is described by Fick's laws of diffusion, and the relationship between electrode potential and current under *potentiostatic* conditions is given by the Cotrell equation. For a planar electrode, the Cotrell equation is given by: (Bard & Faulkner, 2001)

$$|i| = \frac{nFAC^*\sqrt{D}}{\sqrt{\pi t}} \tag{A.6}$$

where $C^*$is the concentration of the electroactive species, D is the diffusion constant, and t is time. From this equation, it is observed that when a large voltage step is applied to an electrode, a large

initial faradaic current will result that will deplete the surface concentration of the reactant after which additional reactant will arrive as fast as diffusion will permit, but will slow as the reactant is reduced in the surrounding diffusion region. Even if the reaction does not consume all reactant at the electrode surface, the concentration will still be reduced compared to bulk solution and Cotrell behavior will be observed. The Cotrell equation is fundamental to potentiostatic experiments in which current is measured in response to a known voltage. In cyclic voltammetry experiments, current is measured in response to repeated voltage ramps applied to the electrode, which reveals peaks in anodic and cathodic currents corresponding to forward and reverse redox reactions. The up-slopes of the current peaks (as voltage moves away from the electrodes equilibrium potential) are a result of dominant Tafel behavior, whereas the down-slopes result from mass-transport limited Cotrell behavior. While the Cotrell equation describes the current-diffusion relationship of a mass transport-limited reaction under potentiostatic conditions, the Sands equation describes this relationship under *amperostatic* (or galvanostatic) conditions, where current is the controlled variable: (Bard & Faulkner, 2001)

$$i = \frac{nFAC^*\sqrt{\pi D}}{2\sqrt{\tau}} \tag{A.7}$$

Here, τ is the transition time for the reaction, which represents the time at which the concentration of the reactant at the electrode-electrolyte is depleted. At the time of depletion, the fixed current can no longer be supported by the redox reaction and so the potential must shift to the redox potential of another electron transfer reaction. For rapid and reversible (Nernstian) redox reactions under amperostatic control, the potential (E) is given by: (Bard & Faulkner, 2001)

$$E = E^0 - \frac{RT}{2nF}\ln\left(\frac{D^{ox}}{D^{red}}\right) + \frac{RT}{nF}\ln\left(\frac{\sqrt{\tau} - \sqrt{t}}{\sqrt{\tau}}\right) \quad \text{(A.8)}$$

Collectively, the Butler-Volmer, Cotrell, and Sands equations provide a comprehensive description of the activation overpotential (η_a) necessary to maintain faradaic current flow across an electrode-electrolyte interface. As current is passed, a concentration gradient will be setup by the transport of electroactive species in response to the redox reactions at the electrode-electrolyte interface. The electrical potential resulting from this gradient is termed the overpotential (η_c). The concentration profile can be modeled by a convective region far from the electrode surface and a thin Nernst diffusion layer very near to the electrode surface. In the convective region, the concentration of an electroactive species is assumed constant (C^*) with respect to the distance from the electrode because of sufficient mixing by convective currents. In the diffusion region, the concentration is assumed to decrease linearly with distance from C^* at the convective boundary to

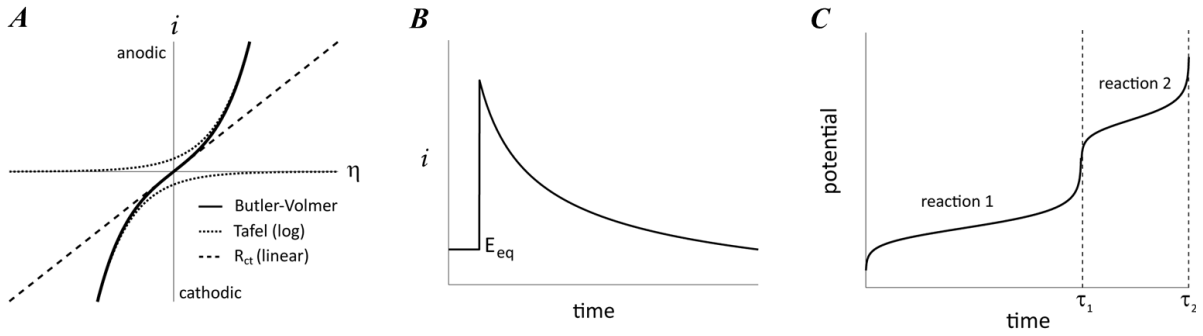

Figure A.1: Relationships Between Current and Potential Across the Electrode Interface

A) The Butler-Volmer equation characterizes the relationship between current and the overpotential when reactants are readily available and mass transport kinetics are negligible. For small potentials, the current-potential relationship is nearly linear. For large potentials, the current-potential relationship becomes logarithmic and is described by the Tafel equation . ***B)*** When a *constant potential* is applied and reactants are consumed at the electrode-electrolyte interface, the reactions mediating charge transfer become mass-transport limited, and the current will progressively decrease as described by the Cotrell equation. ***C)*** When a *constant current* is applied under diffusion-limited conditions, reactants will be depleted within a time, τ, and the potential will shift to the redox potential of a new reaction in order to sustain the necessary charge transfer rate. Figures adapted from Bard & Faulkner, 2001.

a concentration of C^S at the electrode surface. Under these assumptions, η_c can be estimated using a variation of Nernst's Equation: (Bard & Faulkner, 2001)

$$\eta_c = \pm \frac{RT}{nF} \ln\left(\frac{C^*}{C^S}\right) \tag{A.9}$$

where the positive(+) form is used for anodic (oxidative) reactions and the negative (-) form is used for cathodic (reduction) reactions.

The concept of an ideal non-polarizable electrode is used to describe a hypothetical setup in which all current that is passed across the electrode-electrolyte interface is faradaic and the redox reactions that mediate the required charge transfer occur readily enough that the activation overpotential is infinitesimally small. In this case, the electrode does not become polarized as electrical current is passed. This stable behavior is favorable for a reference electrode when recording biopotentials because the voltage signal recorded between the active and reference electrode will be dominated by electrical activity local to the active recording site. The use of a non-polarizable reference is also critical for electrochemical experiments that require a precise measurement of the potential on an electrode in solution. Common electrode materials that demonstrate near non-polarizable behavior are silver/silver-chloride (Ag/AgCl) and saturated calomel.

A.4 Non-faradaic (Capacitive) Currents

In contrast to an ideal non-polarizable electrode, an ideal *polarizable* electrode describes a setup in which *no* charge is transferred across the electrode-electrolyte interface, regardless of the imposed potential. In this case, charge is stored along the electrode surface, which is countered

by oppositely charged ions in solution, leading to an electrical "double-layer". Just the presence of an electrode in solution introduces interactions between the solid and electrolyte that are considerably different than those in solution, even when no potential is applied to the electrode. These interactions involve adsorption, or adhesion, of atoms, ions, biomolecules, and gases that are dissolved in the solution, typically due to weak van der Waals forces and electrostatic attraction. Helmholtz envisaged a thin double layer in which charges on the metal are neutralized by a monomolecular layer of ions of opposite charge. The Helmholtz model predicts a linear change in electrical potential across the double-layer. Gouy and Chapman later introduced a diffuse model of the double-layer in which, ions in solution are not rigidly held to the electrode surface, but form a cloud of diffuse charge in solution that produces a potential gradient that counters the charge on the electrode. The kinetic energy of the counter ions affects the thickness of the diffuse double layer and the concentration of the ions near the electrode surface follows the Boltzman distribution. Stern combined the Helmhotz and Gouy-Chapman models in his theory of the double-layer. According to the Stern model, the finite size of ions prevents them from approaching the electrode surface within a few nm so that a small Helmholtz plane is formed by a molecular layer of water and adsorbed ions, followed by a diffuse layer that extends out into solution. Therefore, the Stern model predicts that the potential will drop linearly across the tightly packed Helmholtz layer and decay exponentially out into solution. More detailed versions of the

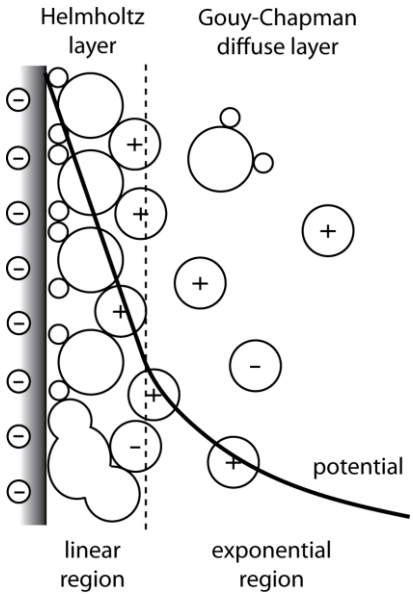

Figure A.2 Capacitive Double-layer

Capacitive double-layer formed by the thin Helmholtz layer and diffuse Gouy-Chapman layer. The thick black line represents the falloff of potential predicted by the Stern model.

Stern model include a molecular water layer at the electrode surface, followed by an inner and outer Helmhotz layer at which electron transfer of redox reactions is proposed to occur, and finally a diffuse layer.

Capacitive charging that results from the separation of charges described by the Helmhotz, Gouy-Chapman and Stern models is termed *electrostatic*. *Electrolytic* capacitive charging results from the storage of charge across a thin, high-dielectric-constant oxide film on the electrode surface. Oxide films may form naturally on exposed electrode surfaces or may be applied directly using electrodeposition and sputtering techniques. In both types of capacitors, the separation of charges across small distances results in a large capacitance across the electrode-electrolyte boundary. This high capacitance produces large capacitve currents with relatively small changes in potential without any direct exchange of electrons across the electrode-electrolyte interface. The relationship between capacitance current and applied voltage is given by:

$$\frac{dV}{dt} = I \cdot \left(\frac{1}{C_H} + \frac{1}{C_{GC}}\right) = \frac{I}{C} \tag{A.10}$$

where dV/dt is the rate of voltage change, I is current, C_H and C_{GC} are the effective capacitances contributed by the Helmholtz and Gouy-Chapman layers, respectively and C is the total capacitance across the electrode-electrolyte interface. In potentiostatic conditions, the current is given by:

$$I(t) = \frac{V}{R} e^{-\frac{t}{RC}} \tag{A.11}$$

where R is a series resistance that may include the resistances of the bulk solution and metal conductor. Under amperostatic conditions, it is clear that the capacitive voltage must vary as a

ramp function, where the slope is directly proportional to the magnitude of current. This property of capacitors is exploited in cyclic voltammetric experiments where the controlled voltage is ramped up and down at a fixed rate so that any variations in current can be attributed to faradaic reactions alone since the capacitive current will be constant.

Due to the direct relationship between capacitance and the area over which charge is separated, etchings and coatings that increase the electrochemical surface area (ESA) beyond that of the geometric surface area (GSA) of an electrode can drastically improve capacitive current injection performance. However, under high current density conditions, porous electrodes with a high ESA/GSA ratio may not have access to their full ESA due to limitations of electrolyte resistance and capacitance on the interior surfaces of the pores, which forms a delay-line with a time constant defined by the pore geometry, electrolyte resistivity, and interfacial double-layer capacitance. (Cogan, 2008) Platinum, Platinum/Iridium alloys, and titanium nitride are common electrode materials used for capacitive bio-electrodes because of their low reactivity in biological tissue.

A.5 Pseudo-capacitive Currents

If a product of a faradaic reaction diffuses away from the electrode surface so that it cannot participate in the reverse redox reaction, the reaction is termed *irreversible* and can have adverse effects on the electrode due to corrosion and also surrounding tissue as byproducts are accumulated. Alternatively, if the products remain close to the electrode surface so that the reactions can be reversed, the reaction is termed *reversible*. For noble metal electrodes like Pt and Pt-Ir alloys, the redox reactions are confined to a thin surface monolayer so that there is a faradaic transfer of electrons across the interface, but the separation of charge across the monolayer

produces capacitive behavior. These types of reactions are described as *pseudocapacitive*. Dielectric coatings like tantalum oxide and iridium oxide films are common materials for producing pseudocapacitive electrodes. (Cogan, 2008)

A.6 Mixed Currents

Most electrodes employ both faradaic and non-faradaic charge transfer mechanisms when transmitting electrical signals across the electrode-electrolyte interface. The ratio of faradaic to non-faradaic charge transfer depends upon properties of the electrode, such as material, size, and roughness, properties of the electrolyte, like concentrations of electroactive species and the associated redox potentials, and also on the magnitudes of current and voltage imposed at the electrode-electrolyte interface. Generally, at low potentials and low current densities, the majority of current will arise from capacitive charge exchange, but as the potential is increased, faradaic currents will become dominate. At sufficiently high voltages, stimulation currents may emerge from the electrolysis of water, which is virtually limitless in biological tissue. Near the cathode, injected electrons will be accepted by hydrogen cations to form hydrogen gas:

$$2H_2O(l) + 2e^- \rightarrow H_2(g) + 2OH^-(aq) \quad \text{(A.12)}$$

Near the anode, electrons stripped from water molecules will result in the production of oxygen gas:

$$2H_2O(l) \rightarrow O_2(g) + 4H^+(aq) + 4e^- \quad \text{(A.13)}$$

The operating region within the potential limits at which electrolysis of water occurs is called the "water window" and operation outside this region should be avoided.

Two common measures of the total amount of charge per unit GSA that is available from an electrode operated within the water window are the charge-injection capacity (Q_{inj}) and the charge-storage capacity (CSC). Q_{inj} is determined by the time integral of a current pulse that is associated with a voltage excursion that just meets the limits defined by the water window, which for platinum electrodes is -0.6 V to +0.8 V. The width of pulses used to determine Q_{inj} vary in literature, but are typically around 200 µsec in length. Q_{inj} is a practical measure of the amount of charge available from an electrode because it is measured directly from current pulsing, which is the most common waveform for stimulating active tissue. CSC is calculated from time integral of total current observed in cyclic voltammetry measurements in which the potential of an electrode is repeatedly ramped between the limits of the water window. It is common to report only the portion of the CSC resulting from cathodic currents (CSC_C) in a slow sweep rate, which is normally in the range of 50 mV/s. CSC is an estimate of the total charge available from an electrode when limitations imposed by mass transport are negligible. In practice, the full CSC is not accessible when stimulating with fast current pulses. (Cogan, 2008)

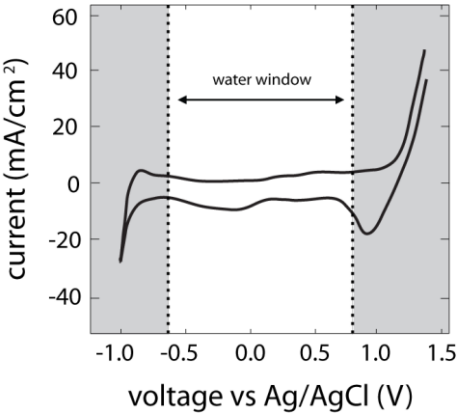

Figure A.3: Water Window

The cyclic voltammogram was measured at 50 mV/s between -1 and 1.5 volts applied to a 300 µm diameter platinum disk electrode. The water window for platinum is defined between -0.6 and 0.8 volts. Beyond these limits, the current displays Tafel behavior as a virtually limitless supply of water is hydrolized.

A.7 Potential and Current Distributions On Disk Electrode Surfaces

When current is passed across an electrode, the current density is often highest at the corners and edges of the electrode. The non-uniform distribution of current is dependent upon the geometry and material of the electrode, the nature of reactions mediating charge transfer, and the concentration gradients of reactants in solution. One of the most commonly encountered electrodes in electrophysiology is the metal disk electrode, and an analytic equation for its current density was provided by the pioneering work of John Newman in 1966 (Newman, 1966). Newman's equations were derived by solving Laplace's equation, $\nabla^2 \Phi = 0$, in elliptical coordinates for a disk electrode embedded in a plane of insulation. Newman made two important assumptions (that defined boundary conditions): 1) the potential is uniform across the surface of the electrode, and 2) mass-transport and reaction kinetics could be ignored. The resulting current distribution is called the *primary distribution* and is given by: (Newman, 1966a)

$$i = \frac{2k\Phi_0}{\pi\sqrt{a^2 - r^2}} \tag{A.14}$$

where i is the linear current density (A/m), k is the solution conductivity, Φ_0 is the uniform potential on the electrode surface, a is the radius of the disk, and r is the radial distance from the center. This equation shows the current density at the center of the electrode is near half of the average (or global) current density for the electrode and that the current density approaches infinity at the edge. Dividing the potential by the integrated current across the electrode surface gives the access resistance R_s: (Newman, 1966a)

$$R_s = \frac{1}{4ka} \tag{A.15}$$

which is seen to be inversely proportional to the electrode radius, a. Newman's equation for the access resistance assumes that the potential falls to zero at an infinite distance from the electrode. Therefore, the equation is valid when a distant reference is used. The accuracy of Newman's equations for the primary distribution and access resistance has been verified experimentally under conditions fitting the assumptions made by Newman (Ahuja, et al., 2008). In particular, these assumptions are met for small, high-frequency signals where the double layer capacitance behaves as a short-circuit. An important consequence of this is that at high frequencies, the impedance of an electrode should approach that of the access resistance, and therefore, the impedance magnitude should be inversely proportional to the electrode radius. Ahula, et al. confirmed this result for platinum electrodes ranging from 11-325 µm. (Ahuja, et al., 2008)

When large current steps or low-frequency signals are applied to an electrode, mass-transport and reaction kinetics can't be ignored and the current density may no longer be described by the primary distribution. Under the extreme condition that all reactants are depleted at the electrode surface, the steady-state current distribution will become uniform (Levich, 1942). In this extreme case, the potential distribution will become non-uniform. Newman analytically derived equations to describe this distribution as well (Newman, 1966b). Under these conditions, the impedance magnitude should be inversely porportional to the electrode area, which was also confirmed by Ahula, et al. for platinum electrodes.

In the study by Ahula, et al., the dependence of impedance magnitude on electrode radius was well fit by a power-law. At high frequencies, the impedance was proportional to $1/R^1$, but as the frequency decreased, the impedance became proportional to $1/R^2$. At intermediate frequencies, the impedance showed a gradual shift between edge dependence and area dependence. This result fits the predicted shift in current distributions proposed by Behrend, et al. based upon finite element models and simulations (Behrend and Weiland, 1966). Behrend showed that when a disk electrode is subjected to a voltage step, the primary current distribution predicted by Newman occurs at t=0. Thereafter, capacitance across the electrode boundary will cause charge to accumulate. The accumulation of charge will occur at a faster rate at the electrode edges due to the primary current

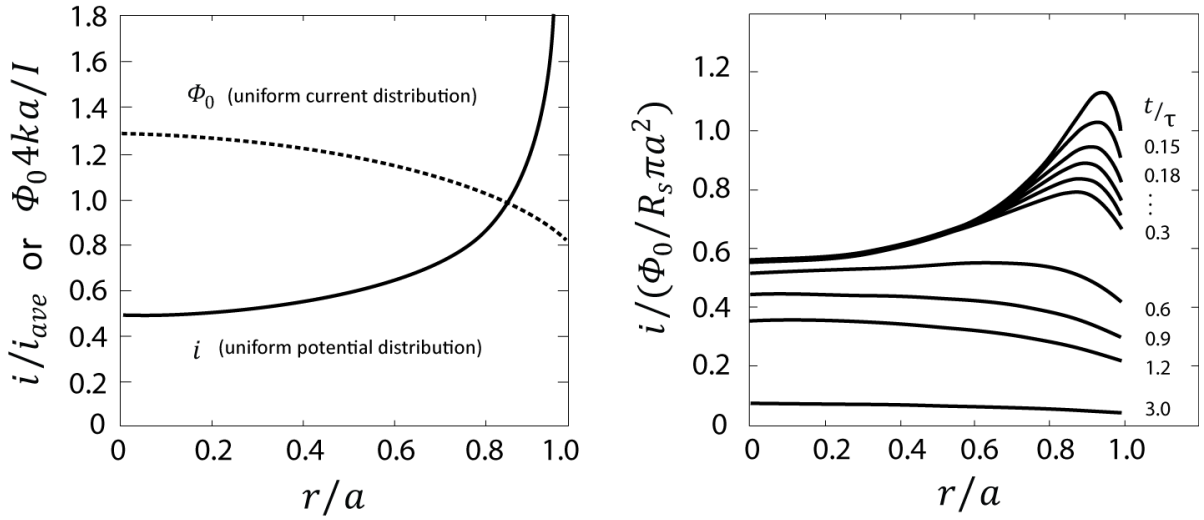

Figure A.4: Newman's Primary and Secondary Distributions

A) Newman's equation gives the primary current distribution that is characterized by large edge effects for a disk electrode at the onset of an applied potential. The primary distribution is maintained as long as reaction and mass-transport kinetics are very fast and the electrode's double layer capacitance is negligible. If mass-transport kinetics are non-negligible, secondary current distributions will occur. When reactants are fully depleted at the electrode-electrolyte interface, the current density will be uniform, but the potential distribution will not. (figure adapted from [6]). ***B)*** When the double layer is non-negligible, the primary distribution will cause non-uniform charging of the double layer, which will result in a time-dependent current density that shifts from the primary distribution to a uniform distribution at a rate characterized by the global time constant ($\tau=RC_{dl}$) of the electrode. Figure adapted from Newman, 1996b.

distribution, which will necessarily cause a disruption of the initially uniform potential field. As the potential field becomes more non-uniform, the edge effects will begin to diminish and the current distribution will tend toward uniformity across the electrode surface. The speed at which this shift in the current distribution occurs is dependent upon the global time constant of the electrode, which is a function of the lumped resistance and capacitance across the interface, $\tau=RC$.

References

Agnew, F., Yuen, H., Mccreery, D. B., & Clayton, C. (1986). Histopathologic Evaluation of Prolonged Electrical Stimulation lntracortical, *185*(I).

Ahuja, A. K., Behrend, M. R., Whalen III, J. J., Humayun, M. S., & Weiland, J. D. (2008). The Dependence of Spectral Impedance on Disc Microelectrode Radius. *IEEE transactions on bio-medical engineering*, *55*(4), 1457–1460. doi:10.1109/TBME.2007.912430.The

Anderson, J. M., Rodriguez, A., & Chang, D. T. (2009). Foreign body reaction to biomaterials. *Semin Immunol.*, *20*(2), 86–100.

Andreas Elschner, H.C. Starck GmbH, Leverkusen, Germany; Stephan Kirchmeyer, H.C. Starck GmbH, Leverkusen, Germany; Wilfried Lovenich, H.C. Starck GmbH, Leverkusen, Germany; Udo Merker, H.C. Starck GmbH, Leverkusen, Germany; Knud Reuter, H.C. Starck GmbH, G. (2011). Conductive Polymers versus Metals and Insulators. In *PEDOT: Principles and Applications of an Intrinsically Conductive Polymer* (pp. 21–30).

Balossier, A., Etard, O., Descat, C., & Vivien D, E. E. (2012). Epidural electrical stimulation to improve chronic poststroke aphasia: a 5-year follow-up. *Brain Stimulation1*, *5*(3), 364–368.

Bard, A. J., & Faulkner, L. R. (2001). *Electrochemical Methods: Fundamentals and Applications*. (D. Harris & E. Swain, Eds.) (2nd ed.). New York: Wiley.

Behrend, M. R., Ahuja, A. K., & Weiland, J. D. (2008). Dynamic current density of the disk electrode double-layer. *IEEE transactions on bio-medical engineering*, *55*(3), 1056–62. doi:10.1109/TBME.2008.915723

Brown, E. N., Frank, L. M., Tang, D., Quirk, M. C., & Wilson, M. a. (1998). A statistical paradigm for neural spike train decoding applied to position prediction from ensemble firing patterns of rat hippocampal place cells. *Journal of Neuroscience*.

https://doi.org/10.1523/JNEUROSCI.18-18-07411.1998

Brown, J. A., Lutsep, H., Cramer, S. C., & Weinand, M. (2003). Motor cortex stimulation for enhancement of recovery after stroke: case report. *Neurol Res*, *25*, 815–818.

Brug, G. J., van den Eeden, A. L. G., Sluyters-Rehbach, M., & Sluyters, J. H. (1984). The analysis of electrode impedances complicated by the presence of a constant phase element. *Journal of Electroanalytical Chemistry*, *176*, 275–295.

Brummer, S B, Robblee, L. S., & Hambrecht, T. (1983). Criteria for selecting electrodes for electrical stimulation: theoretical and practical considerations. *Annals of the New York Academy of …*, 159–171.

Brummer, S B, & Turner, M. J. (1977). Electrical stimulation with Pt electrodes: II-estimation of maximum surface redox (theoretical non-gassing) limits. *IEEE transactions on bio-medical engineering*, *24*(5), 440–3. Retrieved from http://www.ncbi.nlm.nih.gov/pubmed/892838

Brummer, S. B., & Turner, M. J. (1975). Electrochemical considerations for safe electrical stimulation of the nervous system with platinum electrodes. *IEEE transactions on biomedical engineering*, *24*, 59–63.

Brummer, S. B., & Turner, M. J. (1977). Electrical stimulation with Pt electrodes. I. A method for determination of "real" electrode areas. *IEEE transactions on biomedical engineering*, *24*(436-439).

Bundy, D. T., Zellmer, E., Gaona, C. M., Sharma, M., Szrama, N., Hacker, C., … Eric, C. (2015). Characterization of the Effects of the Human Dura on Macro- and Micro-Electrocorticographic Recordings. *Journal of Neural Engineering*, *11*(1), 1–22.

Buzsáki, G., Anastassiou, C. a, & Koch, C. (2012). The origin of extracellular fields and currents--EEG, ECoG, LFP and spikes. *Nature Reviews. Neuroscience*, *13*(6), 407–420. https://doi.org/10.1038/nrn3241

Cicuendez, M., Munarriz, P. M., Castano-Leon, A. M., & Paredes, I. (2012). Dorsal myelopathy secondary to epidural fibrous scar tissue around a spinal cord stimulation electrode. *Journal of Neurosurgery: Spine*, *17*(6), 598–601.

Collinger, J. L., Wodlinger, B., Downey, J. E., Wang, W., Tyler-Kabara, E. C., Weber, D. J., … Schwartz, A. B. (2013). High-performance neuroprosthetic control by an individual with tetraplegia. *The Lancet*. https://doi.org/10.1016/S0140-6736(12)61816-9

Cogan, S. F. (2008). Neural stimulation and recording electrodes. *Annual review of biomedical engineering*, *10*, 275–309. doi:10.1146/annurev.bioeng.10.061807.160518

Cogan, S. F., & Model, A. A. (2006). In vivo and in vitro differences in the charge-injection and electrochemical properties of iridium oxide electrodes. *IEEE EMBS Conference, New York City, USA*, 882–885.

Cole, K. S. (1940). Permeability and Impermeability of Cell Membranes for Ions. *Cold Spring Harbor Symposia on Quantitative Biology*, *8*, 110–122. doi:10.1101/SQB.1940.008.01.013

Crone, N. E., Sinai, A., & Korzeniewska, A. (2006). High-frequency gamma oscillations and human brain mapping with electrocorticography. *Progress in Brain Research*, *159*, 275–295. https://doi.org/10.1016/S0079-6123(06)59019-3

Dymond, a M. (1976). Characteristics of the metal-tissue interface of stimulation electrodes. *IEEE transactions on bio-medical engineering*, *23*(4), 274–80. Retrieved from http://www.ncbi.nlm.nih.gov/pubmed/776814

Fountas, K. N. (2011). Implanted subdural electrodes: safety issues and complication avoidance. *Neurosurgery clinics of North America*, *22*(4), 519–31, vii. doi:10.1016/j.nec.2011.07.009

Fujioka, H., Urasaki, E., Izumihara, A., & Yamashita, K. (2018). Epidural motor cortex stimulation for intractable leg pain. *Clinical Neurophysiology*. https://doi.org/10.1016/j.clinph.2018.01.007

Geddes, L. a. (1997). Historical evolution of circuit models for the electrode-electrolyte interface. *Annals of biomedical engineering*, *25*(1), 1–14. Retrieved from http://www.ncbi.nlm.nih.gov/pubmed/9124725

Geddes, L. a., & Roeder, R. (2003). Criteria for the Selection of Materials for Implanted Electrodes. *Annals of Biomedical Engineering*, *31*(7), 879–890. doi:10.1114/1.1581292

Georgopoulos, A. P., Schwartz, A. B., & Kettner, R. E. (1986). Neuronal population coding of movement direction. *Science*. https://doi.org/10.1126/science.3749885

Göbbels, K., Kuenzel, T., van Ooyen, A., Baumgartner, W., Schnakenberg, U., & Bräunig, P. (2010). Neuronal cell growth on iridium oxide. *Biomaterials*, *31*(6), 1055–67. doi:10.1016/j.biomaterials.2009.10.029

Green, R a, Matteucci, P. B., Hassarati, R. T., Giraud, B., Dodds, C. W. D., Chen, S., … Lovell, N. H. (2013). Performance of conducting polymer electrodes for stimulating neuroprosthetics. *Journal of neural engineering*, *10*(1), 016009. doi:10.1088/1741-2560/10/1/016009

Green, R. A., Poole-warren, L. A., Lovell, N. H., & Member, S. (2007). Novel Neural Interface for Vision Prosthesis Electrodes : Improving Electrical and Mechanical Properties through Layering. *IEEE EMBS Conference on Neural Engineering, Kohala Coast, Hawaii*, (Cv), 97–100.

Green, Rylie a, Lovell, N. H., Wallace, G. G., & Poole-Warren, L. a. (2008). Conducting polymers for neural interfaces: challenges in developing an effective long-term implant. *Biomaterials*, *29*(24-25), 3393–9. doi:10.1016/j.biomaterials.2008.04.047

Grill, W. M., & Mortimer, J. T. (n.d.). Electrical properties of implant encapsulation tissue. *Annals of biomedical engineering*. Retrieved from http://www.ncbi.nlm.nih.gov/pubmed/8060024

Grimnes, S., Rikshospitalet, O., & Schwan, N. (2002). Interface Phenomena and Dielectric Properties of Biological Tissue. In P. Somasundaran (Ed.), *Encyclopedia of Surface and*

Colloid Science (2nd ed., pp. 2643–2652). CRC Press. Retrieved from https://www.matnat.uio.no/fysikk/english/research/projects/bioimpedance/publications/papers/encyclop.pdf

Harrison, R. R. R., & Charles, C. (2003). A low-power low-noise CMOS amplifier for neural recording applications. *IEEE Journal of Solid-State Circuits*, *38*(6), 958–965. https://doi.org/10.1109/JSSC.2003.811979

Heffner, H. E., & Heffner, R. S. (1995). Conditioned Avoidance. In *Methods in Comparative Psychoacoustics (Biomethods)* (pp. 79–93).

Heldman, D. A., Wang, W., Chan, S. S., & Moran, D. W. (2006). Local field potential spectral tuning in motor cortex during reaching. *IEEE Transactions on Neural Systems and Rehabilitation Engineering : A Publication of the IEEE Engineering in Medicine and Biology Society*, *14*(2), 180–183. https://doi.org/10.1109/TNSRE.2006.875549

Hiremath, S. V., Tyler-Kabara, E. C., Wheeler, J. J., Moran, D. W., Gaunt, R. A., Collinger, J. L., … Wang, W. (2017). Human perception of electrical stimulation on the surface of somatosensory cortex. *PLoS ONE*. https://doi.org/10.1371/journal.pone.0176020

Hochberg, L. R., Bacher, D., Jarosiewicz, B., Masse, N. Y., Simeral, J. D., Vogel, J., … Donoghue, J. P. (2012). Reach and grasp by people with tetraplegia using a neurally controlled robotic arm. *Nature*. https://doi.org/10.1038/nature11076

Huang, M., Harvey, R. L., Stoykov, M. E., Ruland, S., Weinand, M., Lowry, D., & Levy, R. (2008). Cortical stimulation for upper limb recovery following ischemic stroke: a small phase II pilot study of a fully implanted stimulator. *Topics in stroke rehabilitation*, *15*(2), 160–72. doi:10.1310/tsr1502-160

Huang, V. M.-W., Vivier, V., Frateur, I., Orazem, M. E., & Tribollet, B. (2007). The Global and Local Impedance Response of a Blocking Disk Electrode with Local Constant-Phase-Element Behavior. *Journal of The Electrochemical Society*, *154*(2), C89. doi:10.1149/1.2398889

Katayama, Y., Oshima, H., Fukaya, C., Kawamata, T., & Yamamaoto, T. (2002). Control of post-stroke movement disorders using chronic motor cortex stimulation. *Acta Neurochir Suppl.*, *79*, 89–92.

Kim, J., Wilson, J. A., Williams, J. C., Microfabrication, A., & Arrays, E. (2007). A Cortical Recording Platform Utilizing μ ECoG Electrode Arrays, *2721*(c), 5353–5357.

Koivuniemi, A. S., Regele, O. B., Brenner, J. H., & Otto, K. J. (2011). Rat behavioral model for high-throughput parametric studies of intracortical microstimulation. *Conference Proceedings : ... Annual International Conference of the IEEE Engineering in Medicine and Biology Society. IEEE Engineering in Medicine and Biology Society. Conference*, *2011*, 7541–7544. https://doi.org/10.1109/IEMBS.2011.6091859

Kopell, B. H., Halverson, J., Butson, C. R., Dickinson, M., Rbholz, J., Harsch, H., … Dougherty, D. D. (2011). Epidural cortical stimulation of the left dorsolateral prefrontal cortex for refractory major depressive disorder. *Neurosurgery*, *69*(5), 1015–1029.

Koyama, S., Castellanos Pérez-Bolde, L., Rohilla Shalizi, C., & Kass, R. E. (2010). Approximate methods for state-space models. *Journal of the American Statistical Association*. https://doi.org/10.1198/jasa.2009.tm08326

Leek, M. R. (2001). Adaptive procedures in psychophysical research. *Perception & Psychophysics*. https://doi.org/10.3758/BF03194543

Lempka, S. F., Miocinovic, S., Johnson, M. D., Vitek, J. L., Mcintyre, C. C., Engineering, B., & Foundation, C. C. (2010). In vivo impedance spectroscopy of deep brain stimulation electrodes. *Journal of neural engineering*, *6*(4), 1–20. doi:10.1088/1741-2560/6/4/046001.In

Leuthardt, E. C., Pei, X.-M., Breshears, J., Gaona, C., Sharma, M., Freudenberg, Z., … Schalk, G. (2012). Temporal evolution of gamma activity in human cortex during an overt and covert word repetition task. *Frontiers in Human Neuroscience*, *6*, 99. https://doi.org/10.3389/fnhum.2012.00099

Levich, B. (1942). The Theory of Concentration Polarization. *Acta Physicochimica URSS*, *17*,

257–307.

Levy, R., Ruland, S., Weinand, M., Lowry, D., Dafer, R., & Bakay, R. (2008). Cortical stimulation for the rehabilitation of patients with hemiparetic stroke: a multicenter feasibility study of safety and efficacy. *Journal of neurosurgery*, *108*(4), 707–14. doi:10.3171/JNS/2008/108/4/0707

Lu, Y., Li, T., Zhao, X., Li, M., Cao, Y., Yang, H., & Duan, Y. Y. (2010). Electrodeposited polypyrrole/carbon nanotubes composite films electrodes for neural interfaces. *Biomaterials*, *31*(19), 5169–81. doi:10.1016/j.biomaterials.2010.03.022

Luo, X., Weaver, C. L., Zhou, D. D., Greenberg, R., & Cui, X. T. (2011). Highly stable carbon nanotube doped poly(3,4-ethylenedioxythiophene) for chronic neural stimulation. *Biomaterials*, *32*(24), 5551–7. doi:10.1016/j.biomaterials.2011.04.051

Marzouk, S. A. M., Ufer, S., Buck, R. P., Johnson, T. A., Dunlap, L. A., & Casico, W. E. (1998). Electrodeposited iridium oxide pH electrode for measurement of extracellular myocardial acidosis during acute ischemia. *Anal. Chem.*, *70*, 5054–5061.

McAdams, E. T., Lackermeier, A., McLaughlin, J. A., & Macken, D. (1995). The linear and non-linear electrical properties of the electrode-electrolyte interface. *Biosensors & Bioelectronics*, *10*, 67–74.

McConnell, G. C., Butera, R. J., & Bellamkonda, R. V. (2009). Bioimpedance modeling to monitor astrocytic response to chronically implanted electrodes. *Journal of neural engineering*, *6*(5), 055005. doi:10.1088/1741-2560/6/5/055005

Merrill, D. R., Bikson, M., & Jefferys, J. G. R. (2005). Electrical stimulation of excitable tissue: design of efficacious and safe protocols. *Journal of neuroscience methods*, *141*(2), 171–98. doi:10.1016/j.jneumeth.2004.10.020

Meyer, R. D., Cogan, S. F., Nguyen, T. H., & Rauh, R. D. (2001). Electrodeposited iridium oxide for neural stimulation and recording electrodes. *IEEE transactions on neural systems and rehabilitation engineering*, *9*(1), 2–11. doi:10.1109/7333.918271

Miller, K. J., Leuthardt, E. C., Schalk, G., Rao, R. P. N., Anderson, N. R., Moran, D. W., … Ojemann, J. G. (2007). Spectral changes in cortical surface potentials during motor movement. *The Journal of Neuroscience : The Official Journal of the Society for Neuroscience*, *27*(9), 2424–2432. https://doi.org/10.1523/JNEUROSCI.3886-06.2007

Molina-Luna, K., Buitrago, M. M., Hertler, B., Schubring, M., Haiss, F., Nisch, W., … Luft, A. R. (2007). Cortical stimulation mapping using epidurally implanted thin-film microelectrode arrays. *Journal of neuroscience methods*, *161*(1), 118–25. doi:10.1016/j.jneumeth.2006.10.025

Moran, D. (2010). Evolution of brain-computer interface: action potentials, local field potentials and electrocorticograms. *Current opinion in neurobiology*, *20*(6), 741–5. doi:10.1016/j.conb.2010.09.010

Myland, J. C., & Oldham, K. B. (2005). How does the double layer at a disk electrode charge? *Journal of Electroanalytical Chemistry*, *575*(1), 81–93. doi:10.1016/j.jelechem.2004.09.004

Nadol, J. B., Shiao, J. Y., Burgess, B. J., Ketten, D. R., Eddington, D. K., Gantz, B. J., … Shallop, J. K. (2001). Histopathology of cochlear implants in humans. *The Annals of otology, rhinology, and laryngology*, *110*(9), 883–91. Retrieved from http://www.ncbi.nlm.nih.gov/pubmed/11558767

Nahas, Z., Anderson, B. S., Borckardt, J., Arana, A. B., George, M. S., Reeves, S. T., & Takacs, I. (2010). Bilateral epidural prefrontal cortical stimulation for treatment-resistant depression. *Biological psychiatry*, *67*(2), 101–9. doi:10.1016/j.biopsych.2009.08.021

Newbold, C., Richardson, R., Millard, R., Huang, C., Milojevic, D., Shepherd, R., & Cowan, R. (2010). Changes in biphasic electrode impedance with protein adsorption and cell growth. *Journal of neural engineering*, *7*(5), 056011. doi:10.1088/1741-2560/7/5/056011

Newman, J. (1966a). Resistance for Flow of Current to a Disk. *Journal of The Electrochemical Society*, *113*(5), 501. doi:10.1149/1.2424003

Newmann, J. (1966b). Current Distribution on a Rotating Disk below the Limiting Current. *Journal of The Electrochemical Society*, *113*(12), 1235. doi:10.1149/1.2423795

Nguyen, J. P., Pollin, B., Fève, a, Geny, C., & Cesaro, P. (1998). Improvement of action tremor by chronic cortical stimulation. *Movement disorders : official journal of the Movement Disorder Society*, *13*(1), 84–8. doi:10.1002/mds.870130118

Nikola, J., Ratko, P., Strahinja, D., & Dejan, P. B. (2001). A novel AC-amplifier for electrophysiology: Active DC suppression with differential to differential amplifier in the feedback-loop. In *Annual Reports of the Research Reactor Institute, Kyoto University*. https://doi.org/10.1109/IEMBS.2001.1019538

Nunez, P. L., & Srinivasan, R. (2006). *Electric Fields of the Brain*. *Oxford University Press*. https://doi.org/10.1093/acprof:oso/9780195050387.001.0001

O'Doherty, J. E., Lebedev, M. A., Ifft, P. J., Zhuang, K. Z., Shokur, S., Bleuler, H., & Nicolelis, M. A. L. (2011). Active tactile exploration using a brain-machine-brain interface. *Nature*. https://doi.org/10.1038/nature10489

Orsborn, A. L., Moorman, H. G., Overduin, S. A., Shanechi, M. M., Dimitrov, D. F., & Carmena, J. M. (2014). Closed-loop decoder adaptation shapes neural plasticity for skillful neuroprosthetic control. *Neuron*. https://doi.org/10.1016/j.neuron.2014.04.048

Otto, K. J., Johnson, M. D., & Kipke, D. R. (2006). Voltage Pulses Change Neural Interface Properties and Improve Unit Recordings With Chronically Implanted Microelectrodes. *IEEE transactions on biomedical engineering*, *53*(2), 333–340.

Penfield, W. (1939). The epilepsies: with a note on radical therapy. *New England Journal of Medicine*, *221*, 209–218.

Penfield, W., & Boldrey, E. (1937). Somatic motor and sensory representations in the cerebral cortex of man as studied by electrical stimulation. *Brain*, *60*, 389–443.

Pliquett, F., & Pliquett, U. (1999). Stress action on biological tissue and tissue models detected by the py value. *Annals of the New York Academy of …*. Retrieved from http://onlinelibrary.wiley.com/doi/10.1111/j.1749-6632.1999.tb09471.x/full

Reilly, J. P. (1998). Applied Bioelectricity: From Electrical Stimulation to Electropathology. In *Applied Bioelectricity*. https://doi.org/10.1007/978-1-4612-1664-3_1

Romito, L. M., Franzini, a, Perani, D., Carella, F., Marras, C., Capus, L., … Albanese, a. (2007). Fixed dystonia unresponsive to pallidal stimulation improved by motor cortex stimulation. *Neurology*, *68*(11), 875–6. doi:10.1212/01.wnl.0000256816.83036.c9

Rouse, A. G., & Moran, D. W. (2009). Neural adaptation of epidural electrocorticographic (EECoG) signals during closed-loop brain computer interface (BCI) tasks. *Conference Proceedings : IEEE Engineering in Medicine and Biology Society.*, 5514–5517. https://doi.org/10.1109/IEMBS.2009.5333180

Rouse, A. G., Stanslaski, S. R., Cong, P., Jensen, R. M., Afshar, P., Ullestad, D., … Denison, T. J. (2011). A chronic generalized bi-directional brain-machine interface. *Journal of Neural Engineering*, *8*(3), 036018. https://doi.org/10.1088/1741-2560/8/3/036018

Rouse, A. G., Williams, J. J., Wheeler, J. J., & Moran, D. W. (2013). Cortical adaptation to a chronic micro-electrocorticographic brain computer interface. *J. Neurosci.*, *33*, 1326–1330.

Rozlosnik, N. (2009). New directions in medical biosensors employing poly(3,4-ethylenedioxy thiophene) derivative-based electrodes. *Analytical and bioanalytical chemistry*, *395*(3), 637–45. doi:10.1007/s00216-009-2981-8

Rubehn, B., Bosman, C., Oostenveld, R., Fries, P., & Stieglitz, T. (2009). A MEMS-based flexible multichannel ECoG-electrode array. *Journal of neural engineering*, *6*(3), 036003. doi:10.1088/1741-2560/6/3/036003

Rubinstein, J. T., Spelman, F. a, Soma, M., & Suesserman, M. F. (1987). Current density profiles of surface mounted and recessed electrodes for neural prostheses. *IEEE transactions on bio-*

medical engineering, *34*(11), 864–75. Retrieved from http://www.ncbi.nlm.nih.gov/pubmed/3319885

Salinas, E., & Abbott, L. F. (1994). Vector reconstruction from firing rates. *Journal of Computational Neuroscience*. https://doi.org/10.1007/BF00962720

Schalk, G., Miller, K. J., Anderson, N. R., Wilson, J. A., Smyth, M. D., Ojemann, J. G., … Leuthardt, E. C. (2008). Two-dimensional movement control using electrocorticographic signals in humans. *Journal of Neural Engineering*, *5*(1), 75–84. https://doi.org/10.1088/1741-2560/5/1/008

Shannon, R. V. (1992). A model of safe levels for electrical stimulation. *IEEE transactions on biomedical engineering*, *39*(4), 424–426.

Schmit, B. D., & Mortimer, J. T. (1997). The tissue response to epimysial electrodes for diaphragm pacing in dogs. *IEEE transactions on bio-medical engineering*, *44*(10), 921–30. doi:10.1109/10.634644

Stanslaski, S., Afshar, P., Cong, P., Giftakis, J., Stypulkowski, P., Carlson, D., … Denison, T. (2012). Design and validation of a fully implantable, chronic, closed-loop neuromodulation device with concurrent sensing and stimulation. *IEEE Trans Neural Syst Rehabil Eng*, *20*(4), 410–421.

Stensaas, S. S., & Stensaas, L. J. (1978). Histopathological evaluation of materials implanted in the cerebral cortex. *Acta Neuropathol*, *41*, 145–155.

Stroncek, J. D., & Reichert, W. M. (2008). Overview of Wound Healing in Different Tissue Types. In W. M. Reichert (Ed.), *Indwelling Neural Implants: Strategies for Contending with the In Vivo Environment* (pp. 1–26). Boca Raton: CRC Press.

Taylor, D. M., Tillery, S. I. H., & Schwartz, A. B. (2002). Direct cortical control of 3D neuroprosthetic devices. *Science (New York, N.Y.)*. https://doi.org/10.1126/science.1070291

Venkatraman, S., Hendricks, J., King, Z. a, Sereno, A. J., Richardson-Burns, S., Martin, D., & Carmena, J. M. (2011). In vitro and in vivo evaluation of PEDOT microelectrodes for neural stimulation and recording. *IEEE transactions on neural systems and rehabilitation engineering*, *19*(3), 307–16. doi:10.1109/TNSRE.2011.2109399

Wang, W., Collinger, J. L., Degenhart, A. D., Tyler-Kabara, E. C., Schwartz, A. B., Moran, D. W., … Boninger, M. L. (2013). An electrocorticographic brain interface in an individual with tetraplegia. *PloS One*, *8*(2), e55344. https://doi.org/10.1371/journal.pone.0055344

Wheeler, J. J., Baldwin, K., Kindle, A., Guyon, D., Nugent, B., Segura, C., … Eskandar, E. N. (2015). An implantable 64-channel neural interface with reconfigurable recording and stimulation. In *Proceedings of the Annual International Conference of the IEEE Engineering in Medicine and Biology Society, EMBS*. https://doi.org/10.1109/EMBC.2015.7320208

Wilks, S. J., Koivuniemi, A. S., Thongpang, S., Williams, J. C., & Otto, K. J. (2009). Evaluation of micro-electrocorticographic electrodes for electrostimulation. *IEEE Engineering in Medicine and Biology Society: Conference proceedings*, *2009*, 5510–3. doi:10.1109/IEMBS.2009.5333178

Wilks, S. J., Richardson-burns, S. M., Hendricks, J. L., Martin, D. C., & Otto, K. J. (2009). Poly (3 , 4-ethylenedioxythiophene) as a micro-neural interface material for electrostimulation. *Frontiers in neuroengineering*, *2*(June), 1–8. doi:10.3389/neuro.16.007

Williams, J. C., Hippensteel, J. a, Dilgen, J., Shain, W., & Kipke, D. R. (2007). Complex impedance spectroscopy for monitoring tissue responses to inserted neural implants. *Journal of neural engineering*, *4*(4), 410–23. doi:10.1088/1741-2560/4/4/007

Williams, J. J., Rouse, A. G., Thongpang, S., Williams, J. C., & Moran, D. W. (2013). Differentiating closed-loop cortical intention from rest: building an asynchronous electrocorticographic BCI. *Journal of neural engineering*, *10*(4), 1–15. doi:10.1088/1741-2560/10/4/046001

Wongsarnpigoon, A., & Grill, W. M. (2008). Computational modeling of epidural cortical

stimulation. *Journal of Neural Engineering*, *5*(4), 443–454. https://doi.org/10.1088/1741-2560/5/4/009

Wongsarnpigoon, A., & Grill, W. M. (2009). Genetic algorithm reveals energy-efficient waveforms for neural stimulation. In *Proceedings of the 31st Annual International Conference of the IEEE Engineering in Medicine and Biology Society: Engineering the Future of Biomedicine, EMBC 2009*. https://doi.org/10.1109/IEMBS.2009.5333722

Yamamoto, T., Katayama, Y., Watanabe, M., Sumi, K., Obuchi, T., Kobayashi, K., … Fukaya, C. (2011). Changes in motor function induced by chronic motor cortex stimulation in post-stroke pain patients. *Steriotact Funct Neurosurg*, *89*, 381–389.

Yamanaka, K. (1989). Anodically electrodeposited iridium oxide films (AEIROF's) from alkaline solutions for electrochromic display devices. *Jpn. J. Appl. Phys.*, *28*, 632–637.

Zaghi, S., Heine, N., & Fregni, F. (2010). Brain stimulation for the treatment of pain: A review of costs, clinical effects, and mechanisms of treatment for three different central neuromodulatory approaches. *Journal of Pain Management*, *2*(3), 339–352.

Zhang, Y., & Chase, S. M. (2015). Recasting brain-machine interface design from a physical control system perspective. *Journal of Computational Neuroscience*. https://doi.org/10.1007/s10827-015-0566-4